University of Mississippi

eGrove

Electronic Theses and Dissertations | Graduate School

1-1-2011

Nano-Materials By Design and Their Applications in Infrastructure

Hunain Said Alkhateb
University of Mississippi

Follow this and additional works at: https://egrove.olemiss.edu/etd

 Part of the Engineering Commons

Recommended Citation

Alkhateb, Hunain Said, "Nano-Materials By Design and Their Applications in Infrastructure" (2011). *Electronic Theses and Dissertations*. 1371.
https://egrove.olemiss.edu/etd/1371

This Dissertation is brought to you for free and open access by the Graduate School at eGrove. It has been accepted for inclusion in Electronic Theses and Dissertations by an authorized administrator of eGrove. For more information, please contact egrove@olemiss.edu.

NANO-MATERIALS BY DESIGN AND THEIR APPLICATIONS IN INFRASTRUCTURE

A Dissertation
presented in partial fulfillment of requirement
for the degree of Doctor of Philosophy
in Engineering Science
The University of Mississippi

by

HUNAIN SAID ALKHATEB

May-2011

Copyright Hunain S. Alkhateb 2011
All RIGHTS RESERVED

ABSTRACT

For utilizing nano materials in infrastructure applications, they should exist in huge quantities, in low cost, and they should be applied efficiently to achieve the ultimate goal design, based on fundamental mechanical and physical laws. To achieve this goal multiscale characterization and modeling is needed to deliver our thorough application effectively. The main objective in this research is to implement multiscale characterization of the nano-micro-meso-macro properties of advanced polymeric and cementitious nanocomposites, to correlate mechanical properties to morphology. This include joint experimental-theoretical approach.

Molecular modeling simulations are employed for an efficient investigation of the mechanical properties of the controlling factors and compatibility of the material design such as; individual constituents properties, interfacial strength, and the composite properties and architecture, at the atomic level.

Atomic force microscopy is utilized for imaging and phase identification at the nanoscale. Scanning electron microscopy is used for mapping the different phases and surface structures in depth at the microscale with a wide range of magnifications. For the chemical composition analysis, x-ray diffraction technique is used to identify information about the chemical composition for designed materials and to connect the quantitative analysis with the physical properties of nano-materials. Electrical impedance spectroscopy measurements are used to evaluate the electrochemical behavior of deigned materials at different moisture contents are

conducted at the mesoscale. Resonance ultrasound spectroscopy, a non destructive method, which utilizes the resonance spectrum is used, to measure the mechanical properties of the material of interest. However, the resonance spectrum depends on the geometry, mass, and density of the examined specimen. Finally, a destructive testing is conducted to measure the elastic modulus and Poisson's ratio of these materials. Stress strain and maximum stress obtained data is recorded for the different samples.

Findings from this work are at the cutting edge to a better understanding of the complex macroscopic phenomena. It provide inputs for multiscale modeling and enhance the mechanical, physical, electrical and chemical relations for advanced engineered materials design.

DEDICATION

All praise and gratitude is due to God.

Thence, this accomplishment is dedicated to my family.

To my family in Palestine, especially my grandmother Um-Nimer, who had a dream that came true, regardless of all her pain and suffering she has been through. I would like to honor my father, Dr.Said Alkhatib, my mother Mrs. Yusra Abu Haweleh, my sisters Alaa, Isra, Ro'aya, my brothers Nimer, Mohammad and Omar, and finally to my little niece Salma. I have no doubt in mind that I would not have completed this accomplishment without their continuous support, extensive care, and unconditional love.

LIST OF ABBREVIATIONS

MD molecular dynamics

MWCNT multi-walled carbon nanotubes

SWCNT single-walled carbon nanotubes

DWCNT double-walled carbon nanotubes

CNT carbon nanotube

GICs graphite intercalated compounds

MM molecular mechanics

VGCF vapor grown carbon fiber

vdW van der Waals

AFM Atomic Force Microscopy

TEM Transmission Electron Microscopy

SEM Scanning Electron Microscopy

RUS Resonant Ultrasound Spectroscopy

EIS Electrochemical Impedance Spectroscopy

TGA Thermal Gravimetric Analysis

XRD X-ray diffraction

MTS Material Testing Systems

2D two dimensional

N number of particles

V Volume

E Energy

P Pressure

T Temperature

H Enthalpy

NMR Nuclear magnetic resonance

COMPASS Condensedphase Optimized Molecular Potentials for Atomistic Simulation Studies

xGnP exfoliated graphene nano platelets

Tg glass transition

C-S-H Calcium Silicate-Hydrate

CH Calcium Hydrate

HD high density

LD low density

ACKNOWLEDGEMENTS

All praise and gratitude is due to God.

Thence, I would like to thank all those who have helped, inspired and supported me through my doctoral study.

I especially want to thank my advisor Dr.Ahmed Al-Ostaz, for his guidance during my research and study at University of Mississippi. His perpetual energy, enthusiasm in research, and all his advice had motivated me. In addition, he was always accessible and willing to help all his students with their research, which resulted in this fruitful dissertation. I was enchanted to interact with him, for his passion in nanotechnology, suggestions and contributions.

I would like to extend my appreciation to my committee members: Prof. Cheng from the civil engineering department and the dean of the engineering school, Prof. O'Haver, from the chemical engineering department and the associate dean of the school of engineering, Prof.Rajendran, professor and chair of the mechanical engineering department, and Dr. Song, associate professor at the civil engineering department. I greatly appreciate their valuable thoughts and constructive suggestions, through my class work, through my research, and my dissertation work.

I would like to express my thanks to Dr. Josh Gladden and his Graduate student, Rasheed Adebisi, from the physics department at the University of Mississippi for their expedited help

to use the RUS to test the elastic properties of my cementitious nanocomposites. I would also like to thank Dr.Ellen Lackey and Dr.James Vaughan, from the mechanical engineering department at the University of Mississippi, who gave me access to their SEM instrument and manufacturing laboratories and for training and helping me in imaging my samples. I would like to mention Dr.John O'Haver and his Graduate student Poh Lee Cheah, from the chemical engineering department at the University of Mississippi for the unlimited access to the AFM instrument, for training, and for the long discussions with Dr.O' regarding imaging, eduction, and cooking. I am also grateful to my friends Dr.Mohammad Irshidat and Dr.Wediong Wu for providing support and creating a friendly and productive work environment. I also acknowledge my colleague Dr.Xiaobing Li for his guidance, help, and support in preparing my samples, especially the dispersion and dilution of my nano additives.

I sincerely thank all my teachers and professors who have inspired me in a way or another, who have enhanced my knowledge even through a small piece of information and who have guided me through constructive support and suggestions. To all my friends and mates in the lab and classes for their unremitting encouragement and great moments we had shared together through the five years towards my masters and doctoral work.

I would like to thank my family, especially my parents. Without them, I would have never achieved what I have been until now and what I ll be in the future. I would also like to thank my special friend Buthaina Jaradat she was the first who introduced me to this great opportunity for graduate school. Her endless support and elongated phone calls through my five year graduate school path had a fruitful impact and inspiration on me.

Finally, the funding received under a subcontract from the Department of Homeland Security-sponsored Southeast Region Research Initiative (SERRI) at the Department of

Energy's Oak Ridge National Laboratory.

Table of Contents

List of Tables

List of Figures

1. INTRODUCTION

1.1 Literature Review

1.1.1 Molecular Dynamics Simulations of Nanocomposites and Constituents

Nanoscience has been defined by Dowling [1] as the study of phenomena and the manipulation of materials at atomic, molecular, and macromolecular scales, where properties differ significantly from those at larger scales. However, nanotechnology is concerned about the design, characterization, production, developing, and application of structures sized between 1-100 nm in at least one dimension. Nanotechnology is very diverse and cuts across and extends many scientific disciplines. It embraces a wide range of materials, tools, and approaches [1].

The first use of the concepts found in "nano-technology" was in "There's Plenty of Room at the Bottom" a talk given by physicist Richard Feynman 1959. Bottom-up approach is the assembly of nanostructures through traditional chemical synthesis, self assembly, and positional assembly. The process described by Feynman enables individual atoms and molecules manipulation to build and operate similar dimensions sets of structures[2]. There has been revolutionary development in essential sciences to improve Feynman's theory in the past 30 years.

Nanomaterials cross the boundary between nanoscience and nanotechnolgy and bridge the two divisions. They generally fall into two categories: fullerenes and inorganic nanoparticles. Fullerenes are any material composed entirely of carbon in the form of a hollow sphere, ellipsoid, or tube. It includes: allotropes of carbon, carbon nanotube (CNT), buckypaper, graphene, nanodiamonds, carbon nanofoams....etc. Until this day there is no accepted international definition of a nanoparticle, but one given in the new PAS71 document developed in the UK is: "A particle having one or more dimensions of the order of 100nm or less." Nanparticles can also come in a wide range of morphologies from spheres, through flakes, and platelets, to dendritic structures, tubes, and ceramics [3].

Materials assembled at the nanoscale might behave differently from their bulk scales, this difference could be due to the size of these particles. The size effect of the nanoparticles changes the physical phenomena in a way; that increases the significance of surface tension and van der Waals forces. This potential difference is what mainly attracts the interest and attention of scientists and engineers. The scientists and engineers role is to influence the fabricating and control of nanostructures, and ultimately design materials to give desired properties. The range of applications which rely on the physical size of particles, can provide enhanced properties that are exceptionally broad [3].

Nature is the best of self assembly bottum-up approach. Tougher, and stronger material can be produced by mother nature. One of the natural nanocomposite material is the red abalone shell. The platelets consist of about 95% inorganic aragonite, a nanosized mineral of calcium carbonate particle bounded by a mortar of carbohydrate protein mix [4, 5]. The uniqueness of the ceramic/polymer structure is due to its highly defined structure and its superior mechanical properties.

layer reinforcement of composite materials can greatly improve these materials' structural and physical performance, such as stiffness, heat deflection temperatures and tensile strengths. It also tends to lower the thermal expansion coefficient and permeation rate without adding significant weight, thereby allowing nanolayer polymers to achieve greater

thermal stability (to become less flammable) and to reduce permeability (improve barrier performance) [6, 7, 8, 9]. Nanolayer-enhanced polymers distribute internal stresses more uniformly by allowing greater dimensional latitude during the forming and shaping processes, as compared to conventional macroscale reinforcements. For example, the unparalleled ability of clay nanolayers to boost mechanical properties of an engineering polymer (nylon-6) was first demonstrated by Toyota researchers. An increase of only 4.2 wt % of clay nanolayers doubled the modulus, increased heat distortion temperatures by 80 C^o (compared to pristine polymer), reduced permeability for water, and increased flame retardant properties.

Molecular modeling (molecular statics and molecular dynamics) is a tool that can be effectively used to investigate the mechanical properties, structure, energy potentials, behavior of Nano based materials at the atomic level. A computational model can reduce the number of time consuming laboratory experiments required for testing and hence it saves a lot of time and money. Advances will only be possible if experimental and computational results support each other. In this way, computational modeling will aid researchers in explaining experiments. Any findings that bring the structure into contact with the mechanical properties of nanocomposites which might develop the research and understanding of advanced and classical nanocomposites.

Earlier discussion emerges the essential role of mechanics, and in specific fracture mechanics and material strength.A multiscale bottom-up approach is conducted to examine the physical and the mechanical properties by Atomic Force Microscopy (AFM), Resonant Ultrasound Spectroscopy (RUS), Electrochemical Impedance Spectroscopy (EIS), Scanning Electron Microscopy (SEM) and Material Testing Systems (MTS)

1.1.2 Cementious Nano Material Simulations and Experimental Evaluation

Cement may be the world's most widely used manufactured material-more than 11 billion metric tons are consumed each year-but it also is one of the most complex materials. The

questions still remain as to just how it works, in particular how it is structured in the nano- and microscale, and how this structure affects its performance. Cement is something of a paradox. It requires just the right amount of water to form properly-technically it's held together by a gel, a complex network of nano particles called Calcium Silicate-Hydrate (C-S-H) that binds a significant amount of water within its structure. C-S-H is the main product of cement hydration, and it is responsible for its strength. The nano crystalline configuration for the C-S-H is not fully discovered. The mechanical, chemical and physical properties vary widely along with the production of the C-S-H.

Cementitious composites are receiving an intensive interest as a new generation of structural materials. This is due the combination of physical, chemical and high durability properties. Nano-concrete is defined as a concrete made with Portland cement of particles size that are less than 500 nm as the cementing agency, compared to an average particle size of 50 μm for a Portland cement average particle size. The uniqueness of the nano particles size can greatly affect the kinetics of the cement. Uniformly dispersed nano particles in a cement paste will expedite cement hydration due to their high activity.

The addition of nano particles to cement will enhance the microstructure of cement and improve the interface between the cement paste and aggregates in concrete. Behavior of cement composed of exclusively nano particles behavior has not yet reported. Nanotechnology can amend the molecular structure of concrete materials. This improvement in the concrete material can be reflected directly on some properties such as bulk, mechanical, volume stability, durability, and sustainability of concrete. The nanocement particles can be mixed with a broad variety of nanoparticles, to enhance desirable performance of the concrete such as conductivity (thermal, and electrical), tensile strength, toughness, ductility, and durability.

1.2 Motivation

During the last two decades, tremendous progress has been made in nanoscience. New classes of nano materials, such as carbon nanotubes, nanofibers, nanowires, quantum dots, are being assembled atom by atom, with various high tech applications in mind-electronics, biomedicine, energy, environment, etc. However, these materials are still very expensive, and can only be produced at a relatively small quantity. For the protection of the nation's critical infrastructure, such as buildings, bridges, tunnels, transportation systems, pipelines, power transmission, and communication systems, against the natural (hurricane, flood, earthquake) and man-made (blast, impact, fire) threat, nano materials that are low in cost and in huge in quantity are needed. In fact, not all nano materials are man-made and expensive. There are abundant naturally occurring and low in cost materials that are at or near nano size, such as nanoclay, volcanic and fly ash, cellulose nano whiskers, and many carbon or silica based minerals.

Recent study of mechanics at micro and nano level has confirmed that the material behavior can be controlled by constituents at the nano size. Mixing a small quantity of clay, graphene, POSS, and carbon nanotube with polymers can significantly alter the material strength and other mechanical properties. The strength of cement is strongly influenced by the packing of the calcium-silica-hydrate gel at micro level. Hence, with the understanding of materials laws at the micro and nano level, it may be possible to design infrastructure materials such as green concrete, and building blast and fire protection materials such as nano particle enhanced polymer spray on the wall.

Nano diamond structures are nanostructure with dangling bonds on the surfaces, facet edges and corners, which are energetically unfavorable and highly reactive. Nano diamonds exist in several crystal shapes such as spherical, octahedron, truncated octahedron, cuboctahedron, and cube. According to the free energy surface calculations the thermodynamically favored shapes are the truncated octahedron, and the cuboctahedron. Electrostatic charge distribution in Nano dimond is dependent on the crystal shape, they have facet dependent

charge distributions.

Mixing nano cement with nano particle size additives can greatly effect kinetics of the cement. More rapid setting and hardening of cement are due to the electrostatic attractive forces and higher specific surface area of the nano sized additives. Compressive and flexural strengths can be enhanced with the addition of POSS, graphene, MWCNT, nano diamonds, SiO2, and many other nano additives. Uniform dispersion will accelerate cement hydration due to their high activity. Improvement of the microstructure of cement and the interface between the cement paste and aggregates is expected.

1.2.1 Molecular Dynamic Simulations of Nano composites and Constituents

Recent interest in the use of polymer based nano composite materials in infrastructure applications requires further improvements in both blast resistance and flammability performance of these materials including reduction in the amount of smoke, carbon monoxide, and corrosive combustion products. A wide range of nano composites were used in this research which can be divided into two main categories: polymeric nano composites and cement nano composites.

A critical issue for the development of nanotechnology is our ability to understand, model, and simulate the behavior of small structures and to make the connection between nano structure properties and their macroscopic functions. Material modeling and simulation helps to understand the process, set the objectives that could guide laboratory efforts, and control material structures, properties, and processes at physical implementation. These capabilities are vital to engineering design at the component and systems level. In this research, coupled experimental-theoretical program was employed to study response of materials to blast loading. The concept that the minimum knowledge of the molecular structure is all the information needed to predict detailed information of the macro behavior and equilibrium properties of any system is the main objective of the molecular dynamic simulation emphasis

in this dissertation.

In order to understand nano composites, atomic structures, interfacial interaction between different matrices, and nano reinforcements; atomic level interactions should be studied in details. Mechanical properties of nano composites could be predicted by realistic computational techniques that vary in time and length scales. Molecular dynamics simulations can provide the structure and the dynamic intercalated molecules.

Theoretical material database is constructed for nano particle reinforced composites and other low-cost, high-strength, innovative materials based on MD simulation. The materials investigated include: (i) SWCNT-polyethylene, MWCNT-Nylon 6, exfoliated graphene nano platelets-vinyl ester, for a range of volume fractions.

1.2.2 Evaluate The Effectiveness of Adding a New Generation of Nano Additives to Nano Cement

Nanocomposites are of current interest, due to their favorable chemical and physical properties. The use of nano reinforcements can improve properties of many traditional materials such as cement. The uniqueness of the nano particles size can greatly affect the kinetics of the cement. Uniformly dispersed nano particles in a cement paste will accelerate cement hydration due to their high activity. Addition of nano particles will improve the microstructure of cement and the interface between the cement paste and aggregates in concrete. Behavior of cement composed exclusively of nano particles behavior has not yet reported.

Cement may be the worlds' most widely used manufactured material, but it also is one of the most complex materials. The questions still remain as to just how it works, in particular how it is structured at the nano and microscale, and how this structure affects its performance. Cement is something of a paradox. It requires just the right amount of water to form properly. Technically it is held together by a gel, a complex network of nano particles called Calcium Silicate-Hydrate (C-S-H) that binds a significant amount of water within its structure. C-S-H is the main product of cement hydration, and it is responsible

for its strength. The nano crystalline configuration for the C-S-H is not fully discovered. The mechanical, chemical and physical properties vary widely along with the production of the C-S-H.

World consumption of hydraulic cements exceeds one billion tons and a production that exceeds three billion tons annually, according the US geological survey for 2009 [10]. CO_2 emission is directly proportional to the volume produced of cement, while strength is inversely proportional with the volume of the structural member. Accordingly, as the structural member strength ascends by x, the environmental footprint is reduced by $1/x$ for pure compressive members such as columns, $1/x^{2/3}$ for bending members such as beams, and $1/x^{1/2}$ for slabs.

Predictions of mechanical properties of cement paste and concrete have been performed by some researchers. Ulm and Lemarchand [11] developed a multiscale micromechanics hydration model, together with an advanced kinetic hydration model and intrinsic material properties, to predict early age elastic properties of cement-based materials. In another study,[12] considered concrete as a poromechanics material. They used a multiscale method to investigate the poroelastic properties of concrete. Feng and Christian [13] proposed a three-phased micromechanics model of cement paste, using theories of mechanics of composite and poromechanics to predict the properties of hardened cement pastes. They adopted existing literature values of solid phases C-S-H, Calcium Hydrate (CH) and cement. However, low density (LD) and high density (HD) C-S-H are not distinguished. Cement paste has been treated like a three-phase composite (C-S-H, CH and unreacted cement paste). Also, the volume fraction of each phase material (C-S-H, CH, Porosity) was not determined by computation. Haecker, et al.[14] quantitatively predicted elastic moduli as a function of degree of hydration using finite element procedures. In this study, a multiscale modeling methodology was developed [15, 16] to relate the nanostructure properties to the micro and macro performance of concrete. Ginebara [17] reported that a reduction in particle size can cause an accelerated setting and hardening of cement due to the stronger electrostatic

attractive forces and the larger specific surface area. Additional studies have shown that the compressive and flexural strengths of cement mortars are enhanced with the addition of SiO_2 and Fe_2O_3 nano-particles or organo-modified montmorillonites in comparison to the plain cement mortar.

Earlier discussion emerges the essential role of mechanics, and in specific fracture mechanics and material strength.

1.3 Objectives

The main objectives of this research are to:

1. Evaluate mechanical properties of selected nano composites and their constituents (matric, reinforcement and interface) using molecular dynamic simulation.

2. Investigate the effect of geometric and simulation parameters on the accuracy of using molecular dynamics approach to simulate nanocomposites.

3. Study the usefulness of using nanoscience, not only in understanding the nano phenomena in nano-concrete, but also to be able to control the material's structure.

4. Assess the viability of using nano additives for improving properties of cementitious nanocomposites.

5. Develop a blast/fire-resistant coating for structural members with good characteristics for infrastructure protection

1.4 Outline of this dissertation

Chapter 2 aims to provide the reviewer an introductory to molecular dynamics (MD).It addresses several thermodynamic ensembles, basics of classical mechanics, assorted thermostats

and barostats algorithms, and some of the MD simulation parameters. MD simulation parameters included in this dissertation are: potential functions, initial state, performance measurements, structure type, time step, and the MD simulation outputs.

Chapter 3 accommodates detailed nanocomposites MD simulation for: atomic structures of polymeric matrices and nanoreinforcements, interfacial interaction between different matrices and nano reinforcements, mechanical properties of nano composites, and equation of state for polymeric coatings.

The models will be equilibrated by a series of energy minimization and molecular dynamics runs. The crystal structures for the semi-crystalline polymers will be generated and the simulated bulk structures will be subjected to the static method for evaluating their mechanical behavior. In the static method, each structure will be subjected to a number of successive deformations followed by a re-minimization in order to map out the energy hyper-surface and subsequently to determine the elastic moduli. This outlined molecular simulations could bridge, by realistic computational techniques that vary in time and length scales, the molecular calculations to the real material scale. MD simulations can provide the structure, and the dynamic intercalated molecules. Multi-scale research, starting from molecular dynamics simulation to developing continuum theory of nano-composite material systems and developing material database for nano-particle reinforced composites and other low-cost, high-strength, innovative materials, such as fly ash and polymer enhanced concrete.

Chapter 4 emerges the essential role of the bottom-up approach to correlate the atomic assembly to the macro properties in specific mechanics and material strength. On the atomic level, the Atomic Force Microscopy (AFM) to examine the physical and chemical properties of the cementitious nanocomposites is proposed, the molecular dynamics approach to predict the interfacial strength between the C-S-H and the nano additives, and the x-ray diffraction analysis for the cementitious nanocomposites to predict their chemical composition. On the micro level, the Scanning Electron Microscopy (SEM) technique to obtain information about the sample's surface topography and composition is implied. On the meso

level, for mechanical properties, are measuring the elastic constants of the tested materials by Resonant Ultrasound Spectroscopy (RUS), and for the electrochemical properties the Electrochemical Impedance Spectroscopy (EIS) technique. Finally on the macro level, Material Testing Systems (MTS) is used to compare and distinguish the differences between regular Portland cement and the cementitious nanocomposites in the compressive strength. Several types of cementitious nanocomposites are proposed such as:(1)Nano Diamond_Cement, (2)Exfoliated Functionalized Graphene Platelets_Cement, (3) Exfoliated Pristine Graphene Platelets_Cement, (4)PEG POSS_Cement, (5) OctaTMA POSS_Cement, and (6)hydrated Nano C_3S.

Chapter 5 will briefly implement the development of a blast-resistant coating for structural members with good characteristics for a fire protection. The strategy of coating concrete walls with hydrocarbon elastomer, to mitigate the effects of a projectile strike and an explosion, necessarily increases the fire hazard to the building and its occupants. While a full assessment of this would require a detailed investigation involving full scale fire tests, it is felt that considerable insights could be gained by performing bench scale tests in conjunction with computer simulations designed to reveal the extent to which specific wall coatings might contribute to the growth of an existing fire.

Since the materials being considered for blast-resistant coatings are polymer-based, it is important to investigate their behavior in fire. Flammability characterization of the coating will provide a thermal barrier to heat. Also, in this study, the multiscale approach is applied to study the effect of thermal degradation on the structural members integrity.

Chapter 6 concludes the work shown in the previous chapters and discusses more research future directions related to this study.

2. MOLECULAR DYNAMICS SIMULATIONS

2.1 Introduction

Molecular dynamics simulation is a computational approach based on statistical mechanics which provides the methodology for detailed microscopic modeling on the molecular scale. It is capable of calculating structural, thermodynamic, mechanical, and transport properties. MD simulates the motions or dynamics of a molecule or a group of molecules numerically by computing a trajectory for the predefined system as a function of time: a virtual experiment. So, MD in many aspects is similar to an actual experiment. An experiment usually proceeds as the following: a sample of the material we wish to study is prepared, the sample is connected to a selected instrument, properties of interest are measured under certain conditions and measurements are averaged for more accurate results and to eliminate any noise affect. On the other hand, for MD simulations a similar procedure is followed. First, a model system is defined which consists of N particles. Second, Newton's equation of motion is solved for the simulated system until the properties of the system no longer change with respect to time (equilibrate system). Third, an actual measurement is performed[18, 19]

Statistical mechanics is the branch of physical sciences that studies macroscopic systems from a molecular point of view. The goal is to understand and to predict macroscopic phenomena from the properties of individual molecules forming the system. The system could range from a single molecule to a nanocomposite structure. In order to connect the

macroscopic system to the microscopic system, time independent statistical averages are often introduced. However, statistical ensembles provide the rigorous mathematical expressions that relate macroscopic properties to the distribution and motion of the atoms and molecules of the N-body system. Molecular dynamics simulations provide the means to solve the equation of motion of the particles and evaluate these mathematical formulas.

Molecular dynamics simulations are traditionally performed under the conditions of constant number of particles (N),Volume (V), and Energy (E). Simulation starts by selecting a model system consisting of N particles. Positions of atoms are determined by applying Newton's equation of motion. The system is simulated until it reaches an equilibrium state. Thence, the elastic properties of the system are determined. Molecular dynamics seeks to determine $6N$ coordinates and momenta, which are sensitivity dependent on the initial conditions. The mechanical or microscopic state of a system is defined by the atomic positions, q, and momenta, p, these can also be considered as coordinates in a multidimensional space called phase space. For a system of N particles, this space has $6N$ dimensions. A single point in phase space, denoted by G, describes the state of the system. An ensemble is a collection of points in phase space satisfying the conditions of a particular thermodynamic state. A molecular dynamics simulation generates a sequence of points in phase space as a function of time; these points belong to the same ensemble, and they correspond to the different conformations of the system and their respective momenta. Several different ensembles are described below. This means that two states with very close initial conditions diverge exponentially through time[19]. As our interest lies only in the equilibrium state, it is important to choose an optimization algorithm that can predict the trajectories of atoms that reach the equilibrium state as quickly as possible.

2.2 Thermodynamic Ensembles

The thermodynamic state of a system is usually defined by a small set of parameters, for example, the Temperature (T) the Pressure (P), and the number of particles (N). Other thermodynamic properties may be derived from the equations of state and other fundamental thermodynamic equations. Two approaches are usually used to simulate MD for different thermodynamic ensembles: (1) mixing Newtonian MD with Monte Carlo technique, or (2) developing the Lagrangian equations of motion of the system[19].

Extended Lagrangian method is first provided by Andersen[20]; he discusses MD simulations under constant Pressure (P), constantTemperature (T), or both constant Pressure (P) and Temperature (T) conditions. The trajectory averages for these three ensembles correspond to the isoenthalpic-isobaric, canonical, and isothermal-isobaric conditions [**?**]. These ensembles have become one of the most important derivations enabling the improvement of the MD performance. Results obtained from one ensemble can be transformed into another ensemble. These transformations, however, are strictly possible only for a periodic unit cell, which represents an infinite system.

At constant temperature, energy associated with MD simulations fluctuate. A system subjected to a constant temperature is equivalent to maintaining the system in a heat bath. Under such conditions, the dynamic energy follows the Boltzmann distribution, and this can be transformed into the following kinetic energy and temperature relation[19]:

$$K_B T = m \left\langle v_\alpha^2 \right\rangle \tag{2.1}$$

where m is the mass of the particle, v_α is the velocity α^{th} component, $\langle\rangle$ indicates the average quantity, K_B is the Boltzmann constant, and T is thermodynamic temperature in Kelvin scale. On the other hand, at constant pressure, the volume associated with the MD simulation fluctuates. This can be obtained by replacing the coordinates of the particles by scaled coordinates ρ_i [20]:

$$\rho_i = \frac{r_i}{\sqrt[3]{V}} \tag{2.2}$$

where, r_i=1,2,3,....N, are the original coordinates, V is the volume of unit cell, N is the number of particles, and ρ_i is a dimensionless number between (0-1). At constant Pressure (P) and Temperature (T),the Energy (E), Pressure (P), and Enthalpy (H) are fluctuating properties. To be able to calculate the trajectories of such system, a stochastic collision method should be introduced, so that the time average of any function is equal to the isobaric ensemble average quantity[20].

2.2.1 Isothermal-Isobaric

This ensemble represents a constant number of atoms, constant pressure, and constant temperature (NPT). Therefore, the NPT ensemble allows control of both temperature and pressure with no new atoms entering the simulation cell. Free surface unit vectors are allowed to change, and the pressure is adjusted by adjusting the volume. Energy fluctuation requires the use of a stochastic model for both forces and kinetic energy acting on the system of atoms. This process will average properties along the trajectories of pressure temperature, energy, volume cell parameters and stress so that the properties become equal to the NVT ensemble. Momentum will be affected instantaneously by the stochastic collision. The state of the system between collisions evolves according to the Hamiltonian of equation motion. Before performing a simulation, the temperature, mean rate of collision, and time at which particles collide are predetermined. The time at which particles suffer collision can be determined using a random number generator which follows the Poisson distribution. Each collision changes the particle momentum to a new value chosen from a Boltzmann distribution. Finally, calculated trajectories of scaled systems are converted to the original system for the calculation of the time averages of any function $\overline{F}$

$$\overline{F} = lim_{T\to\infty} T^{-1} \int_0^T dt F(r^N(t), p^N(t), V^N(t)) \tag{2.3}$$

where $F(r^N(t), p^N(t), V^N(t))$ is the mechanical state of the system at $t \geq 0$

In a typical MD simulation, N and V are fixed, the initial choice for$r^N(0), p^N(0)$ is made, and Hamilton's equation are solved numerically. Trajectory averages are then performed on the thermodynamic properties. The energy is conserved along the trajectory, and it is assumed that the trajectory spends equal times in all equal volumes with the same value of energy. It follows that [20]:

$$\overline{F} = F_{NVE}(N, V, E) \tag{2.4}$$

2.2.2 Ischoric

This ensemble represents constant number of atoms, constant volume, and constant temperature (NVT). It is also referred to as the canonical. The ensemble is obtained by controlling the temperature through direct temperature scaling during the initialization stage and by temperature bath coupling during the data collection phase. The volume is kept constant through the run. This is the appropriate choice when conformational searches of molecules are carried out in a vacuum without periodic boundary defined. Even if periodic boundary conditions are used, and pressure is not a significant factor, the constant temperature and constant volume condition provide the advantage of less perturbation of the trajectory due to the absence of coupling to a pressure bath. For the NVT ensemble, the velocities of the atoms, v_i , are rescaled by introducing an additional degree of freedom, s, which represents the external system. External and physical systems are both related through the expression:

$$v_i = s\dot{r}_i \tag{2.5}$$

This relation could be considered as the exchange of heat between both systems. Potential energy is associated with the degrees of freedom s by $(f+1)kT_{eq}$, where f is the number of

degree of freedom in the physical system, k Boltzmanns constant, T_{eq} is the externally set temperature.

The Lagrangian of the extended system of particles and is thus postulated to be

$$Ł = \sum_i \frac{m_i}{2} s^2 \dot{r}_i^2 \varphi(r) + \frac{Q}{2} \dot{s}^2 (f+1) k T_{eq} ln(s) \tag{2.6}$$

where $\frac{Q}{2}\dot{s}^2$ is a kinetic energy term introduced to take into account a dynamic equation of s, Q determines the time scale of temperature fluctuation, and $\varphi(r)$ is potential energy. For detailed derivations, refer [20, 21].

2.3 Basics of Classical Mechanics

The molecular dynamics simulation method is based on Newton's second law or the equation of motion, $F = ma$, where F is the force exerted on the particle, m is its mass and a is its acceleration. From a knowledge of the force on each atom, it is possible to determine the acceleration of each atom in the system. Integration of the equations of motion then yields a trajectory that describes the positions, velocities and accelerations of the particles as they vary with time. From this trajectory, the average values of properties can be determined. The method is deterministic; once the positions and velocities of each atom are known, the state of the system can be predicted at any time in the future or the past. Molecular dynamics simulations can be time consuming and computationally expensive.

Newton's equation of motion is given by

$$F_i = m_i a_i \tag{2.7}$$

where F_i is the force exerted on particle i, m_i is the mass of particle i and a_i is the acceleration of particle i. The force can also be expressed as the gradient of the potential energy,

$$F_i = -\nabla_i \varphi(r) \tag{2.8}$$

Combining these two equations yields:

$$-\frac{d\varphi(r)}{dr_i} = m_i \frac{d^2 r_i}{dt^2} \tag{2.9}$$

where $\varphi(r)$ is the potential energy of the system. Newton's equation of motion can then relate the derivative of the potential energy to the changes in position as a function of time.

The acceleration is given as the derivative of the potential energy with respect to the position, r:

$$a = -\frac{1}{m}\frac{d\varphi(r)}{dr} \tag{2.10}$$

Therefore, to calculate a trajectory, one only needs the initial positions of the atoms, an initial distribution of velocities and the acceleration which is determined by the gradient of the potential energy function. The equations of motion are deterministic, e.g., the positions and the velocities at time zero determine the positions and velocities at all other times,t. The initial positions can be obtained from experimental structures, such as the x-ray crystal structure by Nuclear magnetic resonance (NMR) spectroscopy.

The initial distribution of velocities are usually determined from a random distribution with the magnitudes conforming to the required temperature and corrected so the overall momentum (p)=0:

$$p = \sum_{i=1}^{N} m_i v_i = 0 \tag{2.11}$$

The velocities, v_i, are often chosen randomly from a Maxwell-Boltzmann or Gaussian distribution at a given temperature, which gives the probability that an atom i has a velocity v_x in the x direction at a temperature T

$$p(v_{ix}) = \left(\frac{m_i}{2\pi k_B T}\right)^{1/2} \exp\left[-\frac{1}{2}\frac{m_i v_{ix}^2}{k_B T}\right] \tag{2.12}$$

The temperature can be calculated from the velocities using the relation

$$T = \frac{1}{3N}\sum_{i=1}^{N}\frac{|P_i|}{2m_i} \tag{2.13}$$

where N is the number of atoms in the system.

2.4 Thermostat and Barostat Algorithms Effect

2.4.1 Berendsen Algorithm

This algorithm is used as a thermostat and a barostat dynamic control. The canonical ensemble does not allow temperature fluctuation. Berendsen thermostat allows the temperature of the system to be coupled to an external heat bath at a fixed temperature T0. In this case the instantaneous temperature is pushed towards desired temperature by scaling velocities at each step. The momenta are adjusted towards the correct T. Temperature fluctuations will grow until trajectories are equivalent to NVE ensemble; however, they will never reach the canonical ensemble.

2.4.2 Anderson Algorithm

This thermostat algorithm is based on the stochastic collision of atoms, and it is the first thermostat algorithm proposed to simulate a canonical ensemble. For a particle after a collision, a new velocity is randomly assigned from the Maxwell-Boltzmann distribution at the desired temperature. The replacement is equivalent to a system being in contact with a heat bath that randomly emits thermal particles colliding with particles in the system and thus; changing their velocity. Between each collision, the system is simulated at constant energy. Thus, the overall effect is equivalent to a series of microcanonical simulations, each performed at a slightly different energy. The distribution of energies of these mini-microcanonical simulations should follow a Gaussian distribution. The Anderson thermostat generally yields good results for time independent properties [20].

2.4.3 Parrinello Algorithm

Parrinello and Rahman [21] are the first to perform a generalized model for crystal structure MD simulations from the Anderson constant pressure ensemble. Time dependent MD simulations allow volume and shape of crystals to vary with time [21]. This is a barostat algorithm, in which the induced dipoles are treated as additional dynamical variables that are included in the extended Lagrangian function. In the algorithm, mass is associated with the motion of dipoles. Given the starting configuration, the algorithm solves for the minimum energy of the electrons, and evaluates the forces through energy derivatives with respect to nuclear positions.

2.5 Molecular Dynamics Simulation Parameters

2.5.1 Potential Functions

Several new computational methods and their applications to nanostructures have been developed: equivalent continuum models [22, 23, 24], quasi-continuum models [25, 26, 27, 28] using Tersoff and Brenner interatomic potential [29, 30] and molecular dynamics simulations [31, 32]. In this article we focus on the modeling and simulation of SWCNT composites using the molecular dynamics approach.

The Born-Oppenheimer approximation

The Born-Oppenheimer approximation is the foundation of molecular dynamics [33]. Noting that the electrons are several thousands of times lighter than the nuclei and therefore move much faster, Born and Oppenheimer proposed that the motion of the electrons can be decoupled from that of the nuclei, giving two separate equations. The first of these equations describes the electron motion where the energy is the function of coordinate of nucleus E(R)

only and is termed as potential energy surface. The second part of the equation describes the motion of the nucleus on this potential energy surface. The solution of the nucleus motion is the basis of molecular dynamics. However, prior to that, one needs to solve the equation pertaining to the motion of the electron for the expression of the $E(R;r)$. Solving the equation for electronic motion is not easy because the potential energy surface is not unique. Thus, an empirical fit to the potential energy surface, commonly called a force field E_{total}, is usually used. Since the nuclei are relatively heavy objects, quantum mechanical effects are often insignificant and equation of motion for nuclei can be replaced by Newton equation of motion given in eqaution. The solution of the above equation is the term $R(t)$ which is called the trajectory of the system.

$$-\frac{d\varphi(r)}{dr_i} = m_i \frac{d^2R}{dt^2}$$

Forcefields:(COMPASS, Tersoff)

A force field in molecular mechanics and molecular dynamics is the average description of the existing interactions among various atoms in a molecule or a group of molecules in terms of functions and parameters sets [34]. The electronic configuration around atoms is not included in the description of these atomic interactions. Generally, the force field parameters are empirical, derived from quantum modeling and, sometimes, from heuristics. The functional forms of various interactions, summed together in order to yield the COMPASS force field can be achieved from the introductory paper on COMPASS by Sun [35]:

$$
\begin{aligned}
E_{Total} = & \sum_{b} \left[K_2(b-b_0)^2 + K_3(b-b_0)^3 + K_4(b-b_0)^4\right] \\
& + \sum_{\theta} \left[K_{2\theta}(\theta-\theta_0)^2 + K_{3\theta}(\theta-\theta_0)^3 + K_{4\theta}(\theta-\theta_0)^4\right] \\
& + \sum_{\phi} \left[K_{1\phi}(1-\cos\phi) + K_{2\phi}(1-\cos 2\phi) + K_{3\phi}(1-\cos 3\phi)\right] \\
& + \sum_{\chi} \left[K_{2\chi}(\chi-\chi_0)^2\right] + \sum_{b,\theta} \left[K_{b\theta}(b-b_0)(\theta-\theta_0)\right] \\
& + \sum_{b,\phi} (b-b_0)\left[K_{1b}\cos\phi + K_{2b}\cos 2\phi + K_{3b}\cos 3\phi\right] \\
& + \sum_{\theta,\phi} (\theta-\theta_0)\left[K_{1\theta\phi}\cos\phi + K_{2\theta\phi}\cos 2\phi + K_{3\theta\phi}\cos 3\phi\right] \\
& + \sum_{b,\theta} \left[(\theta'-\theta'_0)(\theta-\theta_0)\right] + \sum_{\theta,\theta,\phi} \left[K_{\theta\phi}(\theta'-\theta'_0)(\theta-\theta_0)\cos\phi\right] \\
& + \sum_{i,j} \frac{q_i q_j e}{r_{ij}} + \sum_{i,j} \left[2\left(\frac{r^0_{ij}}{r_{ij}}\right)^9 - 3\left(\frac{r^0_{ij}}{r_{ij}}\right)^6\right]
\end{aligned} \tag{2.14}
$$

where the first 10 terms are covalence terms. The first through fourth terms represent the energy associated with bond (b), angle (θ), torsion (ϕ) , and Wilson out-of-plane (χ) internal coordinates, respectively. The rest of the terms excluding the last two terms represent the energies of cross-coupled internal coordinates which are important for calculating the vibration frequencies and structural variations associated with conformational changes. The last two terms represent nonbond interaction between atoms separated by two or more intervening atoms or atoms belonging to different molecules. The second-to-last term is the Coloumb potential that represents electrostatic interactions. The last term of equation 2.14, the Lennard-Johns 9-6 (LJ 9-6) potential, represents the van der Waals interaction. The LJ-9-6 function is considered as a soft function in the repulsive region compare to the conventional LJ-12-6 function.

Tersoff- Brenner forcefield is the most popular forcefield used to simulate CNTs. It is an empirical potential energy formulation that can model intermolecular chemical bonding in hydrocarbons as well as diamond and graphite [30]. However, nonbonding energy, such as

van der Waals force, is not included in Tersoff- Brenner potential. On the other hand, Condensedphase Optimized Molecular Potentials for Atomistic Simulation Studies (COMPASS) forcefield accounts for two function category valence terms, including the diagonal and off-diagonal cross coupling terms and the nonbond interaction terms. In COMPASS forcefield, the valence terms represent internal coordinates of bond, angle, torsion angle, and out-of-plane angle; the cross coupling terms include two or three internal coordinate potentials. The nonbond interaction terms include: Van der Waals for the Lennard-Jones function and a Coulombic function for electrostatic interactions [35]. COMPASS force field is assessed to all MD simulations reported in this work.

2.5.2 Initial State

In Molecular dynamics simulations, a system is generated with an initial set of position and velocities of all of the atoms in the considered system. The potential function is used to integrate Newton's equation of motion of all the atomic velocities and positions. A trajectory is generated of the positions and the velocities as the output from the MD simulation. Newton's equations of motion are numerically integrated, and the force is obtained from the negative gradient of the applied potential function. Thus, the coupled differential equations obtained from Newton's law are a highly nonlinear system of equations. Solving this system of equations can drive the system into an unstable system. So, in order to overcome this obstacle, a long term equilibration should be considered for simulated system to eliminate or reduce the initial conditions sensitivity [36].

The molecular dynamic simulations follow the ergodic hypothesis, in which it correlates between the ensemble average to measurements performed for a single system during the course of its natural evolution. In other words, for a given system; the time average of its properties should be equal to the average of that property over the entire system. MD simulations append the dynamics of a single system and produces averages of the form:

$$\langle G \rangle = \frac{1}{M} \sum_{\mu=1}^{M} G_{\mu}(r_1, ..., r_{N_m}) \tag{2.15}$$

where N: the number of particles, G: the equilibrium average of a certain property, and M: series of measurements made as the system evolves. In this case, statistical mechanics connects similar MD averages to their thermodynamic components, and the ergodic hypothesis can be implemented to justify equating trajectory averages with ensemble-based thermodynamic properties [37]

2.5.3 Molecular Dynamics Simulation Output

Calculating Mechanical Properties

Molecular Modeling is a computational technique to model or mimic the behavior of the molecules. Force fields of computational chemistry and material science are applied for studying small chemical molecular systems and material assemblies. The common feature of molecular modeling techniques is the atomistic level systems; this is in contrast to quantum chemistry. The main benefit of molecular modeling is that it allows more atoms to be considered during the simulation, starting with a small number of molecules and increasing the unit cell size, until periodic system is obtained, with represents the full scale material properties. However, it is recommended to simulate unit cells with 3000 atoms or more, to describe the behavior of any material in order to get the periodic unit cell which represents the

infinite system. A commercially available molecular dynamic simulation software material studio (MS) will be used to calculate the mechanical properties of the nano composites and their constituents.

The commercially available Material Studio Software®[33], has been used for performing molecular dynamic simulations of multi-wall carbon nanotube, graphene, and graphite reinforced polymers to predict their mechanical properties. This was accomplished by using bulk amorphous polymer structures generated by constructing polymeric chains in a periodic cell, taking into account the bond torsion probabilities and bulk packing requirements.

Models are then equilibrated by a series of energy minimization and molecular dynamic runs. Crystal structures for semi-crystalline and amorphous polymers are generated [38, 39] and the simulated bulk structures are subjected to one of the three different methods for evaluating their mechanical behavior: the static method; the fluctuation method; and the dynamic method. After molecular dynamics simulation has been performed, the resulting deformed molecular structure is analyzed for determining elastic constants. Elastic constants of the final atomic configuration are computed using the static approach suggested by Theodorou and Suter [40]. The elastic constants in this approach are defined as:

$$C_{lmnk} = \frac{\partial \sigma_{lm}}{\partial \epsilon_{nk}} \mid_{T,\epsilon_{nk}} = \frac{1}{V_0} \frac{\partial^2 E_H}{\partial \epsilon_{lm} \partial \epsilon_{nk}} \mid_{T,\epsilon_{lm},\epsilon_{nk}} \tag{2.16}$$

where, E_H denotes the Helmholtz free energy, ϵ is the strain component, σ is the stress component and V_0 is the volume of the simulation cell in the undeformed configuration. It is assumed that contributions originating from changes in configurational entropy on deformation, and from the strain dependence of the vibrational frequencies are negligible for glassy polymers. Thus, it is possible to estimate the elastic stiffness coefficients from numerical estimates as:

$$\frac{d^2 E}{d\epsilon_i d\epsilon_j} = \frac{d\sigma_i}{d\epsilon_j} \tag{2.17}$$

where, E is the potential energy of the system.

For each configuration submitted for analysis of static elastic constants, the first step consists of energy minimization using conjugate gradients method. In this study, the target minimum derivative for the initial step is 0.1 kcal/Å. However, to reduce the time required for the calculation, a maximum of 1000 steps were performed in attempting to satisfy the convergence criterion. Following the initial stage, three tensile and three pure shear deformations of magnitude ± 0.0005 were applied to the minimized system, and the system was re-minimized following each deformation. The internal stress tensor was then obtained from the analytically calculated virial and used to obtain estimates of the 6 x 6 elastic stiffness coefficient matrices.

As a result of these simulations, the elastic stiffness coefficients could be obtained by estimating the second derivatives of the deformation energy with respect to strain using a finite difference formula (for diagonal components only), and by calculating $\triangle\sigma_i/\triangle\epsilon_j$for each of the applied strains, where σ_i represents, in vector notation, elements of the stress tensor obtained analytically using the following expression:

$$\sigma = -\frac{1}{V_0}\Big[\Big(\sum_{i=1}^{N} m_i(v_i v_i^T)\Big) + \Big(\sum_{i<j} r_{ij} f_{ij}^T\Big)\Big] \tag{2.18}$$

where, index i runs over all particles 1 through N; m_i, v_i and f_i denote the mass, velocity and force acting on particle i; and V_0 denotes the (undeformed) system volume. In an atomistic calculation, this expression for internal stress tensor is called virial expression.

Generally, it is assumed that the numerical estimation of second derivatives (of the energy) will be less precise than estimation of the first derivatives (of the stress). Therefore, the latter method has been used here for calculating the elastic constants. This approach creates the foundation of calculating elastic constants; however, the potential energy expression can alter depending upon the ensemble of thermodynamic variables of the simulation experiment.

In this work, we used COMPASS force field because it supports all the energy interaction terms, in the material simulated. Different ensembles were applied for the different dynamic thermostat or barostat steps, such as NVT, constant volume/constant temperature dynamics, NPT, or constant pressure/constant temperature dynamics.

The equations of motion were solved with Anderson for the NVT, and Berendsen for NPT as velocity algorithms. The time step of integration was set to 1 fs in all cases that is chosen referring to the atoms are considered. The summation methods for van der Waals and Coulomb forces were all atom based (cutoff, spline width and buffer width was 9.5Å) unless it was set for an assigned value.

The Discover module within Materials Studio Software was used. Discover provides several methods for controlling temperature and pressure. Depending on which state variables (for example, the energy E, volume V, temperature T, pressure P, and number of particles N) are kept fixed, different statistical ensembles can be generated. A variety of structural, energetic, and dynamic properties can then be calculated from the averages or the fluctuations of these quantities over the ensemble generated.

3. MOLECULAR DYNAMICS SIMULATIONS OF NANOCOMPOSITES AND THEIR CONSTITUENTS

3.1 Introduction

A critical issue for the development of nanotechnology is the ability to understand, to model, and to simulate the behavior of these nano structures and to make the connection between nano structure properties and their macroscopic functions. Material modeling and simulation aid in understanding this process, help in setting objectives that guide laboratory investigation, and assist in setting controls on material structures, properties, and processes for physical implementation. These capabilities are vital to engineering design at the component and systems levels [18, 41, 42, 43, 44, 45] Nanolayer reinforcement of composite materials can greatly improve these material's structural and physical performance, such as stiffness, heat deflection temperatures and tensile strengths. It also tends to lower thermal expansion coefficient and permeation rate without adding significant weight, thereby allowing nanolayer polymers to achieve greater thermal stability (to become less flammable) and to reduce permeability (improve barrier performance) [6, 7, 8, 9]. Nanolayer-enhanced

polymers distribute internal stresses more uniformly by allowing greater dimensional latitude during the forming and shaping processes, as compared to conventional macroscale reinforcements. For example, the unparalleled ability of clay nanolayers to boost mechanical properties of an engineering polymer (nylon-6) was first demonstrated by Toyota researchers. An increase of only 4.2 wt % of clay nanolayers doubled the modulus, increased heat distortion temperatures by 80 C^o (compared to pristine polymer), reduced permeability for water, and increased flame retardant properties.

3.2 Molecular Dynamics Simulations of Polymeric Matrices

3.2.1 Literature Review

Nylon6,6 (PA66) is a semi crystalline polyamide that is commonly used as an engineering material in many fabric applications due to its good abrasion resistance and self lubricating properties. The nylon6,6, got its name because each repeated unit of the polymer chain has two stretches of carbon atoms, each being six carbon atoms long figure 3.1. Other nylons can have different numbers of carbon atoms in these stretches.

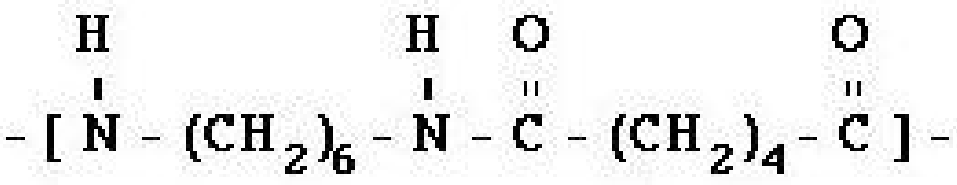

Figure 3.1. Chemical Chain for Nylon6,6

Two basic reactions are used to synthesize polyamide engineering polymers: (1) polycondensation of a dibasic acid and a diamine or (2) polymerization of an amino acid or lactam.

Generally, the polyamide analogs exhibit good chemical resistance and low moisture absorption at the expense of heat resistance, impact properties in wet environments, and stiffness. Water acts as a plasticizer in polyamides, reducing most mechanical and electrical properties while improving toughness and elongation. This problem, perhaps the major shortcoming of the nylons, is a function of the concentration of the amide groups. Water actually replaces the amide-amide hydrogen bonds with an amide-water hydrogen bond. It also provides very good mechanical and thermal properties in their dry-as-molded state. But, they are most susceptible to deterioration due to moisture absorption. They also provide many desirable properties to fulfill end-use requirements and account for the major share of the polyamide resins.

Glass transition (Tg), is the temperature at which the amorphous polymer is converted between rubbery and glassy states. It is considered the most important mechanical property for all polymers, thats because some physical properties undergo a drastic change under different glass transition temperature, such as hardness, Young's module, and volume. For simulation considerations, it was considered to be $348K$.

Vinylester is a copolymer thermoset resin produced by the esterification of an epoxy resin with unsaturated monocarboxylic acid. The reaction product is then dissolved in a reactive solvent, such as styrene, to (35-45)% content by weight. Vinylester can be used as an alternative to polyester and epoxy materials in matrix or composite material because its distinctive characteristics, strength, and bulk cost lie intermediately between polyester and epoxy. Vinylester has low resin viscosity, less than polyester and epoxy [46, 47], but the epoxy-based vinylester has remarkable corrosion resistance, physical properties, and improved adhesion compared to polyester due to their chemical composition, and the presence of polar hydroxyl and ether groups. Simulated vinylester chains are 65% epoxy and 35% styrene; figure 3.2 shows a schematic vinylester chemical chain.

Polyurea may be classified as an elastomeric material. The resilience and large strain

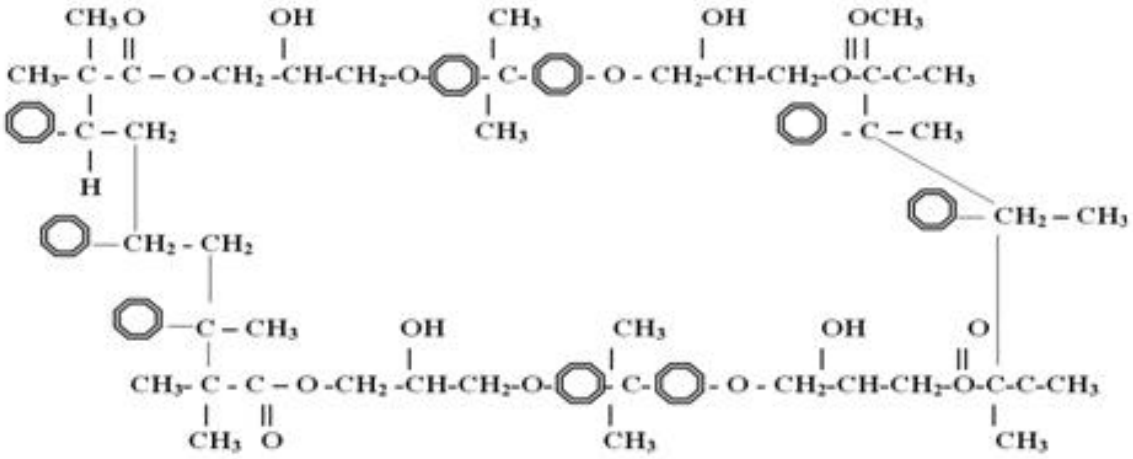

Figure 3.2. Single VE Chain: 35% Styrene, 65% Epoxy

capacity of elastomers can be exploited to absorb blast energy and contain building debris. Elastomers are composed of long polymer chains, usually cross-linked or connected by chemical bonds. Cross linking makes elastomers reversibly stretchable within a significant range of deformations. In the unstretched state, the polymer chains are oriented in random directions. When stretched, the polymer chains become elongated and ordered along the deformation direction. When no longer stretched, the cross-links guide the elastomer back to its original shape as the chains once again randomize. During deformation, molecules rub against each other causing damping (energy dissipation). In pure elastomeric materials, this effect is viscoelastic (strain-rate-dependent. Often this causes internal friction (strain-rate-independent energy dissipation). Interspersed particles (filler: e.g. nano reinforcement) is expected to influence the damping of these materials. The elastomer used in this study was polyurea figure 3.3.

Polyurea is a type of elastomer that is derived from the reaction product of an isocyanate component and a synthetic resin blend component through step-growth polymerization. The isocyanate can be aromatic or aliphatic in nature. It can be monomer, polymer, or any variant reaction of isocyanates, quasi-prepolymer or a prepolymer. The prepolymer, or quasi-prepolymer, can be made of an amine-terminated polymer resin, or a hydroxyl -terminated

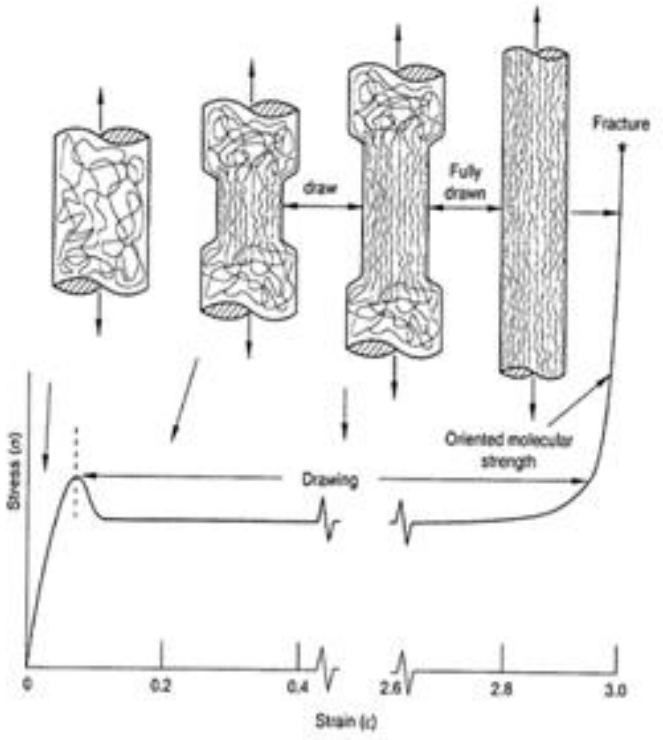

Figure 3.3. Schematic of deformation in Polyurea

polymer resin.

The resin blend may be made up of amine-terminated polymer resins and/or amine-terminated chain extenders. The amine-terminated polymer resins will not have any intentional hydroxyl moieties. Any hydroxyls are the result of incomplete conversion to the amine-terminated polymer resins. The resin blend may also contain additives or non-primary components. These additives may contain hydroxyls such as pre-dispersed pigment in a polyolcarrier. Normally, the resin blend will not contain a catalyst(s). Polyureas are characterized by high elongation, high tear strength, and superior modulus of elasticity. Typical molecular structure of polyurea is shown in figure 3.4.

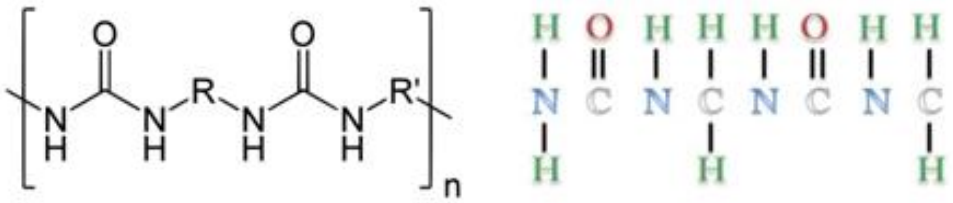

Figure 3.4. Molecular Structure of Polyurea (a) Generic Molecular Structure of Polyurea (b) Molecular structure of Polyurea Used in This Study

3.2.2 Molecular Simulation Setup

Thermoplastic and thermoset polymeric matrices are simulated. Several amorphous cell sizes are constructed coupled with the effect of simulation factors, such as thermodynamic ensembles (NVT, NPT) and cutoff point distance, to calculate the elastic engineering constants. A detailed simulation procedure for each simulated polymer will be explained in details in the correspondent section.

Nylon6,6

A single chain of twenty monomers connected repeatedly was built figure 3.5a. The total number of atoms for each chain was 382 with molecular weight of 2265 gm/mol. The chain was minimized using the conjugate gradient method. An amorphous periodic cubic lattice with lattice parameters a=b=c=33.3$\mathring{A}$ figure 3.5b, ten polymer chains with total number of 3820 atoms and final target density of 1.07 gm/cm^3, are constructed. A minimum potential position confirmation is adopted by conjugate gradient method. Each simulated amorphous cell is subjected to periodic boundary conditions in order to simulate the behavior bulk polymer.

Initially, minimized periodic cell was equilibrated after 100ps using either isochoric or isobaric thermodynamic controls at a rate of 1fs per time step. The system was heated to 400K which is beyond the glass transition of nylon6,6. This was followed by another thermodynamic step to cool each system back to room temperature at the same reaction

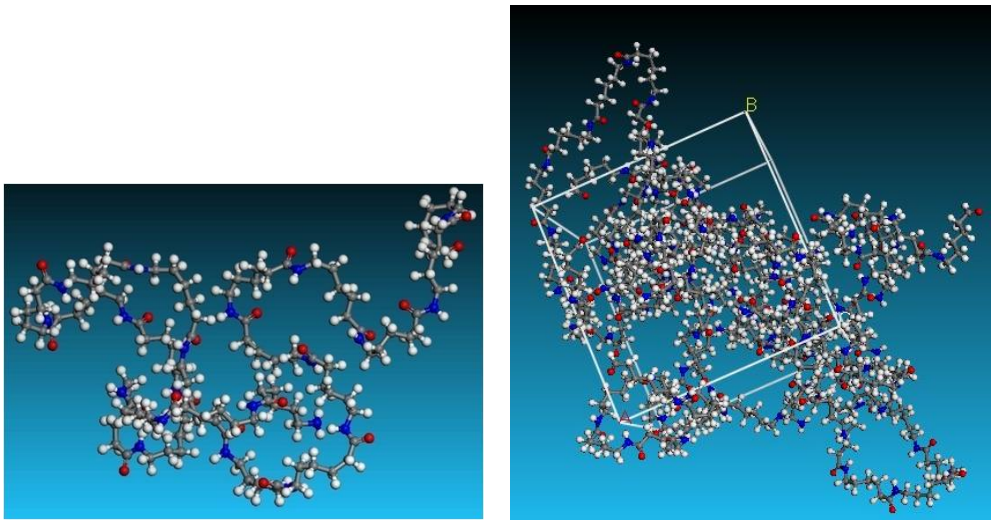

Figure 3.5. MD simulation of (a) single, (b) ten chains of nylon6,6 polymer

rate.

Total energy of the nylon6,6 chain molecular structure is calculated using an analytical function which is the sum of a number of individual energy terms. At its simplest level, this function includes bond stretching, torsion, angle bending, and nonbonding interaction terms, which determine the energetic penalty of the structure based upon deviations from the idealized equilibrium geometry. Since, terms of nonbonded energy interactions is a function of a distance which considers the energy between several atoms this will produce a mechanical properties effect on simulated systems. Choices of $9.5\mathring{A}$ and $6.5\mathring{A}$ cutoffs were considered for both isochoric (NVT), and isobaric (NPT) ensembles.

Van der Waals interaction potential is relatively short range and dies out at a separation distance of 8-10 $\mathring{A}$. Choosing how to treat long-range nonbond interactions is an important factor in determining the accuracy of energy evaluation. Our initial simulations resulted in higher mechanical properties compare to experimental ones. However, by adjusting the cutoff point more realistic values were obtained. Default setup of cutoff points is 9.5 $\mathring{A}$, so a $6.5\mathring{A}$ system was constructed to study the effect of nonbonded energy effect on mechanical properties. Table 3.1 summarizes calculated engineering constants for the different simulation

systems conditions considered.

(Vinylester, Brominated Vinylester)

An Amorphous cell molecular dynamics module is recommended for amorphous polymers to optimize their mechanical behavior, surface characteristics, and interface interactions. An Amorphous module is a suite of computational tools that allow assembly of representative models of complex amorphous system that anticipate the key properties. Simulation parameters which are required to setup the simulation include: system composition chemical chain, temperature, and density. Representative volume element (RVE) models are established from equilibrated vinylester/brominated vinylester atomic structures governed by COMPASS forcefield. The RVE is constructed of ten atomic vinylester/brominated vinylester chains each of 230 atoms. Vinylester simulation parameters are bulk periodic cell density 1.04 gm/cm^3 at room temperature 298 K, and Tg =400 K, figure 3.6. Brominated vinylester simulation parameters are bulk periodic cell density 1.53 gm/cm^3 at room temperature 298 K, and Tg =400 K, figure 3.7. Bromination of vinyl ester will increase the density due to the replacement of some of the hydrogen atoms. There are four bromine (Br) atoms replacing four hydrogen (H) atoms. Br has a large atom weight (79.904g/mol) compared to H (1g/mol). Considering chemical chain structure shown in figures 3.2 the calculated molecular weight of the regular vinyl ester is 1190, while that of the brominated vinyl ester is 1822. Assuming that the unit cell volume is about the same, the density will increase by about 53%.

RVE molecular systems are condensed with NPT (constant number of atoms, pressure, and temperature, MD simulations at 300K and 1 atm for 50ps. This process is followed by NVT (constant number of atoms, volume, and temperature for 100ps raising the molecular system temperature from 300K to 400K in stepwise dynamic simulation. For each polymeric system temperature, this is followed by an NPT dynamic step-wise temperature reduction back to room temperature 300K. Static mechanical properties are calculated for

each equilibrated cell.

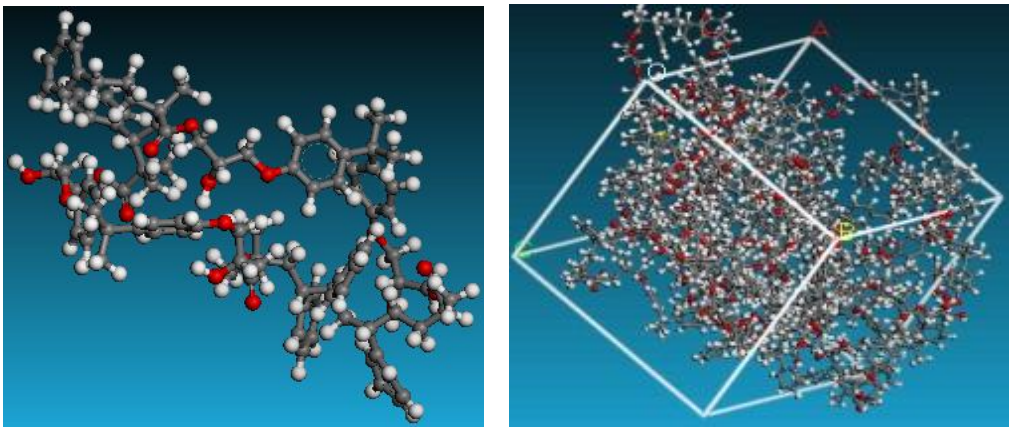

Figure 3.6. (a) Atomic Vinylester Single Vinylester Chain (230) Atoms (b) 10 Chain Vinylester Unit Cell (2300) Atoms

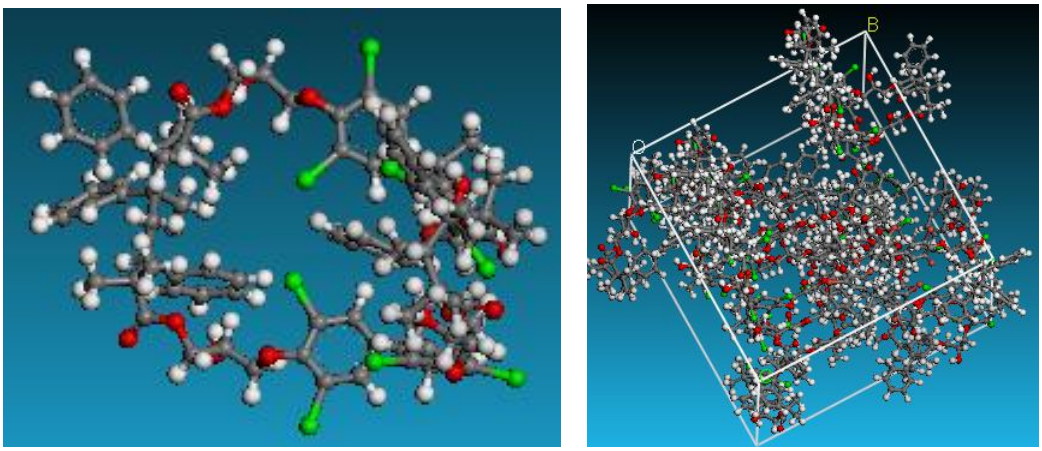

Figure 3.7. (a) Atomic Single Brominated Vinylester Chain (230) Atoms (b) 10 Chain Brominated Vinylester Unit Cell (2300) Atoms

Polyurea

Following the molecular dynamics simulations setup for nylon6,6, molecular dynamics simulations for polyurea are constructed. Figure 3.8 displays the molecular structure of the simulated single chain and periodic unit cell.

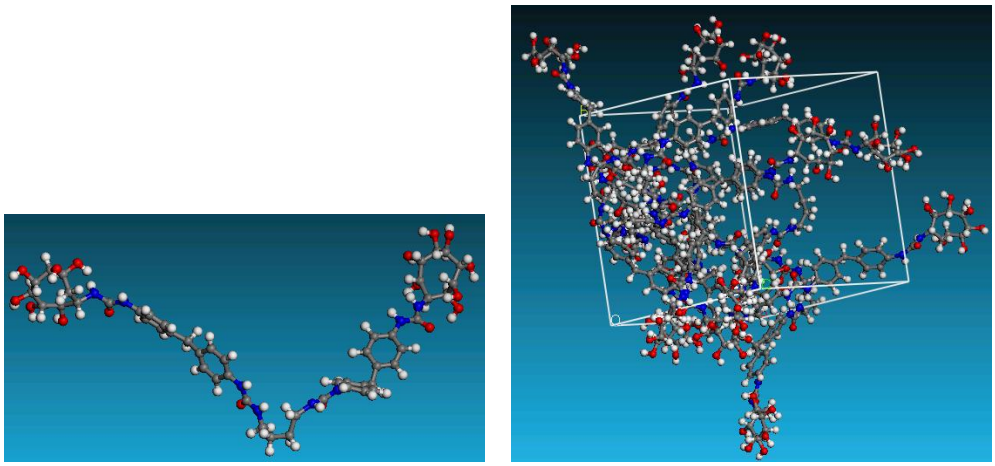

Figure 3.8. (a) Atomic Single Polyurea Chain (362) Atoms (b) 6 Chain Polyurea Unit Cell (2172) Atoms

3.2.3 Mechanical Properties Results

Nylon6,6

Table 3.1. Nylon6,6 Engineering Constants

Engineering Constants	NPT $9.5\mathring{A}$	NPT $6.5\mathring{A}$	NVT $6.5\ \mathring{A}$
E_{11}(GPa)	4.00	2.8	3.4
υ_{12}	0.24	0.28	0.37

Vinylester

Table 3.2 shows the engineering constants of a vinylester amorphous cell for 6, 10, and 12 chains. From the results shown, an amorphous cell of 10 chains of vinylester and 3200 total atoms is the periodic cell of such a polymeric structure. Hence, increasing the amorphous cell atomic size and simulated number of atoms will not induce any mechanical property

variation or improvement beyond the 2300 atom periodic cell.

Table 3.2. Vinylester Engineering Constants versus Number of Chains

Engineering Constants	6 Chains	10 Chains	12 Chains
E_{11}(GPa)	2.83	3.7	3.7
υ_{12}	0.30	0.31	0.31

Brominated Vinylester

Table 3.3 demonstrates the engineering constants for a brominated vinylester amorphous cell of 10 chains. The results indicate as expected that the bromination of vinylester did not vastly affect the mechanical properties.

Table 3.3. Brominated Vinylester Engineering Constants

Engineering Constants	10 Chains
E_{11}(GPa)	3.5
υ_{12}	0.32

Comparing the MD results shown in tables 3.2 and 3.3, the calculated elastic modulus of vinylester is higher than that of brominated vinylester. This result does not match observed experimental values where bromination is expected to increase stiffness of vinylester. However, in these simulations an ideal vinylester chain, that does not include unreacted epoxy, is used. The presence of unsaturated vinylester reduces the mechanical properties. Different amounts of unreacted epoxy molecules may exist for cases of brominated and unbrominated vinylester. This paper, indirectly, suggests that bromination could reduce the amount of unreacted epoxy molecules in vinylester.

Polyurea

Mechanical properties obtained are shown in table 3.4.

Table 3.4. Polyurea Engineering Constants

Engineering Constants	6 Chains
E_{11}(GPa)	3.36
υ_{12}	0.34

3.3 Molecular Dynamics Simulations of Nanoreinforcements

3.3.1 Literature Review

Carbon-based nanomaterials have been attracting much attention during the last decade because of their superior mechanical, electrical and thermal properties. Since the late 1990's, research has been reported that intercalated, expanded, and/or exfoliated graphene nano platelets could also be used as nano-reinforcements in polymer systems. The key point of utilizing graphite as a nano-reinforcement is in its ability to be exfoliated into platelelts of nanometer dimensions using graphite intercalated compounds (GICs). Natural graphite is abundant, and its cost is low compared to the other nano size carbon materials. The graphite nanoplatelets are expected to be marketed at approximately \$10-20/lb once high demand and full production is achieved. This is significantly less expensive than single-walled carbon nanotubes (SWCNT) ($<\$45,000/lb$) or vapor grown carbon fiber (VGCF) (\$40-50/lb), yet the mechanical, electrical, and thermal properties of crystalline graphite flakes are comparable to those of SWCNT and VGCF.

Obtaining the mechanical properties of carbon nanotube (CNT) experimentally or theoretically is the focus of many researchers in nanomechanics. A wide range of values are obtained depending on the method used. For example, Transmission Electron Microscopy (TEM) is used to obtain Young's modulus of multi-walled carbon nanotubes (MWCNT)s by measuring the mean-square vibrational amplitudes of MWCNTs [48] This technique results in a Young's modulus of 1.8±0.9 TPa. Other experimental techniques, such as Atomic Force Microscopy (AFM), results in Young's modulus of 0.81±0.41 TPa [49] Parallel to experimental efforts, theoretical models are used to estimate mechanical properties of MWCNT. These models have some inconsistencies as well. For example, modeling MWCNTs as simple

structural elements (e.g., bar, beam, or shell) ignores certain MWCNT molecular structural details [50]. Li and Cho [51] accounted for the Van der Waals forces between tube layers by introducing a nonlinear truss rod model. The results show that Young's modulus of MWCNTs is in the range of 1.05±.05 TPa.

Alternatively, molecular mechanics (MM) and molecular dynamics (MD) are used as a tool to model MWCNTs. For example, Batra and Sears [52] use MM to determine double-walled carbon nanotubes (DWCNT)s structures and to analyze their infinitesimal extensional, torsional, radial expansion/contraction and bending deformations, based on a continuum model. Al-Ostaz et al. [39] SWCNTs using MD approach to simulate SWCNT's elastic constants for different chiralities are calculated, and the effect of clustering of SWCNTs on their effective properties is evaluated. Zhang et al.[53] performed MD simulations on MWCNTs under axial compression to investigate the effects of the number of walls, and their van der Waals (vdW) interaction on buckling behaviors.

Graphene is a single layer sp^2-bonded carbon sheet forming a honeycomb crystal lattice [54], first introduced by Mouras, et al. (1987) as the two dimensional (2D) form of graphite. Novoselov et al. (2004) [55, 56] reported that these two dimensional (2D) carbon materials formed gigantic flat fullerene molecules and first described their electronic properties. Lee et al. reported a Young's modulus of 1.0 TPa and an intrinsic strength of 130 GPa measured by nanoindentation atomic force microscope for the monolayer graphene sheet [57]. By those measurements, Lee categorized the graphene monolayer sheet as the strongest material ever measured. Consequently, graphene nanocomposites are expected to perform extremely enhanced mechanical properties. Exfoliated Graphite Nano Platelets (xGnP) are new types of nanoparticles consisting of graphene stacks that are 1-15nm thick and with diameters ranging from $<\mu m$ 1 to 100μm.Exfoliated graphene nano platelets share chemical structures with CNT. In fact, their edges could be easily modified chemically for dispersion enhancement in polymeric composites[58]. Figure 3.9 shows the morphology of exfoliated graphene nano platelets. These nanoplatelets are typically less than 5 nm thick and can be

synthesized with lateral dimensions ranging from less than $1\mu m$ to up to $100\mu m$. The use of exfoliated graphite flakes exfoliated graphene nano platelets opens up many new applications where electromagnetic shielding, electrical conductivity, high thermal conductivity, gas barrier resistance, high fracture toughness, or low flammability are required.

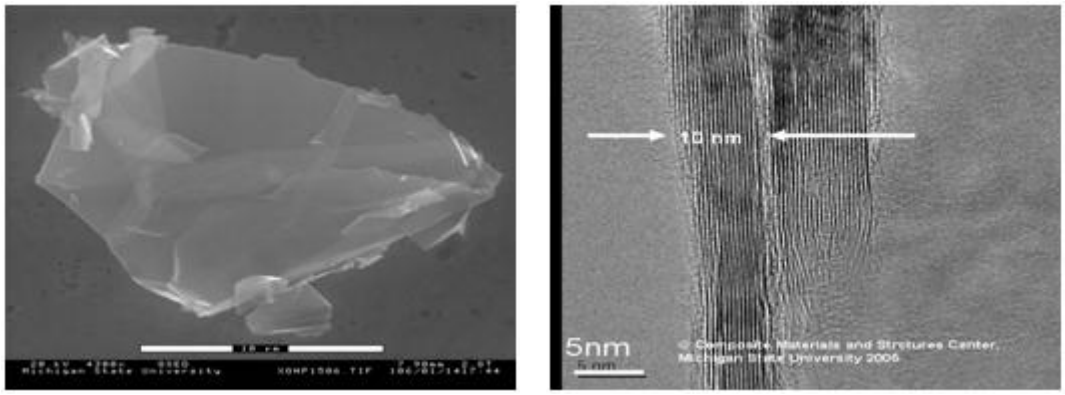

Figure 3.9. Images of Exfoliated Graphene Nano Platelets:(a)Lateral View Using SEM (b)Edge View Using TEM Micrograph (Courtesy of L. T. Drzal)

3.3.2 Molecular Simulation Setup

Simulations of multi-walled carbon nanotubes

Molecular dynamics (MD) simulations are used to calculate the equivalent continuum mechanics elastic constants for multi-walled carbon nanotubes. These elastic constants are found to be sensitive to the carbon nanotube geometry (chirality, aspect ratio, and number of walls) and the MD simulation conditions (temperature, thermodynamic ensemble, barostat and thermostat algorithms). Our analysis shows that the chirality of carbon nanotubes, for a fixed radii and separation distance, does not affect the obtained value of elastic modulus. The minimum number of super cells required for the periodic cell is correlated to the number of CNT layers. A three wall CNT is found to be the optimum number of walls beyond which longitudinal elastic modulus of MWCNTs will not change. For the simulation parameters, the NVT (constant number of atoms, constant volume, and constant temperature) thermodynamic ensemble results in the most realistic values of elastic constants when combined with Anderson thermostat algorithm. For the NPT (constant number of particles, constant pressure, and constant temperature) thermodynamic ensemble, the Berendsen barostat coupled with Parrinello thermostat it is recommended.

1. **GEOMETRICAL PARAMETERS**

   (a) *Effect of MWCNT Building Method*

   Building a MWCNT structure is usually done by either maintaining a constant chiral innermost tube then progressively adding the outer tubes (case 1) or by fixing the outermost tube and then adding the inner tubes (case 2). Previous studies exhibit that using case 1 construction, elastic modulus increases with the increasing number of walls. However, using case 2, elastic modulus and Poissons

ratio decrease with the increasing number of walls [53]. Neither of these cases account for the true affect of chirality. Therefore, in this paper two methods are used to build the MWCNTs: individual and sequential. In the individual setup, the chirality of each wall of the MWCNT is specified. When the sequential setup the MWCNT is constructed automatically, by predetermining the number of layers, most inner tube chirality, and minimum separation distance are accomplished. Then the software randomly defines the chiral vector for each layer. In this paper, for the individual setup, the simulated MWCNTs chiral vectors are chosen as $(5xn, 5xn)$, n: refers to the layer number, n =1, 2, 3, ... In this configuration the interwall distance is very close to the one observed experimentally [33, 52, 59]. For the sequential setup, the minimum separation distance is set to the interlayer distance of graphite sheets (3.347 Å), and the innermost chiral vector is fixed to be (5, 5). This work is mainly focused on $(5n, 5n)$ MWCNTs, because mixed chiral nanotubes with incommensurate periods along their axis will lead to a non-periodic system, which violates the Bloch theorem [60, 61]. Thus, it makes calculations more difficult [62].

Typical stiffness matrices for MWCNT obtained using NPT thermodynamic ensemble and Berendsen (thermostat, barostat) velocity algorithm are shown in figure (3.18,3.19) for the case of four walls:

$$C_{ij} = \begin{bmatrix} 202 & 21.6 & 11.2 & 0 & 0 & 0 \\ 15.9 & 45.5 & 11.9 & 0 & 0 & 0 \\ 21.7 & 36.9 & 23.7 & 0 & 0 & 0 \\ 0 & 0 & 0 & 3.2 & 0 & 0 \\ 0 & 0 & 0 & 0 & 10.41 & 0 \\ 0 & 0 & 0 & 0 & 0 & 1 \end{bmatrix} GPa$$

Figure 3.10. Sequential Simulation

$$C_{ij} = \begin{bmatrix} 202 & 21.6 & 11.2 & 0 & 0 & 0 \\ 15.9 & 45.5 & 11.9 & 0 & 0 & 0 \\ 21.7 & 36.9 & 23.7 & 0 & 0 & 0 \\ 0 & 0 & 0 & 3.2 & 0 & 0 \\ 0 & 0 & 0 & 0 & 10.41 & 0 \\ 0 & 0 & 0 & 0 & 0 & 1 \end{bmatrix} GPa$$

Figure 3.11. Individual Simulation

By examining the above matrices, one can conclude that MWCNTs are transversely isotropic with five independent engineering constants. Shen and Li [63] report analytical expressions for these constants based on five independent experiments: axial tension and compression stresses, torsional moment, in-plane biaxial tension, and in-plane shear loadings at small strain conditions. The engineering constants are calculated using the following relation[64]:

$$E_{11} = C_{11} - \frac{2C_{12}^2}{C_{22} + C_{23}} \tag{3.1}$$

$$E_{22} = C_{22} + \frac{C_{12}^2(-C_{22} + C_{23}) + C_{23}(-C_{11} + C_{23} + C_{12}^2)}{C_{11}C_{22} - C_{12}^2} \tag{3.2}$$

$$\upsilon_{12} = \frac{C_{12}}{C_{22} + C_{23}} \tag{3.3}$$

$$K_{23} = \frac{C_{22} + C_{23}}{2} \tag{3.4}$$

$$G_{23} = \frac{C_{22} - C_{23}}{2} \tag{3.5}$$

where E_{11} and E_{22}, are the longitudinal and transverse modulus, υ_{12} is Poissons ratio, K_{23} is the bulk modulus, and G_{23} is the shear Modulus. C_{ij} are the elastic constants of shown below, where i,j=1,2,3:

$$C_{ij} = \begin{bmatrix} C_{11} & C_{12} & C_{13} & 0 & 0 & 0 \\ C_{21} & C_{22} & C_{23} & 0 & 0 & 0 \\ C_{31} & C_{32} & C_{33} & 0 & 0 & 0 \\ 0 & 0 & 0 & C_{44} & 0 & 0 \\ 0 & 0 & 0 & 0 & C_{55} & 0 \\ 0 & 0 & 0 & 0 & 0 & C_{66} \end{bmatrix} GPa$$

(b) *Effect of Number of Layers*

Since MWCNTs consist of several coaxial tubes with an outer diameter of (1.4∼100) nm, and the number of walls ranges from two to tens [65], a second geometric parameter which include effect of number of layers is assessed in figure 3.12.

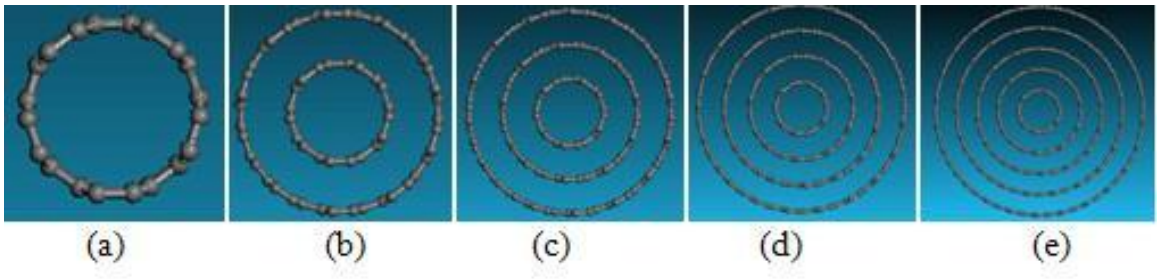

Figure 3.12. MWCNTs with chiral angle of (5n, 5n) for the cases of (a) SWCNT (b) DWCNT (c) Three-walled CNT (d) Four-walled CNT (e) Five-walled CNT

(c) *Effect of Super Cell Size*

The unit cell is regarded as the basic building block of a crystal. This unit cell is an artificial cell used to represent the size, shape, and number of objects contained

within a crystal. The unit cell is generally parallelepiped, defined by certain lattice parameters, based on the characteristic angles and magnified distances of a crystal. The CNT unit cell block is a triclinic unit cell with γ=β=90°, α=120° see figure 3.13. The chirality and diameter of CNT define the length parameters B and C in figure 3.13. The value of A defines the simulated length of the CNT.

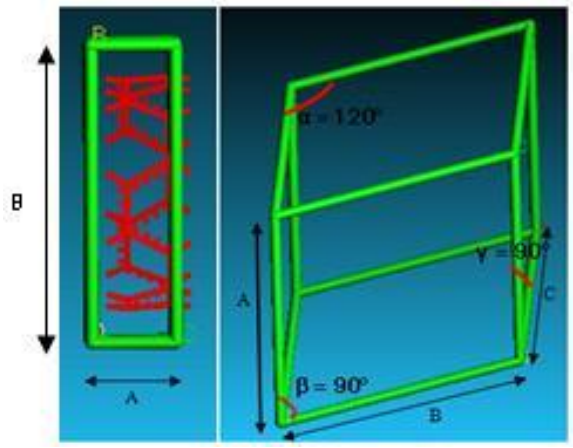

Figure 3.13. Schematic triclinic unit cell showing lattice parameters

A super cell is constructed by repeating unit blocks in any of the symmetry axes. In order to simulate an infinite length, periodic boundary conditions (periodic cell) are usually used. A limitation of a periodic cell is the impossibility to achieve fluctuations that have a wave length greater than the length of the unit cell. The range of interactions is also important. If the cell size is large compared to the range over which interactions act, there should be no problem. For example, for the relatively short range Lennard-Jones potential, the cell should have a side greater than 6σ (where σ is the depth of potential well), which corresponds to about $20.4\mathring{A}$ for carbon [66, 67, 68]. For longer range electrostatic interactions, the situation is more complicated. However, long-range order interactions, such as Columbic and dipolar, need to be imposed upon the system and their potential forces should be considered.

The effects of imposing a periodic boundary can be evaluated empirically by comparing results obtained using a variety of cell shapes and sizes [69]. The limitations of molecular modeling include not only the size of the unit cell but also the time required to equilibrate the unit cell for energy interaction calculations between atoms. Several cell sizes for MWCNTs are considered to study the effect on engineering constants (figure 3.14).

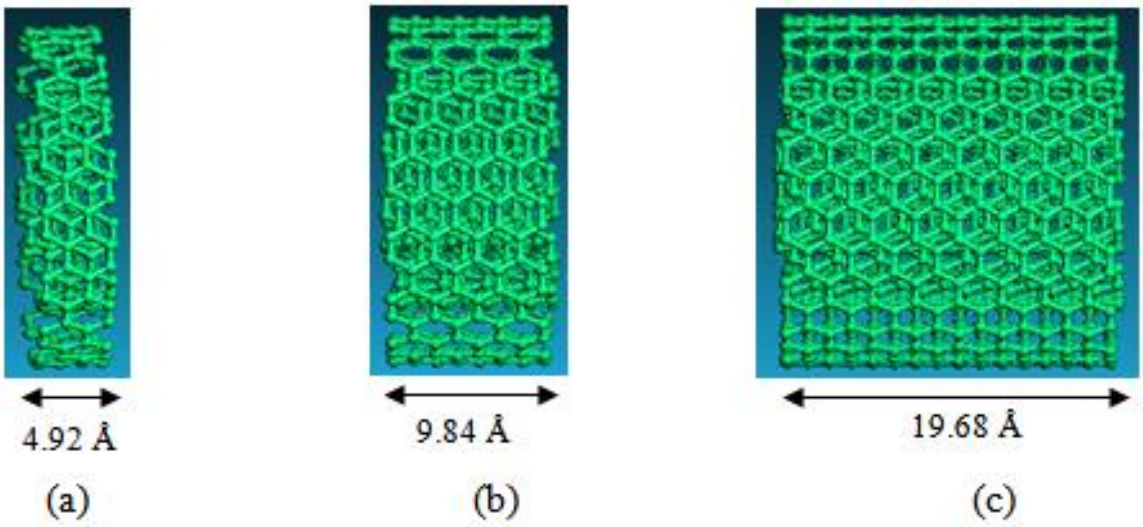

Figure 3.14. Typical simulated MWCNT for (a) two (b) four and (c) eight unit cells

2. SIMULATION PARAMETERS

(a) *Heat Effect*

CNTs can be created using arc discharge [70, 71, 72] laser vaporization[73, 74] or catalytic decomposition of hydrocarbons [75]. Jacques et al. [76] demonstrates that high purity MWCNTs can be produced in bulk quantities on quartz substrates from a catalytic decomposition of a ferrocene-xylene mixture at $937K$ [77, 78, 79]. Since CNTs are produced at high temperatures, a three-walled MWCNT is exposed to target temperatures of 400, 600, 800, 1000, and $1200K$.

Simulations of Graphene/Graphite

Graphite atomic hexagonal crystal group 186 P63MC is constructed with dimensions shown in Figure 3.15. Molecular dynamic geometry parameters, such as periodic cell size and number of layers, are simulated to study their effect on graphene mechanical properties. NVT associated with Anderson thermostat is the thermodynamic ensemble applied through the entire simulated configurations.

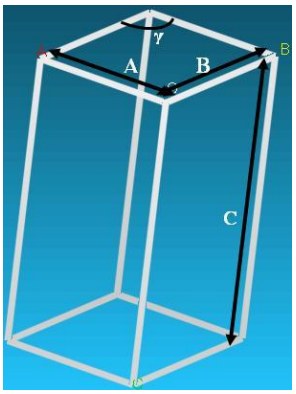

A	B	C
2.47 Å	2.47 Å	6.79 Å
α	β	γ
90 °	90 °	120°

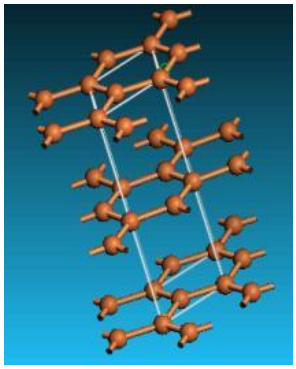

Figure 3.15. Molecular Graphite Structure: (a) Crystal dimensions, (b) Atomic crystal structure

A structure energy minimization followed by a dynamic system equilibration under NVT ensemble is applied for pre-determined dynamic time. Dynamic time for simulated atomic structures is proportional to the number of atoms included in each supercell. A dynamic step of $0.1fs$ and a 100 kcal/mol energy deviation are kept constant for all graphene conducted simulations.

3.3.3 Mechanical Properties Results

MWCNT

1. **GEOMETRICAL PARAMETERS**

(a) *Effect of MWCNT Building Method*

Figure 3.16 shows a plot of MWCNT's longitudinal elastic constant, E_{11}, for sequential (SEQ) and individual (IND) build setups using NPT thermodynamic ensemble. The results show that different building ensemble has a minor effect on the calculated elastic constants. The drop of value in the case of the 4 walls is due to the effect of super cell size as discussed in details in section 3.3.2.

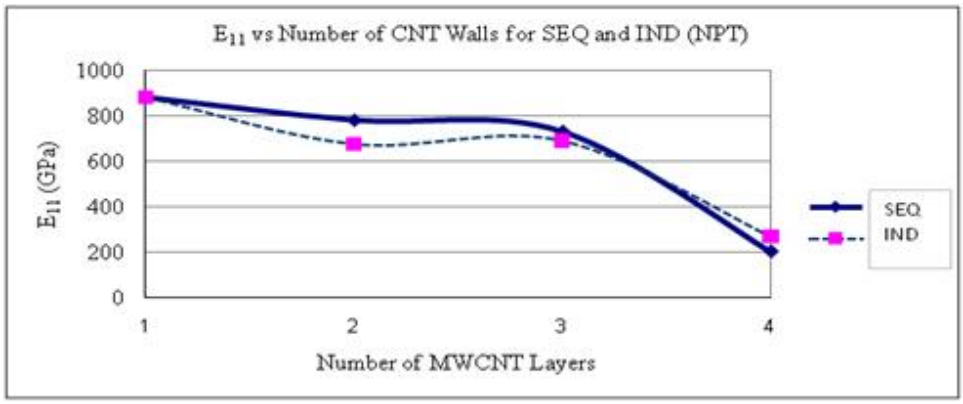

Figure 3.16. E_{11} versus number of 20 supercells of CNT layers using NPT ensemble for both sequential (SEQ) and individual (IND) setups

(b) *Effect of Number of Layers*

Figure 3.17 shows the effect the of number of layers on E_{11} for NPT ensemble. It is observed that the SWCNT has the highest E_{11} elastic constant. Increasing the number of layers results in a drop of mechanical properties. However, the modulus approaches a constant value after three layers. Therefore, three layers are chosen as the optimum number of layers for simulation purposes in this study.

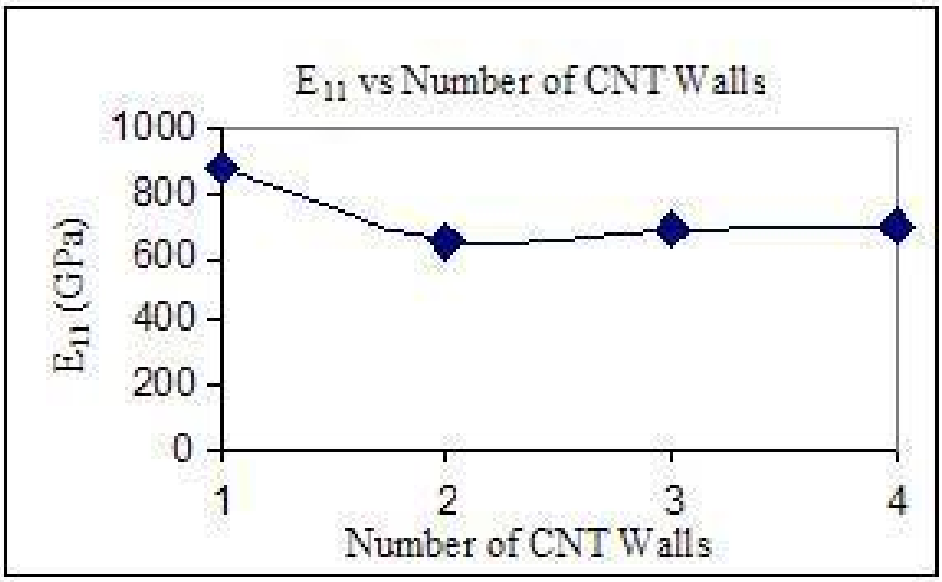

Figure 3.17. E_{11} versus number of layers for periodic MWCNT

(c) Effect of Super Cell Size

Typical stiffness matrices for eight- and twenty-unit cell MWCNTs are given below:

$$C_{ij} = \begin{bmatrix} 606.5 & 31.1 & 29.6 & 0 & 0 & 0 \\ 31 & 68 & 50.2 & 0 & 0 & 0 \\ 29.6 & 50.2 & 67.4 & 0 & 0 & 0 \\ 0 & 0 & 0 & 0.8 & 0 & 0 \\ 0 & 0 & 0 & 0 & 0.7 & 0 \\ 0 & 0 & 0 & 0 & 0 & 9.2 \end{bmatrix} GPa$$

Figure 3.18. Eight unit super cell

$$C_{ij} = \begin{bmatrix} 698.1 & 25 & 25 & 0 & 0 & 0 \\ 25 & 66.2 & 49 & 0 & 0 & 0 \\ 25 & 49 & 66.4 & 0 & 0 & 0 \\ 0 & 0 & 0 & 0.8 & 0 & 0 \\ 0 & 0 & 0 & 0 & 0.6 & 0 \\ 0 & 0 & 0 & 0 & 0 & 8.6 \end{bmatrix} GPa$$

Figure 3.19. Twenty unit super cell

All simulations are performed under NPT ensemble (barostat: Berendsen; thermostat: Parrinello), where the boundaries of the unit cell are set to be free to allow for volumetric change during dynamic loading. The unit cell temperature is raised from $298K$to $400K$ and then cooled back to room temperature. The same procedure is applied for all the cases shown in table 3.5. Different dynamic time is used for equilibrating the system at a rate of $1fs$ per dynamic step. The total dynamic time is proportional to the total number of atoms (proportional to the length of CNT). From table 3.5, it is reasonable to assume that, for this study

case, $20\mathring{A}$ CNT is an optimal simulation length because engineering properties are approaching constant values beyond that length.

Table 3.5. Engineering constants versus aspect ratio of MWCNT super cells

Three Wall	Length $\mathring{A}$	L/d I*	L/d O**	E_{11} (GPa)	E_{22} (GPa)	υ_{12}	G_{23} (GPa)	K_{23} (GPa)
2 units	4.92	0.72	0.25	439	36	0.20	11	47.3
4 units	9.84	1.5	0.50	493	36	0.26	7.7	47.15
8 units	19.68	3.63	1.20	590	31.1	0.26	9.0	59.2
20 units	49.2	7.3	2.4	687	30	0.26	8.6	57.6
30 units	73.8	11	3.6	690	27.5	0.33	7.9	52.6
40 units	98.4	14.4	4.8	720	28.6	0.33	8.3	54.9

*innermost**outermost

2. SIMULATION PARAMETERS

(a) *Heat Effect*

Two simulation sets are considered. In the first set, the temperature of MWCNT is raised from room temperature to target temperature and then cooled back to room temperature, at which elastic constants are calculated (see figure3.20 (a)). In the second set, the temperature is raised to target temperature, and elastic constants are calculated at that temperature (see figure 3.20(b)). Figures 3.20 (a) and (b) show that the elastic properties of MWCNTs are not affected by temperature scheme.

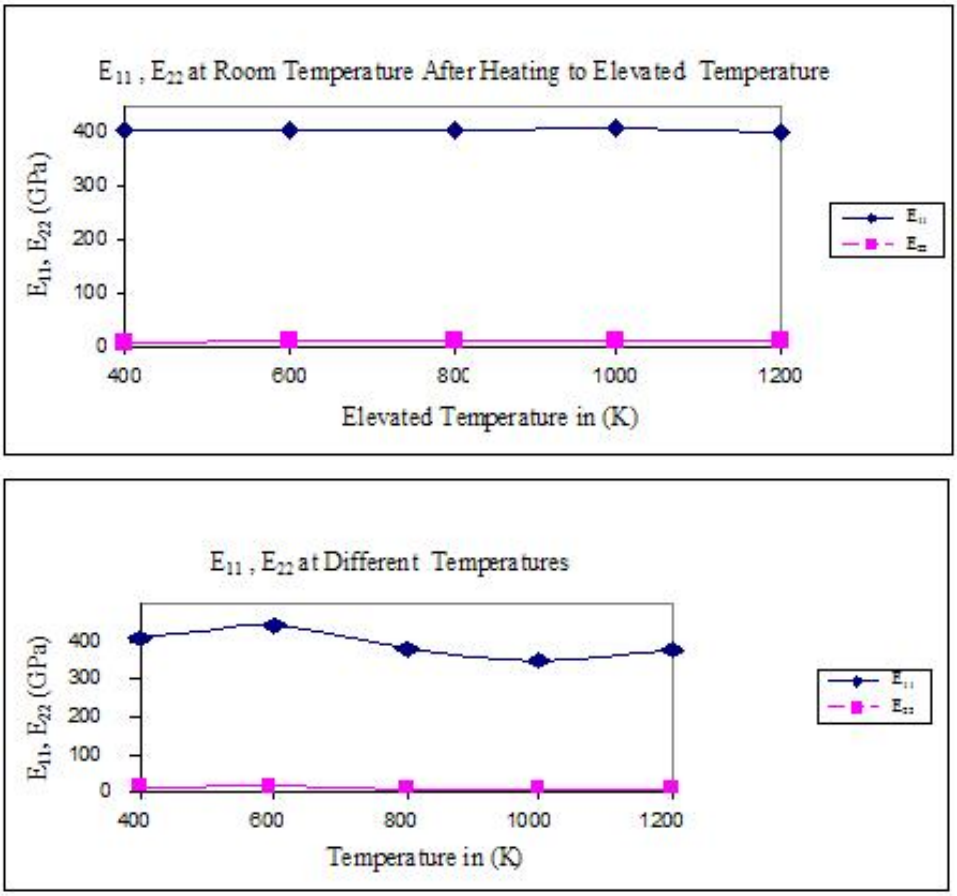

Figure 3.20. Elastic constants E_{11} and E_{22} of three-walled CNT for the case of (a) heated to different target temperatures and then cooled back to room temperature and (b) heated to different target temperatures (NVT, Berendsen thermostat)

(b) *Thermodynamics Ensemble Effect*

Figure 3.21 shows the longitudinal elastic constant versus the number of CNT walls for fixed super cells length. The drop in modulus in cases of four and five walls is the consequence of using a periodic cell of limited size; this result is different from the results shown in figure 3.17 which are for a larger unit cell. The figure 3.21 shows that the results for the thermodynamic ensembles are relatively small.

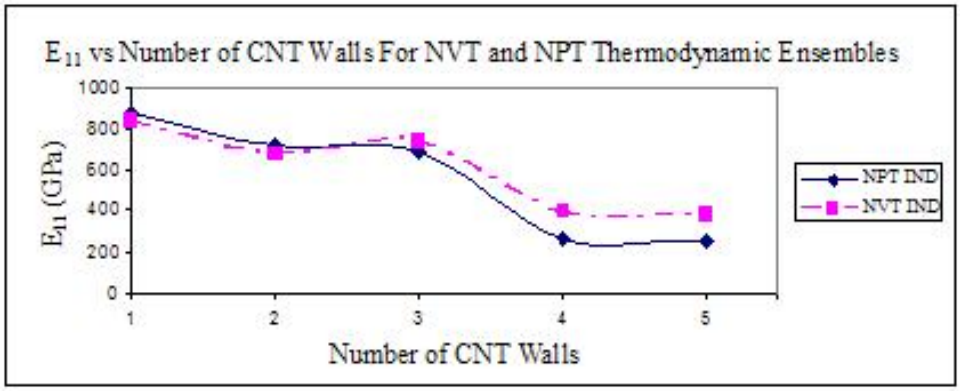

Figure 3.21. E_{11} versus number of layers for NPT and NVT ensembles for a 20 super cell

(c) *Thermostat and Barostat Algorithms Effect*

Figure 3.22 demonstrates that the effect on the elastic modulus deduced different thermostat and barostat algorithms. For some cases, the difference is considerable. For example, for the case of DWCNT simulated under NVT ensemble, the longitudinal modulus is about 400 GPa for Berendsen barostat and Berendsen thermostat, whereas they are about 750 GPa when Berendsen thermostat and Parrinello barostat are used. Berendsen thermostat is not a canonical algorithm. A small energy variation in the dynamic equilibration will result in a divergence in the calculated mechanical properties. On the other hand, Anderson thermostat is a stochastic ensemble. Berendsen barostat does not generally produce trajectories from any known ensemble, and non physical vibrations of the volume may occur. Meanwhile, Parrinello barostat induces dipoles which are treated as additional dynamical variables that are included in the extended Lagrangian function [80, 81]. Coupling the Berendsen thermostat with Parrinello barostat leads to a statistical ensemble. Referring to [82], the prescription for generating state points in the NPT ensemble must clearly provide for changes in the sample volume as well as energy. Based on the fluctuation of mechanical properties for NPT, it is recommended to use the Berendsen barostat coupled with Parrinello thermostat, and, for NVT Anderson, thermostat is recommended.

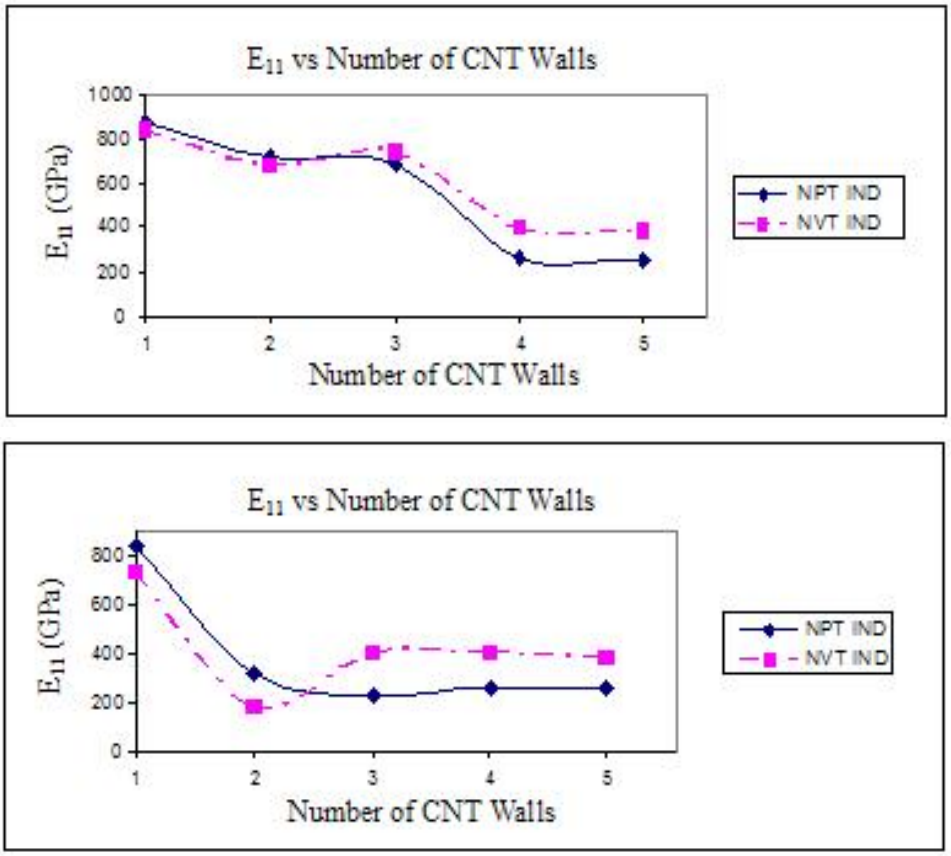

Figure 3.22. E_{11} versus MWCNT layers for different thermostat and barostat algorithm: (a) Berendsen Thermostat and Parrinello Barostat (b) Berendsen Thermostat and Berendsen Barostat

Graphene

Graphene supercells of different sizes are shown in Figure 3.23. Elastic constants of the numerous super cells are shown in table 3.6. From the results shown in table 3.6 it can be concluded that the periodic cell size for the graphene is a 2x2 supercell crystal. Where E_{11} is the longitudinal elastic modulus, E_{22} is the transverse elastic modulus, υ_{12} is the Poisson's ratio 12 direction, G is the shear modulus, and K is the bulk modulus.

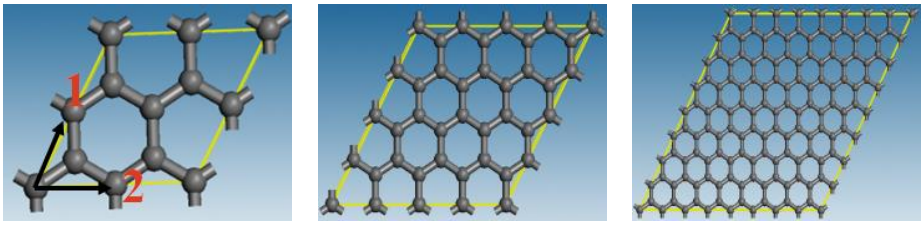

Figure 3.23. Graphene Atomic Supercell (a) Graphene 2x2 Supercell, (b) Graphene 4x4 Supercell, (c) Graphene 8x8 Supercell

Table 3.6. Graphene Engineering Constants versus Number of Supercells

Engineering Constants	Graphene Unit cell (NVT)			
	Single Graphene Layer			
	Number of Supercells			
	2x2 (8 atoms)	4x4 (32 atoms)	6x6 (70 atoms)	8x8 (128 atoms)
E_{11}(GPa)	1373.3	1373.7	1373.9	1373.7
E_{22}(GPa)	830.3	831.8	832.1	832.3
υ_{12}	0.30	0.31	.31	.31
G(GPa)	340.5	340.5	340.5	340.5
K(GPa)	621.1	625.4	626.3	626.6

Graphite

1. **Effect of Unit Cell Size**

Figure 3.24 shows a double layered graphite molecular supercell (side and top views). Several graphite supercells are simulated to study the effect of the supercell size on graphite mechanical properties and to obtain the periodic cell dimensions for the graphite atomic structure.

Table 3.7, and table 3.8 show the engineering constants for the graphite molecular structure of different supercell sizes. From tables 3.7, and 3.8 it can be seen that the engineering constants tend to remain steady for both supercell structures at 4x4 size for the double layer and at 8x8 for the four layered graphite. Increasing the number of

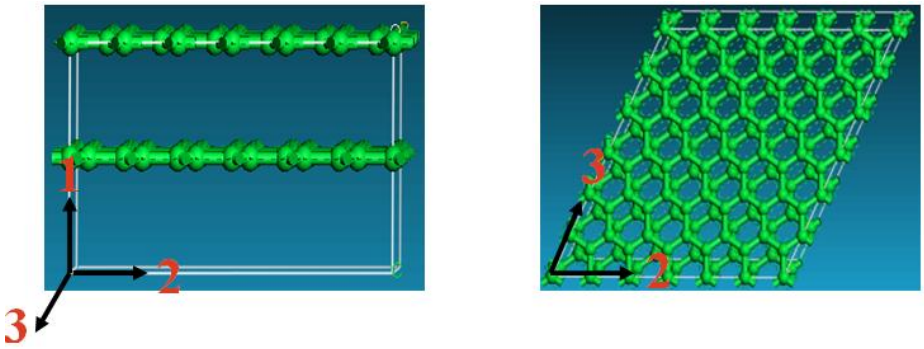

Figure 3.24. Double Layered Graphite Super Cell (a) Side view, (b) Top view

layers simulated requires a larger supercell to represent the periodic simulated graphite cell. Where E, G, K are the Young's, shear, and bulk moduli respectively, and υ is the Poisson's ratio

Table 3.7. Double Layer Graphite Engineering Constants versus Number of Supercells

Engineering Constants	Graphite (NVT) Number of Supercells				
	Double Graphene Layer				
	Number of Supercells				
	4x4 (64 atoms)	6x6 (144 atoms)	8x8 (256 atoms)	10x10 (400 atoms)	12x12 (576 atoms)
E_{11}(GPa)	26.9	27.5	27.5	27.6	27.7
E_{22}(GPa)	1159.6	1160.3	1160.3	1160.2	1160.2
υ_{12}	0	0	0	0	0
M(GPa)	406	406.2	406.2	406.2	406.1
G(GPa)	1014	1014.8	1014.8	1015	1015

Table 3.8. Four Layer Graphite Engineering Constants versus Number of Supercells

Engineering Constants	Graphite (NVT) Number of Supercells	
	Four Graphene Layer	
	Number of Supercells	
	8x8 (512 atoms)	12x12 (1152 atoms)
E_{11}(GPa)	29.2	29.1
E_{22}(GPa)	1161.3	1160.6
υ_{12}	0	0
G(GPa)	406.4	406.4
K(GPa)	1015.4	1014.7

2. **Effect of Number of Layers**

Several layers are simulated to study their geometrical effect on graphite mechanical properties. Figure 3.25 shows a molecular crystal structure for a four-layered and a ten-layered graphite supercell. Table 3.9 demonstrates the engineering constants for double, four, and ten layered graphite periodic cells. The results recorded in table 3.9 affirm that the variation of the engineering constants for the multi layered graphite periodic cells is less than 5%.

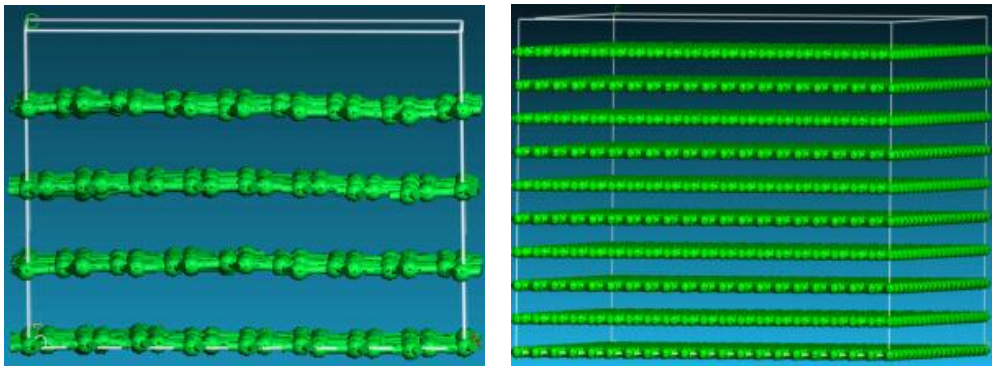

Figure 3.25. Multi Layered Graphite Super Cell: (a) Four Layer, (b) Ten Layer

Table 3.9. Periodic Graphite Cells Engineering Constants versus Number of Layers

Engineering Constants	Graphite (NVT) Number of Layers		
	Number of Layers		
	Number of Supercells		
	2 Layers (64 atoms)	4 Layers (512 atoms)	10 Layers (9640 atoms)
E_{11}(GPa)	26.9	29.2	27.8
E_{22}(GPa)	1159.6	1161.3	1160.1
υ_{12}	0	0	0
M(GPa)	406	406.6	406.05
G(GPa)	1014	1015.4	1015

3.4 Molecular Dynamics Simulations of Interfacial Strength

3.4.1 Literature Review

Vinylester-resin systems have other challenges: poor resistance to crack propagation, brittleness, and large shrinkage that occurs during polymerization. Methods of incorporating nanoparticles into polymer matrices could be ex-situ, like dispersion of the synthesized nanoparticles into resin solution, or in-situ, like monomer polymerization process in the presence of the nanoparticles.

The interactions between the nanoparticles and the matrix for the ex-situ fabricated composites are normally Van der Waals force; however, the in-situ synthesis methods may create strong chemical bonding within the composite. Introducing good interfacial bonding between nanofillers and the resin is often used to alleviate volume shrinkage and void formation and improve surface dispersion along with toughness. Control of interfacial adhesion appears to be crucial since a major cause of impact-related problems is believed to be associated with the level of adhesion at the interface between fiber and matrix. A variety of fiber surface treatment and modification techniques is used to control the interfacial bonding. The strong interface favors a brittle fracture mode with relatively low energy absorption; whereas, a weak interface favors a multiple shear mode with high energy absorption. Therefore, optimization of the interfacial adhesion is required to obtain excellent interfacial strength along with enhanced impact properties. According to Gou, et al. [83], molecular dynamic simulations can provide detailed information on interface structure and interaction. The Vinylester bromination effect is simulated to study the effect of bromination on the interfacial strength of vinylester-graphene and vinylester-graphite nanocomposites. High interfacial strength will result high stiffness, strength, and toughness in the composite [83, 84]. Figure 3.26 shows a schematic chemical chain for a brominated vinylester.

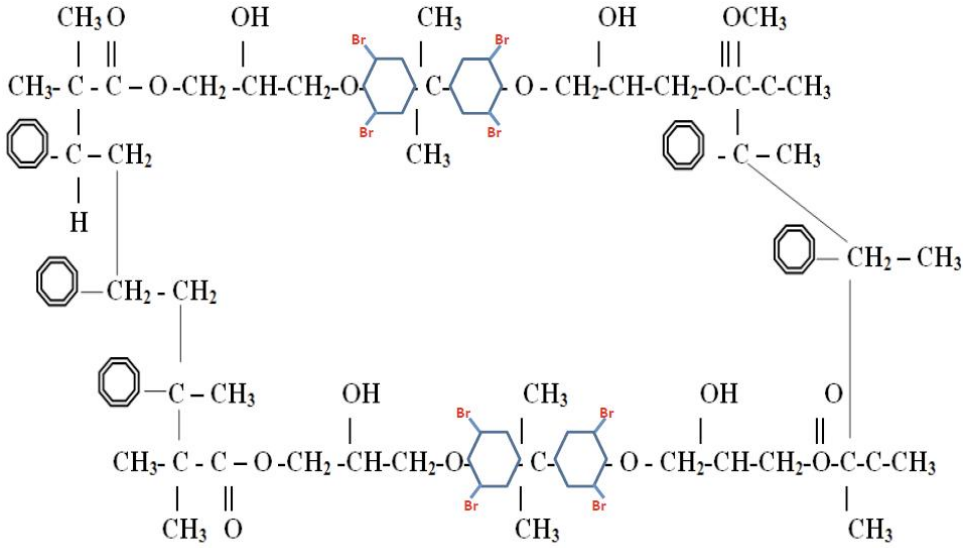

Figure 3.26. Molecular Structure of Brominated Vinylester

3.4.2 Molecular Simulation Setup for Interfacial Strength

Simulations of Graphene-Vinylester and Graphene-Brominated Vinylester Interfacial Properties

The pullout energy,$E_{pull-out}$, is defined as the energy difference between the fully embedded graphene plate and the complete pull-out configuration. It can be related to the interfacial shear stress, τ_i, by the following equation 3.6-3.8:

$$E_{pull-out} = \int_0^L 2(W+t)(L-x)dx \tag{3.6}$$

$$E_{pull-out} = (W+t)L^2 \tag{3.7}$$

$$\tau_i = \frac{E_pull - out}{(W+t)L^2} \tag{3.8}$$

where, W, L and t are the width, length, and thickness of the graphene plate, respectively, and x is the displacement of the graphene sheet. Molecular dynamics simulations are carried out for the following fiber polymer pull-out energies: graphite-vinylester interface figure 3.27, graphene-vinylester interface figure 3.28, graphite-brominated vinylester interface figure 3.29, and graphene-brominated vinylester interface figure 3.30.

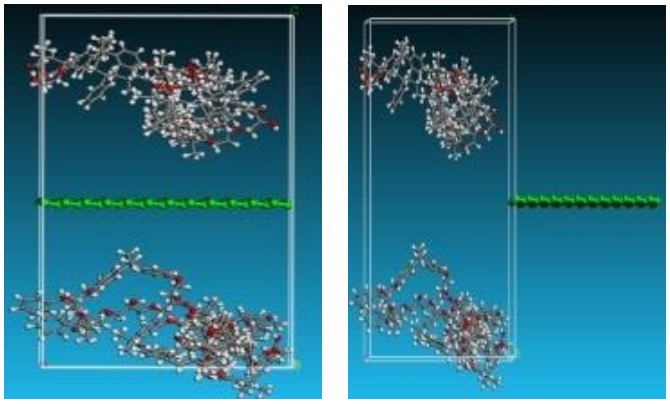

Figure 3.27. Atomic Model for Graphene-Vinylester Reinforcement Interfacial Pull-out

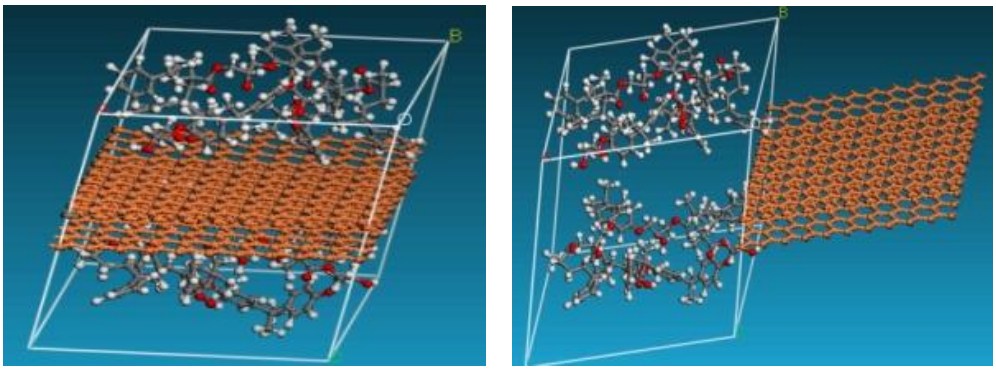

Figure 3.28. Atomic Model for Graphite-Vinylester Reinforcement Interfacial Pull-out

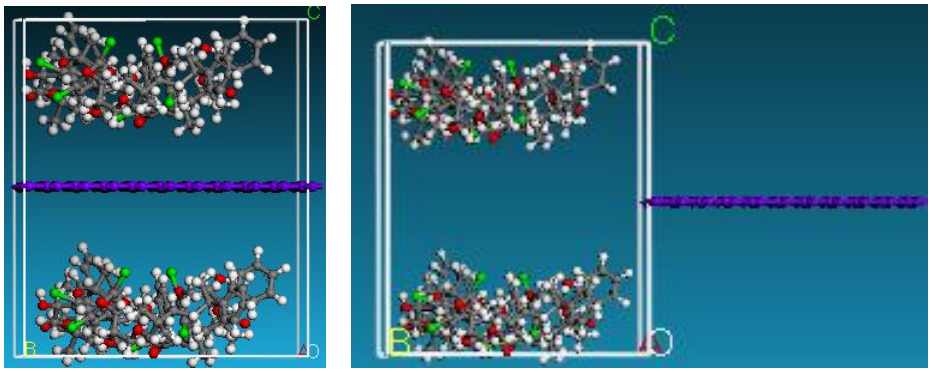

Figure 3.29. Atomic Model for Graphene-Brominated Vinylester Reinforcement Interfacial Pull-out

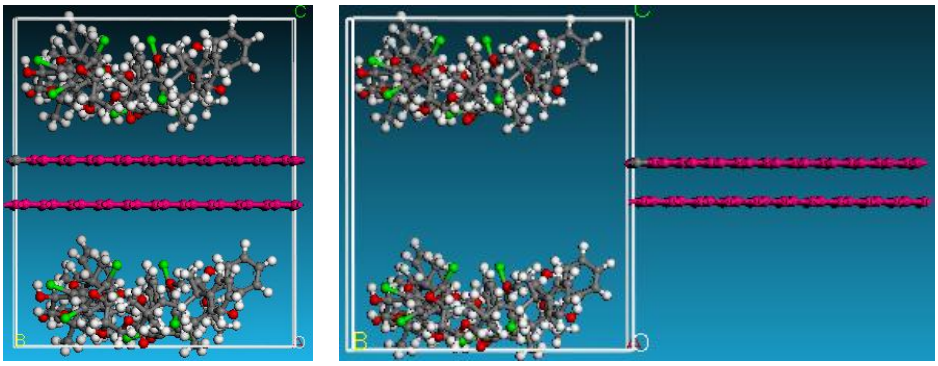

Figure 3.30. Atomic Model for Graphite-Brominated Vinylester Reinforcement Interfacial Pull-out

3.4.3 Interfacial Strength Results

Interfacial Strength (Graphene/Graphite-Vinylester/Brominated Vinylester)

The $E_{pull-out}$ calculated from MD simulation for the vinylester-graphene is 149.61 kcal/mol. The energy plot is shown in Figure 3.31(a). The properties of the unit cell simulated for the pull-out energy are: density of 0.37 gm/cm^3, molecular weight of 10672 gm/mol, and cell dimensions of $L = 29.64\mathring{A}$, $W = 29.64\mathring{A}$, $t = 3.4\mathring{A}$. Figure 3.27. According to equations 3.6-3.8, the interfacial strength is calculated to be = 256 MPa, which is double the calculated interfacial strength value for the SWCNT- Polyethylene reported in [39, 83].

A similar atomic cell structure is constructed for the graphite figure 3.28 to study the

interfacial strength of a multi layered graphene nanoplatelet. Double layered graphite is chosen with a density of 0.572 gm/cm^3, molecular weight of 13104 gm/mol, and cell dimensions of $L = 29.64\mathring{A}$, $W = 29.64\mathring{A}$, $t = 3.4\mathring{A}$. E_$pull - out$ for the double layer of graphite is 69.8k-cal/mole figure 3.31(b). The interfacial strength calculated from equations 3.6-3.8 is 125 MPa, which is less than half of the graphene interfacial strength.

The vinylester bromination effect on interfacial strength of vinylester bromination- graphene/ graphite is simulated in this study . Although the mechanical properties of the brominated vinylester are comparably close to vinylester, a great interfacial strength enhancement is shown in the simulated pull-out energy configurations. Potential energy variation plots for a pull-out simulation for (a) graphene-brominated vinylester and (b) graphite-brominated vinylester are shown in figure 3.32. An interfacial strengths summary is shown in table 3.10.

Figure 3.31. Potential Energy Variation for a Pull-out Simulation for Reinforced Vinylester Composite: (a) Graphene, (b) Graphite

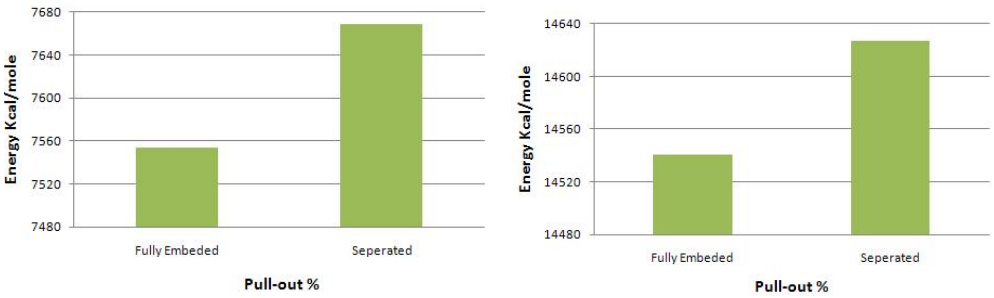

Figure 3.32. Potential Energy Variation for a Pull-out Simulation for Reinforced Brominated Vinylester Composite: (a) Graphene, (b) Graphite

Table 3.10. Interfacial Strength for Graphene-Vinylester Nanocomposites

Composite	Interfacial Strength (MPa)
SWCNT-Polyethylene	133
Graphene -Vinylester	256
Graphite -Vinylester	125
Graphene -Brominated vinylester	534.4
Graphite -Brominated vinylester	368

3.5 Molecular Dynamics Simulations of Nanocomposites

3.5.1 Literature Review

In order to understand nanocomposites, atomic structures, and interfacial interaction between different matrices and nano reinforcements; atomic level interactions should be studied in details. Mechanical properties of nanocomposites could be predicted by realistic computational techniques that vary in time and length scales [85, 86]. MD simulations can provide the structure, and the dynamic intercalated molecules could provide MD used to model nano layered graphite polymeric nanocomposites and their constituents elastic properties. After MD simulation is performed, the resulting deformed molecular structure is analyzed to determine the elastic constants. Following the initial stage, three tensile and three pure shear strains with magnitudes of 0.0005 are applied to the energy minimized system, with the system re-minimized following each deformation [33].

In the work presented in this paper, molecular interactions are described by Condensed-phase Optimized Molecular Potentials for Atomistic Simulation Studies (COMPASS) force-field. COMPASS force field acounts for two function categories, valence terms including the diagonal and off- diagonal cross coupling terms, and nonbond interaction terms. The valence terms represent internal coordinates of bond, angle, torsion angle, and out-of-plane angle. The cross coupling terms include two or three internal coordinates potentials. The

nonbond interaction terms include Van der Waals for the Lennard-Jones function, and a Coulombic function for electrostatic interactions [35]. The MD simulations are performed using commercial software, Material Studio 4.0 [33].

In general, nanoplatelet composites are classified into four types: conventional composite, intercalated composite, long range ordering composite (LRO), and disordered composite figure 3.33. In a conventional composite figure 3.33 (a), clay or graphite exists as a layered material with layers held together by Van der Waals forces without any intercalation or exfoliation. In an intercalated composite figure 3.33 (b), polymer chains are introduced into the graphite galleries, but the graphite still retains its layered structure. The distance between layers is in the range of $(10 \sim 30)$ $\mathring{A}$. The size of the layered graphite extends from several hundred nanometers (nm) to several microns. Exfoliated composites have both exfoliated and dispersed graphite platelets with 1 nm thicknesses and several hundred-nm widths. This type can be divided into two groups: long-range ordered (LRO) figure 3.33 (c) and disordered composites figure 3.33 (d). LRO composites have intercalated separate graphite platelets within $(30 \sim 105)\mathring{A}$ so that the adjacent platelets do not interact with each other. This configuration allows a comparable reinforcing effect for disordered composites. The key reasoning behind making platelet nanocomposites is intercalation of polymers inside the galleries and exfoliation of platelets in the matrix. Exfoliation leads to the improvement of bulk reinforcement by increasing its mechanical properties and aspect ratio.

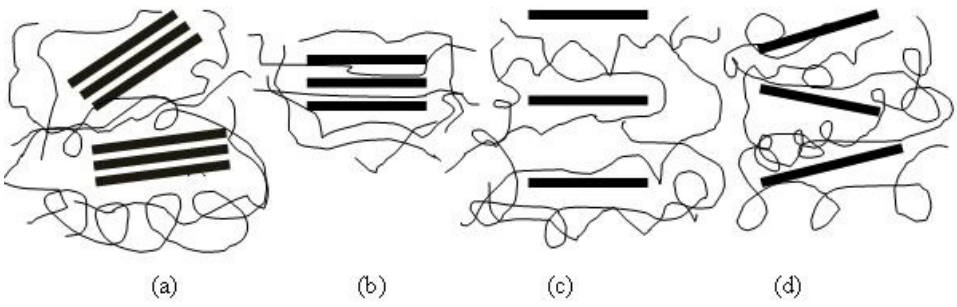

Figure 3.33. Schematic Diagram of Nanocomposites: a) Conventional, b) Intercalated, c) Long Range, and d) Disordered

3.5.2 Molecular Simulation Setup for Nanocomposites

Simulations of MWCNT-Nylon6,6 Composites

MWCNT- Nylon6,6 composites reinforced with different weight fractions (2.5%, 5%, 10%, and 20%) are simulated. Molecular modeling limitations such as the time scale, dynamic time, number of atoms that can be simulated, and periodic unit cell size prevented predicting the effective weight fractions of nylon6,6 reinforced with MWCNT's for small weight fractions.

An infinite crystal of the MWCNT reinforced nylon6,6 containing a given mass/volume fraction of the nanotube reinforcements is constructed using a cubic periodic unit cell of corresponding dimensions (see table 3.11). A three wall CNT with individual setup chirality of 5_5, 10_10, and 15_15 is immersed in 20 monomers nylon6,6 chains of 382 atoms each. Unit cell lattices parameters (a, b and c) are aligned with the three coordinate axes (x, y and z) respectively with the nanotube longitudinal axis aligned with the z-axis (figure 3.34). The atomic configuration of the cell corresponding to the cross-linked molecules of the nylon matrix and the MWCNT are generated using the following procedure:

1. A single molecule of the nylon was first constructed using the Visualizer [33] program from Accelrys, figure 3.5a

2. The molecule generated in (1) was duplicated several times depending on the weight fraction of interest, figure 3.5b

3. The nylon6,6 molecules generated in (2) are used as fragments within the amorphous cell program from Accelrys to generate a cubic computational cell of a given size containing the nylon6,6 polymer chains of a specified density according to equation 3.9

4. The atomic configuration corresponding to the MWCNT is then constructed using the procedure described earlier

5. Segments of the molecules generated in (3) are translated and rotated in order to create an amorphous cell with different configurations to insert the MWCNT at the center of plane xy as shown in figure 3.34

6. The atomic configuration obtained in (5) is subjected to a series of energy minimization and dynamic relaxations under NPT condition, starting with a dynamic time of $20ps$ at a rate of $1fs$ per time step. The temperature is raised from room temperature to $400K$ (beyond the glass transition temperature of nylon6,6) then cooled down to room temperature

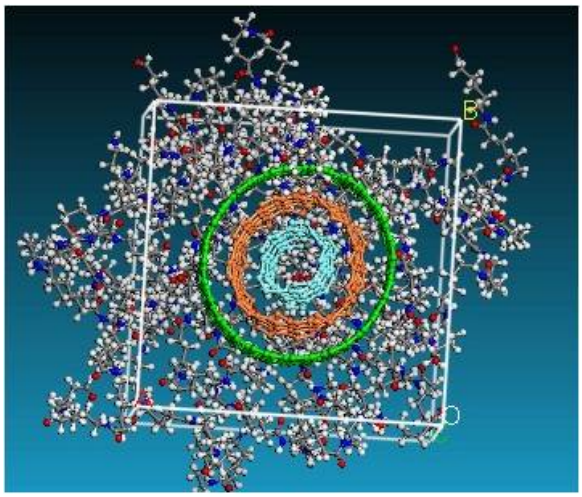

Figure 3.34. MD Simulation of Nylon 6,6 Reinforced with MWCNT

Table 3.11. Composite Simulated Unit Cell Properties

Weight Fractions	Unit Cell Size $\mathring{A}^3$	Number of Nylon6,6 Chains	Number of Nylon6,6 Atoms	Number of Composite Atoms
2.5%	54872	14	5348	5468
5.0%	54872	14	5348	5588
10.0%	37595.4	10	3820	4066
20.0%	32768	8	3056	3536

The unit cell volume was calculated according to the required weight percent of the reinforcement according to the following relations:

$$w\% = \frac{w_r}{w_c} \tag{3.9}$$

$$w_t = w_r + w_m \tag{3.10}$$

$$w_r = \rho_r * \upsilon_r \tag{3.11}$$

$$w_m = \rho_m * \upsilon_m \tag{3.12}$$

where w is the weight, ρ is the density, υ is the volume, r refers to reinforcement, c refers to composite and m refers to matrix.

The plot of nylon6,6 cubic unit cell volume versus number of chains, density 1.0 g/cm^3 figure 3.35

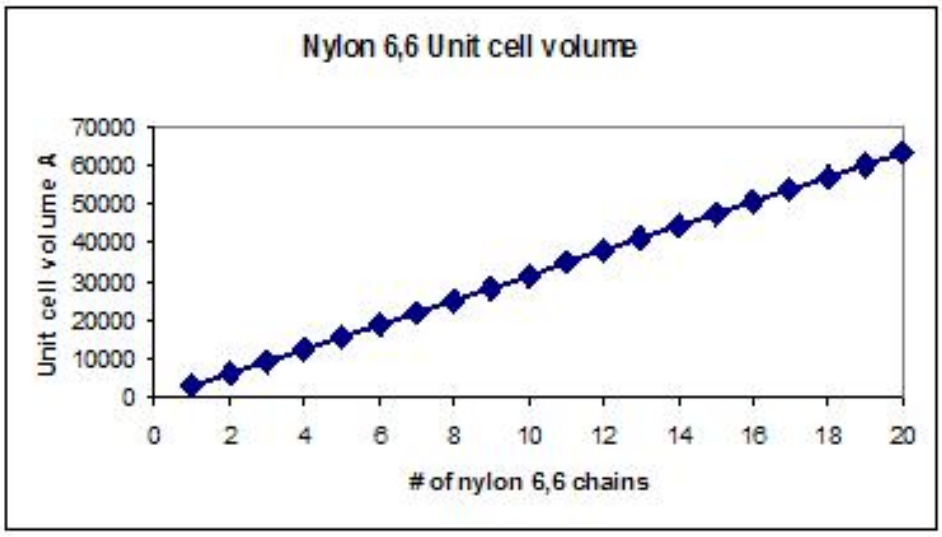

Figure 3.35. Number of Polymer Chains versus Unit Cell Volume in $\mathring{A}^3$

Modeling MWCNT composites is dependent of the local load transfer along the longitudinal direction of the CNT. Since the minimum unit cell size for a three MWCNT of (5_5, 10_10, 15_15) chirality is $20\mathring{A}$ super cells, a large number of chains is required to construct

the periodic composite unit cell. The required unit cells for accurate calculations of elastic constants are summarized in table 3.12

Table 3.12. Recommended for a Periodic Unit Cell Dimensions for MWCNTNylon6,6

Weight Fractions	Unit Cell Size $\mathring{A}^3$	Number of Nylon6,6 Chains	Number of Nylon6,6 Atoms	Number of Composite Atoms
1.25%	1122615	299	114218	114338
2.5%	554203	148	565236	56656
5.0%	269996	72	27504	27624
10.0%	127899	35	13370	13490
20.0%	56842	16	6112	6232

For the twenty percent weight fraction reinforcement, two unit cell sizes were considered for the same thermodynamic and construction conditions. The first was constructed using 1768 atoms and a unit cell size of $(22.24)^3 \mathring{A}^3$ figure 3.36 a. The second one is constructed using 3536 atoms and unit cell dimensions of table 3.11 figure 3.36 b.

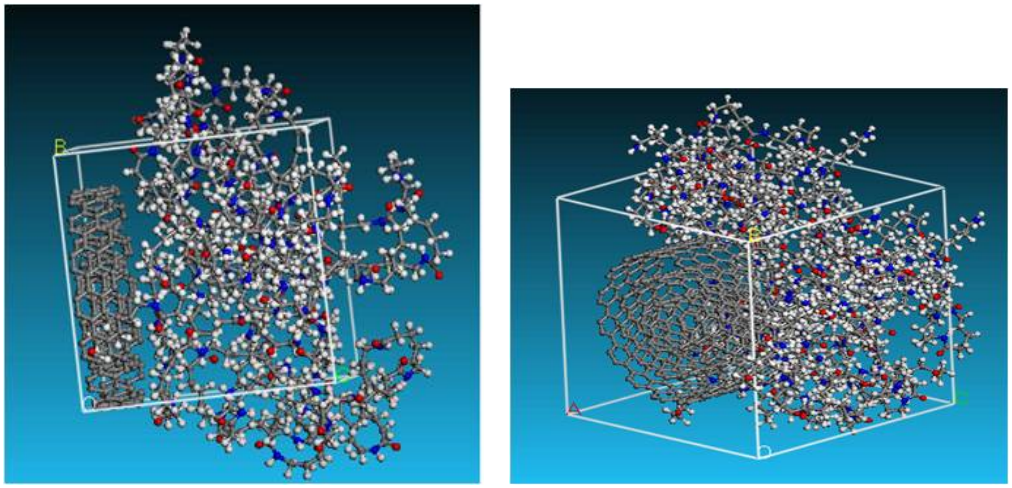

Figure 3.36. Simulated 20% Reinforced Nanocomposite With (a) Two Super Cell Fiber and (b) Four Supercell Fiber

Simulations of Graphene Composites

Simulations are carried out for 10 and 20 percent of graphite-vinylester figure 3.37, and for exfoliated graphene-vinylester composites figure 3.38. The simulation conditions and cell sizes that have been constructed are mentioned later in Table VIII. The NVT and NPT step simulations described earlier in matrix molecular modeling are applied to the composite simulations. Hence, the temperature of the system is maintained at 298K throughout the simulation.

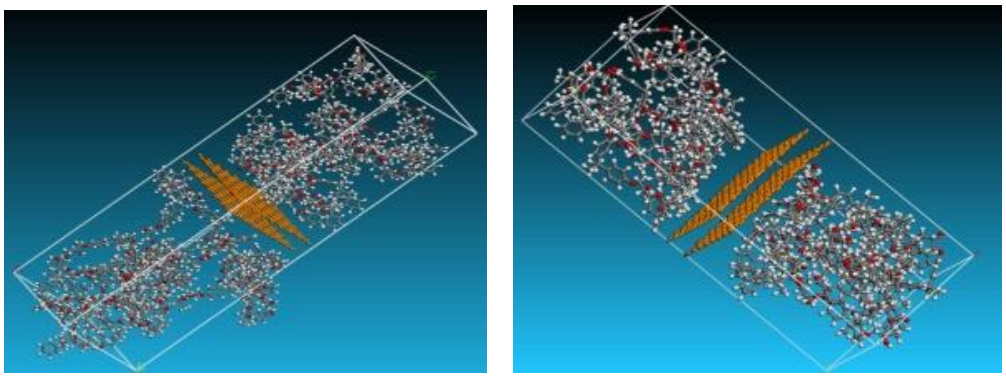

Figure 3.37. (a)10%Graphene-Vinylester Composite, (b) 20%Graphene-Vinylester Composite

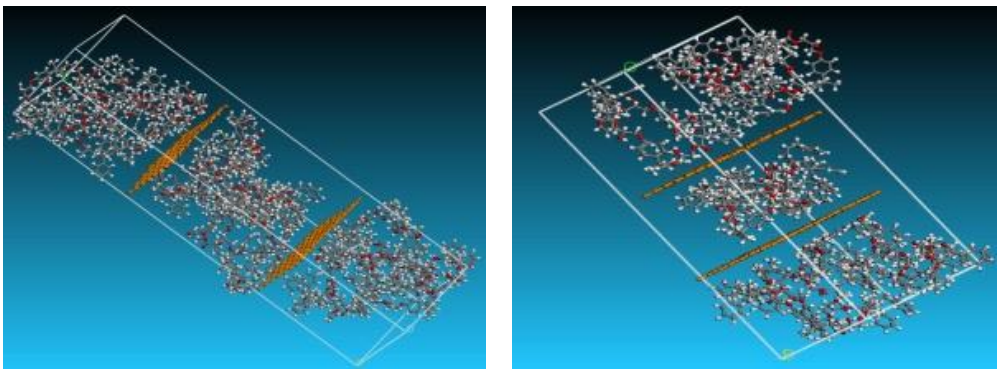

Figure 3.38. (a)10% Exfoliated Graphene-Vinylester Composite, (b)20% Exfoliated Graphene-Vinylester Composite

3.5.3 Mechanical Properties Results

MWCNT-Nylon6,6

The results of simulations for both unit cells are summarized in table 4.15. The large difference in engineering constants is due to the size of the simulated unit cell and the associated potential energy.

Figure 3.39 shows two images for a 20% unit cell with a total number of atoms equal to 3565 after energy minimization. It is obvious that the MWCNT is being deformed, misaligned and pulled under the effect of the Van der Waals forces. Also, the layers of the MWCNT are misaligned. The simulated length is not enough to develop full load transfer between the CNT and its surrounding polymer chains.

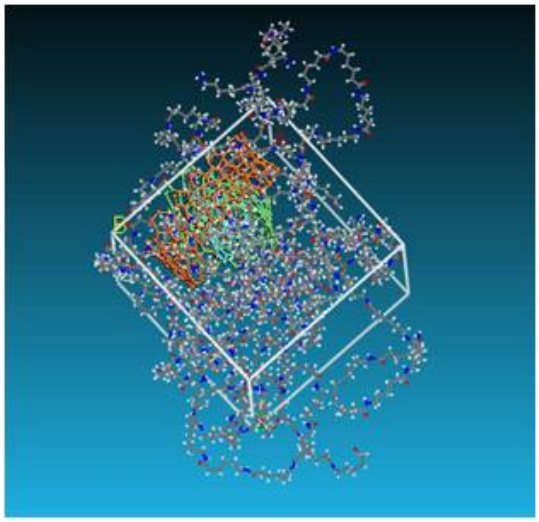

Figure 3.39. Unit Cell of Nylon6,6 Reinforced with 20% Weight Fraction MWCNT After Energy Minimization

Table 3.14 summarized the results obtained for engineering constants of nylon6,6- MWCNT composites with different weight fractions using MD simulations.

Table 3.13. Effect of Unit Cell Size on Engineering Constants of Nylon6,6 Reinforced with 20% Weight Fraction of MWCNT

Composite Engineering Constants	20% 1768 atoms/cell	20% 3536 atoms/cell
$E_1$1(GPa)	71.06	42.72
υ_{12}	0.58	0.15
K(GPa)	139.5	20.22
G(GPa)	22.42	18.6
Lame Constant λ (GPa)	154.5	47.81
Lame Constant μ (GPa)	22.42	18.6

Table 3.14. Nylon6,6 MWCNT Composite Engineering Constants

Composite Engineering Constants	2.5%	5%	10%	20%
E_{11}(GPa)	1.7	5.5	13.6	73.5
E_{22}(GPa)	0.9	5.0	9.6	40.6
υ_{12}	0.6	0.32	.31	0.5
G(GPa)	1.4	5.3	10.5	18
K(GPa)	0.33	1.8	6.3	8.6

For the case of 2.5% weight fraction, the obtained results are surprisingly smaller than those of un-reinforced nylon6,6. However, by examining figure 3.40, which shows total deformation of the MWCNT through the unit cell for the case of nylon6,6 reinforced with 2.5% weight fraction of MWCNT, one observes excessive deformation of the CNT. The large deformation is due to the Van der Waals forces between the carbon atoms in the MWCNT and the carbon atoms in the polymer itself. Table 3.15 which shows the maximum Van der Waals radius for carbon atoms to be 1.55$\mathring{A}$. Since the length of the MWCNT simulated is less than the Van der Waals radius for carbon atoms, the obtained results in MD simulations are smaller than experimental ones.

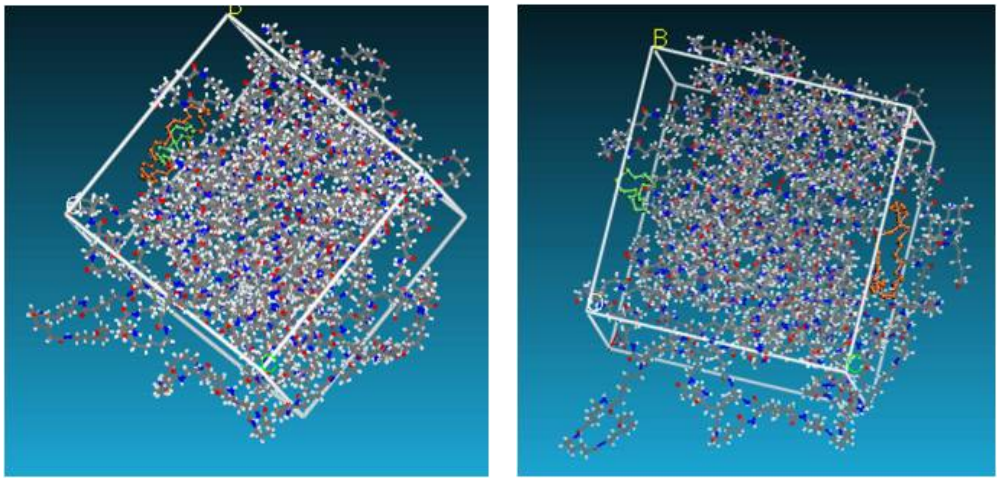

Figure 3.40. 2.5% MWCNT-Nylon6,6 Composite a) Before minimization. b) After minimization

Table 3.15. Van der Waals Radius

Atom	Van der Waals Radius ($\mathring{A}$)
H	1.1
C	1.55
N	1.4
O	1.35

Graphene Nano Platelets-Vinylester

Stiffness matrices for 10 and 20 weight percentage reinforcements are shown in table 3.16, and 3.17. Results demonstrate that the mechanical properties of the vinylester-graphene nanocomposites are higher for the 20% compared to 10% of graphene reinforcements.

Table 3.16. Stiffness Matrices of Graphene-Vinylester Nanocomposite10%

Graphene-Vinylester Composite Stiffness Matrix: 10%
Unit Cell size: (19.76x19.76x58.6) Å Triclinic cell:(α=β=90°, γ=120°) Thermodynamic: NVT Number of Atoms: (2232) Temperature: $400K$ Elastic Properties: at $298K$

$$C_{ij} = \begin{bmatrix} 5.9 & 1.0 & 1.8 & 0 & 1.9 & 0 \\ 3.3 & 147 & 34.2 & 0 & 0 & 88.7 \\ 3.9 & 35.7 & 142.5 & 0 & 0 & 88.3 \\ 0 & 0 & 0 & 15.2 & 13.9 & 0 \\ 0 & 0 & 0 & 13.3 & 15.1 & 0 \\ 0 & 87.7 & 89 & 0 & 0 & 94.5 \end{bmatrix} GPa$$

Table 3.17. Stiffness Matrices of Graphene-Vinylester Nanocomposite20%

Graphene-Vinylester Composite Stiffness Matrix:20%
Unit Cell size: (19.76x19.76x91.54) Å Triclinic cell: (α=β=90°, γ=120°) Thermodynamic: NVT Number of Atoms: (3246) Elastic Properties: at 298K

$$C_{ij} = \begin{bmatrix} 3.2 & 1.5 & 2.5 & 0 & 0 & 0 \\ 1.8 & 228 & 56.8 & 0 & 0 & 137 \\ 1.3 & 57.6 & 229.5 & 0 & 0 & 139 \\ 0 & 0 & 0 & 20.6 & 20.8 & 0 \\ 0 & 0 & 0 & 20.3 & 20.9 & 0 \\ 0 & 139 & 139.9 & 0 & 0 & 143.2 \end{bmatrix} GPa$$

Exfoliated Graphene Nano Platelets-Vinylester

Stiffness matrices for 10 and 20 weight percentage reinforcements are shown in table 3.18, 3.19. Results shown demonstrate that exfoliated graphene platelets nanocomposites have a slight increament in the elastic properties in comparison to the graphite nanocomposites. However, it is expected to have a higher improvement in the mechanical properties than what is shown in the simulated results, to the fact that the speration distance between the graphene platelets is still considered in the low range non-bond interactions.

$$C_{ij} = \begin{bmatrix} 18.4 & 9.3 & 7.2 & 0 & 0 & 0 \\ 6.7 & 135.9 & 52.4 & 0 & 0 & 0 \\ 8.1 & 63.7 & 129.2 & 0 & 0 & 0 \\ 0 & 0 & 0 & 11.7 & 0 & 0 \\ 0 & 0 & 0 & 0 & 7.9 & 0 \\ 0 & 0 & 0 & 0 & 0 & 37.7 \end{bmatrix} GPa$$

Table 3.18. Stiffness Matrices of Exfoliated Graphene-Vinylester Nanocomposite10%

Exfoliated Graphene-Vinylester Composite Stiffness Matrix: 10%
Unit Cell size: (19.76x19.76x58.6) Å Triclinic cell: (α=β=90°, γ=120°) Thermodynamic:NVT Number of Atoms: (2232) Temperature: $400K$ Elastic Properties: at $298K$

Table 3.19. Stiffness Matrices of Exfoliated Graphene-Vinylester Nanocomposite 20%

Exfoliated Graphene -Vinylester Composite Stiffness Matrix: 20%
Unit Cell size: (19.76x19.76x91.54) Å Triclinic cell: (α=β=90°, γ=120°) Thermodynamic: NVT Number of Atoms: (3246) Elastic Properties: at 298K

$$C_{ij} = \begin{bmatrix} 4 & 1.4 & 3.2 & 0 & 0 & 0 \\ 2.1 & 230 & 57.7 & 0 & 0 & 140.6 \\ 1.6 & 59.7 & 230.3 & 0 & 0 & 140 \\ 0 & 0 & 0 & 20.6 & 22.02 & 0 \\ 0 & 0 & 0 & 20.7 & 22.0 & 0 \\ 0 & 138 & 140 & 0 & 0 & 142.5 \end{bmatrix} GPa$$

4. CEMENTITIOUS NANOCOMPOSITES SIMULATIONS AND EXPERIMENTAL EVALUATION

4.1 Introduction

In general, the word cement can be translated into a binder. A substance, which can set and harden independently, and it can bind other materials together. Cement used for construction can be categorized as hydraulic or non-hydraulic. The hydraulic cement hardens through a hydration process where chemical reactions in the presence of water take place continuously. When the anhydrous cement powder is mixed with water, it produces hydrates that are insoluble in water. Meanwhile, to maintain the strength of the non-hydraulic cement, they must be kept dry [87].

Modern cement is produced by annealing limestone (calcium carbonate) with small quantities of other materials to 1450 C° in a kiln. This process is known as calcination, in which a molecule of carbon dioxide liberated from the calcium carbonate to form calcium oxide (quicklime). However, the calcium oxide is blended with other materials, which are included in the mix. The result is a hard substance called "clinker". The clinker is then crushed with a small amount of gypsum into a powder of (5-45) μm range of particles size. The cement produced in the introduced process, is often referred to as "Ordinary Portland Cement" [88]. Portland cement can vary in the mixture and additives percentages, which is control

the desired properties. The most common components of Portland cement are di-calcium silicates $2CaO.SiO_2$ and tri-calcium silicates $3CaO.SiO_2$. Usually in literature di-calcium silicate is referred to (C_2S), and tri-calcium silicate is referred to (C_3S)

Portland cement is the main ingredient of concrete. Concrete in general, is a composite material which consists of aggregates, cement and water. It is very important to balance between the economical cost and the properties desired for a particular concrete mix. For the current study type I/II Portland cements is selected. Type I/II Portland cement, which is the most popular cements used by concrete producers, and can provide acceptable levels of strength and durability.

4.1.1 Hydration of Cement

All compounds present in portland cement clinker are anhydrous , but when brought with water, they are all attacked or decomposed forming hydrated compounds. When tri- or di -calcium silicates react with water a calcium silicate hydrate gel is formed. The Basic chemical reactions that take place during hydration process are the following:

- Tri-Calcium Silicate

  $2(3CaO.SiO_2) + 6H_2O \rightarrow 3CaO.2SiO_2.3H_2O + 3Ca(OH)_2$

  C_3S produces C-S-H and $Ca(OH)_2$ at early stages of hydration.

- Di-Calcium Silicate

  $2(2CaO.SiO_2) + 4H_2O \rightarrow 3CaO.2SiO_2.3H_2O + Ca(OH)_2$

  C_2S produces C-S-H and $Ca(OH)_2$ at later stages of hydration.

- Tri-Calcium Aluminate

  $3CaO.Al_2O_3 + 6H_2O \rightarrow 3CaO.Al_2O_3.6H_2O$

  Aluminates hydrate faster therefore stiffening and setting of cement pastes is generally attributed to aluminate minerals

- Tetracalcium Aluminoferrite

  $4CaO.Al_2O_3.Fe_2O_3 + 2Ca(OH)_2 + 10H_2O \rightarrow 3CaO.Al_2O_6.6H_2O + 3CaO.Fe_2O_3.6H_2O$

  Hydration of C_3A and C_4AF results are Ettringite (AFt), and Monosulfate(AFm)

Hardening of cement paste is mainly attributed to the silicate minerals. Two classes of pores usually are present in hydrated cement. First class are gel pores, which are conceived to be part of the C-S-H gel with characteristic diameters $<10nm$. Second class are large capillary pores, which are on the order of 10nm to 10 micrometer. Water that is not consumed in the hydration process remains in the microstructure capillary pores. These pores make the concrete weaker due to the lack of strength forming C-S-H bonds. In additional, there might be some air voids and larger empty spaces where the pastes has not been properly consolidated. Total pore volume depends on the water/cement ratio, degree of hydration, curing condition. For (w/c=.5) % volume of C-S-H is 50%, CH 12%, AFm(Monosulfate) & Aft(Ettringate) 13%, unreacted cement 5%, and capillary pores 20% [87].

4.2 Cementitious Nanocomposites Sample Preparation

Two types of cements are used in this study. The first type is synthesized nano tri-calcium silicate. The second type is the Type I/II Portland cement. In the case of the Portland cement, nano-additives are introduced, which include nano_diamond, graphene nano platelets (pristine, functionalized) and two types of Polyhedral oligomeric silsesquioxanes (POSS).

4.2.1 Nano C_3S Synthesis

The sol-gel process is utilized to synthesize some of cement components. The sol-gel method relies on colloid chemistry, where the solid raw materials are dissolved in predetermined solvents. For the sol-gel method, the reaction occurs under a predefined temperature, and pressure, and a hydration process assembles a homogenous solution [89].

In this study, the following properties will be evaluated, structure morphology, hydration rate, mechanical and physical properties and compressive strength, of either the synthesized nano cement or the ordinary Portland cement mixed with selected nano-additives.

Procedure of the Sol-gel method adopted:

1. Each component is synthesized by dissolving the solid particles in water to form a homogenous solution 4.1.

2. The solution is heated to 100C° until a paste is formed, figure 4.2.

3. Samples are placed in tubes and annealed at 1000C° enabling the particles to crystallize, figure 4.2.

4. Samples are grounded to a submicro powder, then placed in glass tubes and sealed with para film for protection from moisture, figure 4.3, using vertical ball milling process

Table 4.1. Nano C_3S Pure Components Composition

Material	Properties	C_3S
PEG	MW 3400 g/mol	4g
$Ca(C_2H_3O_2)2$	MW 18 g/mol	4.74g
SiO_2	ZL(40-41)%	0.01mol
Water	De-ionized	15g

Figure 4.1. C_3S Paste Formed After Heating Solution to 100C°

Figure 4.2. C_3S Crystals After Annealing at 1000C°

Figure 4.3. C_3S Samples are being Packaged for Milling

4.2.2 Cement Samples Mixed with Nano Additives

Five types of nonomaterials are mixed with cement, to evaluate the effect of nano-additives on mechanical and electrical properties of reinforced cementitious nanocomposites and to correlate performance to morphology.

Nano Diamonds

Nano diamonds, particles of diamond dust measured in nanometers, have been found in meteorites, protoplanetary nebulae, and interplanetary dust. In 1963 a group of Soviet scientists discovered single crystals of cubic diamond particles in soot produced by detonating an oxygen-deficient TNT/hexagon composition in inert media without using any extra carbon source [90]. Nowadays, detonation nano diamonds are produced in huge quantity by industries in Russia and China. These nano diamonds, however, are in an "agglutinated" form, that is, they are embedded in soot (amorphous carbon) to form particle of sizes 100-200 nm. Small quantities of agglutinated nano diamonds have been added to cement [91], and found to somewhat increase cement's strength, and greatly enhancing its bio-protection.

Prof. Eiji Osawa of NanoCarbon Research Institute, has grinded the agglutinated nano diamonds into 4-6nm, single crystal nano diamonds [92], in which is used in this study.

Nano Graphene Platelets Dispersion

The nanoscience of carbon materials has been immensely investigated in the last 2-3 decades. More recently, a renewed interest in graphene has emerged. Nobel Prize in physics for 2010 went to Andre Geim, and Konstantin Novlesov, University of Manchester, UK, for groundbreaking experiments regarding the two-dimensional material graphene. Understanding the properties of exfoliated graphene platelets mixed with cement, has not been under focus. In the work presented in this dissertation, and as a part of interest in nanoscience, nanotechnology and their applications in civil engineering, a detailed experimental and numerical evaluation for cementitious graphene-nanocomposites is examined.

Fifty μm exfoliated pristine graphene platelets are being mixed with cement mortar by a 0.5% weight. Graphene platelets are suspended in water by sonicating the solution of, $0.162g$ exfoliated graphene platelets and $8.955g$ of water for 3 minutes to confirm a homogenous distribution of the nanoparticles. Figure 4.4 Thermal Gravimetric Analysis (TGA) shows a noticeable instability for the different sizes of exfoliated graphene platelets weight losses, which could be due the existence of organic/inorganic impurities in analyzed graphene samples.

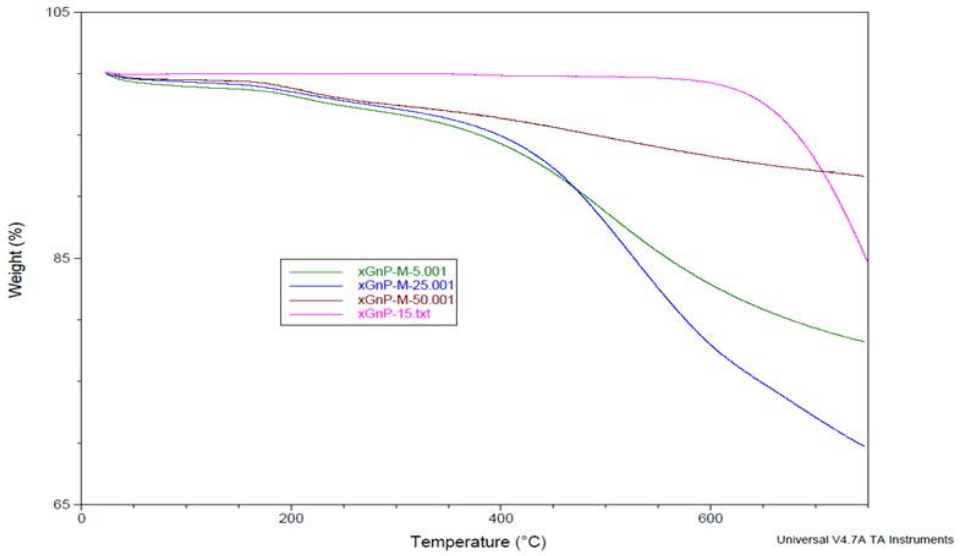

Figure 4.4. TGA result for exfoliated graphene nano platelets

Nano Graphene Platelets Functionalization

By operating 3 minutes sonication for a 1:55.27 (graphene:water) solution, functionalized graphene can be dispersed in water.

The functionalization of pristine graphene is referred to the work of [93]. One example is as:

1. Three grams of pristine graphene and 300 ml 60 wt% nitric acid in a 500 ml one glass flask are sonicated for 15 minutes.

2. The mixture is stirred and refluxed for 24 hours. A condenser is connected on top of the flask.

3. After cooling, the mixture is purified by filtration using distilled water. Before each filtration, graphenes/distilled water is sonicated for 5 minutes.

4. Procedure in step (3) is repeated 6 times.

Thermal Gravimetric Analysis (TGA) results are shown in figure 4.5, test conditions in nitrogen, with a 10 C°/min rate. The results show that functionalized graphene has less weight loss than that of the pristine because HNO_3 may remove the impurities while oxidizing graphene.

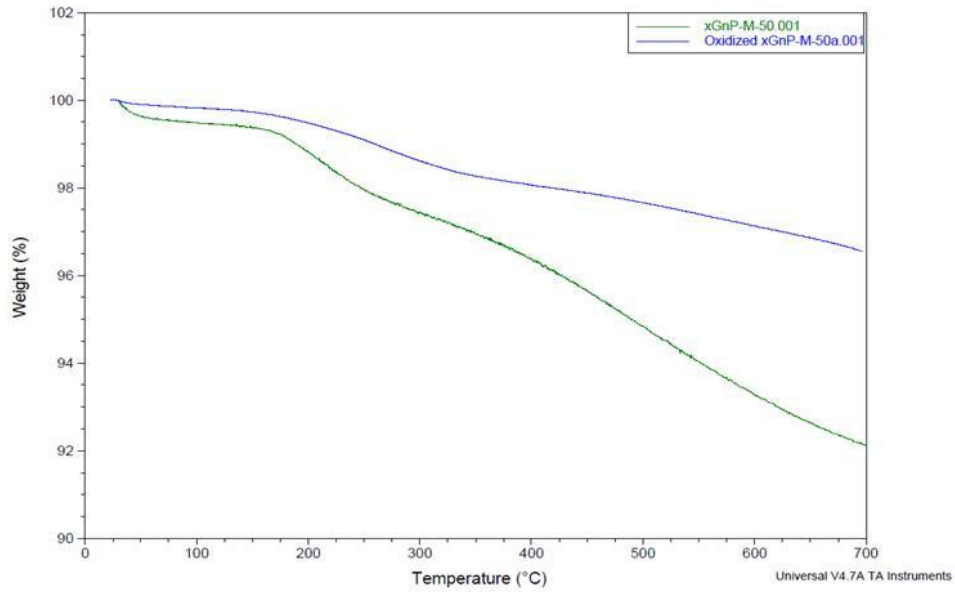

Figure 4.5. TGA result for exfoliated graphene nano platelets

POSS

Polyhedral oligomeric silsesquioxanes (POSS) been a revival of many global interest since 1990. The cage-like shape of the molecule has attracted a lot of the researchers, for its

unique molecule properties and branching possibilities. The cage of silica, POSS, has a high elastic modulus compared to the conventional polymers. When POSS is mixed with polymers, the elastic modulus of the polymer is not reduced. Although, adding low molecular weight organic molecules such as POSS usually results in a lower elastic modulus, POSS has little to no effect on the modulus of polymers, unlike fillers, it is not added to improve modulus. The addition of POSS to polymers acts similar to plasticizers. However, in this case, the large-flexible organic groups dominate the POSS modulus. Enhancements in the physical properties of polymers incorporating POSS segments result from POSS's ability to control the motions of the chains while still maintaining the processability and mechanical properties of the base resin. In the work presented in this dissertation, two types of POSS has been studied, PEG POSS, and OctaTMA POSS, provided by Hybrid Plastics®. a brief description is incorporated:

Polyethylene Glycol POSS (PEG POSS), is liquid at room temperature, very soluble and non reactive in water. The molecular chain formula for the PEG POSS is $[C_{2m+3}H_{4M+7}O_{m+1}]_n(SiO_{1.5})_n$.

Octa(tetramethylammonium) polyhedral oligomeric silsesquioxanes (OctaTMA POSS), is powder at room temperature, soluble and non reactive in water. The molecular chain formula for the OctaTMA POSS is $C_{32}H_{96}N_8O_{20}Si_8 \sim 60H_2O$.

Nevertheless, mixing POSS with cement has not been investigated yet. The chemical diversity of the POSS molecules, is interesting and worthy a detailed investigation. The direct result of POSSs nanoscopic size and its relationship to cement dimensions, might lead to a high impact on the cement industry.

Sample Preparation of Portland Cement Type I/II Enhanced with Nano-additives

Portland cement type I/II that complies with ASTM C-150 standards is utilized in sample preparation. The samples are constructed using a water/cement ratio (0.45). A collection

of different nano-additives such as nano diamonds, exfoliated graphene nano platelets, functionalized graphene nano-platelets, PEG POSS, and OctaTMA POSS, of a 0.5% by weight are added to cement paste mixture see figure 4.6. The mixture is casted in ice-cube molds figure 4.7, and cured at 100% RH for 7 days. After the initial curing process, cubes are cut in the range of (1cm*1cm*1.5cm) using a diamond saw , polished for RUS, EIS, and compressive strength testing figure 4.8. Slices of (1cm*0.5cm*0.10cm), for SEM and AFM imaging, are cut from original cement ice-cubes. Prepared samples are immersed in the water again for another 5 days. However, for RUS testing, samples are entered in the drying oven at 60 C° for 7 hours then temperature is raised to 75 C° over night. The temperature control is followed by a vacuum control for one hour; to get rid of any excessive humidity in cement samples. Mass and density measurements are taken prior to and after the drying process figure 4.9.

Figure 4.6. Preparing Cementitious Nanocomposite Paste (a)Portland Cement Type I/II Powder, (b) (0.50% Nano Additive Dispersed in Water, (c) Cementitious Nanocomposite Paste (w/c=0.45))

Figure 4.7. Cement Paste Casted in Cubical Molds (1.5"*1.5*1.5)

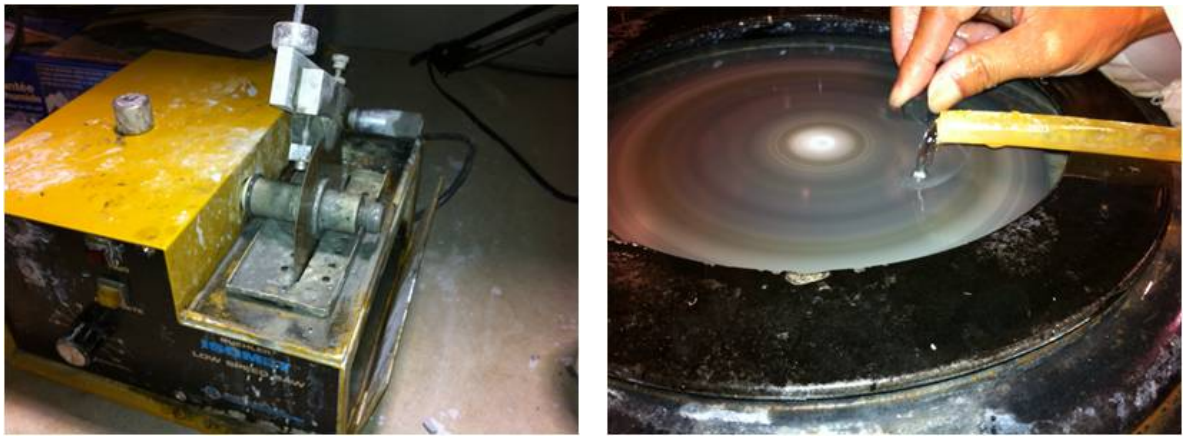

Figure 4.8. Cubes Are Cut in The Range of (1cm*1cm*1.5cm) Using a Diamond Saw , Polished for RUS, EIS, and Compressive StrengthTesting

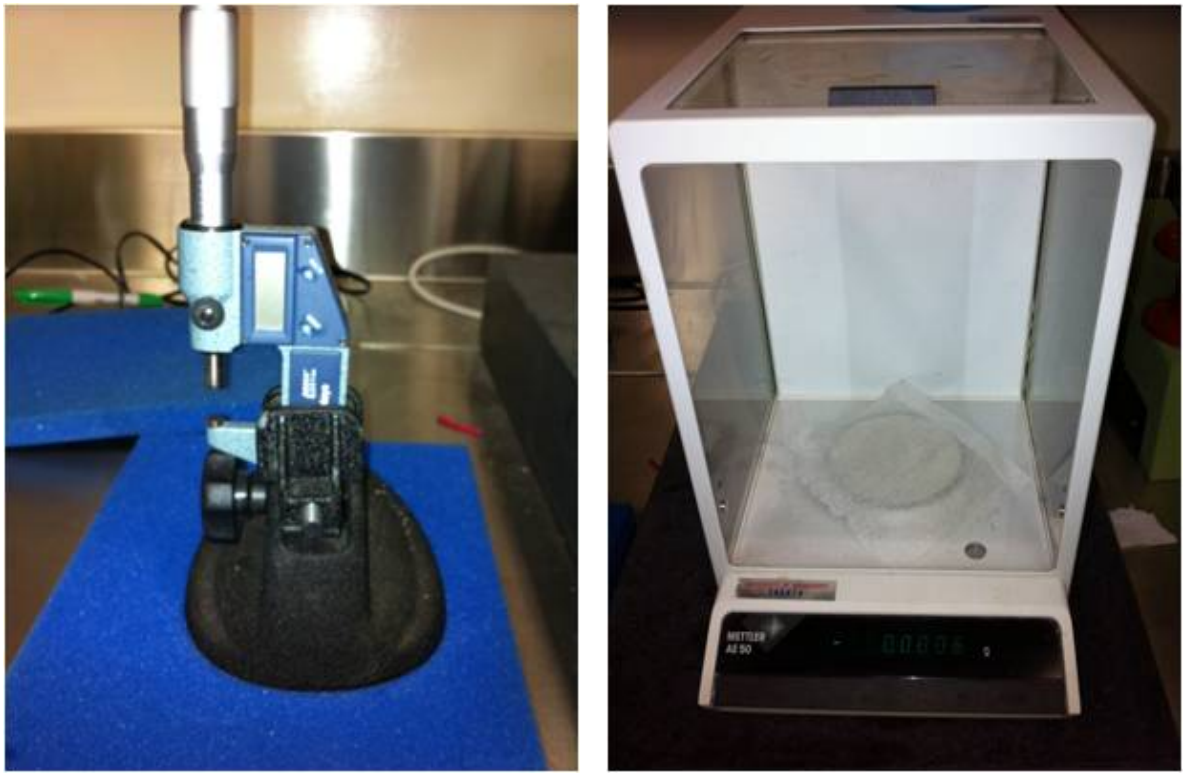

Figure 4.9. Cement Samples are Being Weighed and Dimensions are Measured For EIS, RUS, MTS Testing

4.3 Numerical Simulation

The addition of small amounts of nano additives to cement causes a great increase in the composite material toughness and tensile, flexural, and impact strength. In order to understand how cement properties are improved by nano additives and to understand the level of adhesion and interfacial failure mode which are necessary to obtain optimum nano reinforced cement properties, various functionalized graphitic platelets are embedded in C-S-H. Their effects on the graphene-cement adhesion and the composite material properties are determined using fiber pull-out molecular dynamics simulations.

4.3.1 Calcuim Silicate Hydrates Molecular Structure

Strength of the concrete is originated from hydration products. The major portion of the hydration products is in the form of a rigid gel called C-S-H. C-S-H gel is believed to be responsible for strength and cohesion of concrete structures. Pallenq [94] provided limited insight about the factors that affect setting and hardening of cement paste. However, it is suggested that the short and medium range attractive electrostatic forces are the prime components of the cohesion of C-S-H gel. Other evidences indicate that the surface force between C-S-H nano particles is solely responsible for the cohesion. More functional C-S-H requires reliable information about the structure and properties of C-S-H gel [94].

C-S-H gel is a complex structure comprising of elements and pores. Some researchers have suggested an amorphous structure, others suggested a crystalline nature. The amorphous structure, is hard to model for the bond and non-bond water interaction calculations, and quantitative measurements such as surface area extremely challenging. Stoichiometry for C-S-H is not fixed, the chemical composition changes from point to point within the cement paste. Nevertheless, C-S-H is defined by the Ca/Si ratio gel range (0.6-2.3)[95].

The essential role in the C-S-H molecular models is the C/S ratio. Grove[96], used dispersive X-ray analysis of C-S-H in hardened Portland cement pastes aged 1 day to 3.5 years, to

reveal a composition variation in C/S ration from 1.2-2.3 with a mean value of 1.7, this variation also depends on the W/C ratio. Richardson [97] suggested a two-fold classification to clarify the C-S-H chemistry. This classification is referenced as: Tobermorite/Jennite (T/J) models, and Tobermorite/Calcium hydroxyl (T/CH)models. The latter model consists of solid Tobermorite layers sandwiched with calcium hydroxyl, which allows achieving a higher C/S ratio than in Tobermorite alone. The T/J model is assembled of tobermorite regions followed by jennite domains. This will suggest that the C-S-H gel structure contains both glass-likes short range order and crystalline properties of the mineral Tobermorite. Atomic structures are based on the HFW Taylors [98] model for the essential two C-S-H minerals: Tobermorite 14$\mathring{A}$ [$Ca_5Si_6O_{16}(OH)_{2.7}H2O$], and Jennite [$Ca_9(Si_6O_{18})(OH)_{6.8}H_2O$]. Tobermorite has a molecular structure characterized by C/S ratio =.83 and density of 2.18gm/cm^3, meanwhile; Jennite has a C/S ratio =1.5 and a density of 2.27gm/cm^3. Small angle neutron scattering measurements have established the C/S ratio at 1.7 and a density of 2.6gm/cm^3.

C-S-H structure that has been revealed has a layered structure at short length scales (1-5)nm, the layers stack to form compact domain in the order of a few nm (the same order of interlayer distance of Tobermorite or Jennite crystals). At larger length scales (5-100)nm these ordered stacks form three-dimensional structures called C-S-H particles. C-S-H (TEM) revealed the shape of C-S-H as disks of a thickness 5 nm, during hydration these C-S-H particles multiply and aggregate to form low-density and high density C-S-H gel. Low and high density C-S-H have different mechanical properties. The proportion of the high and low density C-S-H depends on the mix design of cement paste. Jennings [99] proposed colloidal structure for C-S-H, a fundamental aspect in the proposed model is the presence of different packing densities issue. As the packing density increases, the number of contacts between the particles increases. Therefore, the HD C-S-H will have a higher stiffness and hardness compared to LD C-S-H, due the existence of higher contact number of points. However, the model doesn't quantify the bond between the C-S-H particles.

The molecular model (figure 4.10) that has been chosen for this work is the C-S-H suggested by [100]. Short silica monomers, dimers, and pantamers are allowed and distributed for CaO, SiO_2, and H_2O to interact, and provide realistic values of C/S ratios and densities. The proposed chemical C-S-H atomic model predicts other elementary structural characteristics and fundamental physical properties. Pellenq at el.[94] showed that once C/S is constituted correctly, a number of distinctive structural features and physical properties follow naturally in atomistic simulations. A prospective chemical composition for C-S-H is adopted to describe the properties obtained from the small-angle neutron scattering measurements [100].

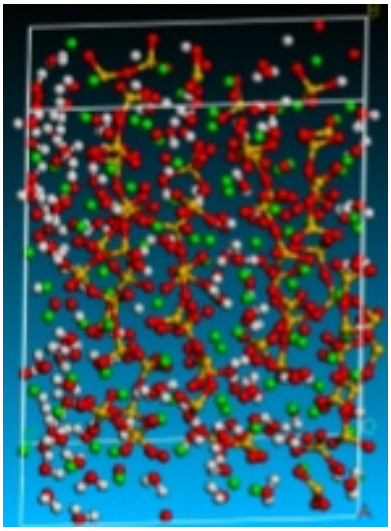

Figure 4.10. Atomic Model for MIT C-S-H

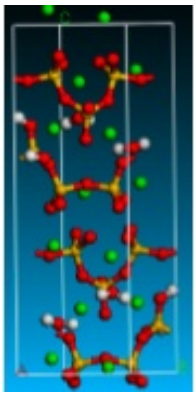

Figure 4.11. Atomic Model for Tobermorite (11Å)University of Arkansas

Table 4.2. Mechanical Properties of Different Proposed Structures for C-S-H

Engineering Constants	MIT C-S-H	AU (Tobermorite 11Å)
E_{11}(GPa)	46.70	89.14
υ_{12}	0.38	0.29

4.3.2 Functionalized Graphene Atomic Structure

A Periodic unit cell graphene platelet is constructed with lattice parameters of $a = b = 2.46\mathring{A}, c = 3.4\mathring{A}$, α=β=90°, and γ=120°. The unit cell is then replicated in 5 times along the $a-axis$, and 11 times along the $b-axis$, lattice angles α=92.65°, β=80.01°, and γ=121.68° are adjusted accordingly to match the C-S-H atomic structure. The pristine graphene structure is made of 110 atoms, and is utilized to construct the functionalized graphene platelets. Figures 4.12-4.16 display the atomic structures for the simulated graphene platelets. The functional groups considered for this study are: $PristineGraphene$, $= O$, $-OH$, $-NH_2$, and -$COOH$. Each of the functionalized graphene platelets has 10 functional groups along the $b-axis$, and is capped with hydrogen bonds along the $a-axis$. However, this functionalization will lead to a 18.18% coverage of the total area of the graphene sheet.

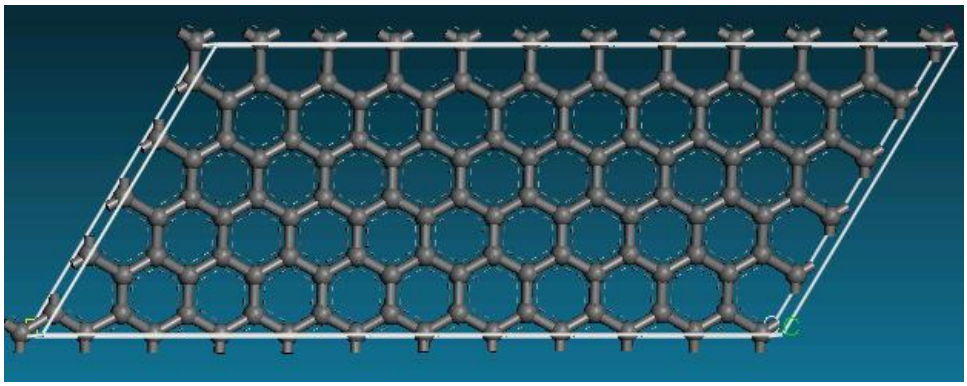

Figure 4.12. Atomic Model for Pristine Graphene G

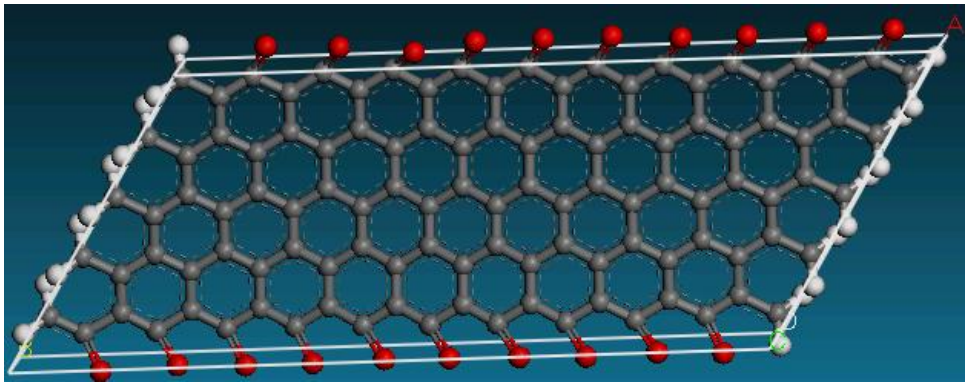

Figure 4.13. Atomic Model for Functionalized Graphene G(O)

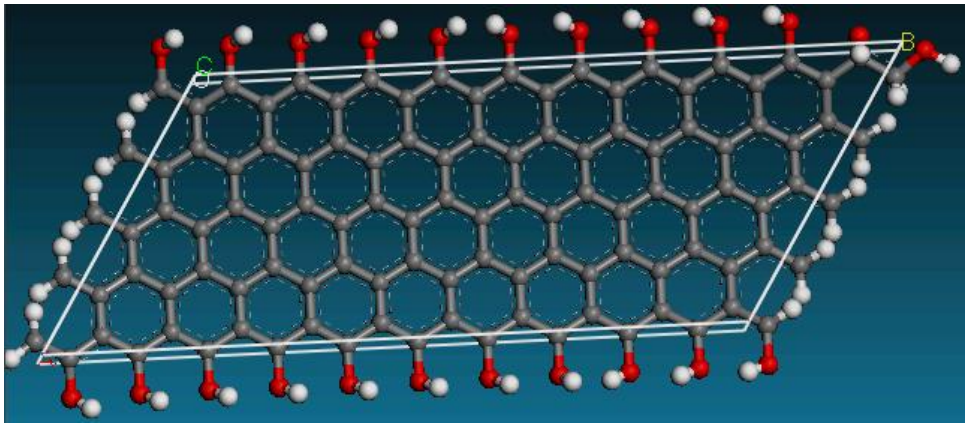

Figure 4.14. Atomic Model for Functionalized Graphene G(OH)

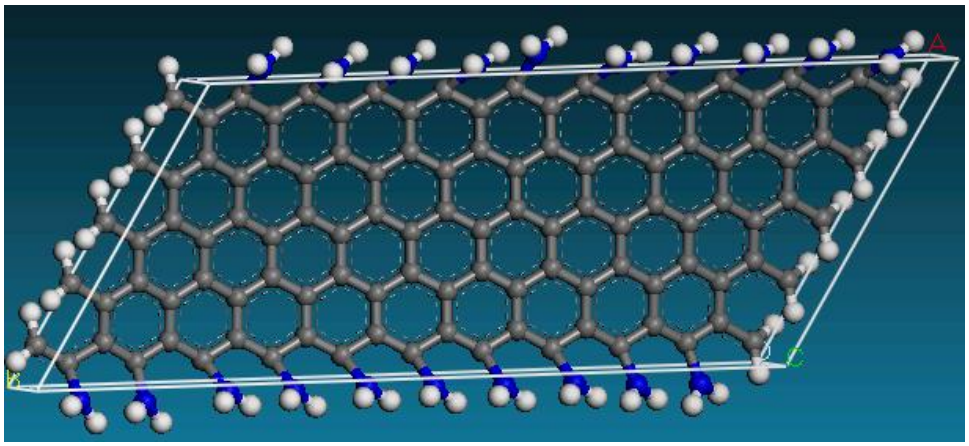

Figure 4.15. Atomic Model for Functionalized Graphene G(NH2)

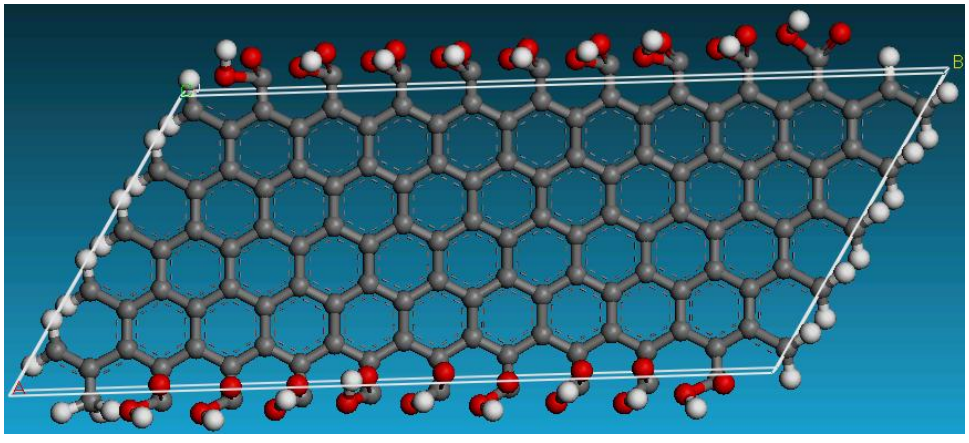

Figure 4.16. Atomic Model for Functionalized Graphene G(COOH)

MD simulations performed by allowing the constructed computational cells to evolve according to Newtons law motion and the predefined forcefield COMPASS. The procedure followed in this study is developed by Sanchez at. el [101].

4.3.3 Interfacial Strength

Molecular dynamics simulations are performed to study the atomic interfacial strength between C-S-H and functionalized graphitic structures. The MIT C-S-H [100] structure is used as a C-S-H model. Four functionalized graphitic structures are simulated; carbonyl $(=O)$, hydroxyl $(-OH)$, amine $(-NH_2)$, and carboxyl $(-COOH)$. Additionally, interfacial strength of C-S-H- pristine graphene is simulated.

The computational cell of the G()-C-S-H composite is constructed using Materials Studio version5.5. Figures 4.17-4.21, display molecular snapshots for the simulated structures. The three layered sandwich layout of C-S-H$-G()-$C-S-H is assembled, and a vacuum of $30\mathring{A}$ is introduced to simulate the graphene pull-out energy, molecular structure properties are shown in table 4.3.

Table 4.3. Molecular Computational Cell Properties for C-S-H-Graphene Composites

Composite	Number of Atoms	ρ (gm/cm^3)	Volume $(\mathring{A}^3)$
C-S-H-G()	1490	1.56	24807.2
C-S-H-G$(=O)$	1530	1.58	24968.2
C-S-H-G$(-OH)$	1550	1.58	24893.4
C-S-H-G$(-NH_2)$	1570	1.56	252173
C-S-H-G$(COOH)$	1584	1.59	25252.4

The total number of geometry optimization steps for the simulated computational cells are in the range of 3000 steps for each individual hybrid structure. As for the start, the molecular structures are subjected to an NVT-ensemble of $200ps$ at $300K$, to drive the system into a thermodynamic equilibration. The Hoover thermostat, is used to control the

temperature with a time step $0.1ps$ for all NVT MD simulations. This is followed by $400ps$ NVT with $1ps$ time step for subsequent statistical analysis. The atom- based summation method with a cut-off point $8.5\mathring{A}$ is adopted for the Van der Waals interactions, and the Ewald summation method is implied to evaluate the long range Coulumbic interactions.

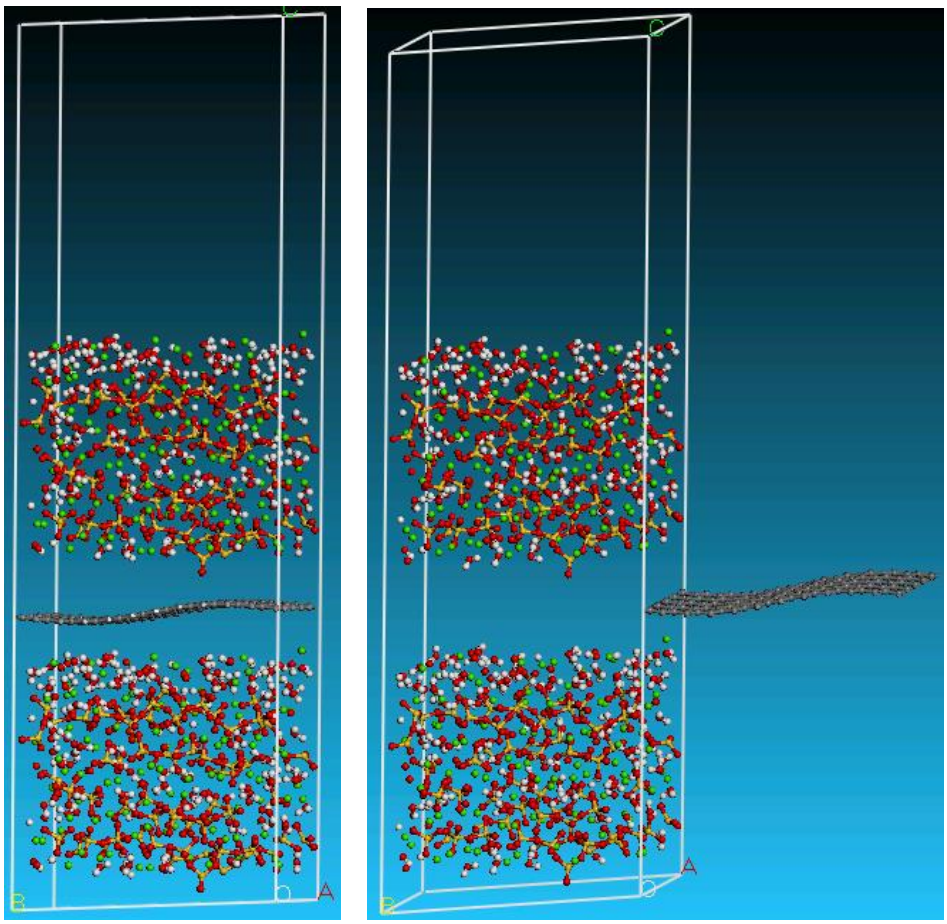

Figure 4.17. Atomic Model for Pristine Graphene G-(C-S-H) Reinforcement Interfacial Pull-out

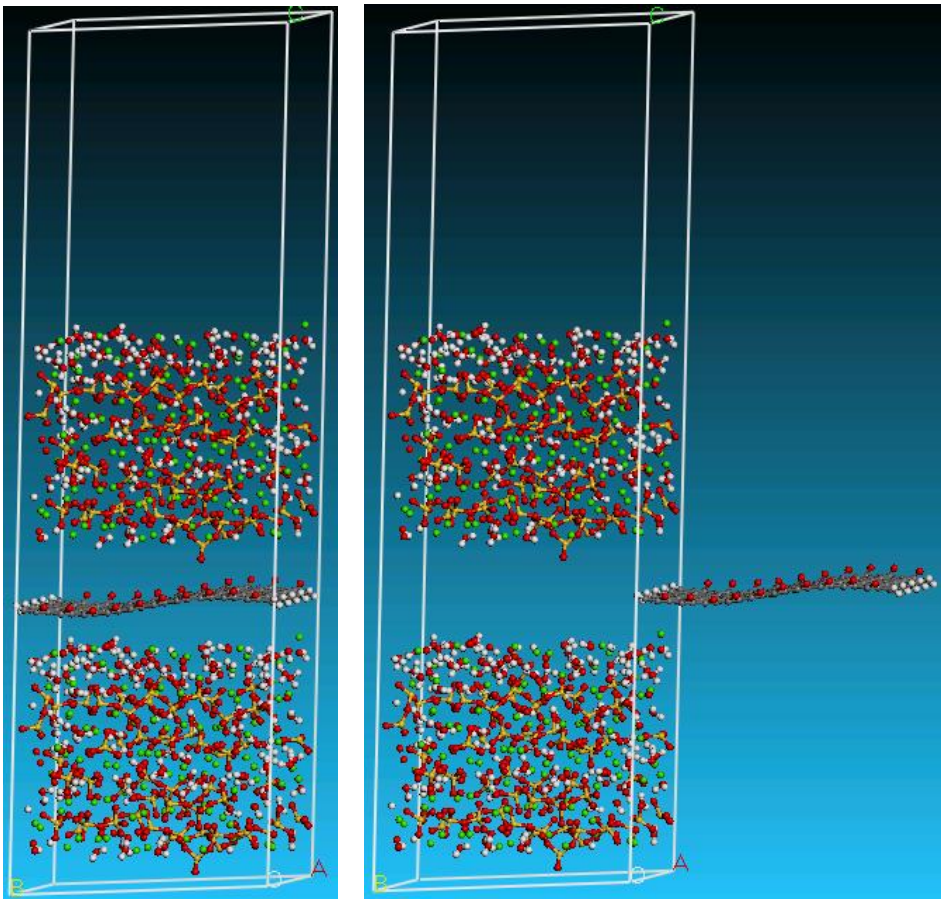

Figure 4.18. Atomic Model for Functionalized Graphene G(O)-(C-S-H) Reinforcement Interfacial Pull-out

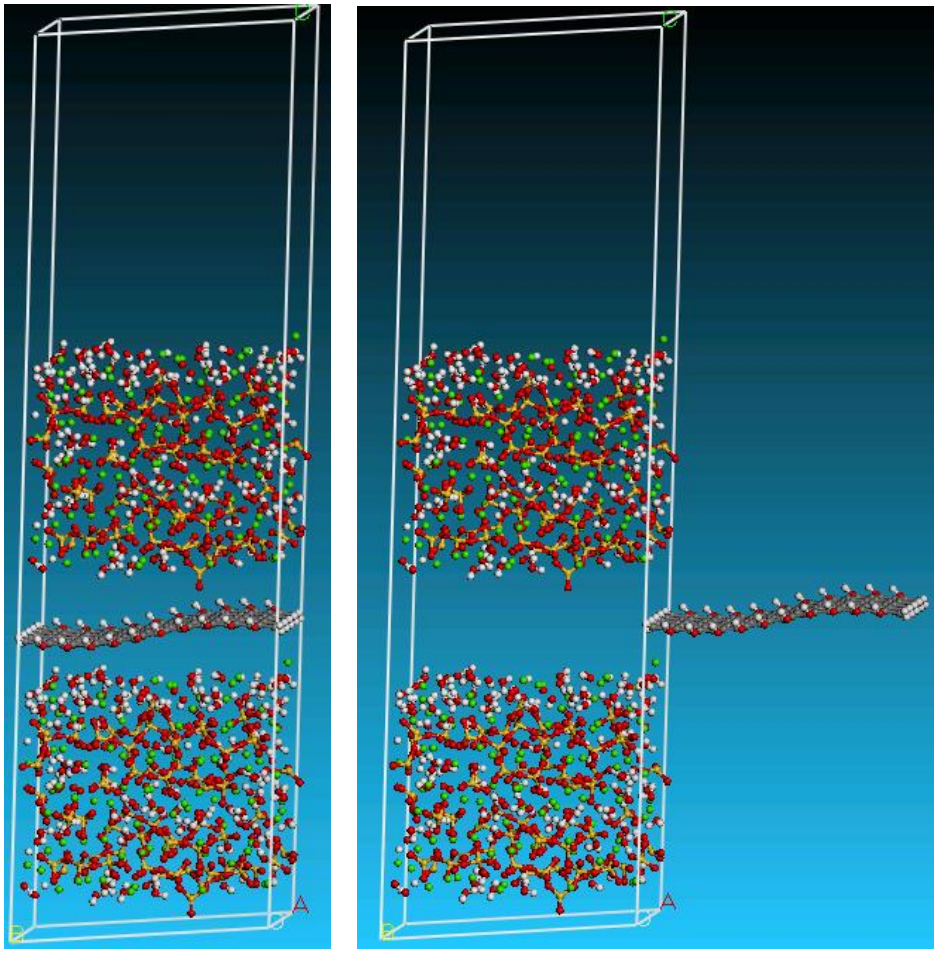

Figure 4.19. Atomic Model for Functionalized Graphene G(OH)-(C-S-H) Reinforcement Interfacial Pull-out

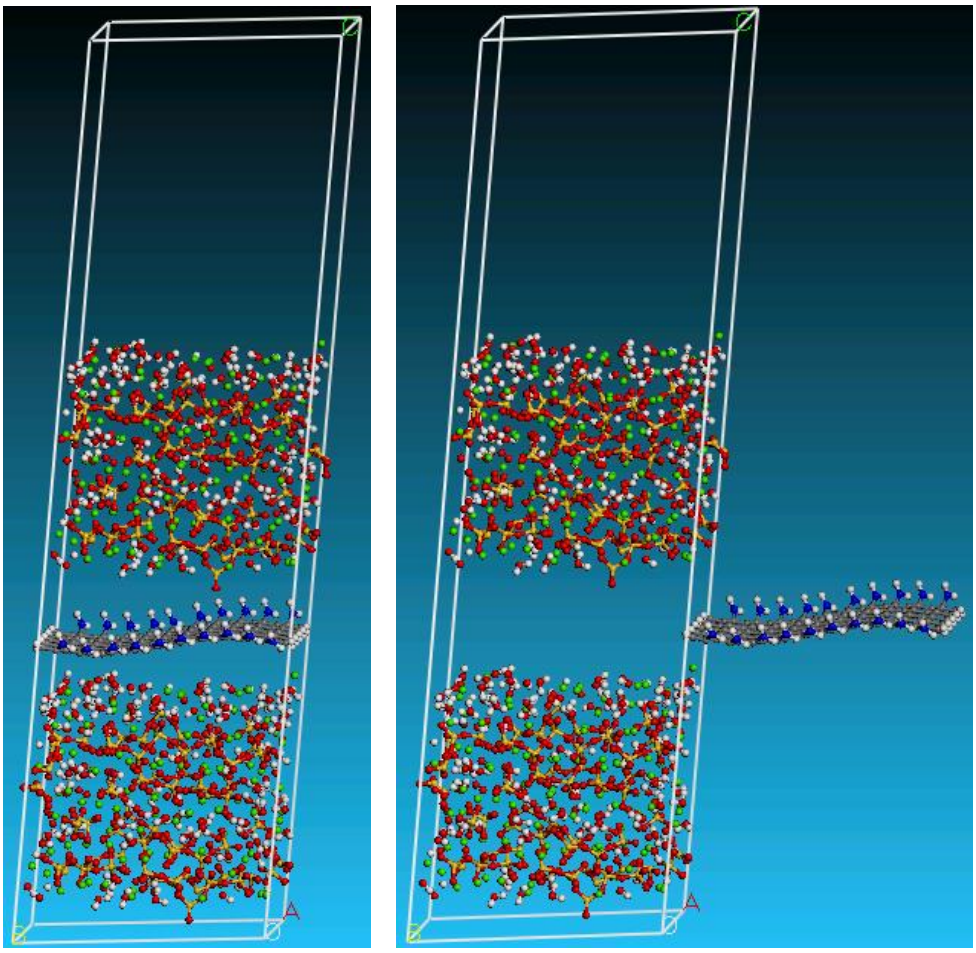

Figure 4.20. Atomic Model for Functionalized Graphene G(NH2)-(C-S-H) Reinforcement Interfacial Pull-out

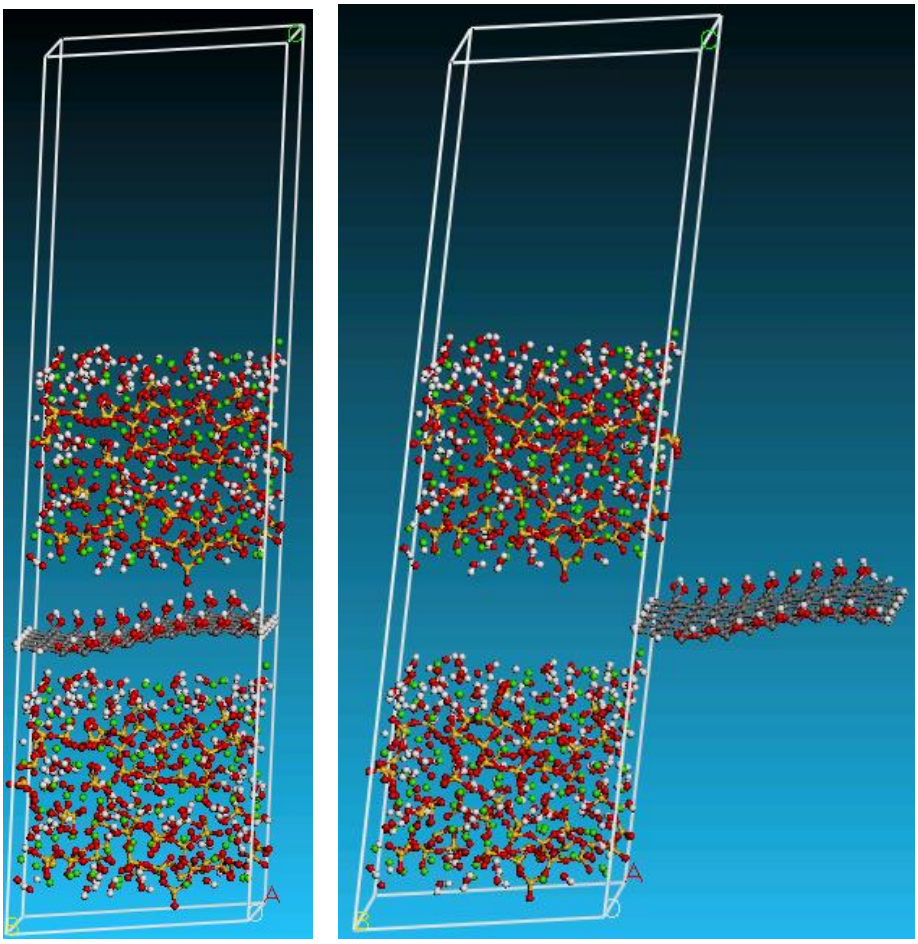

Figure 4.21. Atomic Model for Functionalized GrapheneG(COOH)-(C-S-H) Reinforcement Interfacial Pull-out

For the interfacial strength calculations, each system is equilibrated and optimized by performing the molecular dynamics simulations cited in[101]. Thence, the energy difference between a fully embedded graphene platelet and the pulled out graphene configuration for the hybrid system C-S-H-G()-C-S-H is calculated. However, from calculations executed, an increase in interaction energy with increasing polarity of the functional group is observed. The interfacial strength calculations followed section 3.4.2, and results are demonstrated in table 4.4.

Table 4.4. Interfacial Strength for Graphene-(C-S-H) Nanocomposites

Composite	Interfacial Strength (GPa)
C-S-H-G()	1.2
C-S-H-G($=O$)	—
C-S-H-G($-OH$)	13.5
C-S-H-G($-NH_2$)	6.1
C-S-H-G($COOH$)	11.8

4.4 Experimental Evaluation

Six types of experiments are used to evaluate the effect of nano-additives on mechanical and electrical properties of reinforced cementitious nanocomposites and to correlate performance to morphology.

4.4.1 X-ray Powder Diffraction (XRD)

Introduction

The microstructure of a material is the fundamental link between the process that forms the material and its properties. Although, cement complexity, heterogeneity, and physical structural have not yet fully revealed, the identification of the phase composition is a key to understand the properties relationships. A quantitative analysis of the crystalline and amorphous phases of hydrated cementitious nanocomposites is studied using the internal standard XRD technique.

Experimental Setup

The X-ray diffraction (XRD) pattern of each crystalline phase is unique. The positions of the peaks are determined by the spacing of the crystallographic planes according to Bragg's law 4.1:

$$n\lambda = 2d\sin\theta \tag{4.1}$$

where n is an integer, λ is the wave length of the radiation used, d the spacing of the crystal planes, and θ is the angle of the diffraction pattern. The intensity of the peaks is determined by the types and positions of the atoms in the crystal lattice according to the structure factor

4.2:

$$F(hkl) = \sum_{I}^{N} f_n exp 2\pi i(hx_n + ky_n + lz_n) \tag{4.2}$$

where hkl are the miller indices of the reflecting planes, f_n the atomic structure factor, and x_n,y_n, z_n, are the coordinates of the nth atom in the unit cell containing N atoms.

Since the amorphous phases do not produce additional visible reflexes, determination of the amorphous content in cement cannot be detected directly by XRD. However, by using a defined quantity of crystalline standard material it is possible to determine the ratio of the crystalline material in the sample to the crystalline standard and thus calculate the content of amorphous material in the sample [102] by the backward calculation principle.

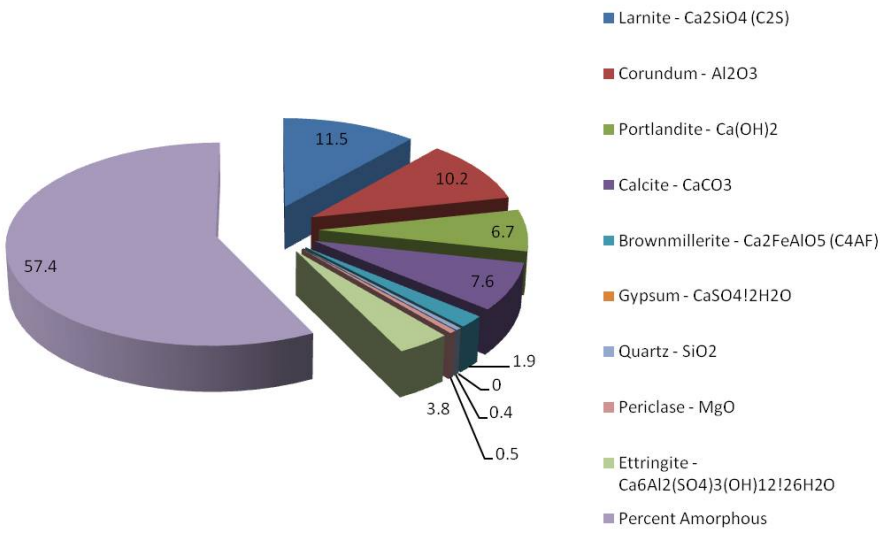

Figure 4.22. Phases in Hydrated Portland Cement From Powder Specimens

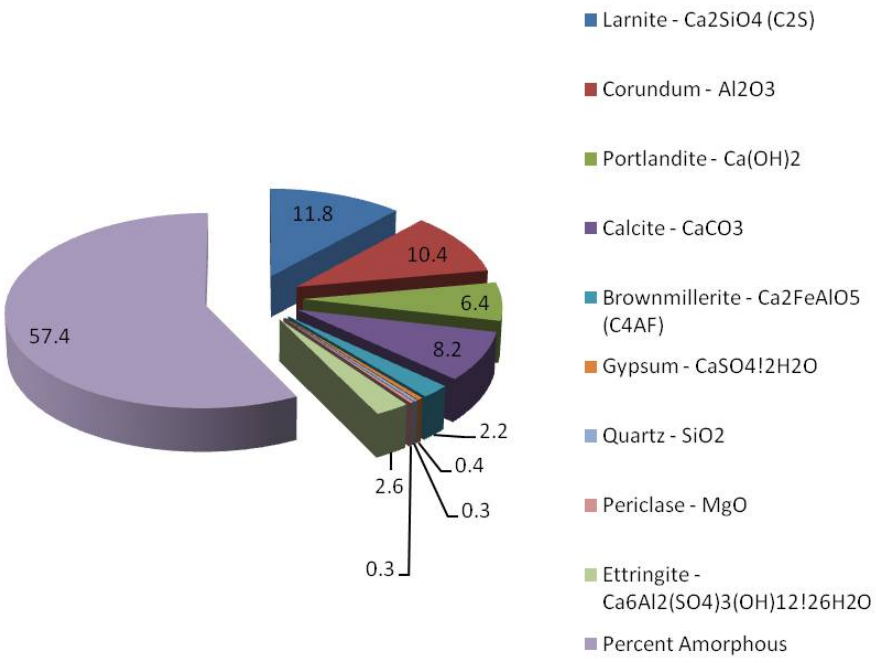

Figure 4.23. Phases in Hydrated Nano Diamond-Cement From Powder Specimens

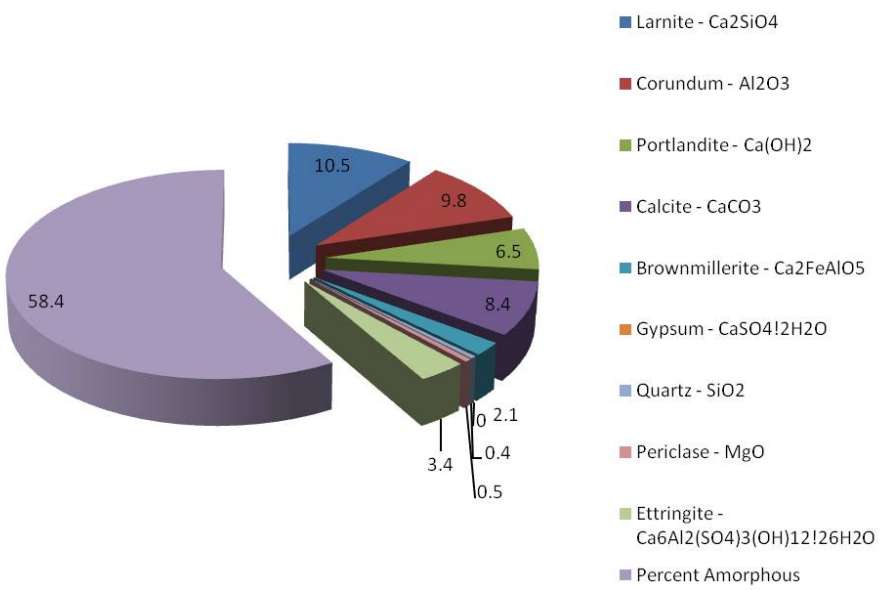

Figure 4.24. Phases in Hydrated Functionalized Graphene-Cement From Powder Specimens

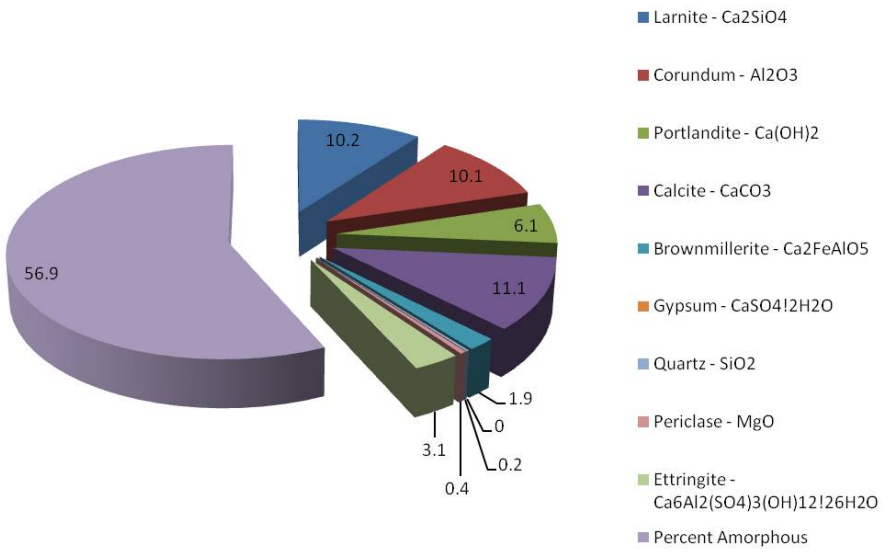

Figure 4.25. Phases in Hydrated PEG POSS-Cement From Powder Specimens

Figures 4.28-4.29 show quantifications of different cementitious nanocomposites demonstrating the percentages of the hydrated cement crystalline and amorphous phases. Alumina is added in $\sim$ 10% by weight, in order to insure the precision of the quantification. All the tested specimens are consistent in their chemical phase composition. However, this consistency ensures, that there is no correlation between the chemical composition of the cementitious nanocomposites and the improvement in the chemical properties.

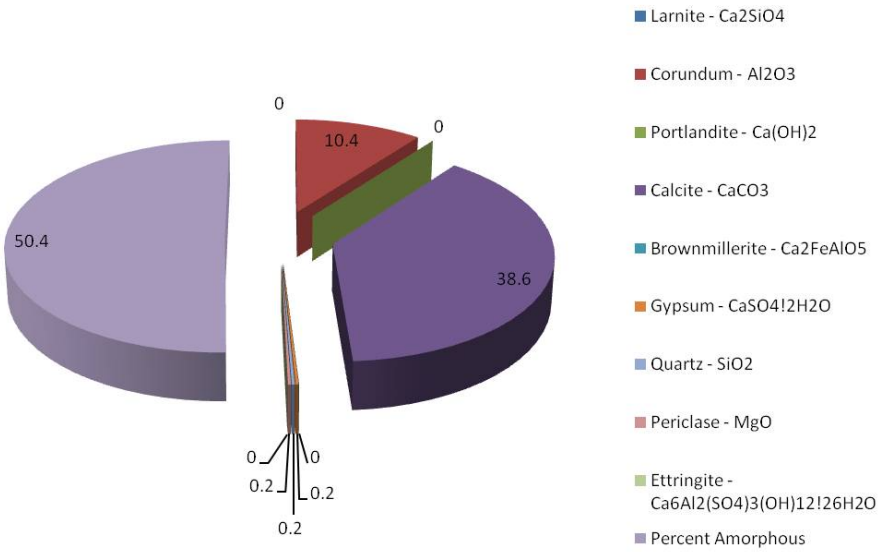

Figure 4.26. Phases in Hydrated Nano C_3S From Powder Specimens

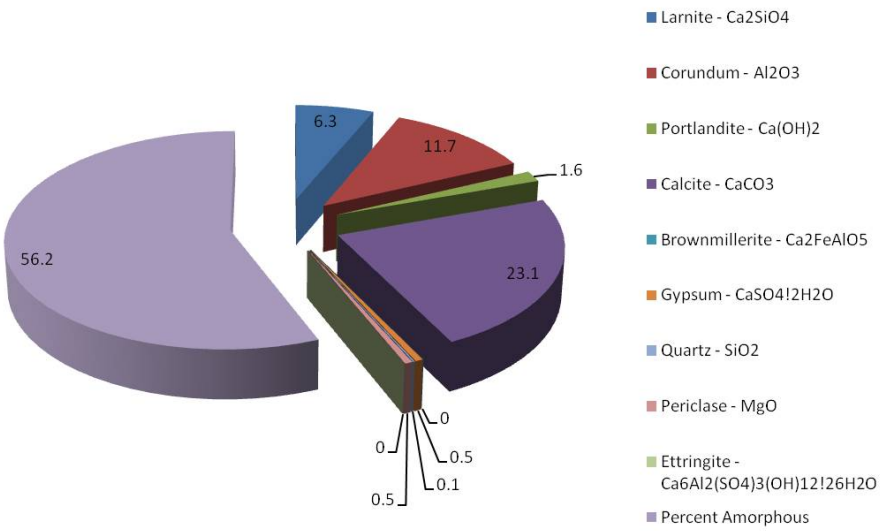

Figure 4.27. Phases in Anhydrous Nano C_3S From Powder Specimens

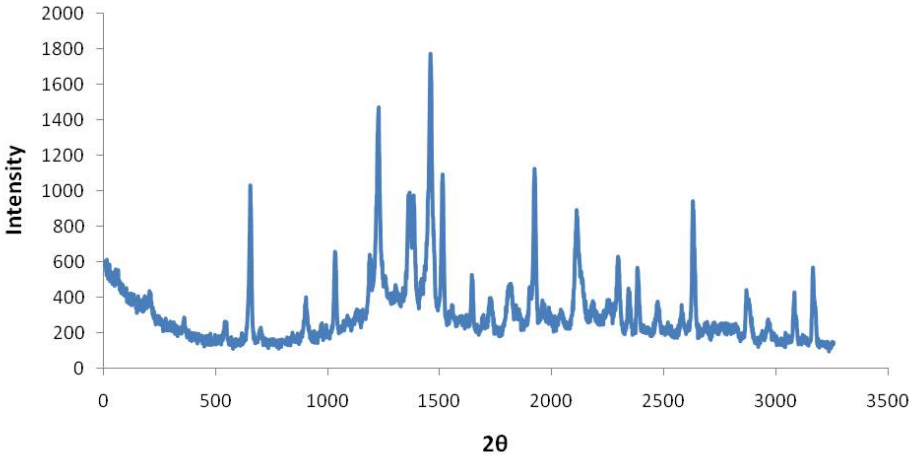

Figure 4.28. X-ray Diffraction Pattern of Hydrated Portland Cement From Powder Specimens

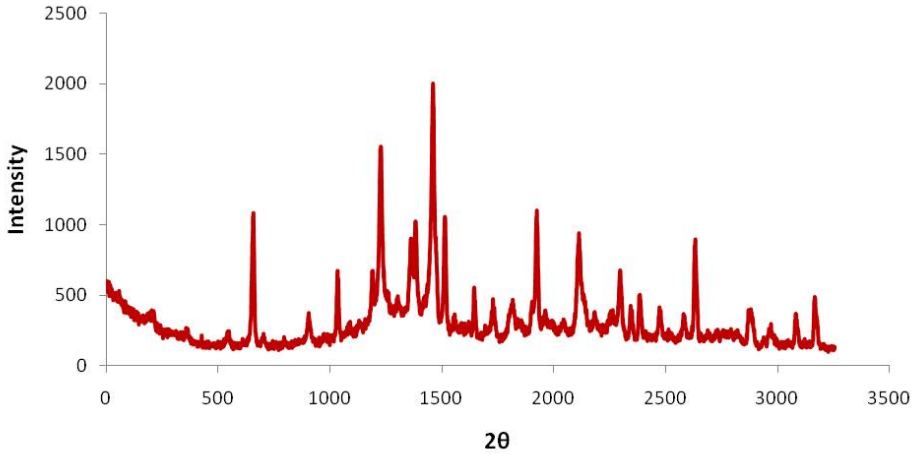

Figure 4.29. X-ray Diffraction Pattern of Hydrated Nano Diamond-Cement From Powder Specimens

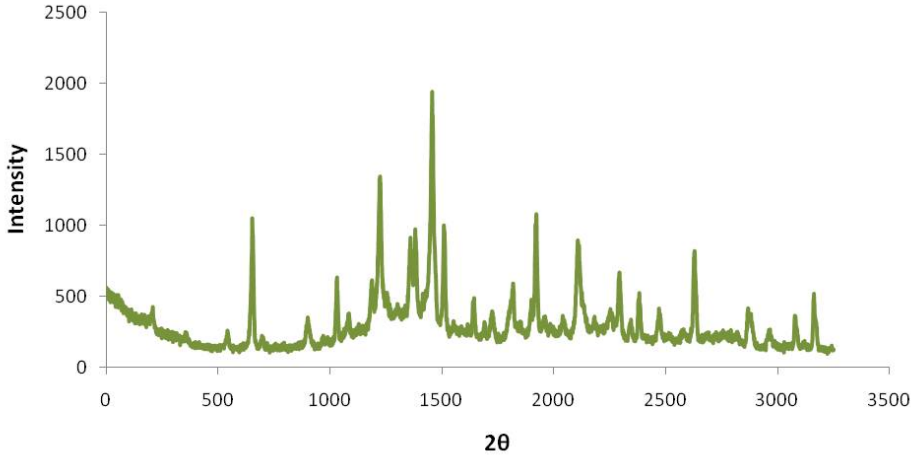

Figure 4.30. X-ray Diffraction Pattern of Hydrated Functionalized Graphene-Cement From Powder Specimens

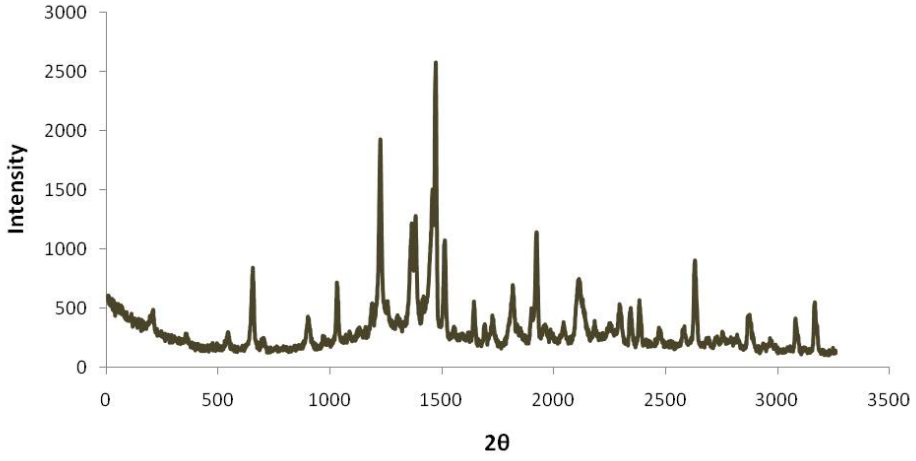

Figure 4.31. X-ray Diffraction Pattern of Hydrated PEG POSS-Cement From Powder Specimens

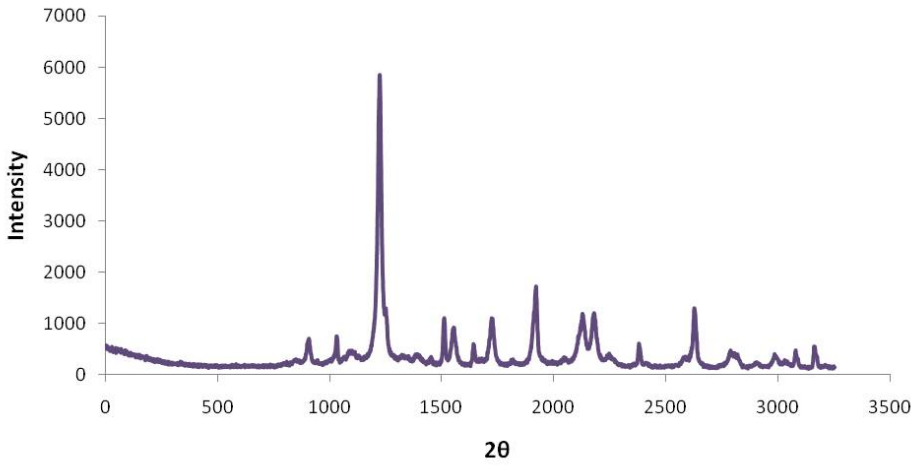

Figure 4.32. X-ray Diffraction Pattern of Hydrated Nano C_3S From Powder Specimens

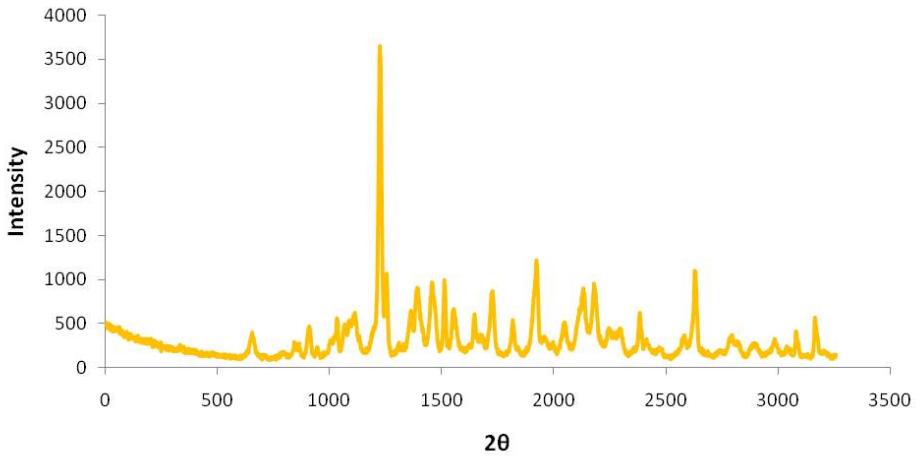

Figure 4.33. X-ray Diffraction Pattern of Anhydrous Nano C_3S From Powder Specimens

4.4.2 Atomic Force Microscopy (AFM)

Introduction

The Atomic Force Microscopy is an imaging technique used for microscopic level characterization. Binning and Gerber [103] invented the AFM in 1986. AFM is operated by scanning a sharp nano tip over a sample surface, and 3D images with a nano resolution can be obtained at atmospheric conditions. AFM imaging does not acquire a conductive surface. Different forces either repel or attract the tip such as: Van der Waals forces, capillary forces, chemical bonding, electrostatic forces, and magnetic forces. The change in force interaction between the scanned surface and the tip lead to a deflection in the tip attached to the cantilever. Deflections due to tip-surface interaction are monitored using an optical lever detection system. Figure 4.34 shows a schematic atomic force microscope, and figure 4.35 shows the AFM instrumentation setup. A laser beam is reflected from the back of a cantilever onto a position-sensitive photodiode in the cantilever deflection detection system. The deflection of the cantilever is monitored by a photodiode detector. Depending on the mode of operation, a particular operating parameter such as a tip-sample force or a tip-sample distance is maintained at a constant level. These deflections are recorded and processed using an imaging software; this is represented by the topographical changes in the scanned sample.

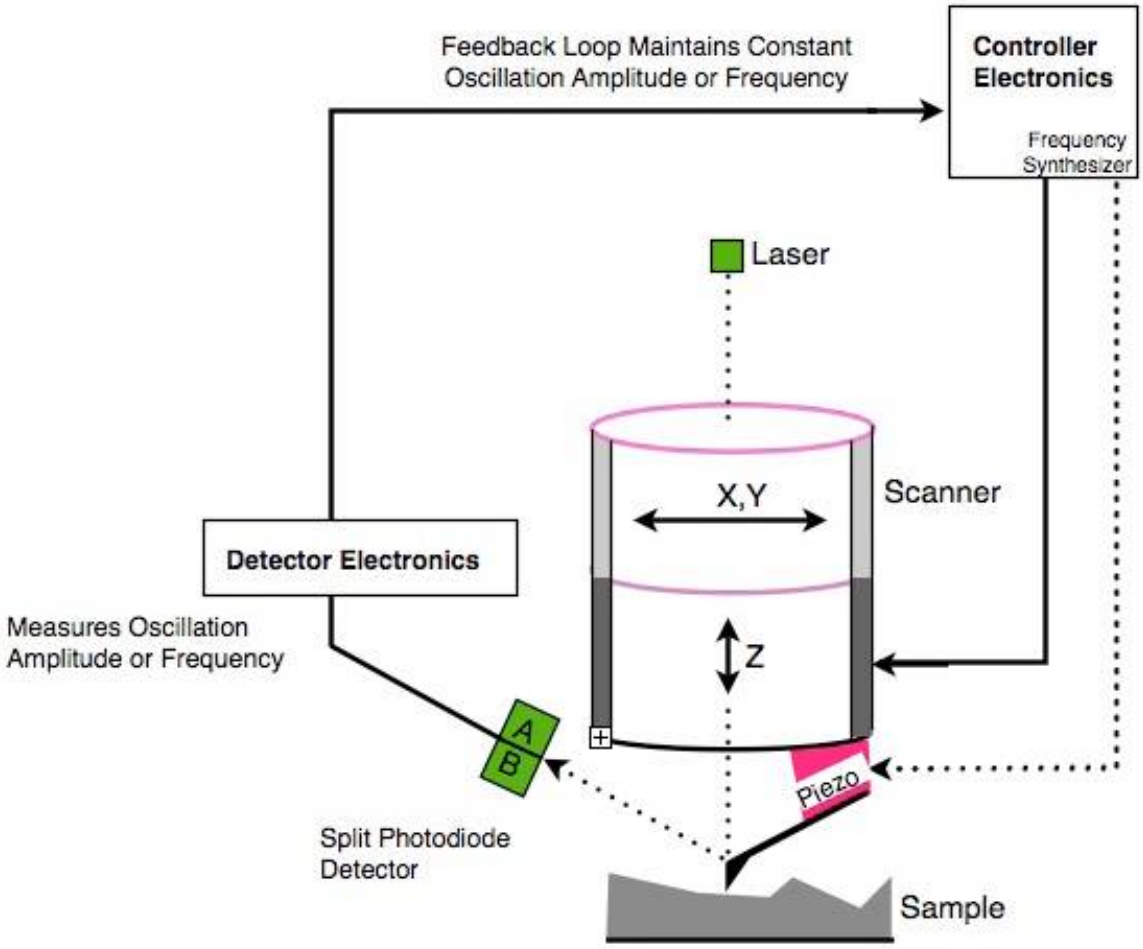

Figure 4.34. Schematic Atomic Force Microscope Diagram

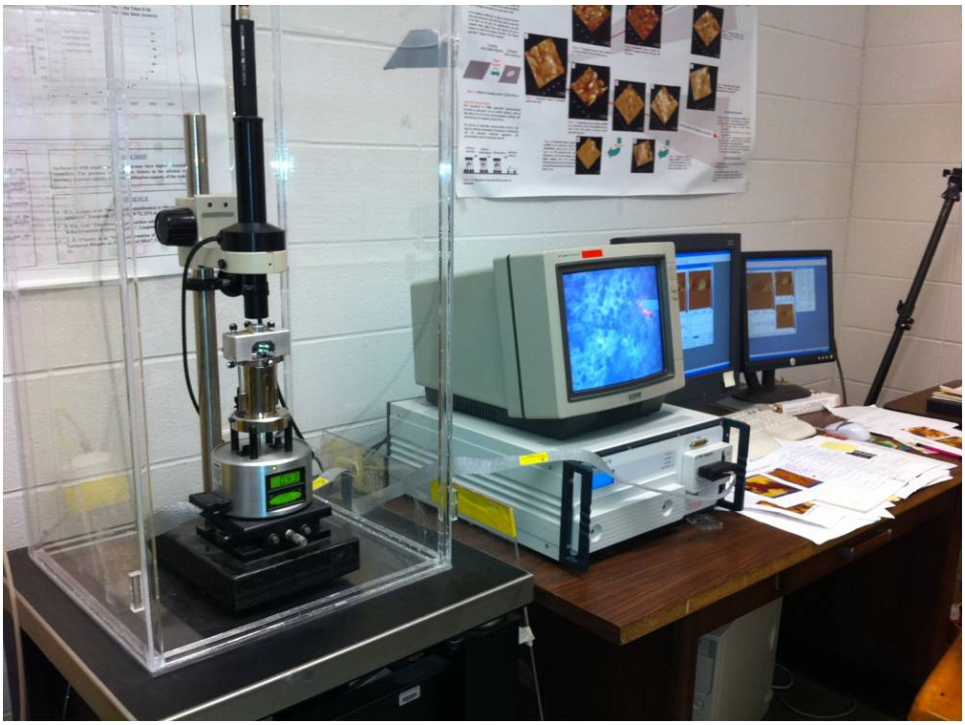

Figure 4.35. AFM Instrumentation Setup

There are three basic imaging modes: contact mode, non-contact mode, and tapping mode. In the contact mode, the sample surface is scanned by the cantilever nano tip. During scanning, as the topography of the sample changes, the z-scanner simultaneously moves and adjusts the relative position of the tip with respect to the sample to maintain a constant cantilever deflection. However, a low constant spring <1 N/m probe is used to minimize the force applied to scan the sample surface.

Experimental Setup

In the AFM contact mode, a cantilever is usually scanned over the surface of the sample and can be used efficiently to fish for single molecules to investigate their physical structures and mechanical properties. In AFM spectroscopy, the cantilever tip is moved toward the surface of the sample until it is engaged with specimen surface, and then it is retracted again while the interaction between the tip-surface is recorded. This can be repeated several times at several locations to give a full statistical understanding of the tip-surface interaction and to collect force curves.

A typical AFM screen setup for a contact mode is shown in figure 4.36, where it is clear that the tracing and retracing plots are fitted well together and confirms that the parameters used in scanning are compatible with the scanned surface.

The forces measured by the cantilever as it approaches from several microns above the sample surface, can be related to the long-range interactions, such as the electrostatic effects. However, as the cantilever moves closer to the surface, nanometers or atomic distances, shorter-range forces can be captured. Similarly, Van der Waals or capillary forces can be detected. An attractive force is recorded, when the tip may jump into contact with surface, this is referred to as "snap-in".

The data recorded from a force curve experiment, can be displayed as a simple plot shown in 4.37. Height position of the cantilever for the approach and the retract are recorded on the x-axis, and the cantilever property that is being measured is displayed on the y-axis.

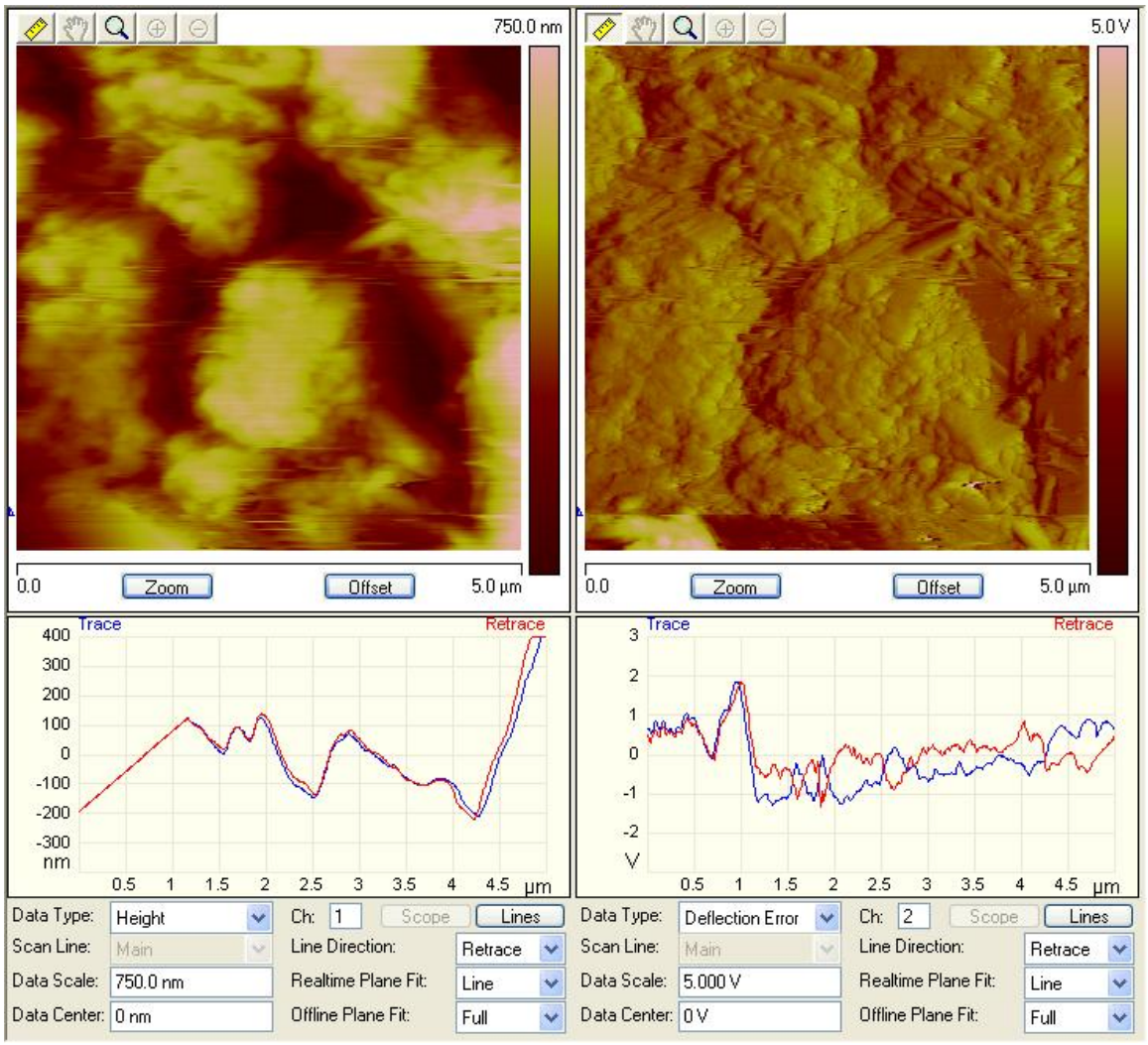

Figure 4.36. Contact Mode Screen Setup

A cantilever property that is usually recorded in similar measurements is the deflection which can give a direct measure of the interaction forces. The deflection is measures by an optical beam deflection setup, which delivers an electrical signal in Volts (the signal from the photodiode) that is proportional to the cantilever deflection. Figure shown in 4.37 reflects a typical interaction for a coated cantilever tip in air approaching a hard, incompressible cementious surface.

The approach (blue) and retract (red) curves are both plotted on the same figure. At the beginning, while the cantilever is approaching the surface, the forces will be very small

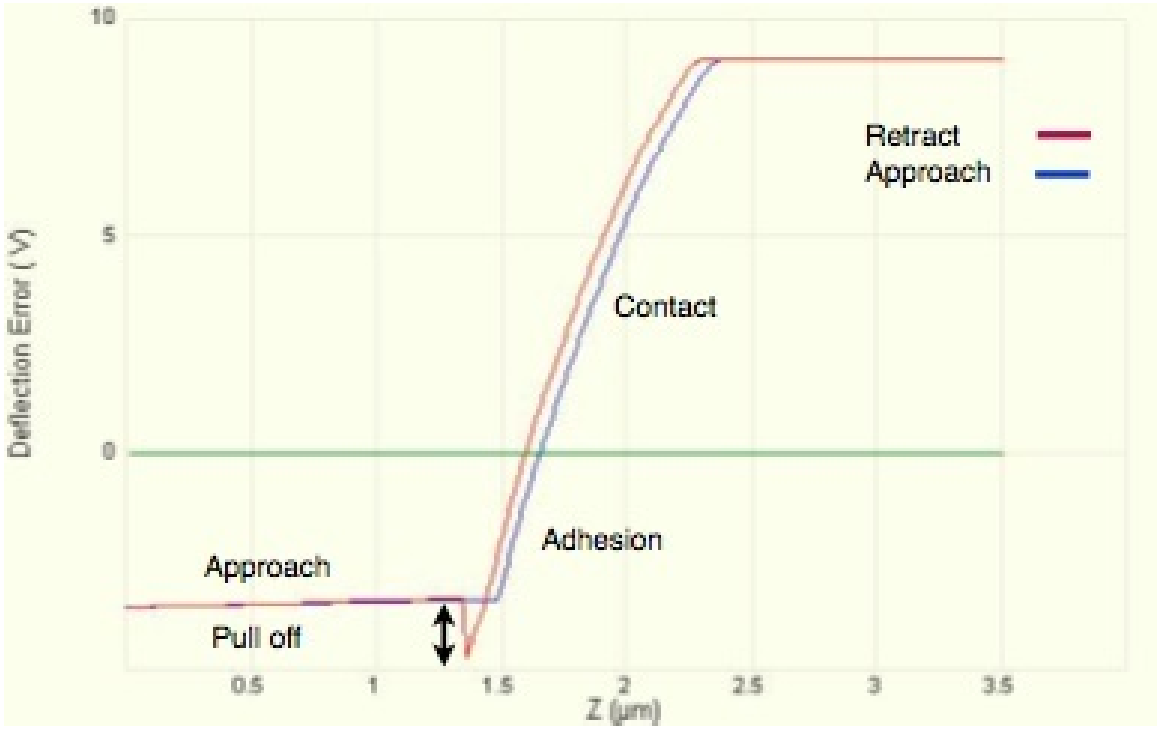

Figure 4.37. Plot of approach (blue), and retract (red) curves for a contact mode cantilever and PEG POSS mixed with Cement Surface in Air

and the deflection of the cantilever cannot be detected. As the tip gets closer to the surface, the attractive short range forces overcome the cantilever spring constant, the tip snaps-in the surface, and a jump in the red curve is recorded. This contact between the tip and the surface remains; the deflection in the cantilever increases and the repulsive forces increases.

As the cantilever retracts from the surface the tip usually persists in contact with the surface due to some adhesion, and it is recorded as a jump in the blue curve. For measurements in the air, the adhesion is due to capillary forces between the tip and the sample's surface.

Results

1. **Tapping Mode Imaging**

AFM imaging is used to study the micro-nanostructure of Portland cement type I/II mixed with several nano additives discussed in 4.2.2. Topographic images and force-deflection curves are obtained in contact mode using a silicon nitride tip of a 0.06 N/m spring constant. For scans shown in figures 4.38 to 4.51, the resolution is kept 512x 512 pixels, a scan rate is kept constant at $0.50Hz$, and a scan size 5μm x 5μm.

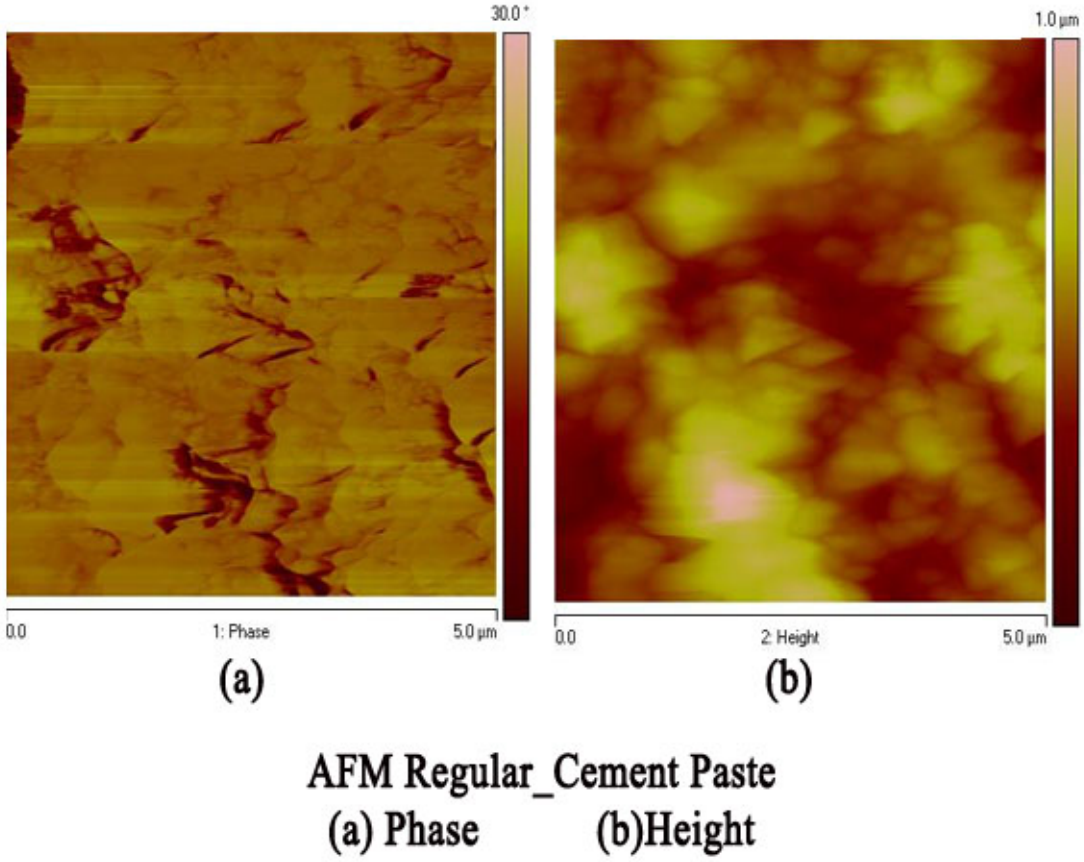

Figure 4.38. 5 μm x 5 μm Atomic Force Microscopy Image of Portland Cement Type I/II With w/c =0.45 (a)Phase (b) Height

From Figures 4.38 and 4.39, AFM imaging for the Portland cement type I/II, the high and low density C-S-H structures can be identified. The 3D phase image provides

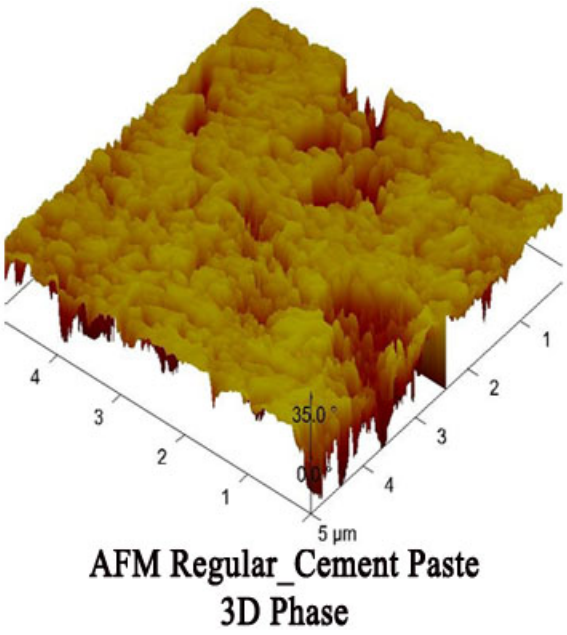

Figure 4.39. 5 μm x 5 μm Atomic Force Microscopy Image of Portland Cement Type I/II With w/c =0.45 3D phase

an encoding for the stiffness variation of the scanned sample. For figure 4.38 (b), the coloring scheme reflects the height variation between (0-1μm). The dark brown reflects a deep topography, and the bright pink reflects a high topography.

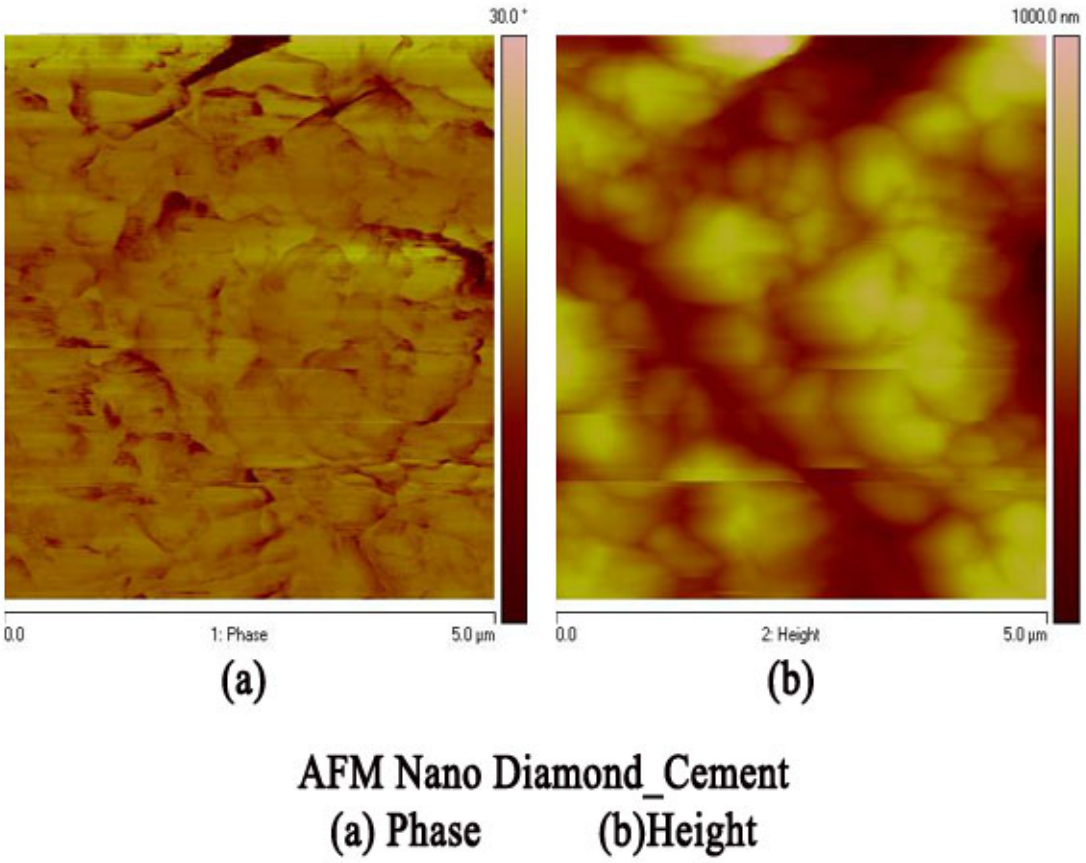

Figure 4.40. 5 μm x 5 μm Atomic Force Microscopy Image of Portland Cement Type I/II Mixed With Nano Diamonds w/c =0.45 (a)Phase (b) Height

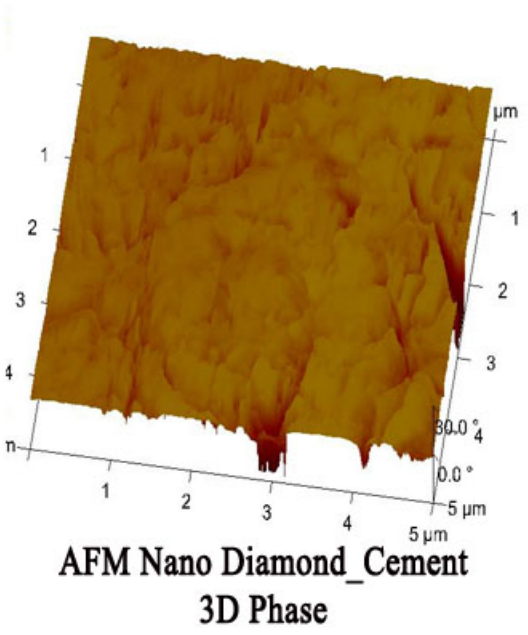

Figure 4.41. 5 μm x 5 μm Atomic Force Microscopy Image of Portland Cement Type I/II Mixed With Functionalized Graphene Platelets w/c =0.45 3D phase

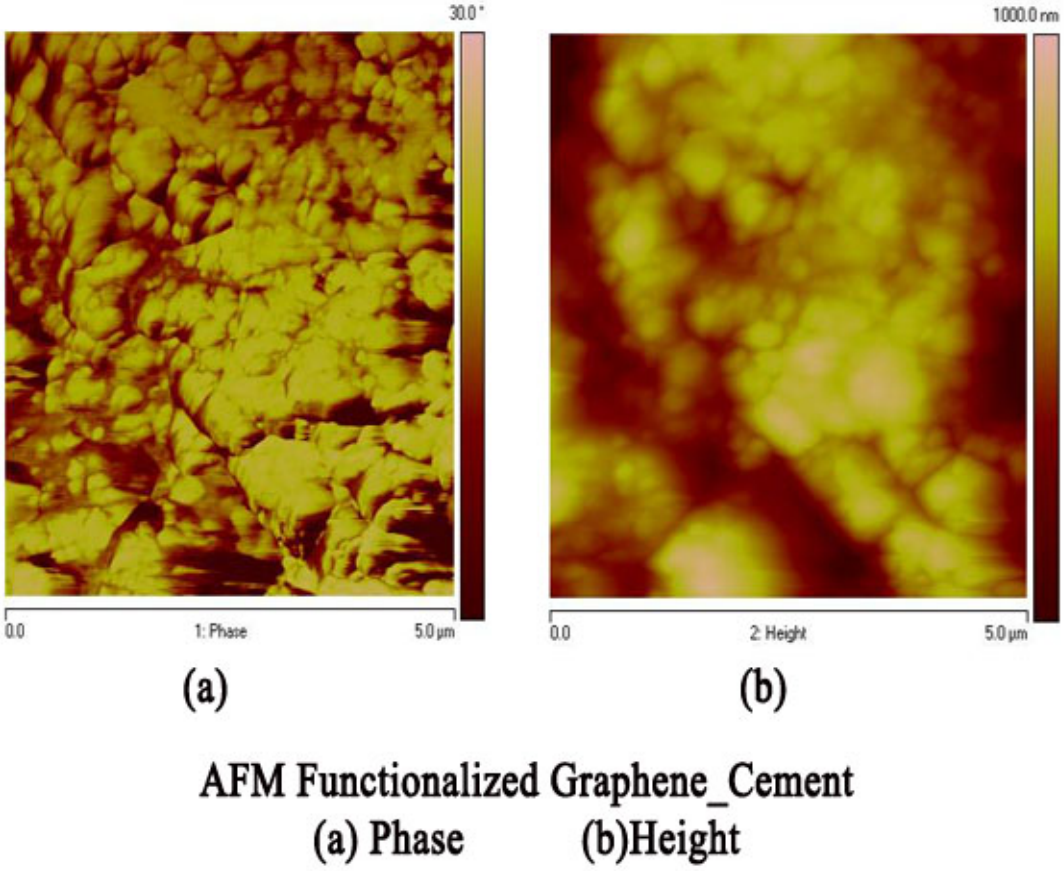

Figure 4.42. 5 μm x 5 μm Atomic Force Microscopy Image of Portland Cement Type I/II Mixed With Functionalized Graphene Platelets w/c =0.45 (a)Phase (b) Height

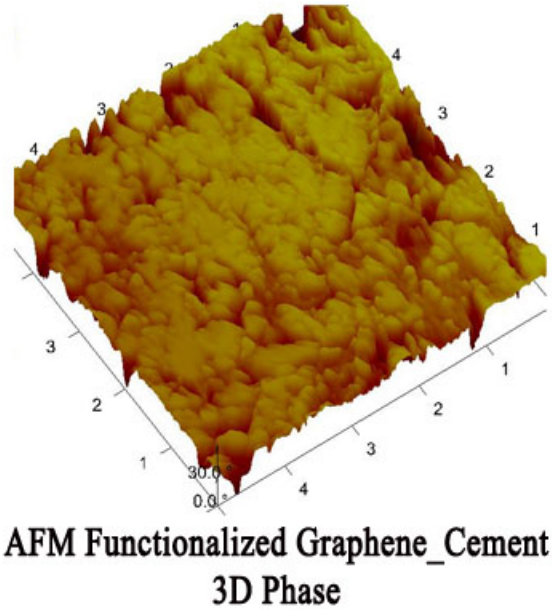

Figure 4.43. 5 μm x 5 μm Atomic Force Microscopy Image of Portland Cement Type I/II Mixed With Functionalized Graphene Platelets w/c =0.45 3D phase

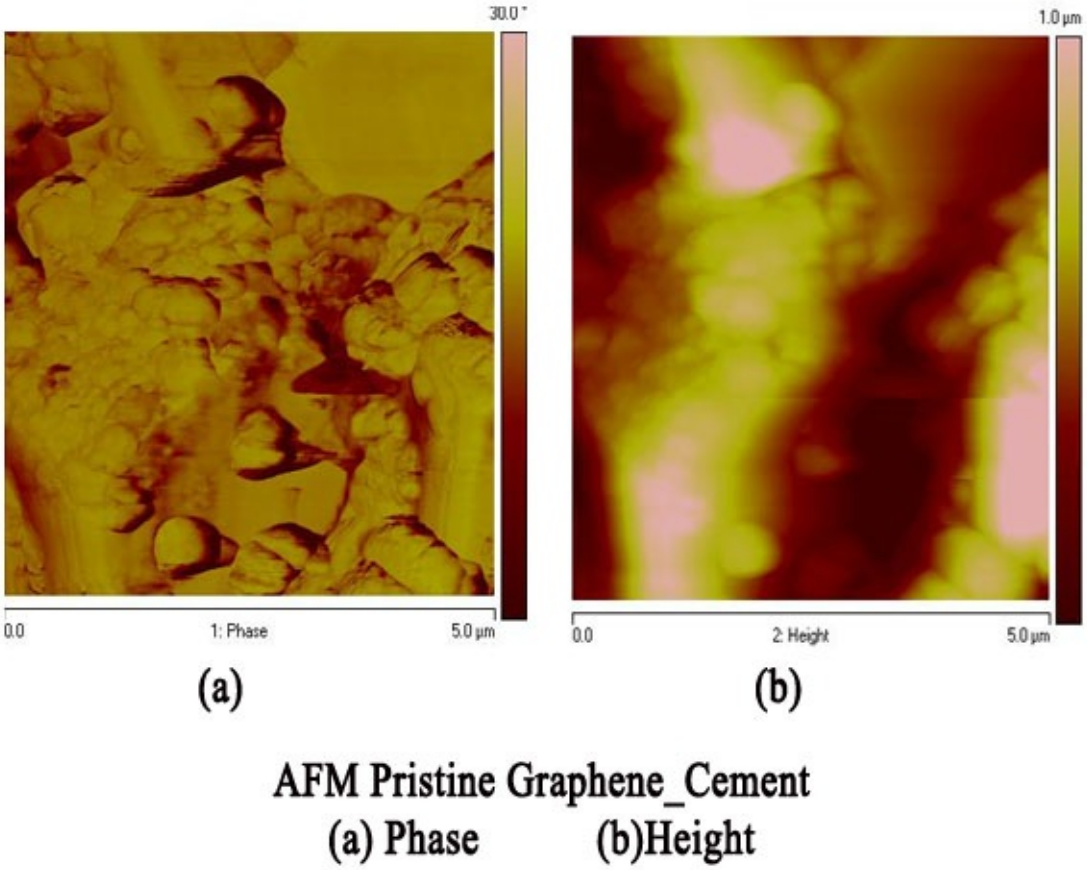

Figure 4.44. 5 μm x 5 μm Atomic Force Microscopy Image of Portland Cement Type I/II Mixed With Pristine Graphene Platelets w/c =0.45 (a)Phase (b) Height

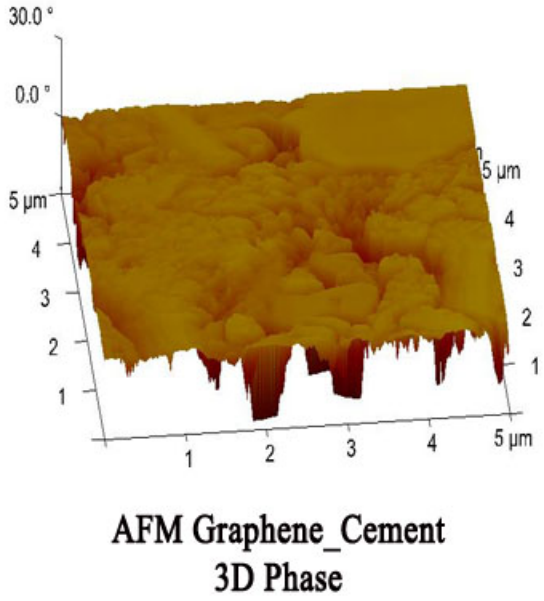

Figure 4.45. 5 μm x 5 μm Atomic Force Microscopy Image of Portland Cement Type I/II Mixed With Pristine Graphene Platelets w/c =0.45 3D phase

From Figures 4.44 and 4.45, AFM imaging for the Portland Cement type I/II mixed with pristine exfoliated graphene, the high and low density C-S-H structures are identified, the scattering of the C-S-H particles differs from the images shown in 4.38. Nevertheless, this observation is very interesting and could affect the physical structure of the cement. The variation in the low and high density of C-S-H distribution and packing could be effected by the presence of the graphene platelets. The 3D phase image provides an encoding for the stiffness variation of the scanned sample. For figure 4.44 (b), a graphene platelet at the top right corner is identified. However, the 3D phase image in figure 4.45 confirms the graphene platelet clearly correlated to the high stiffness phase topography.

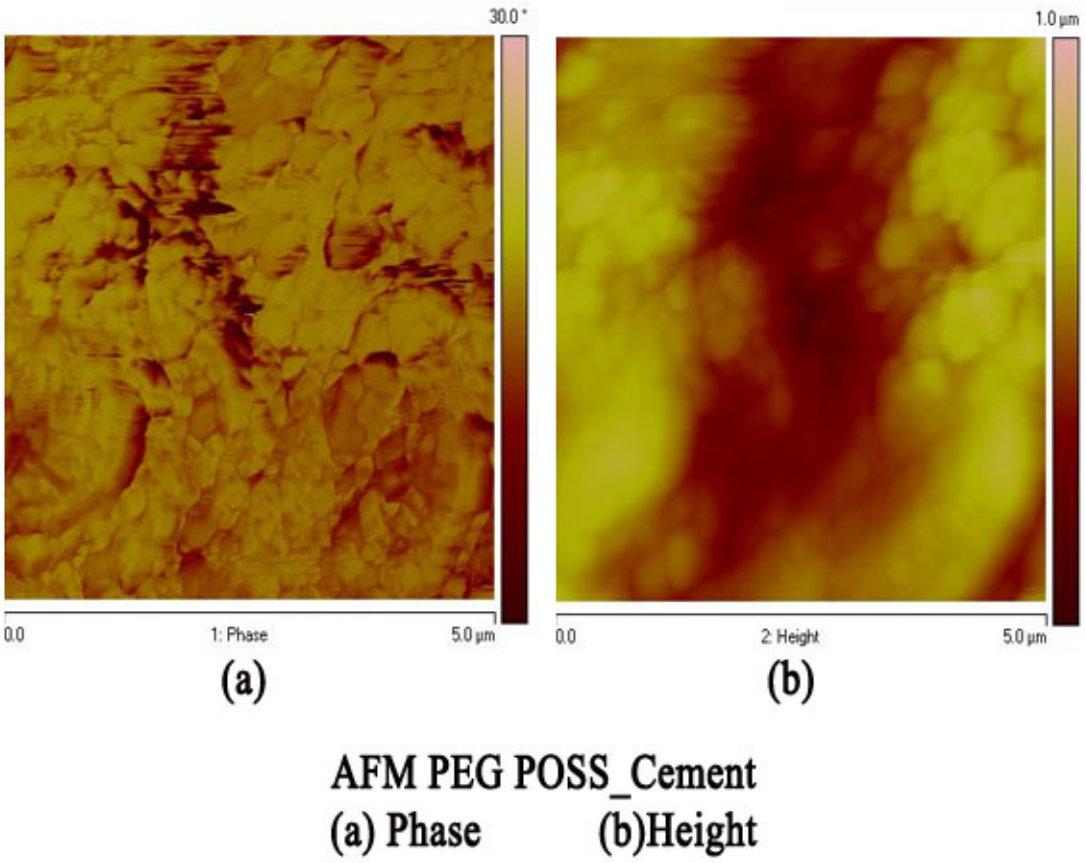

Figure 4.46. 5 μm x 5 μm Atomic Force Microscopy Image of Portland Cement Type I/II Mixed With PEG POSS w/c =0.45 (a)Phase (b) Height

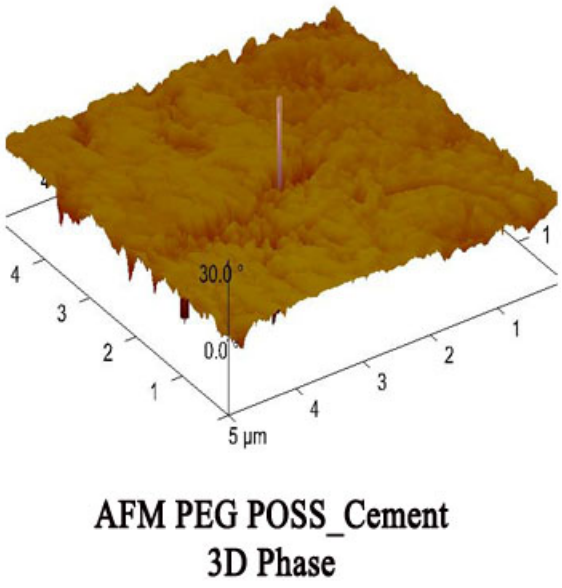

Figure 4.47. 5 μm x 5 μm Atomic Force Microscopy Image of Portland Cement Type I/II Mixed With PEG POSS w/c =0.45 3D phase

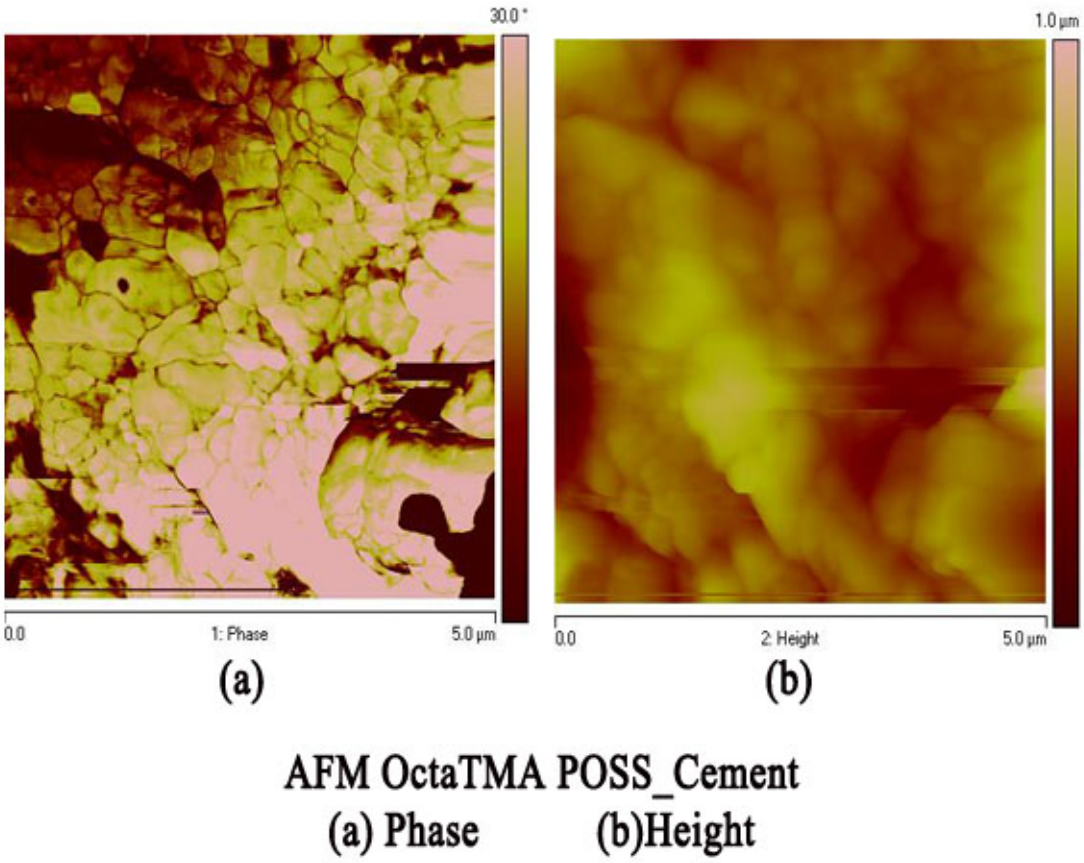

Figure 4.48. 5 μm x 5 μm Atomic Force Microscopy Image of Portland Cement Type I/II Mixed With OctaTMA POSS w/c =0.45 (a)Phase (b) Height

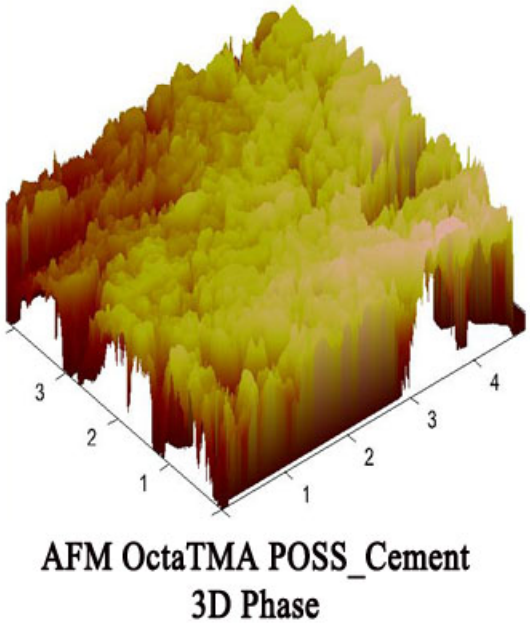

Figure 4.49. 5 μm x 5 μm Atomic Force Microscopy Image of Portland Cement Type I/II Mixed With OctaTMA POSS w/c =0.45 3D phase

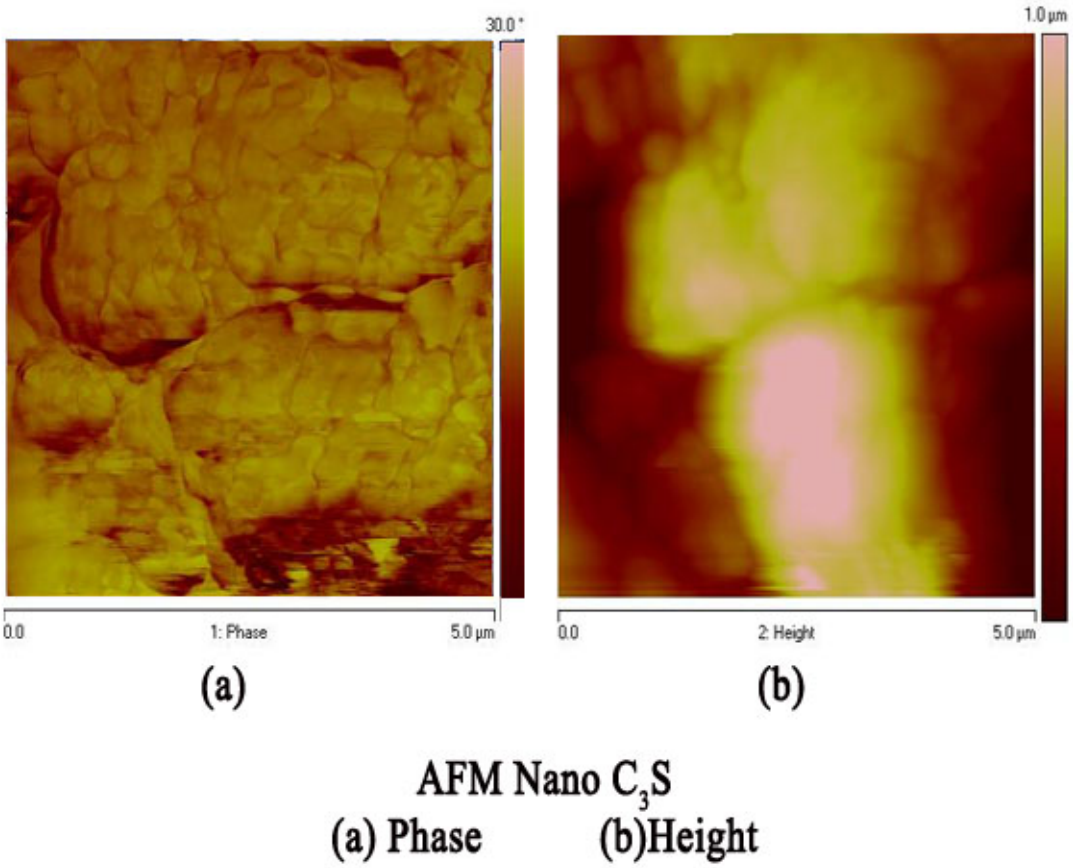

Figure 4.50. 5 μm x 5 μm Atomic Force Microscopy Image of Nano C_3S w/c =1.25 (a)Phase (b) Height

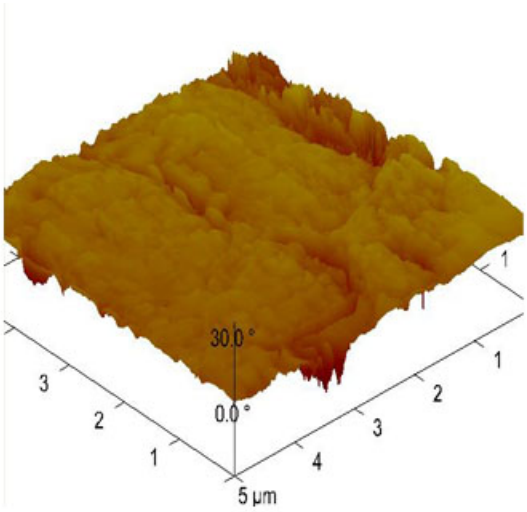

Figure 4.51. 5 μm x 5 μm Atomic Force Microscopy Image of Nano C_3S with w/c =1.25 3D phase

From figures 4.38-4.49, it is found that the AFM is a promising technique to image and characterize the different phases of the cementitious nanocomposites. The C-S-H gel, and CH crystals are identified by spherical particles of different sizes and different packing densities. The particle sizes are in the range of $> 100nm - 500nm <$. Phase imaging for the different cementitious specimens demonstrates the effect of the nano additive on the phase formation, surface roughness, and the C-S-H structures clusters distribution. Whereas, for the nano C_3S a lower packing density and less evidence of C-S-H gel, compared to the other cementitious nanocomposites, figure 4.50.

2. **Contact Mode Force Deflection Calculations**

The deflection of the cantilever is directly proportional to the tip-sample interaction force. However, a two- step conversion is required to convert the photodetector voltage signal into a force a quantitative force value. The first step; is to calibrate the actual distance of the cantilever deflection for a measured change in the photodetector voltage. This calibration depends on the type of the cantilever and the optical path of the AFM laser detection. When the deflection of the cantilever is known as distance x, the spring constant, k, is required to convert this value into a force, F, by Hooke's law in equation 4.3:

$$F = k * x \tag{4.3}$$

The repulsive contact region slope is used to convert the Volts into nanometers. This measurement can be used to calibrate the forces applied on specimen surface. However, the interaction forces, when the cantilever is far from the surface, are virtually zero. The offset (for the flat part of the force curve) should be subtracted from all the deflections data; in order to calculate the true interaction force.

Force deflection curves shown in figure 4.52, show a variation in the force slopes, which is a typical reflection of the materials mechanical properties. However, it is also

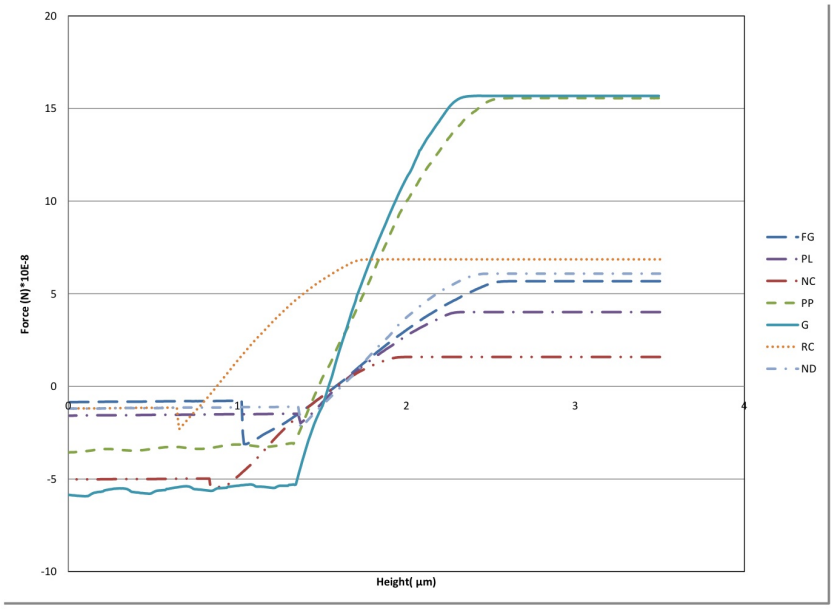

Figure 4.52. Force Curve Plots for a Contact Mode Cantilever AFM Scan on Cement Surface Mixed with Nano additives in Air

demonstrated from figure 4.52, that the adhesion between the tip and the surface of the sample alters respectively with the nano addictive. The difference in the adhesion is a reflection of the Van der Waal forces present between the tip and specimen surface. The force plots above need further statistical analysis, to describe accurately, the variation in adhesion and stiffness, at the surfaces of the scanned specimens.

4.4.3 Scanning Electron Microscopy (SEM)

Introduction

Scanning Electron Microscopy (SEM) is developed due the limitations of light microscopes, which are restrained to the light wave length. Theoretical limit has been reached early 1930's, in which scientific research required fine details of interior structures. First SEM debuted in 1942 by Vladimir Kosmo Zworykin.

SEM is widely used to examine surfaces down to a $50nm$ resolution. The surface is scanned by a focused electron beam, and the intensity of secondary electrons is monitored. The secondary electrons are viewed on a cathode-ray tube (CRT) [**?**]. SEM images characteristically have a wide range in contrast and great depth of focus. SEM, can characterize the topography, morphology, composition, and crystallographic information.

Experimental Setup

Figure 4.53 represents a schematic scanning electron microscope. The virtual source at the top represents the electron gun, which generates a stream of monochromatic electrons. The first condenser lens operates according to electron condenser lens. However, this lens is used to articulate the beam, and to control the amount of the current in the beam. It works in conjunction, with the condenser gap to discard the high-angle electrons from the beam. The beam is then limited by the condenser openning. Whereas, the electrons are formed into a thin, definite, and tight beam by the second condenser lens, this can be controlled by the fine probe current knob. The objective gap, is user selectable, which further eliminates high-angle electrons from the beam. The set of coils, scan or sweep the beam in a mesh configuration awaiting on points for a certain period of time, which is controlled by the scanning speed mode. For the final lens, the objective focuses the scanning beam on a part of interest on the specimen surface. When the beam strikes the sample, an interaction occurs

inside the sample, which is detected by various instruments. Prior to beam moving, to the next focus point, these instruments count the number of e^- interaction, which is displayed by a pixel on a cathode ray tube (CRT), whose pigment is determined by this number, the higher the number the brighter the shade. This process is repeated until the mesh scan is finished and then repeated, the entire pattern can be scanned 30 times/sec figure 4.54 shows SEM instrumentation used.

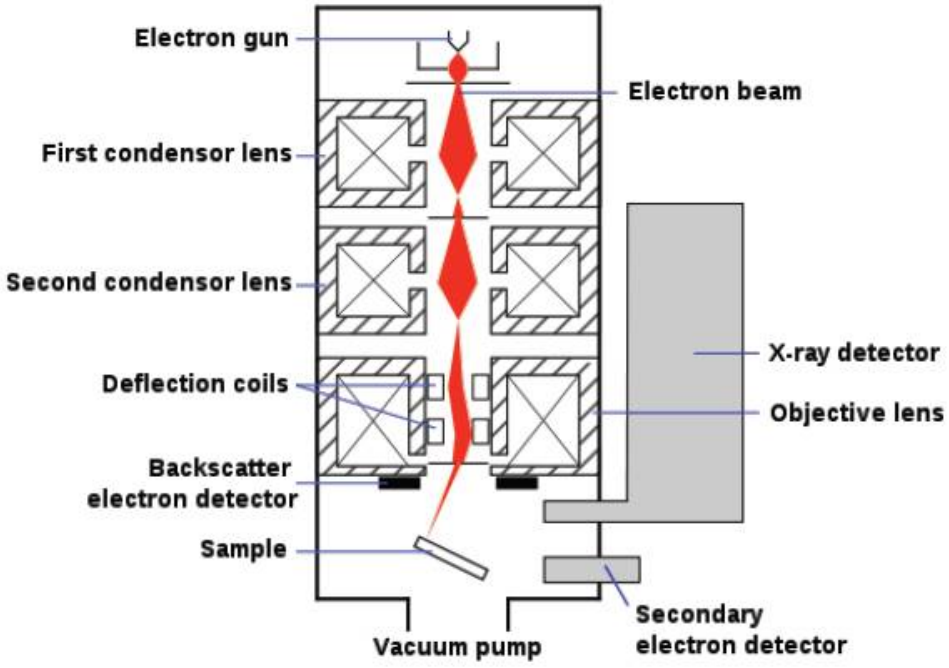

Figure 4.53. Schematic Scanning Electron Microscope Diagram

For conventional imaging in the SEM, specimens must be electrically conductive at least at the surface, and electrically grounded to prevent the accumulation of electrostatic charge at the surface. For nonconductive specimens as cement samples, are therefore coated with a thin layer of Au (gold), this is usually deposited on the sample by a low vacuum sputter coating evaporation figure 4.55, and carbon tapes are adhered at the specimens edges.

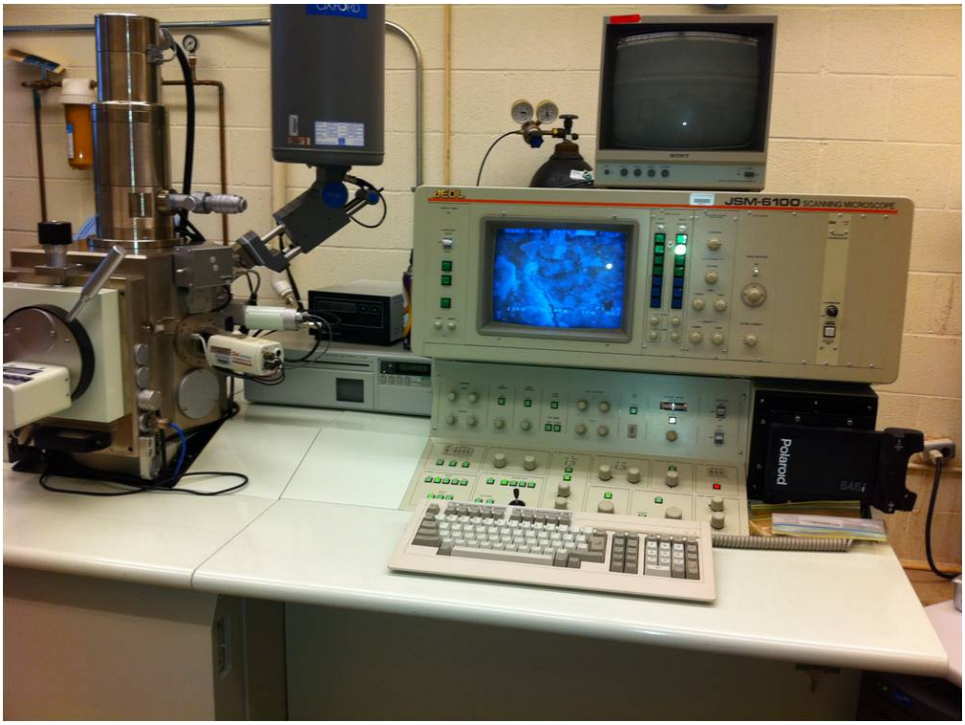

Figure 4.54. SEM Instrument Setup

Figure 4.55. Sputter Coating Setup for SEM sample Preparation

Results

The understanding of the phase composition of hydraulic cementitious nanocomposites should provide a new vision into early-age hydration characteristics, nano additives-cement interaction, in which will help in promoting the new materials generation. These measurements can be achieved by imposing the SEM imaging.

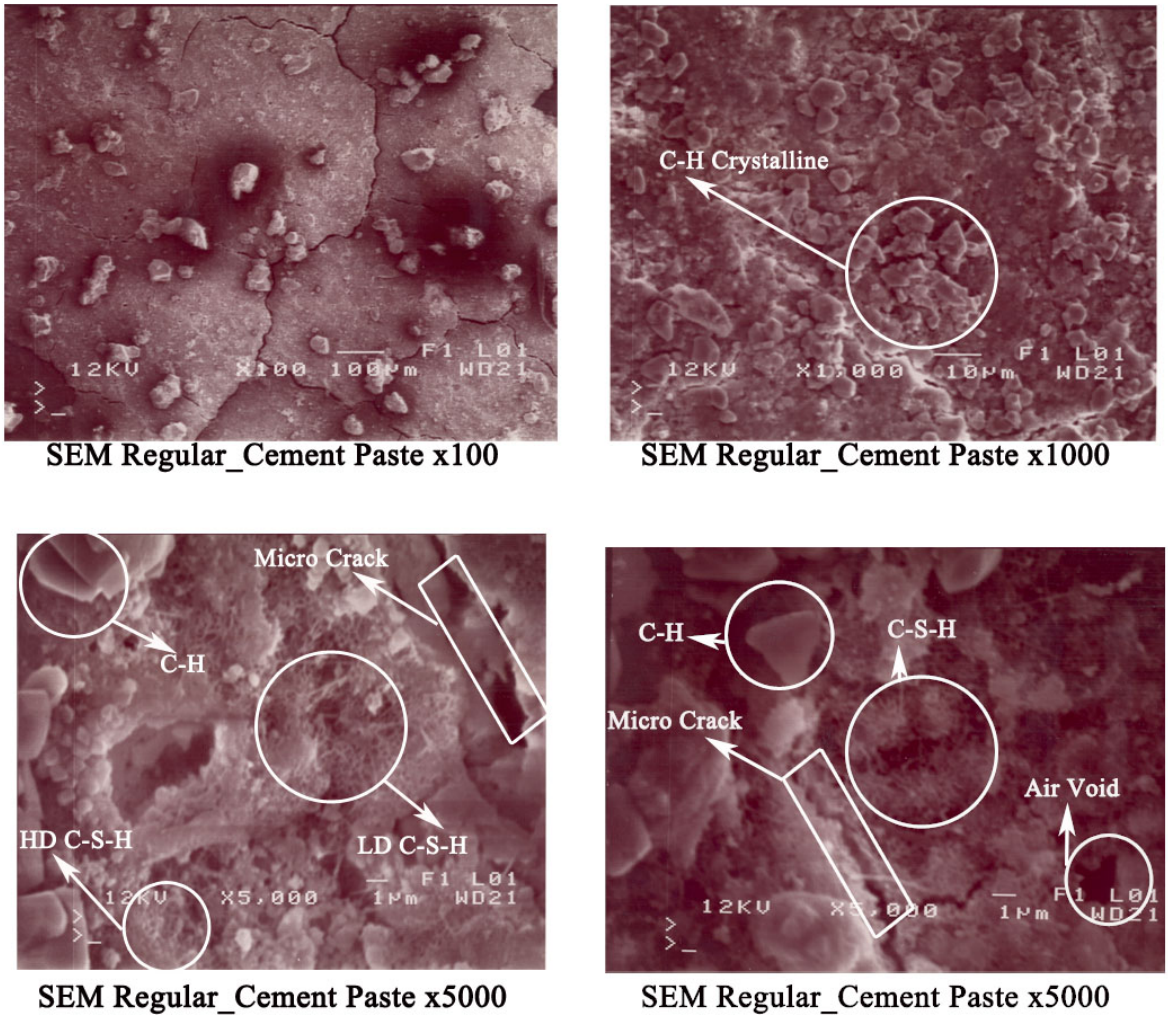

Figure 4.56. SEM for Portland Cement Type I/II

From figure 4.56, several magnification images are captured for the hydrated Portland cement. Figure 4.56(b) C-H is dominating, which is expected as referred to the clinker

hydration process at early stages.

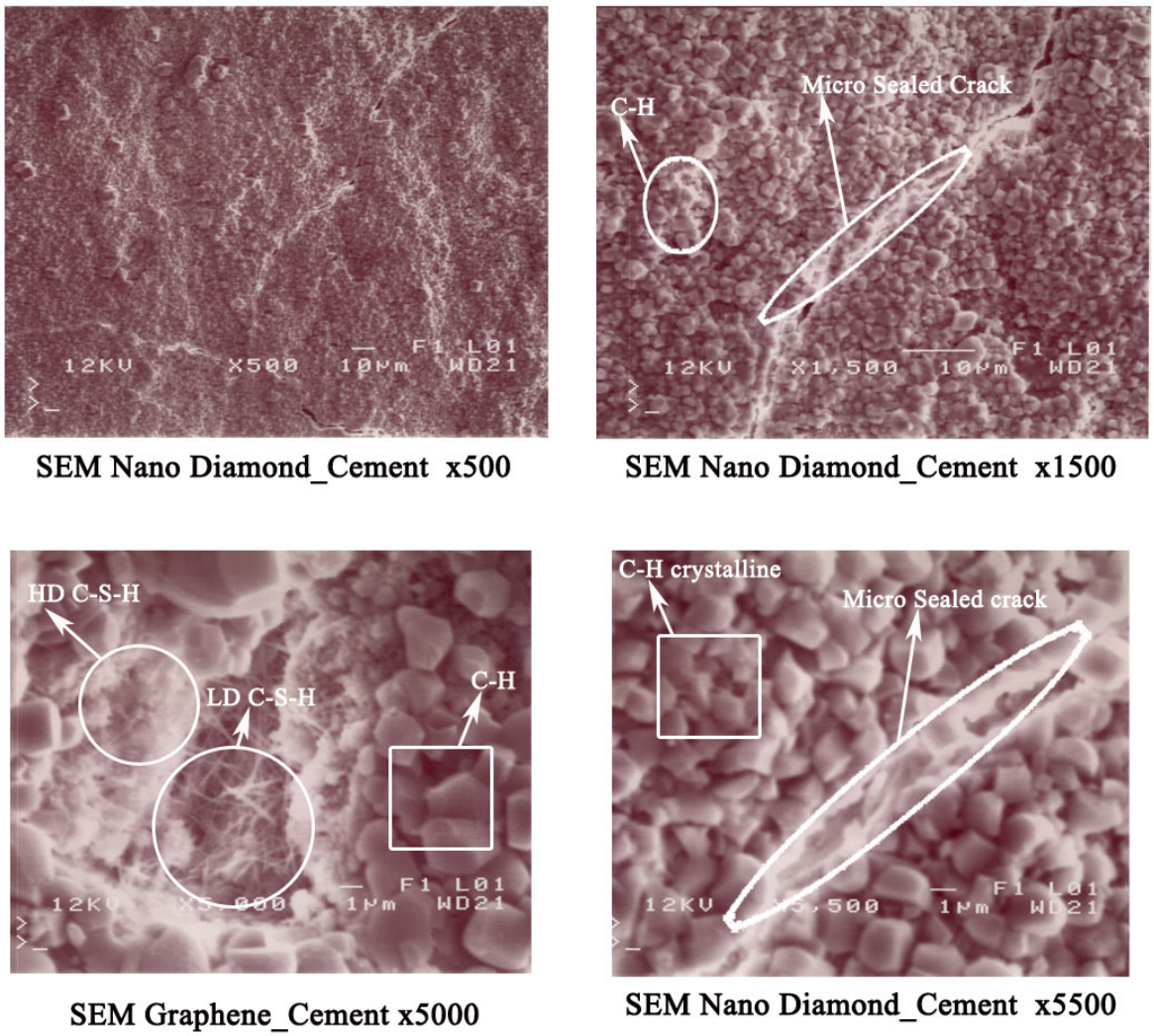

Figure 4.57. SEM for Portland Cement Type I/II Mixed With Nano Diamonds

From the SEM imaging figure 4.57 for gold sputtered cementitious specimens, it is confirmed that the nano additives favor the formation of small-sized crystals of portlandite ($Ca(OH)_2$), this result coincides with the chemical composition analysis.

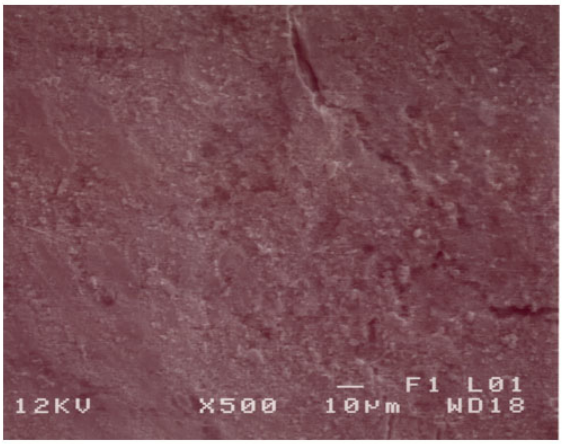

SEM Functionalized Graphene_Cement
x500

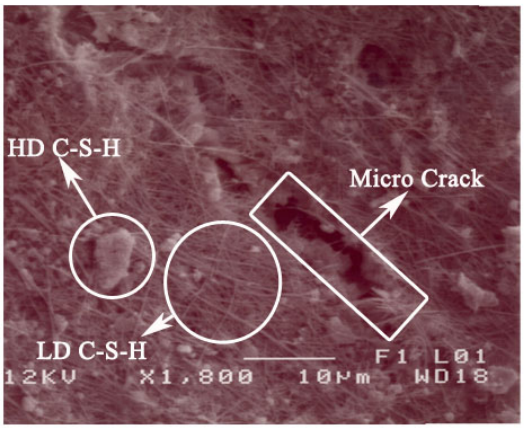

SEM Functionalized Graphene_Cement
x1800

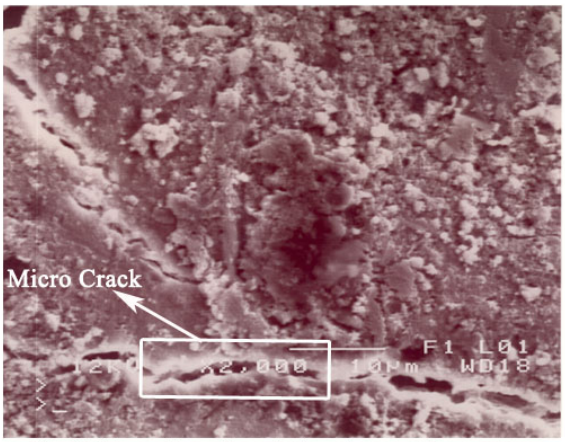

SEM Functionalized Graphene_Cement
x2000

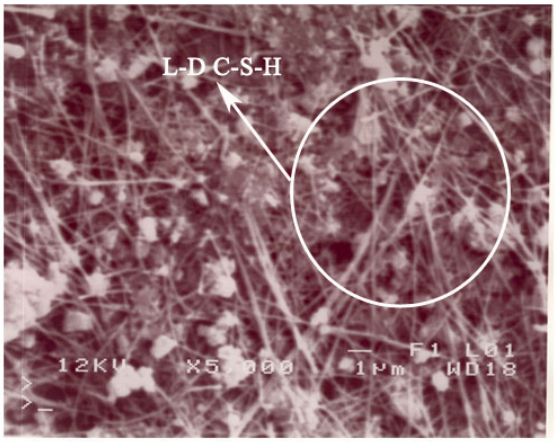

SEM Functionalized Graphene_Cement
x5000

Figure 4.58. SEM for Portland Cement Type I/II Mixed With Functionalized Graphene

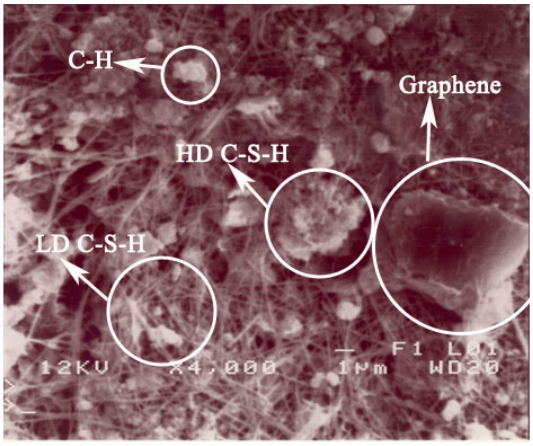

SEM Graphene_Cement x4000

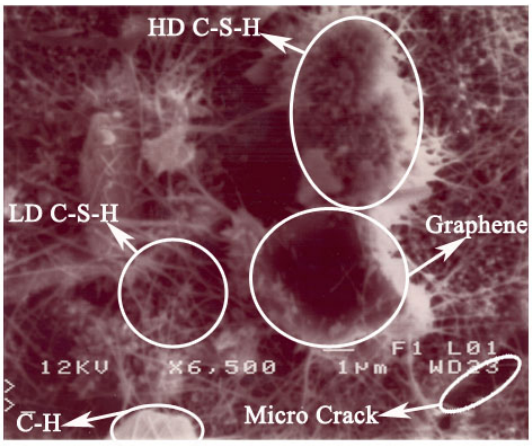

SEM Graphene_Cement x6500

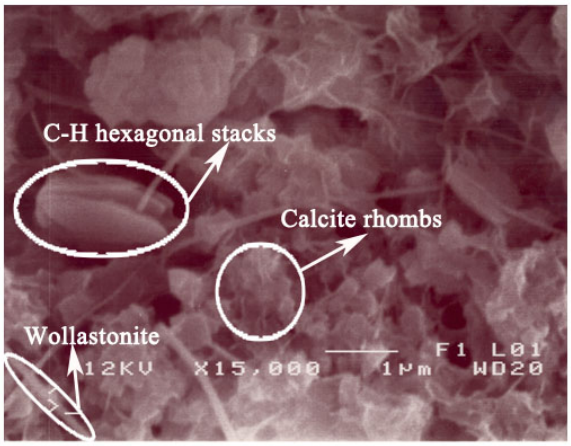

SEM Graphene_Cement x15000

Figure 4.59. SEM for Portland Cement Type I/II Mixed With Pristine Graphene

For the exfoliated graphene-cement samples, the SEM imaging has distinguished a graphene platelet in the presence of a HD C-S-H figure 4.59, which coexists with our MD interfacial strength simulations, in which it shows a high interfacial strength in the order of 1.00 GPa between the C-S-H and the exfoliated graphene platelet.

Some of the nano additives, such as the Nano Diamonds and the OctaTMA POSS, seem to exhibit healing properties. This is illustrated by the healed micro-cracks in some of the demonstrated SEM images see figure 4.57, 4.61.

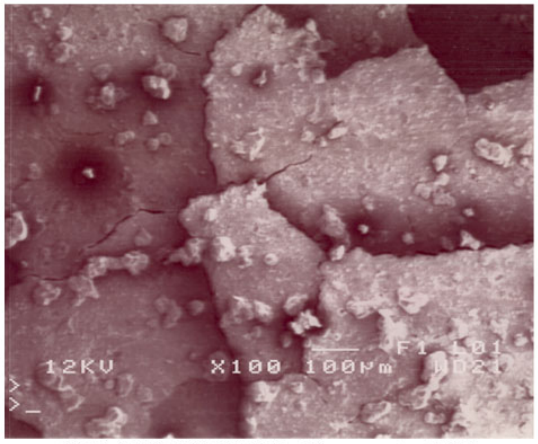

SEM PEG POSS_Cement x100

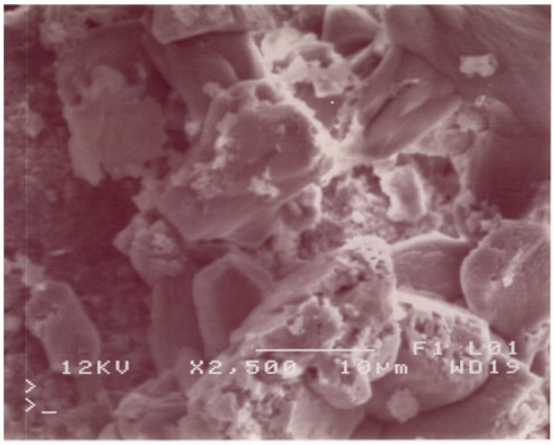

SEM PEG POSS_Cement x2500

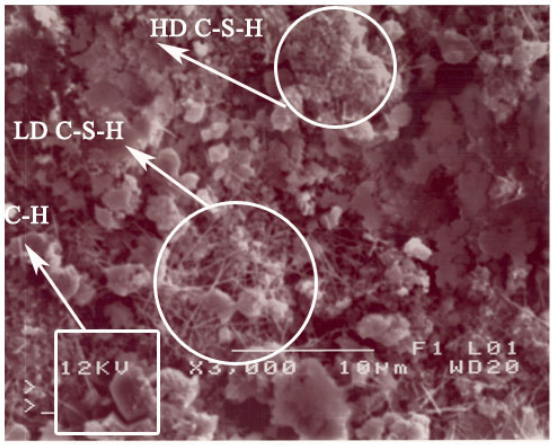

SEM PEG POSS_Cement x3000

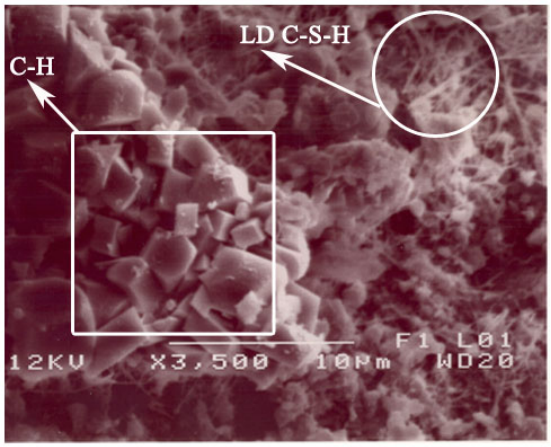

SEM PEG POSS_Cement x3500

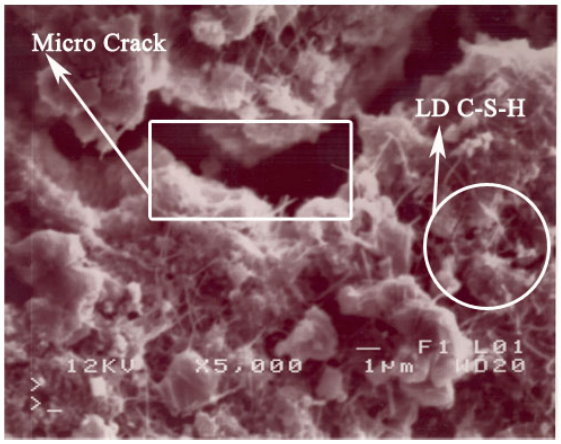

SEM PEG POSS_Cement x5000

Figure 4.60. SEM for Portland Cement Type I/II Mixed With PEG POSS

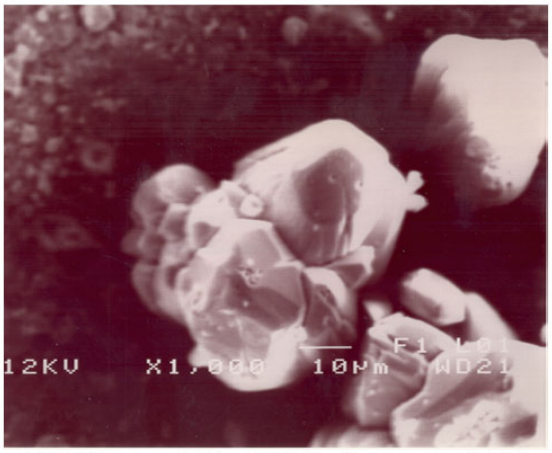

SEM OctaTMA POSS_Cement x1000

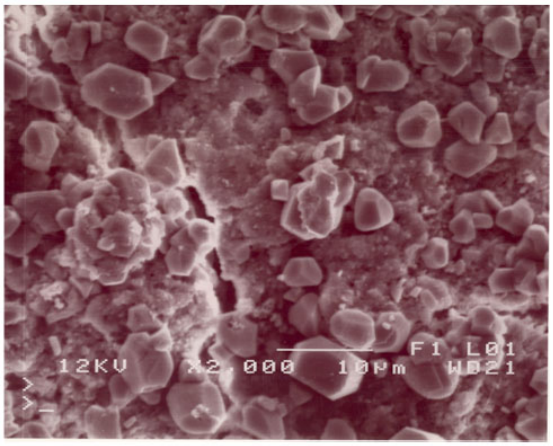

SEM OctaTMA POSS_Cement x2000

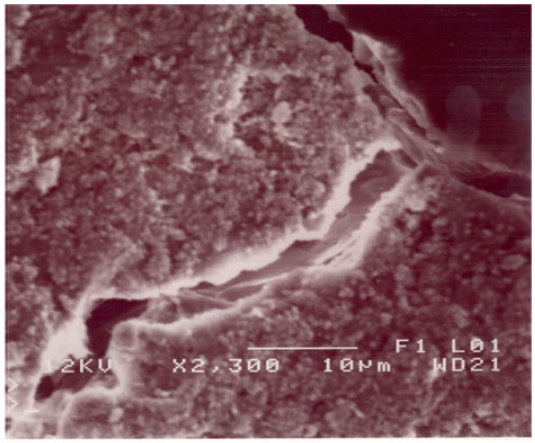

SEM OctaTMA POSS_Cement x2300

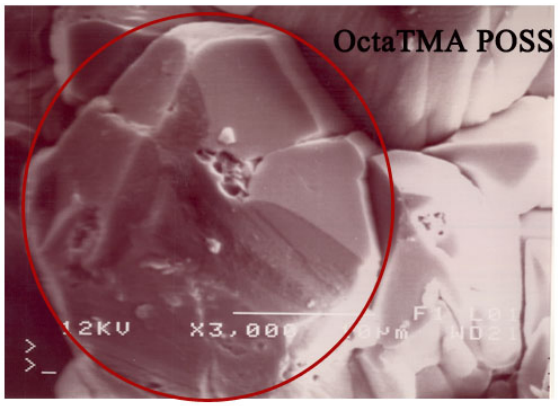

SEM OctaTMA POSS_Cement x3000

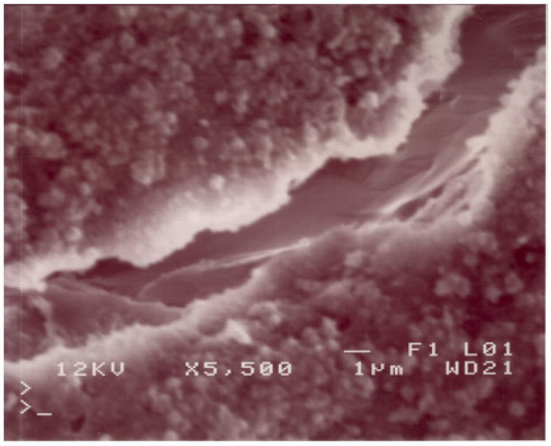

SEM OctaTMA POSS_Cement x5500

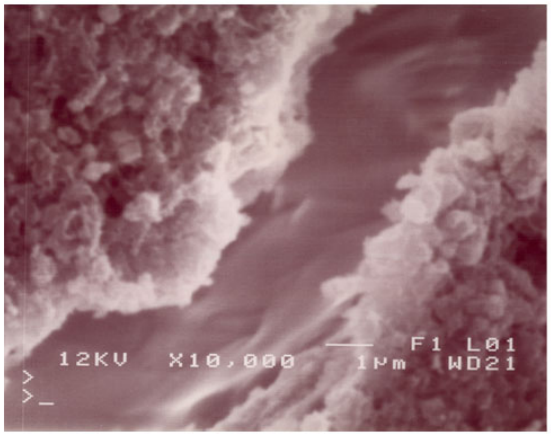

SEM OctaTMA POSS_Cement x10000

Figure 4.61. SEM for Portland Cement Type I/II Mixed With OctaTMA POSS

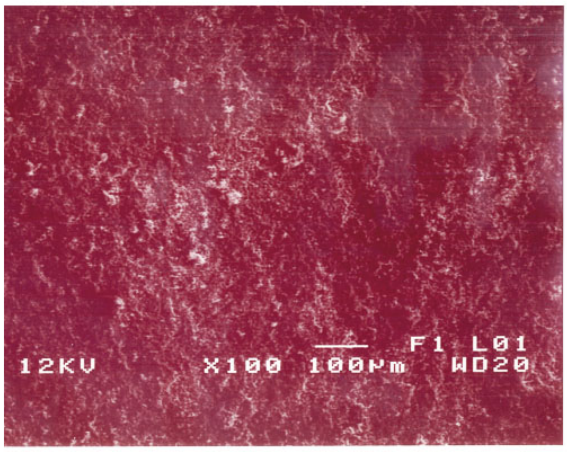

SEM Nano C_3S x100

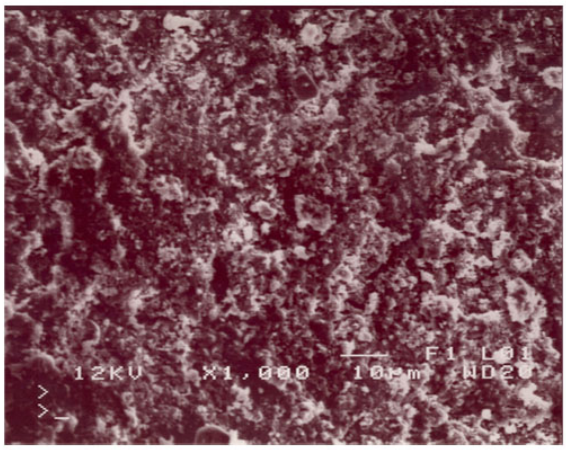

SEM Nano C_3S x1000

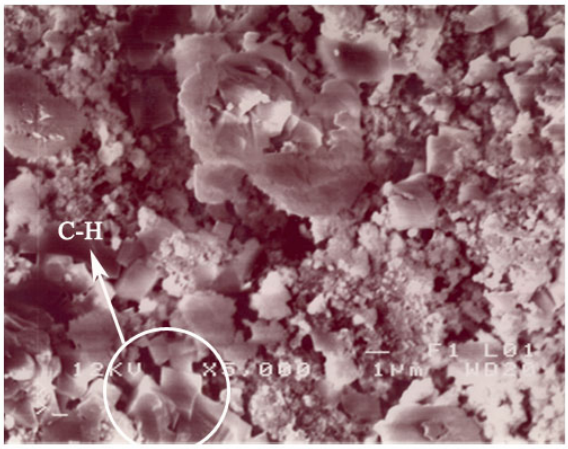

SEM Nano C_3S x5000

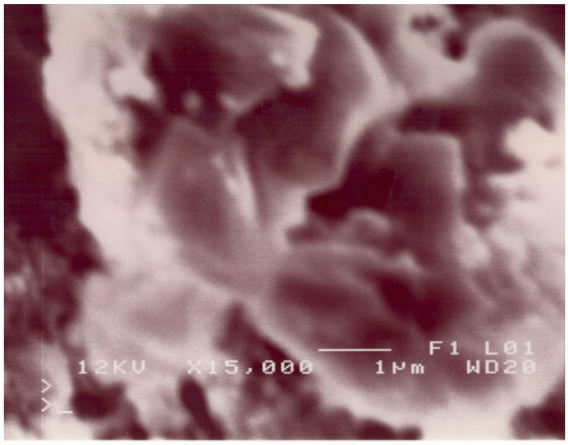

SEM Nano C_3S x15000

Figure 4.62. SEM for Nano C_3S with w/c =1.25

From figure 4.62, SEM imaging for the nano C_3S demonstrates a calcium carbonate domination. This implies the uncontrolled milling for the unhydrated nano C_3S samples. However, a small percentage of calcium hydroxide is traced in the hydrated C_3S samples, in comparison to the other cementitious nanocomposite samples.

4.4.4 Resonant Ultrasound Spectroscopy (RUS)

Literature Review

Several non destructive mechanical methods will be investigated to measure the elastic properties of nanocement constituents. A complete elastic tensor can be inferred from a single resonance ultrasonic spectroscopy (RUS) measurement for any crystalline or noncrystalline solid material. RUS in principle, measures for the natural frequencies of elastic vibration for a number of samples normal modes. It bridges between low-frequency stress-strain methods and ultrasonic time-delay methods. The resonant response of a specimen confides on the following: specimen shape, elastic constants, crystallographic orientation, density, and dissipation [106]. Various sample shapes can be prepared for RUS measurements. Crystalline material samples do not demand to be oriented with respect to their crystallographic axes. RUS samples may be small as a few hundred microns with masses less than 100 micrograms, or they may have dimensions several centimeters and masses of several kilograms [107].

Ultrasonic measurements may be considered as a type of elastic wave spectroscopy. The velocity and extinction of ultrasonic waves are usually measured. Elastic constants can be derived from velocity measurements. The elastic constants are the second derivatives of the free energy with respect to strain and are directly related to the atomic bonding of the material [106]. Furthermore, they are connected to the thermal properties of solids through Debye theory.

RUS will be adapted to estimate the hydrated nano cement and regular cement mixed with the selected nano additives elastic modulus and Poissons ratio with high precision and superb efficiency. A polished specimen, often in a regular parallepiped, is placed between two acoustic transducers. The first one drives the specimen with a sinusoidal stress; and the second one encounters the specimen response. As soon as the drive frequency couples the natural vibration frequency of the object, the surface displacement amplitudes increase by

a quality factor (Q) of the resonance. The measured spectrum is an arranged list of center frequencies, which are extracted from the collected resonance peaks of Lorentzian line shape [108].

The principle theory of RUS can be simply expressed as 4.4:

$$C_{ijkl}\frac{\partial^2 u_k}{\partial x_i \partial x_l} = \rho\frac{\partial^2 u_i}{\partial^2 t} \tag{4.4}$$

where C_{ijkl}:stiffness tensor, ρ:density of the specimen, and u:displacement. This expression is a result of the combination of; linearized Langrangian strain tensor, generalized Hook's law, and classic Newton's second law, this is listed in equations 4.5, 4.6, 4.7 below respectively:

$$e_{kl} = \frac{1}{2}(\frac{\partial u_k}{\partial x_i} + \frac{\partial u_l}{\partial x_k}) \tag{4.5}$$

$$\sigma_{ij} = C_{ijkl}e_{kl} \tag{4.6}$$

$$\frac{\partial \sigma_{ij}}{\partial x_i} = \rho\frac{\partial^2 u_i}{\partial^2 t} \tag{4.7}$$

where e_{kl}:strain tensor, σ_{ij}:stress tensor. Equation 4.7 can be recasted as net force due to spatial variation of the stress. However, solving equation 4.4 is not a straight forward calculation. Essentially, an estimated solution can be extracted from equation 4.4 to an eigenvalue problem [106]:

$$\Gamma a = (\rho\omega^2)Ea \tag{4.8}$$

where $\lambda = \rho\,\omega^2$: eigenvalues, ω: resonant frequencies, a:expansion coefficients, and Γ and E : are matrices in the expression of the Lagrangian for a three-dimensional (3D) solid body. In order to calculate the natural frequencies for a certain 3D solid body, it is essential to calculate Γ and find the eigenvalues from equation 4.8. However, for RUS, this is an invert

problem in which the elastic constants can be obtained from the natural frequencies for tested specimen [107].

Nevertheless, from stated above, calculating the elastic constants for a 3D solid body requires a forward calculation, in which, the spectrum frequencies are estimated from; the specimen dimensions, measured density, and an initial estimate for the elastic constants, this calculation is referred to as the "forward" problem. On the other hand, the "inverse" problem performs the calculations required to determine all the elastic constants from the measured spectrum and the known parameters of; density, specimen dimensions. After performing the forward calculation and estimating the natural frequencies, for tested specimen, an inverse measurement is conducted; where the calculated frequencies are compared to measured natural frequencies. Parameters are adjusted accordingly through each iteration until a good agreement is obtained between measured and estimated frequencies. The adjustable parameters include; initial frequency, final frequency, time step, and voltage amplitude see figure 4.63.

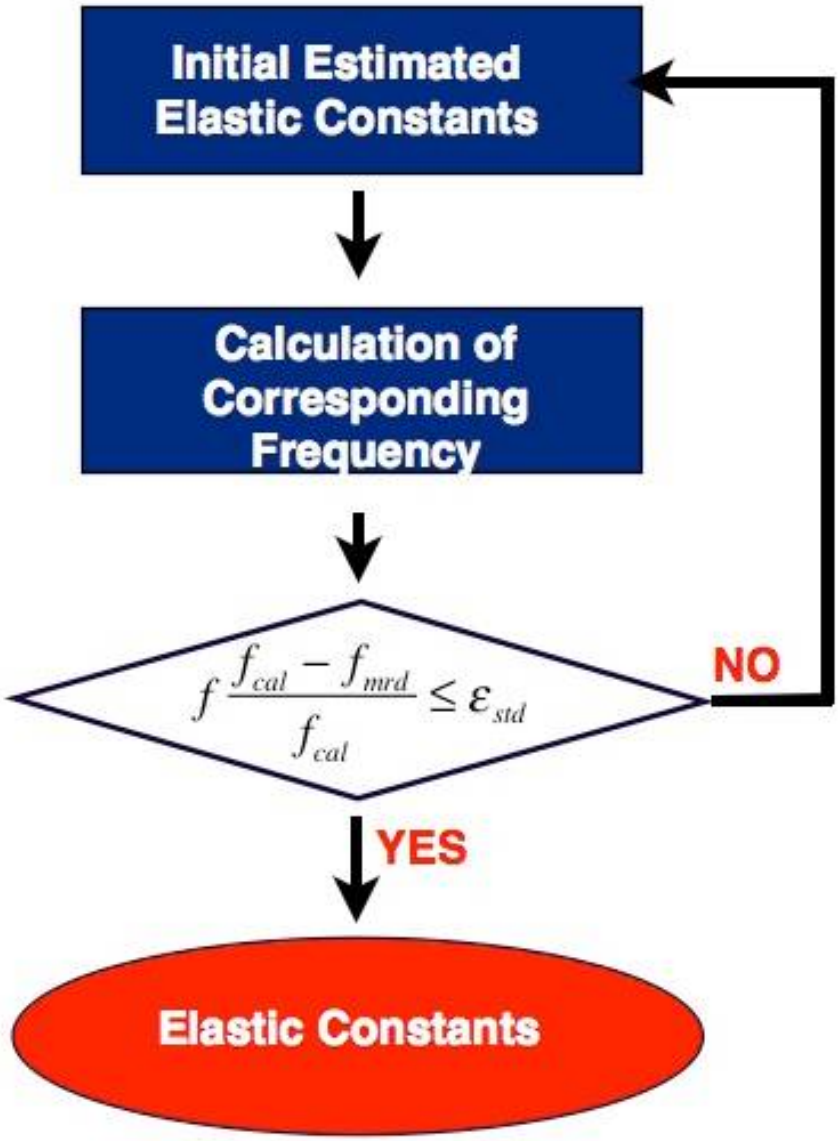

Figure 4.63. Forward and Inverse Calculation Setup for RUS testing

Experimental Setup

The tested samples are prepared as shown in section 4.2.2. All samples are cut and polished in parallel piped shapes, exact density and dimensions are presented in table 4.5. Samples are nicely cut using a diamond saw, and polished; to eliminate the shape distortions effect on measurements specially skewing, and unparalleled surfaces. However, other concerns in sample preparation are homogeneity and isotropy of the tested samples.

During the test, the samples are supported gently by transducers 4.65 at diametrically opposite corners, to ensure capturing the different modes. The sample is excited by one transducer with a driving voltage of 5 Volts, while the other transducer collects the resonance response 4.64. An average of 5 measurements is recorded. Frequency sweep; initial 0.050 MHz, and a final of .20 MHz.

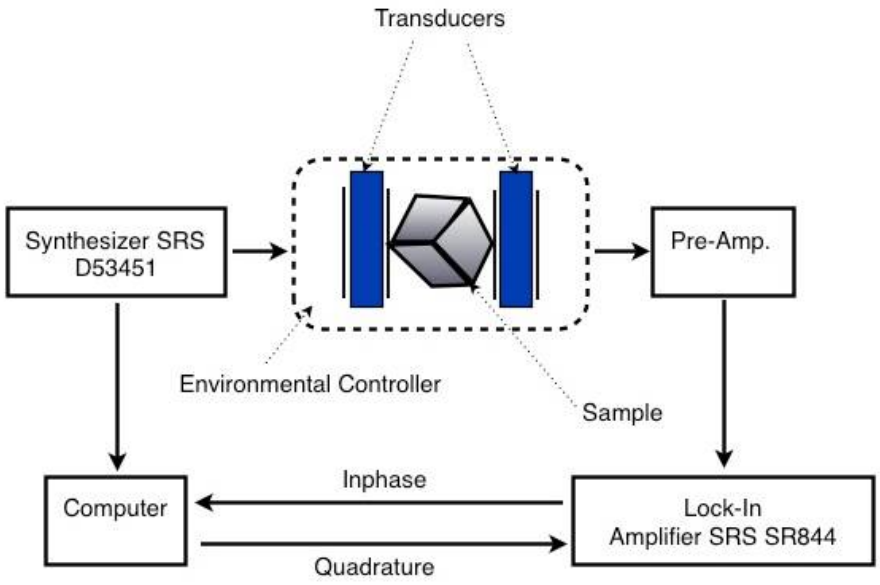

Figure 4.64. Schematic RUS Experiment Setup

Figures 4.70 -4.71 shows the measured spectrum for the tested samples accordingly.

Figure 4.65. Room Temperature RUS Experiment Setup

Table 4.5. RUS Specimens: Density and Dimensions

Material	Mass (gm)	x (cm)	y (cm)	z (cm)	ρ (gm/cm^3)
Portland Cement	6.62	1.27	1.73	1.73	1.63
Nano Diamond-Cement	6.62	1.27	1.73	1.73	1.63
Functionalized Graphene-Cement	0.98	.83	.80	0.86	1.72
Pristine Graphene-Cement	1.52	.93	1.02	.92	1.73
PEG POSS-Cement	1.56	1.23	.84	.82	1.85
OctaTMA POSS-Cement	6.62	1.27	1.73	1.73	1.63

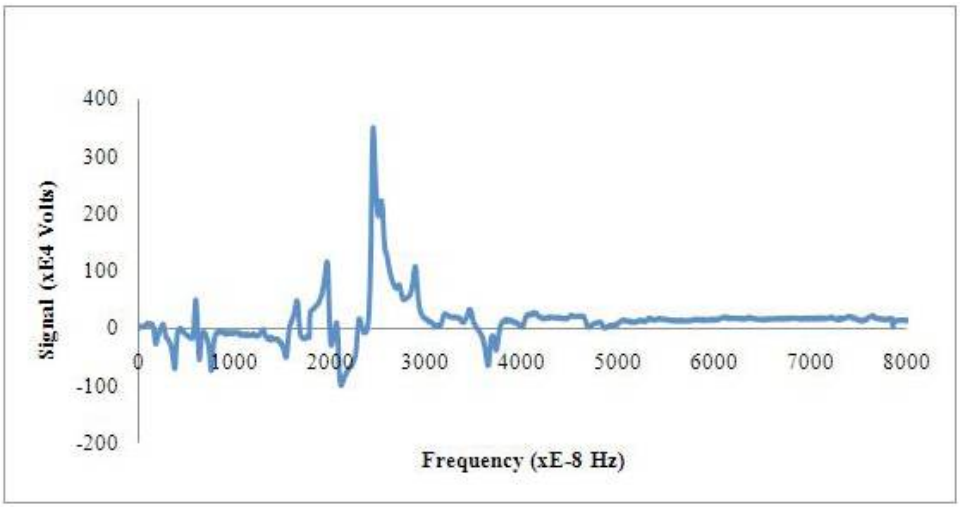

Figure 4.66. The Spectrum for a Parallelepiped Shape Portland Cement Paste Sample

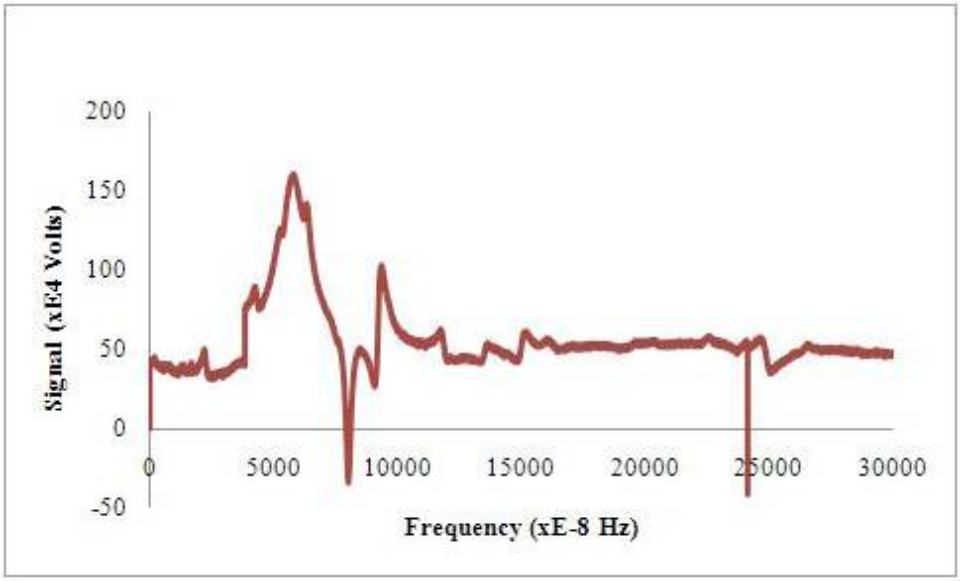

Figure 4.67. The Spectrum for a Parallelepiped Shape Nano Diamond-Cement Paste Sample

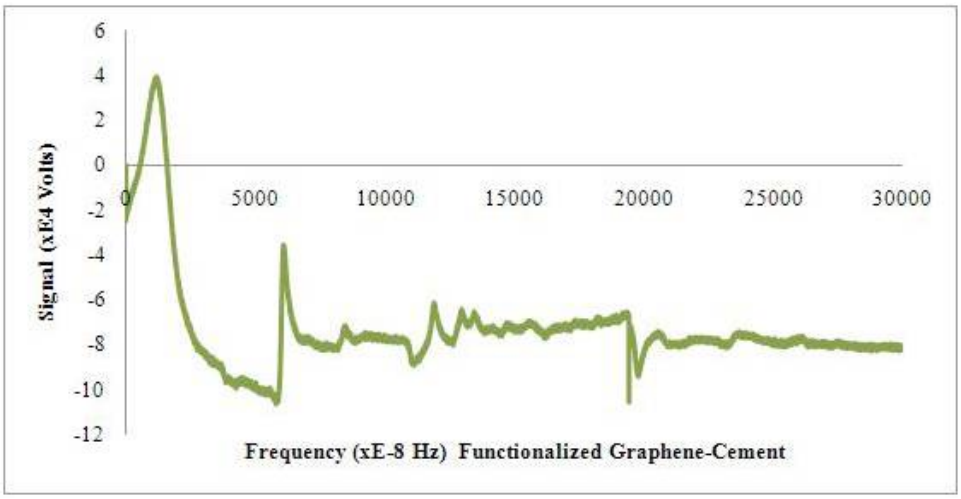

Figure 4.68. The Spectrum for a Parallelepiped Shape Functionalized Graphene-Cement Paste Sample

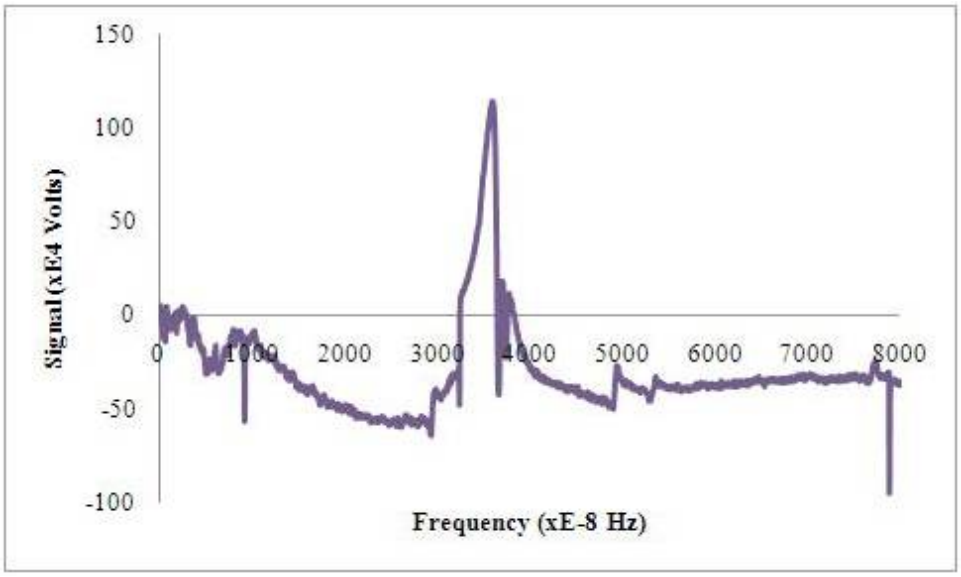

Figure 4.69. The Spectrum for a Parallelepiped Shape Graphene-Cement Paste Sample

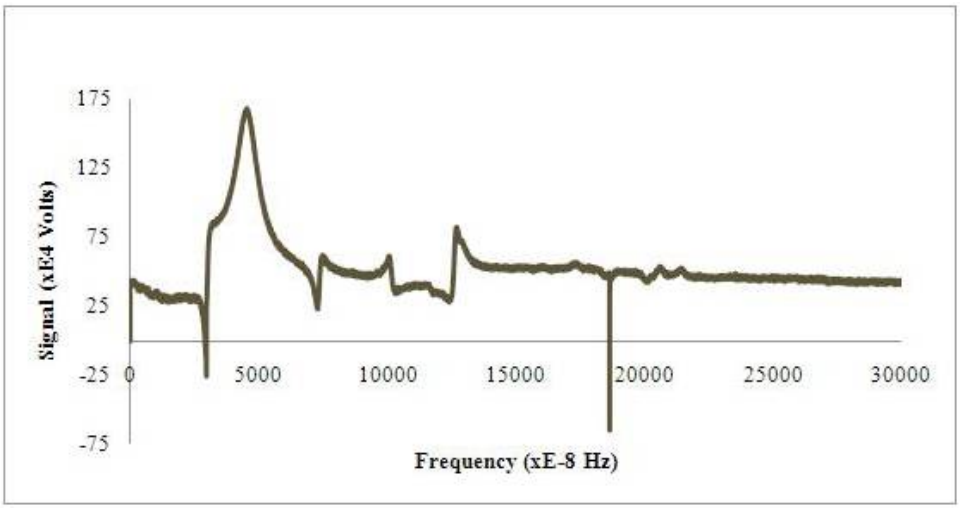

Figure 4.70. The Spectrum for a Parallelepiped Shape PEG POSS-Cement Paste Sample

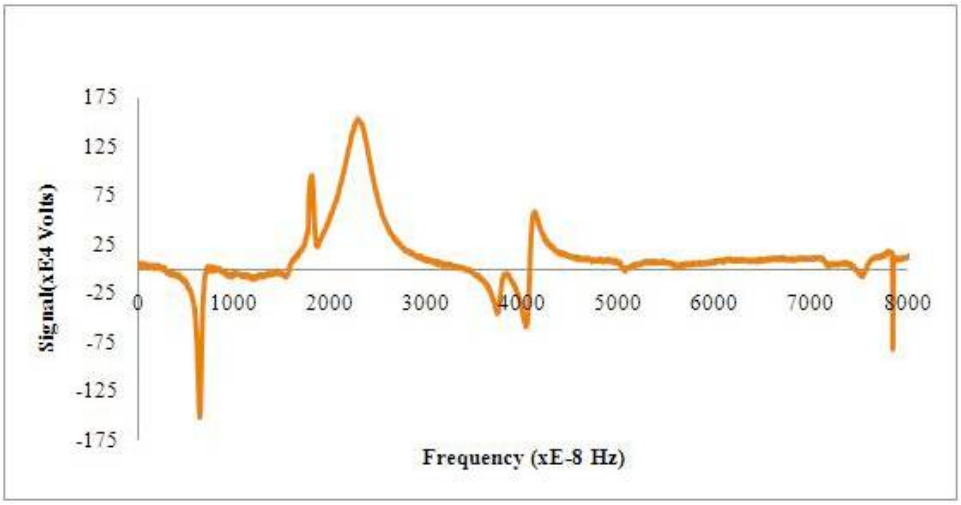

Figure 4.71. The Spectrum for a Parallelepiped Shape OctaTMA POSS-Cement Paste Sample

Results

The resonance frequencies are determined by fitting the resonance peaks to the Lorentzian functions. The measured peaks and the last set of calculated peaks after few iterations are listed in tables 4.6-4.11. For an isotropic material, two elastic constants are required to calculate the independent elastic constants. The average error % magnitudes of included peaks are listed under each table respectively. Nevertheless, the average errors recorded for both the Nano Diamond_Cement and the PEG POSS_Cement composites are higher than the % average error for the rest of the tested samples. This could be as a result of; the inhomogeneity of the mixed samples, or that the material's resonance measurements are highly sensitive to the asymmetry in the polished samples, or could be due to their anisotropic properties. Further investigation is required to conclude on these results.

Table 4.6. The Fitting of The Measured resonances and Calculated Resonances for Portland Cement

Peak	Measured Frequency (MHz)	Calculated Frequency (MHz)	Error %	Included*/ Excluded**
1	0.059878	0.046427	28.972	EXC
2	0.064525	0.064496	0.044	INC
3	0.067463	0.06847	-1.471	INC
4	0.072796	0.070844	2.756	EXC
5	0.074267	0.074822	-0.741	INC
6	0.076153	0.075767	0.509	INC
7	0.079578	0.080016	-0.548	INC
8	0.080243	0.080159	0.105	INC
9	0	0.081638	0	–
10	0.082327	0.081849	0.584	INC
11	0	0.088001	0	–
12	0	0.088635	0	–
13	0.091056	0.088886	2.442	EXC
14	0.095056	0.094381	0.715	INC
15	0.103754	0.105838	-1.969	EXC
16	0.107158	0.106734	0.397	INC
17	0.109522	0.109613	-0.083	INC
18	0	0.109872	0	–
19	0.111044	0.111267	-0.2	INC
20	0	0.11369	0	–
21	0	0.113793	0	–
22	0.114026	0.114359	-0.291	INC
23	0	0.114502	0	–
24	0.116848	0.116891	-0.037	INC
25	0.121271	0.120741	0.439	INC
26	0	0.122743	0	–
27	0.124637	0.124739	-0.082	INC
28	0	0.124846	0	–
29	0.126095	0.126204	-0.086	INC
Average error magnitude of included peaks=0.396%				

Table 4.7. The Fitting of The Measured resonances and Calculated Resonances for Nano Diamond_Cement

Peak	Measured Frequency (MHz)	Calculated Frequency (MHz)	Error %	Included*/ Excluded**
1	0.10593	0.101887	3.968	EXC
2	0.110738	0.106984	3.509	INC
3	0.119004	0.136748	-12.976	EXC
4	0.124817	0.138941	-10.166	EXC
5	0.137539	0.141133	-2.546	INC
6	0.139781	0.141799	-1.423	INC
7	0	0.142847	0	–
8	0.145674	0.144202	1.021	INC
9	0.152917	0.154608	-1.093	INC
10	0.157879	0.158542	-0.418	INC
11	0	0.16039	0	–
12	0	0.16053	0	–
13	0	0.162452	0	–
14	0	0.164377	0	–
15	0	0.167976	0	–
16	0.171731	0.169984	1.028	INC
17	0.174498	0.172877	0.937	INC
18	0.179422	0.185405	-3.227	INC
19	0.189445	0.187411	1.085	INC
20	0.195355	0.197988	-1.33	INC
21	0.200839	0.199629	0.606	INC
22	0	0.201165	0	–
23	0	0.202272	0	–
24	0	0.202801	0	–
25	0	0.203113	0	–
26	0.209063	0.204808	2.078	INC
27	0.219072	0.217395	0.772	INC
28	0.22036	0.223505	-1.407	INC
29	0	0.223983	0	–
30	0.227504	0.225538	0.872	INC
31	0	0.232983	0	–
32	0	0.234443	0	–
Average error magnitude of included peaks=1.46%				

Table 4.8. The Fitting of The Measured resonances and Calculated Resonances for Functionalized Graphene_Cement

Peak	Measured Frequency (MHz)	Calculated Frequency (MHz)	Error %	Included*/ Excluded**
1	0.119141	0.121971	-2.321	EXC
2	0.130174	0.131218	-0.796	INC
3	0.16463	0.164634	-0.002	INC
4	0.167331	0.167698	-0.219	INC
5	0.17107	0.170445	0.367	INC
6	0.173113	0.173064	0.028	INC
7	0	0.174116	0	–
8	0.17772	0.175981	0.988	INC
9	0.190872	0.1914	-0.276	INC
10	0	0.193102	0	–
11	0	0.196822	0	–
12	0.198765	0.197837	0.469	INC
13	0	0.200434	0	–
14	0	0.202056	0	–
15	0.203858	0.204651	-0.388	INC
16	0	0.20895	0	–
17	0.21701	0.213631	1.582	EXC
18	0.230799	0.23078	0.008	INC
19	0	0.23429	0	–
20	0.237073	0.237688	-0.259	INC
21	0	0.243096	0	–
22	0	0.24475	0	–
23	0	0.247274	0	–
Average error magnitude of included peaks=0.345%				

Table 4.9. The Fitting of Measured resonances and Calculated Resonances for Graphene_Cement

Peak	Measured Frequency (MHz)	Calculated Frequency (MHz)	Error %	Included*/ Excluded**
1	0.092145	0.096659	-4.67	EXC
2	0.109278	0.109171	0.098	INC
3	0	0.130542	0	–
4	0.13426	0.130977	2.507	EXC
5	0.136342	0.138243	-1.375	INC
6	0.141972	0.138774	2.305	EXC
7	0.143466	0.144916	-1	INC
8	0.145025	0.144938	0.06	INC
9	0.15374	0.15441	-0.434	INC
10	0	0.154998	0	–
11	0	0.156473	0	–
12	0	0.159736	0	–
13	0	0.162198	0	–
14	0	0.164789	0	–
15	0.167468	0.165168	1.393	INC
16	0	0.171077	0	–
17	0.172257	0.172084	0.101	INC
18	0.183268	0.183337	-0.038	INC
19	0	0.188242	0	–
20	0	0.188457	0	–
21	0.193765	0.196909	-1.597	EXC
22	0.199402	0.200035	-0.316	INC
23	0	0.200234	0	–
24	0.202825	0.201429	0.693	INC
25	0	0.203086	0	–
Average error magnitude of included peaks=0.551%				

Table 4.10. The Fitting of The Measured resonances and Calculated Resonances for PEG POSS_Cement

Peak	Measured Frequency (MHz)	Calculated Frequency (MHz)	Error %	Included*/ Excluded**
1	0.098732	0.094512	4.465	EXC
2	0.126138	0.128931	-2.166	INC
3	0.14384	0.145501	-1.142	INC
4	0.1535	0.152269	0.809	INC
5	0.159436	0.156503	1.874	INC
6	0.161021	0.165574	-2.75	INC
7	0	0.175826	0	–
8	0.17801	0.177267	0.419	INC
9	0	0.179738	0	–
10	0.182174	0.181675	0.275	INC
11	0.189402	0.18981	-0.215	INC
12	0.19677	0.200073	-1.651	INC
13	0.205945	0.202694	1.604	INC
14	0.209742	0.206064	1.785	INC
15	0.240864	0.246401	-2.247	INC
16	0.244906	0.247318	-0.975	INC
17	0.250843	0.247697	1.27	INC
18	0	0.254536	0	–
19	0	0.257947	0	–
20	0	0.261019	0	–
21	0.270667	0.267606	1.144	INC
22	0	0.274974	0	–
23	0	0.278711	0	–
24	0	0.279692	0	–
25	0	0.282769	0	–
26	0	0.283001	0	–
27	0.288213	0.288877	-0.23	INC
28	0.29572	0.29449	0.418	INC
29	0	0.296383	0	–
30	0	0.296558	0	–
Average error magnitude of included peaks=1.23%				

Table 4.11. The Fitting of The Measured resonances and Calculated Resonances for OctaTMA POSS_Cement

Peak	Measured Frequency (MHz)	Calculated Frequency (MHz)	Error %	Included*/ Excluded**
1	0.080622	0.080587	0.044	INC
2	0.099715	0.100718	-0.995	INC
3	0	0.101741	0	–
4	0.131058	0.131652	-0.451	INC
5	0	0.134029	0	–
6	0.136066	0.134258	1.347	EXC
7	0.136967	0.136162	0.592	INC
8	0.152793	0.152838	-0.029	INC
9	0.15748	0.159923	-1.527	EXC
10	0.161833	0.164534	-1.642	EXC
11	0.167587	0.167989	-0.239	INC
12	0	0.168284	0	–
13	0.169857	0.170248	-0.23	INC
14	0.176193	0.174776	0.811	INC
15	0	0.181162	0	–
16	0	0.185491	0	–
17	0.18574	0.186327	-0.315	INC
18	0.193568	0.193345	0.115	INC
19	0	0.194471	0	–
20	0.200746	0.200301	0.222	INC
21	0	0.203729	0	–
22	0.204437	0.205276	-0.409	INC
23	0	0.206057	0	–
24	0.207795	0.208941	-0.548	INC
25	0	0.211016	0	–
26	0.212898	0.212299	0.282	INC
27	0	0.214457	0	–
28	0	0.214477	0	–
29	0	0.218752	0	–
30	0	0.226593	0	–
31	0.230789	0.229165	0.709	INC
32	0	0.234409	0	–
33	0	0.240196	0	–
34	0.246403	0.247012	-0.247	INC
Average error magnitude of included peaks=0.39%				

It has been affirmed that the mechanical properties of the cementitious nanocomposites can be measured through a non-destructive technique with a high precision, calculated mechanical properties are shown in table 4.12. Although, the percentage of nano additives is relatively small 0.5%, the results read an enhancement in the mechanical properties of higher percentages. Young's and shear elastic constants, obtained from the RUS testing for the Portland cement specimen, are in a good agreement with reported literature values at early ages. This technique is highly recommended, and it has proven the possibility of obtaining the mechanical properties of the hydrated cement products at different time schemes, and different environmentally controlled conditions.

Table 4.12. Mechanical Properties of Cementitious Nanocomposites: RUS Testing

Material	Young's Modulus (GPa)	Shear Modulus (GPa)
Portland Cement	18.53	6.71
Nano Diamond-Cement	20.95	8.72
Functionalized Graphene-Cement	22.8	9.17
Pristine Graphene-Cement	19.72	8.12
PEG POSS-Cement	21.31	8.73
OctaTMA POSS-Cement	22.35	9.72

4.4.5 Electrochemical Impedance Spectroscopy (EIS)

Introduction

The impedance methods, rely on electronic AC circuit analysis, in which both instrumentation and data analysis techniques being analogous. The primary accession of EIS is applying a spectrum of low amplitude sinusoidal voltage excitations to examine the system of interest and to measure the system's response. Impedance methods do not require a complicated sample preparation and a complex experiment setup. See figure 4.72, it demonstrates the experimental setup while testing a cement specimen.

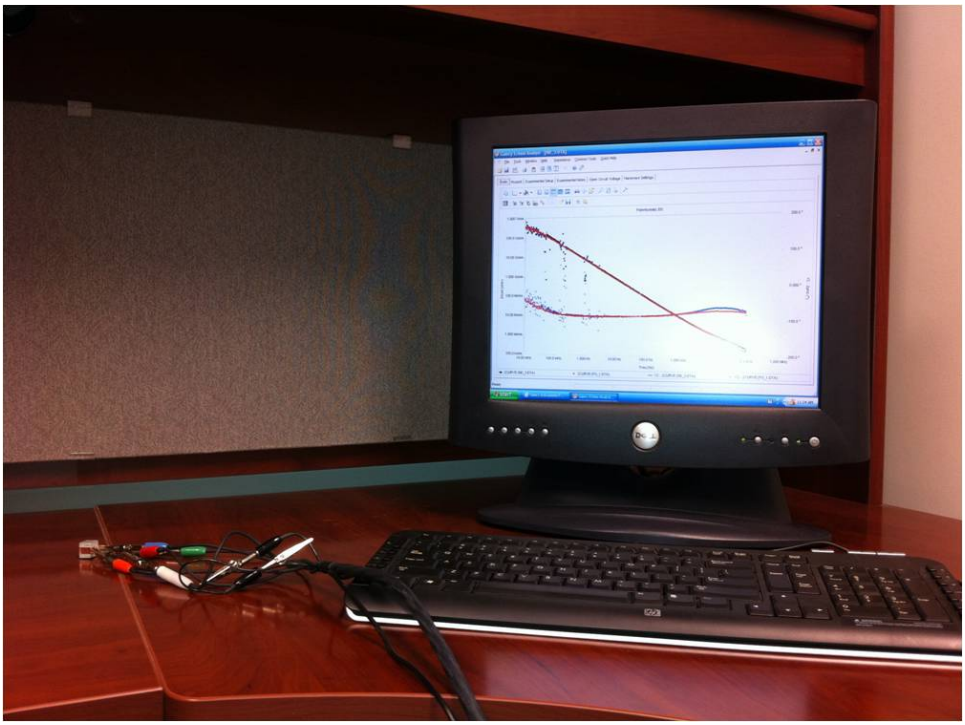

Figure 4.72. EIS Experimental Setup: Instrument Connection

One of the most attractive aspects of EIS as a tool for investigating the properties of materials and their environments is the direct connection that exists between the electrical

behavior of an existing system and a model circuit consisting of, discrete electrical components, resistors, capacitors, and inductor. However, the idealized circuit can represent the experimental impedance data. A resistance represents a conductive path and might count for the bulk conductivity of the specimen. Capacitances and inductances are affiliated to space charge polarization.

Electrical impedance extends the concepts of resistance to AC circuits, characterizing the relative amplitudes of the voltage, the current, and the relative phases. Impedance magnitude is usually represented by Z and can be defined in several equation forms. For this purpose of this analysis, equation 4.9 has been chosen to define the electrical impedance.

$$Z = Z_0 e^{j\phi} = Z_0 \cos(\phi) + iZ_0 \sin(\phi) \tag{4.9}$$

where Z_0: impedance magnitude, $Z_0 \cos(\phi)$ resistive behavior, $iZ_0 \sin(\phi)$: capacitance behavior, ϕ: phase difference between the voltage and the current, it is zero for purely resistive behavior.

Impedance can be represented in several ways; nyquist plots where the imaginary part is plotted on the Y axis and the real part is plotted on the X axis (figure4.73), it could be also depicted as an amplitude-phase versus frequency plot ($Y_1 : amplitude, Y_2 : phase, X : frequency$) (figure 4.74), could be described by an equivalent-circuit model (figure 4.75), and could be represented by calculating the electrical relative permittivity, see equation 4.10.

$$C = \frac{\epsilon \epsilon_0 A}{d} \tag{4.10}$$

where C: capacitance, ϵ: relative permittivity (F/m) , ϵ_0: is the vacuum permittivity ($8.85 * 10^{?12}$ F/m), A: area (m^2), d: distance m.

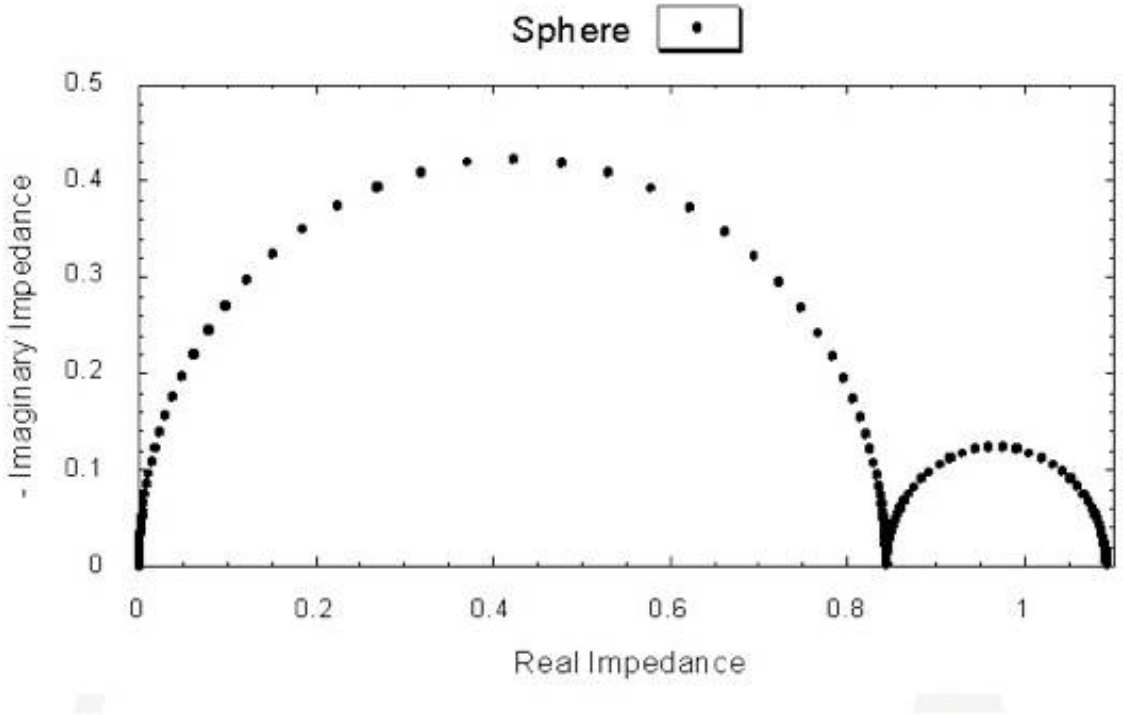

Figure 4.73. EIS Representation: Nyquist Plot

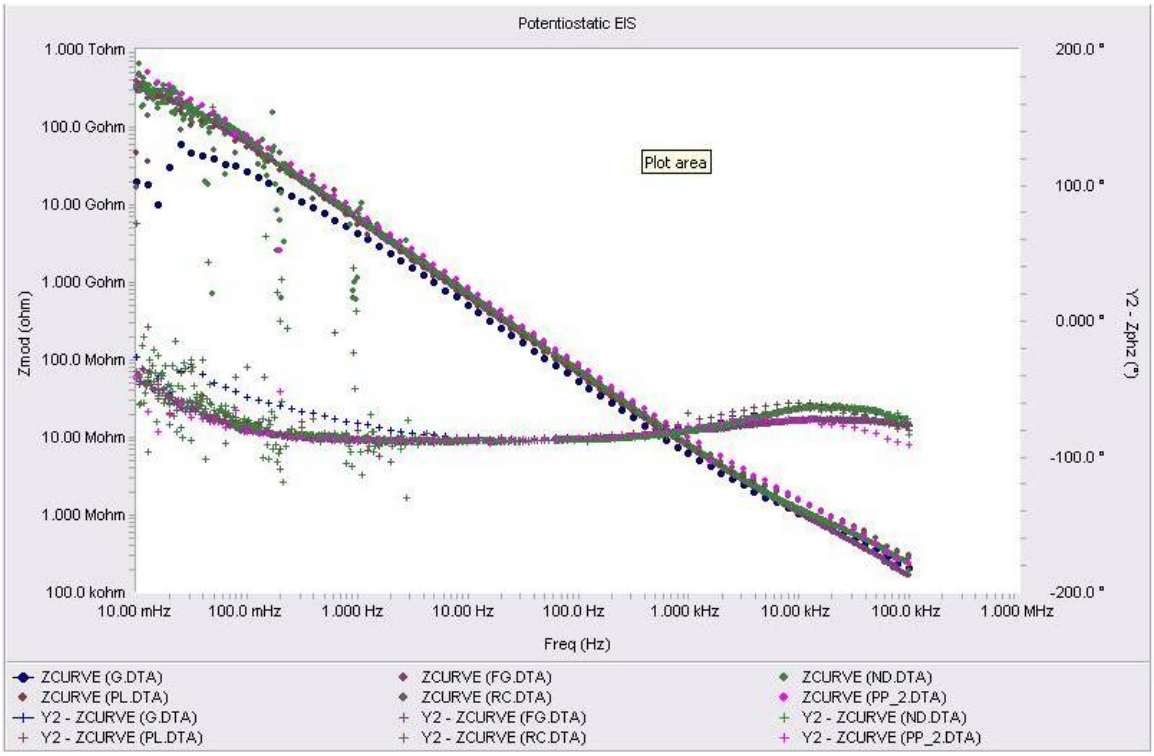

Figure 4.74. EIS Representation: Amplitude-Phase

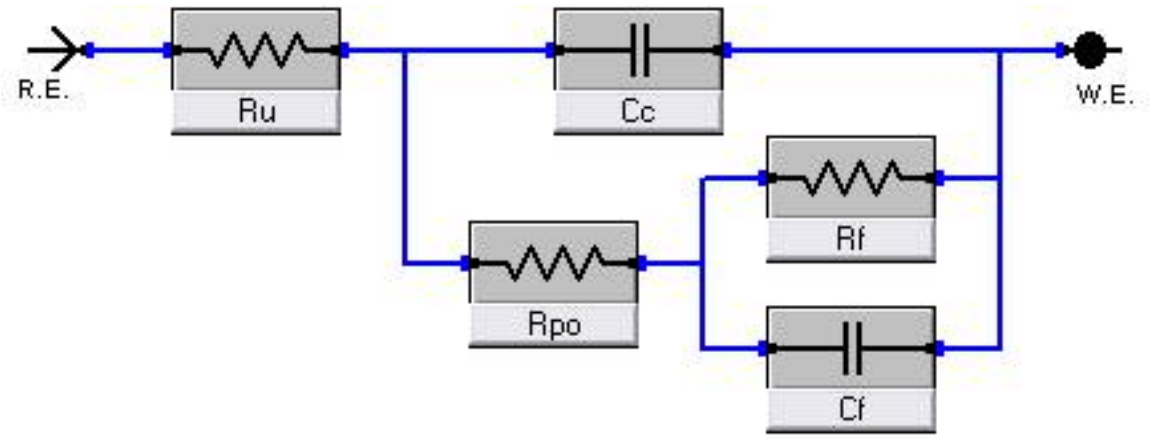

Figure 4.75. EIS Representation: Equivalent Circuit Model

The main objective of this study, is to optimize the electrical conductivity for use in solid state electrochemical devices and sensors. The microstructural structures of the cementitious nanocomposite models can describe the grains, and the grain boundaries of different phase composition, nano additives dispersion, and porosity.

Experimental Setup

Electrochemical properties of hydrated cement specimen composition at different moisture conditions have been investigated. The relative permittivity values are measured for the hydrated cement at room temperature. The dry samples tested are prepared according to section 4.2.2, for moist conditions the specimens are soaked in water for 24 hours thence tested figure 4.76. In the work presented, the frequency range considered is from 10 KHz to 1000 KHz for the relative permittivity measurements.

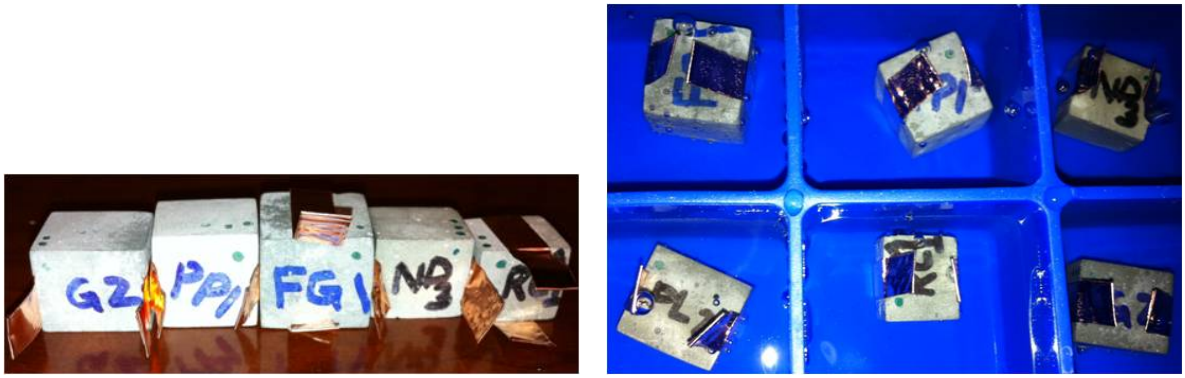

Figure 4.76. Cement Samples Preparation for EIS Testing: (a)Dry Specimens (b)Wet Specimens

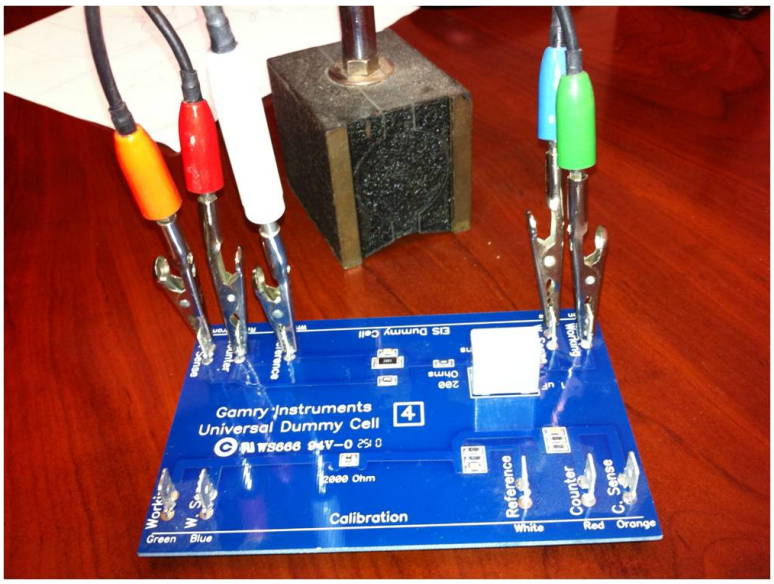

Figure 4.77. EIS Dummy Cell Calibration Setup

Results

AC Electrochemical impedance spectroscopy is proposed to estimate the resistance and capacitance parameters for the cement mixed with different nano additives, which could be related to the microstructure of tested specimens. The relative electrical permittivity has been estimated, by:

1. Dry EIS Testing Conditions

   Figures 4.78-4.83, demonstrate the electrochemical impedance variation for the cementitious nanocomposites relatively with Portland cement samples, under dry conditions. Although, the amplitude-phase plots appear to have a similar behavior, they tend to alter broadly. To illustrate the distinct behavior corresponding to each material relative electrical permittivity is calculated, results are displayed in table 4.13.

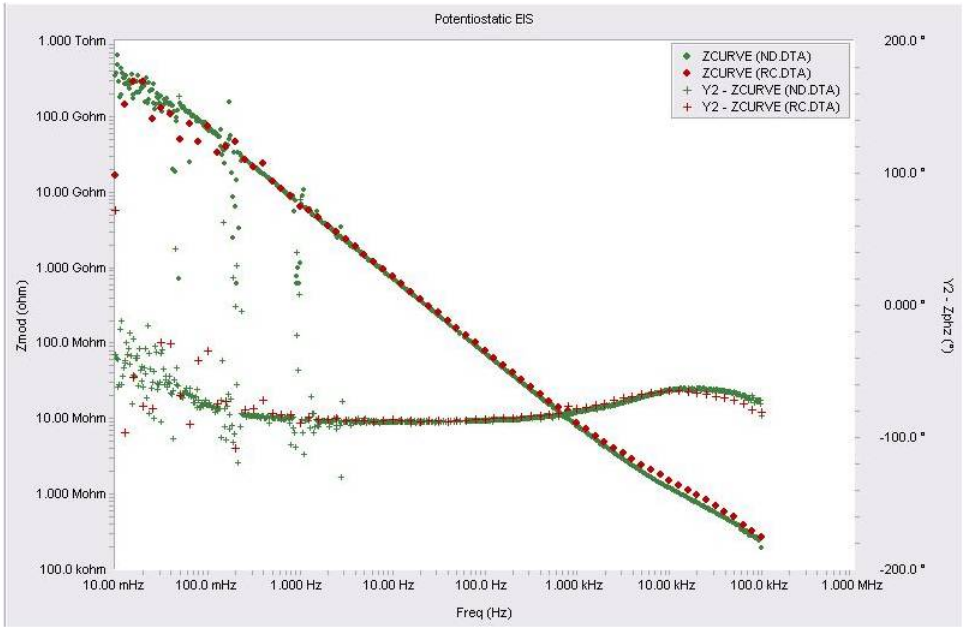

Figure 4.78. Amplitude-Phase (Dry) Plot For Nano Diamond-Cement and Portland Cement Paste

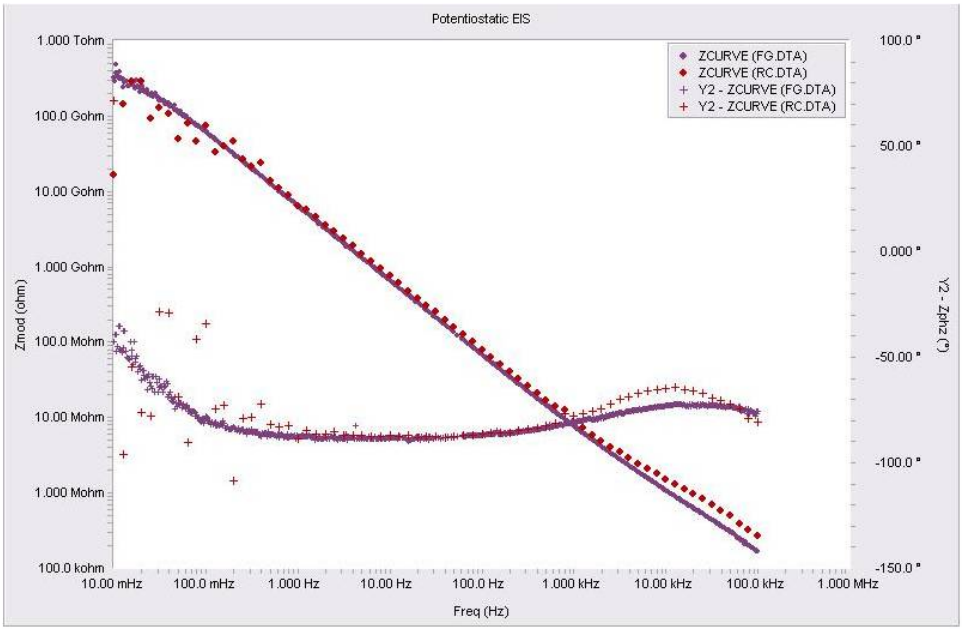

Figure 4.79. Amplitude-Phase (Dry) Plot For Functionalized Graphene-Cement and Portland Cement Paste

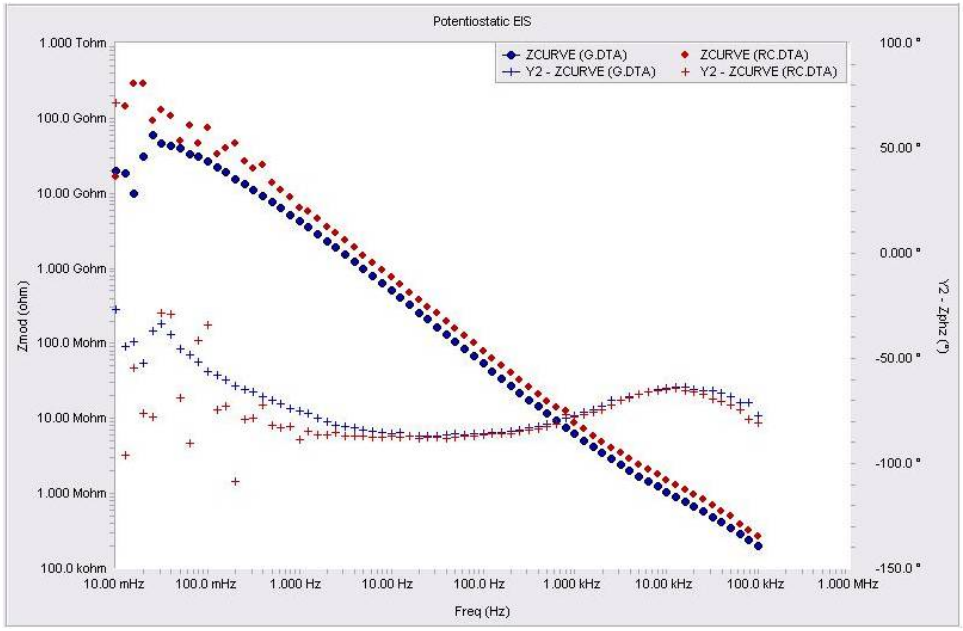

Figure 4.80. Amplitude-Phase (Dry) Plot For Pristine Graphene-Cement and Portland Cement Paste

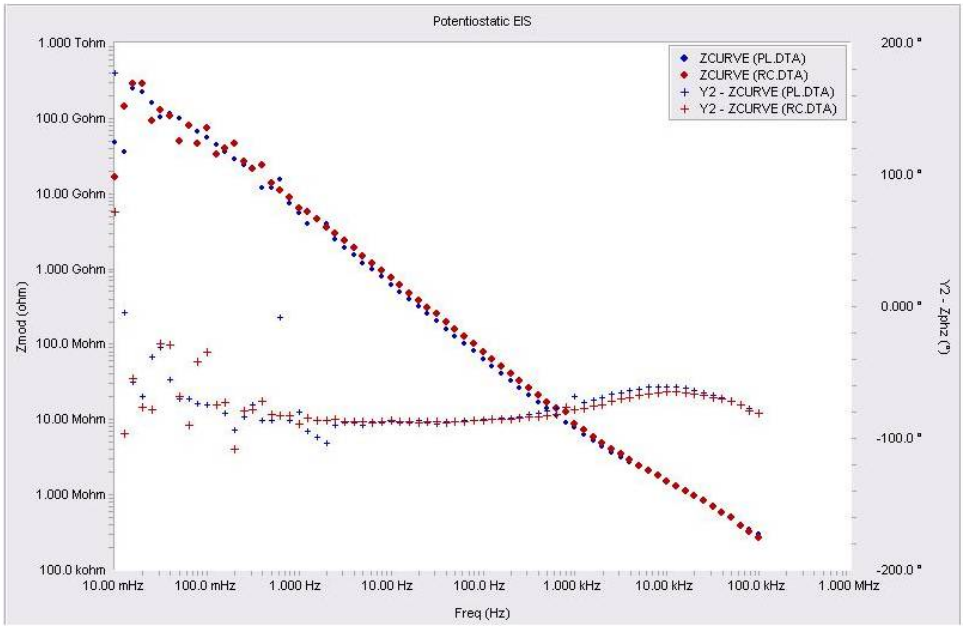

Figure 4.81. Amplitude-Phase (Dry) Plot For PEG POSS-Cement and Portland Cement Paste

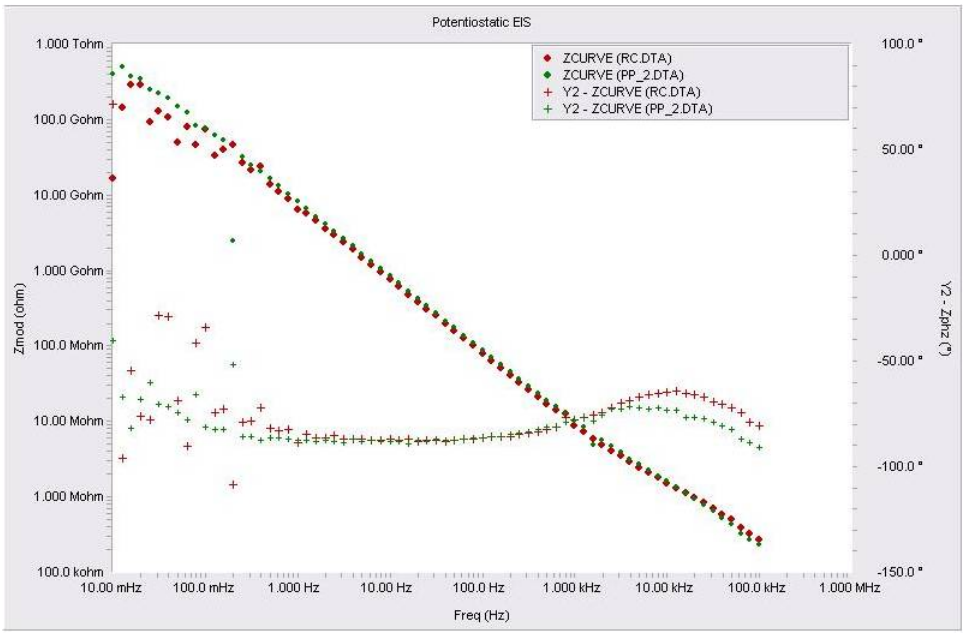

Figure 4.82. Amplitude-Phase (Dry) Plot For OctaTMA POSS-Cement and Portland Cement Paste

Table 4.13. Relative Permittivity Dry Conditions for Cementitious Nanocomposites: EIS Testing

Material	$\epsilon(F/m)$
Portland Cement	18.5
Nano Diamond-Cement	22.52
Functionalized Graphene-Cement	0.38
Pristine Graphene-Cement	6.27
PEG POSS-Cement	2.0
OctaTMA POSS-Cement	0.88

From the relative permittivity calculations displayed in table 4.13, it is shown that the there is a broad variation in the relative permittivity derived from the fitted capacitance behavior of the cementitious nanocomposites. Based on the results shown variety of applications can be implemented accordingly. However, comparing the functionalized graphene to pristine graphene cementitious nanocomposites, the obtained results illustrate the degradation in the electrical properties of the graphene, due functionalization. PEG-POSS cementitious nanocomposite has a higher conductivity characterization than the OctaTMA POSS, this could be the solubility index in water. Nano Diamond has the highest electrical conductivity, which implies a homogenized and a dense microstructure. It should also be mentioned that, the amplitude data points recorded, are fitted into a single capacitance model for the frequency range of (10 kHz-1Hz). In order to capture a higher precision of the electrical properties; a multi-capacitance model should be fitted. The proposed ranges are low frequency (10mHz -1.0Hz), intermediate frequency (1.0Hz-1.0kHz), and the high frequency (10khz-100kHz).

2. Wet EIS Testing Conditions

Figures 4.83-4.87, proclaim the electrochemical impedance variation for the cementitious nanocomposites relatively with Portland cement samples, under wet conditions.

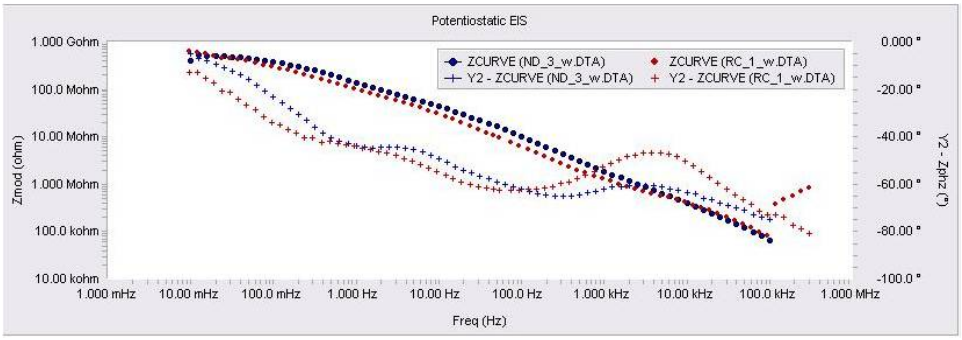

Figure 4.83. Amplitude-Phase (Wet) Plot For Nano Diamond-Cement and Portland Cement Paste

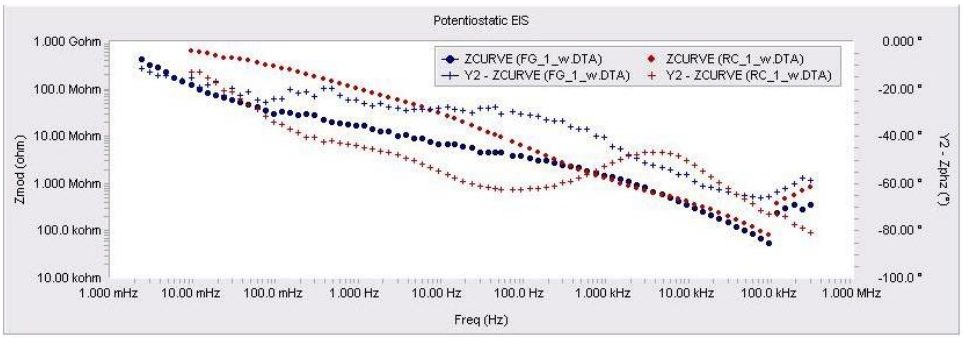

Figure 4.84. Amplitude-Phase (Wet) Plot For Functionalized Graphene-Cement and Portland Cement Paste

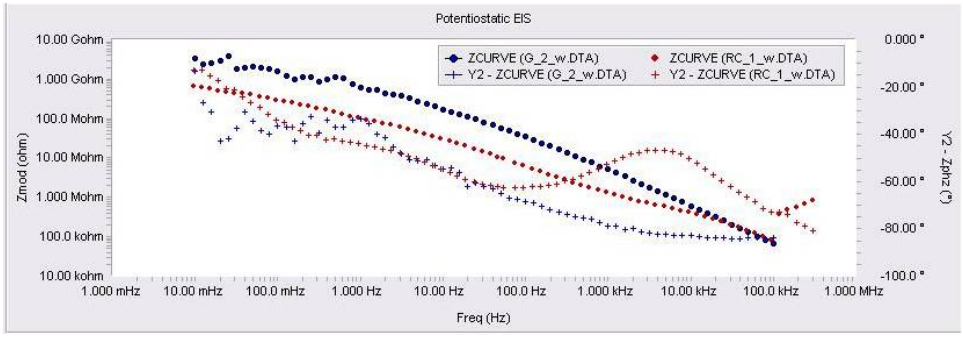

Figure 4.85. Amplitude-Phase (Wet) Plot For Pristine Graphene-Cement and Portland Cement Paste

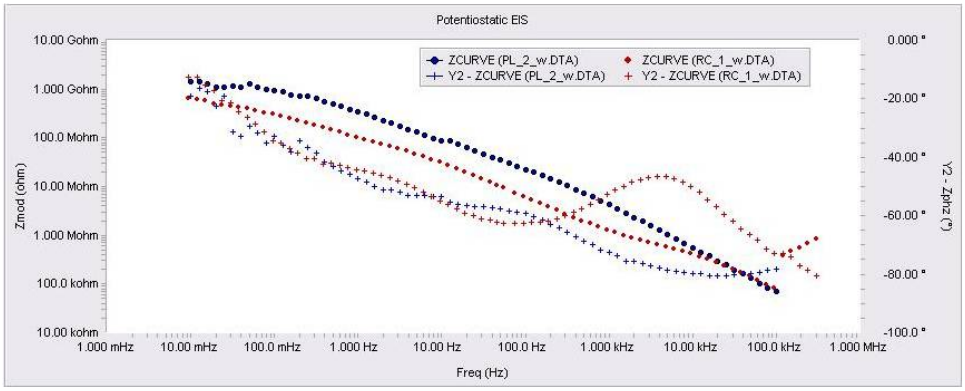

Figure 4.86. Amplitude-Phase (Wet) Plot For PEG POSS-Cement and Portland Cement Paste

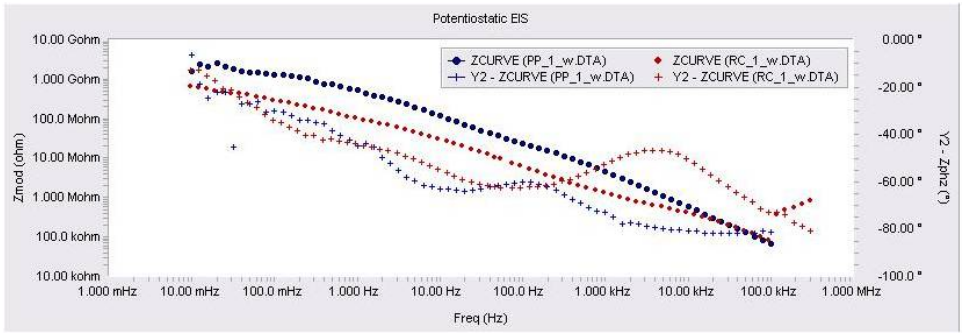

Figure 4.87. Amplitude-Phase (Wet) Plot For OctaTMA POSS-Cement and Portland Cement Paste

From the results obtained from figures 4.83-4.87, it is illustrated the distinctness in the electrochemical impedance characterization of the cementitious nanocomposites for a high moisture content compared with Portland cement. The amplitude-phase plots exhibit a resistance behavior at low frequency ranges, contrary to dry testing conditions. However, a phase disturbance is observed, this could be affected by the microstructure, and implies phase hetrogeneity. For a future detailed characterization, equivalent circuit models will be proposed and checked into thoroughly.

4.4.6 Compression Test

Introduction

The tensile strength of any material can be characterized as; the resistance of the atoms or molecules to be pulled a part, under a tensile force. If the material has multiple grain boundaries or cracks, then a minimum force is acquired to pull the material a part. Meanwhile, to characterize a compressive strength for a specified matter, it is required that the atoms and molecules do not slide against each other. Whereas the grains remain in place, the material can resist compression without necessarily having an optimal tensile strength. In case of unmodified cementitious materials, a poor tensile strength is the primary issue. Many researchers [] have shown that fiber reinforcement is capable of increasing the tensile strength of cement, as for as other properties. A wide range of different types of fibers has been used with cement, including asbestos, steel, glass, nylon, polypropylene, polyethylene, aramid, polyester, acrylic, cellulose, and CNTs []. Small percentage by weight nano additive can improve the crack resistance, wear durability, tensile strength, enhance a controlled shrinkage, ductility, impact energy adsorption, electrical conductivity, and chemical-physical properties of cement pastes.

For further understanding of the compressive strength performance of nano cementitious composites, we have performed a compressive strength test on the nano-cementitous composites. However, in this work, ASTM standards is not followed for the compressive strength test. Specimen dimensions do not meet the minimum requirements for a precise evaluation. Whereas, for a relative comparison of compressive strength measurements, one can predict an imprecise indicator from standardized testing results.

Experimental Setup

Cementitious nanocomposites cubes of (1.5*1.5*1.5)in dimensions, are casted for destructive compressive strength testing.

Results

From results displayed at table 4.14, it is shown that nano diamond-Cement composite, has performed the best in terms of ultimate compressive strength. A 41% increment with respect to regular cement for a w/c ratio of 0.45 and a weight percentage of 0.5% by weight nano additive. On the other hand, the OctaTMA POSS-Cement composite, indicate an additional 21%, for the measured compressive strength, similarly, a w/c ratio of 0.45 and a weight percentage of 0.5% by weight nano additive. This could be due the healing properties both of the materials exhibit mixed with cement, or due to packing densities of the cementitious nanocomposites, or compatibility with hydrated cement particles, or homogeneity of specimens, ...etc. To verify these remarks, an ASTM standardized test is required, and further micro and nano characterization are compulsory.

Table 4.14. Ultimate Strength Results: MTS Testing

Material	Ultimate Strength (MPa)
Portland Cement	40.64
Nano Diamond-Cement	57.33
Functionalized Graphene-Cement	39.66
Pristine Graphene-Cement	34.76
PEG POSS-Cement	38.51
OctaTMA POSS-Cement	49.15

5. EXPERIMENTAL EVALUATION AND NUMERICAL SIMULATIONS OF NANO-MATERIALS IN INFRASTRUCTURE FIRE APPLICATIONS

5.1 Introduction

The development of a blast-resistant coating for structural members with good characteristics in a fire event will provide buildings with protection against explosions and a fire following the blast, as well as against regular building fires. An important characteristic of this coating will be to provide a thermal barrier to heat, such that the temperature of the structure remains for as long as possible below the critical temperature at which its strength will be weakened. Since the materials been considered for blast-resistant coatings are polymer-based, it is pivotal to investigate their behavior in fire. Wang et al. addressed fire retardancy in polymeric-clay nano-composites fire and flammability characteristics [109]. Polymers included in the study are; polystyrene (PS), acrylomtrile-butadiene-styrene (ABS), high-impact polystyrene (HIPS), polypropylene (PP), ethylene-vinyl acetate (EVA), epoxy resins, PMMA, poly (vinyl chloride) (PVC), polyamides (PA), and others. Polymeric-clay nano-composites reduced flammability and exhibited improved mechanical properties. Their results show that the mechanisms by which the nano-composites can enhance the thermal and fire stability of polymers studied.

An important perspective of building fire safety is the flammability characteristics of the interior walls, columns, and ceilings finishing. The interior walls finishing represent a large surface area over which flame can spread. Such flames can magnify a small fire and accelerate spreading leading to room flashover [110]. If the burning duration of a surface element is longer than the ignition time of a neighboring element, flame spreading is likely to happen. If not, then a local burnout is expected [111]. Flame surface spreading has been modeled theoretically [111, 112, 113, 114]. The models are mainly concerned about the critical nature of the flame spread, specifically for thin combustible layers coated on noncombustible substrates.

Fire Growth as a function of time is another important feature in the fire building safety. Clearly [115] first formulated a theoretical model of fire growth output as a function of time, in terms of material properties and orientations for flat surfaces in application of floors, walls and ceilings. Quintiere [111] developed a mathematical model to simulate fire growth on the wall and ceiling materials when subjected to a room-corner fire test exposure. The model predicts the area of burning, the upper layer gas temperature, and the rate of energy release as a function of time.

Brown et al. (1988) [116] evaluated the fire performance and flammability of composite materials to assist the Navy selection criteria for ship components by cone calorimeter measurements. The materials used in Brown et al. study mainly polymer resins reinforced with fiber glass fabric. Cone Calorimeter flammability measurements for painted gypsum wallboards are inspected by McGraw and Mowrer (1999) [117]. Experiments for eight coats of latex paint over one of prime are run through at heat fluxes ranges of 25 kW/m^2 -75 kW/m^2. Gilman et al. [118] studied the flammability properties of polymer-layered silicate polypropylene/polystyrene nanocomposites. They reported a far reduction in flammability due the delaminated montmorillonite (MMT) clay existence.

Coupled simulations of fire dynamics and thermal response of world trade center (WTC) towers are conducted by Parasad et al. [119]. A radiative heat transfer model is used to

connect between gas phase energy release and transport phenomena coupling, and the stress analysis in the load-bearing materials [119]. The large thermophysical gas properties are predicted by the National Institute of Standards and Technology (NIST) Fire Dynamic Simulator (FDS). The radiative transport equation solves the explicit formulae for the heat flux obtained as a function of temperature, hot layer depth, soot concentration, and orientation of the structures. These formulae outputs are imported into finite element codes widely used for time-independent three-dimensional structural analysis, to account for thermal material strength degradation and effect of elastic -plastic stress-strain relationships.

As of this date, limited work has been reported on realistic validation of material losses and actual fire behavior for thin combustible polymeric layers coated on noncombustible substrates such as concrete. Coated concrete-structural elements are the most commonly used building materials in the USA. A vital approach for fire characterizations, particularly flame spreading and material properties at high temperatures, is tested and simulated to validate the different structural components and to evaluate the fire safety in different structural system models. A series of heat release rate (HRR) measurements on polymeric nano-composite plaques and polymeric nano-composite coated concrete blocks has been conducted with NIST. Flammability fire description for different structural components and structural systems is simulated using the NIST Fire Dynamic Simulator (FDS).

5.2 Material Research

Two Material categories used for the work presented in this paper: First Category is blast-resistant materials, where an elastomer polymer (polyurea) and a thermoset polymer (epoxy) are reinforced with advanced new materials such as exfoliated graphene nanoplatelets and polyhedral oligomeric silsesquioxane (POSS). Second Category is fire-protection material, such as LR, LR HP, LR F CF. A detailed description for material fabricated summarized at the following sections:

1. **Blast-Resistant Materials**

Flexible epoxy used is made of 100phr Epon 828/50phr Jeffamine D-400/25phr Jeffamine D-2000. Polyurea LINE-X XS-350 used is a two- component polyurea supplied by Protective Coating Inc. Polyurea mixed with Polyhedral Oligomeric Silsesquioxane (POSS). POSS used is a class of silicon based nanochemicals designed to fulfill various mechanical functions supplied by Hybrid Plastics Inc. Epoxy reinforced with exfoliated graphene nanoplatelets is used produced at Michigan State University. Exfoliated graphene nano platelets-15 made from Asbury 3772 using High Power Microwave. Prior to use exfoliated graphene nano platelets are kitchen-microwaved for 1 min/ 10-15g. Finally polyurea reinforced with exfoliated graphene nano platelets.

2. **Fire Protection Materials**

LR, Tyfo®LR, is a liquid (ethylene propylene) rubber coating used supplied from Fyfe Inc. LR HP, Tyfo®HP is a two-component epoxy fire retardant-intumescent coating used based on non-halogenated phosphates. LR FC F, Tyfo®FC F used is a two part epoxy coating system specially formulated to provide an increase in existing fire rating. Tyfo®F is a single component formulation designed to be applied over Tyfo®FC. The Tyfo®FC F system provides an increase to the fire rating of an element as per ASTM E-119 (2-hours wall rating) and provides a class 1, ASTM E-84 flame and smoke rating. Type 4 Tyfo®Blast-Flex Type 4 used a two-component polyurea based system with fire-resistance additive. The fire protection material supplied by Fyfe Inc..

5.3 State Examination of Fire

5.3.1 Flammability Characterization

1. **Experimental Measurments**

   (a) Cone Calorimeter Setup

   Cone calorimeter HRR measurements are applied on a number of blast resistant and fire resistant coating materials. Cone calorimeter experiments are conducted on a FTT dual cone calorimeter at incident heat flux settings of 30, 40, 50 kW/m^2 with an exhaust flow of 24 L/s using the standardized test procedure (ASTM E-1354-07) with some modifications as described below.

   All samples are tested without frame and grid, but the solid coating samples (polyurea, epoxy, and LR on cinder block) are tested, in a shallow thick-walled aluminum dish, to capture any dripping that may have occurred from the samples as they deformed and flowed under fire conditions. The coatings on cinder block samples are wrapped with aluminum foil on the back side of the sample only to form a small pan, that would capture any dripping off the sample surface during burning. The aluminum foil is not wrapped adequately around the sample so that any dripping behavior could be clearly observed.

2. **Numerical Simulations**

   The FDS is, a computer software which solves the equations that describe the fire evolution [120]. Smokeview is companion software to produce the imaging and animation of the FDS output files [121]. Coupled thermal structural finite element analysis using ANSYS is adapted to determine the maximum stresses and displacements in the different structural components.

Heat release rate (HRR) is the most important fire reaction property as a result of the heat released by igniting a material. HRR can sustain the additional thermal energy necessary for the growth and spread of fire. It is the prominent reaction property which influence on the fire behavior of composites. However, several other reaction properties are used to characterize the fire behavior of composites which are HRR dependent, such as surface spread of flame, smoke formation and CO emission [122]. A series of heat release rate simulations for the following blast-resistant and fire-protection materials are conducted using the NIST Fire Dynamic Simulator (FDS): polymeric coated blocks (Polyurea, Polyurea + POSS, Polyurea + 6% graphene, Epoxy, Epoxy + 6% graphene, LR, LRFCF, LRHP, and Type 4) at incident thermal flux of a 30 kW/m^2 and ignition temperature of 350C°.

The objective of this work, is to calculate the heat flux (Q) Q(t) and temperature (T) T(t) time evolution functions, and to compare the flammability of the different applied polymeric blast-resistant and fire-protection performance.

Structural Systems

(a) *Single Room Fire Model*

FDS simulations are performed to determine the extent to which various candidate materials contributed to a fire confined to an office space ($6m$ x $3m$ x $3m$ high) in a building. The office space has three walls and is open in front. The ($533 \pm 50kW$) fire is located near the back wall, which is specified by assigning thermo physical properties consistent with a 3 mm coating of the candidate material on concrete. The floor and ceiling are assigned properties typical of gypsum, while the front of the space is left open to the air.

(b) *Concrete Column*

Typical concrete columns assembled to run the numerical simulations for both

FDS and FEA. The following geometry dimensions are used cross section of (18"x18"=45.72cmx45.72cm). Height of (3m). Polymeric coating applied thickness of ($3mm$). Solid phase thermocouple devices are inaugurated on the front side of the column (near fire), to capture the heat flux and the coated column temperature during the simulation, at the following intervals: (0, 0.1, 0.2, 0.3, 0.4, 0.5, 1.0, 1.5, 2.0, 2.5, 2.6, 2.7, 2.8, 2.9) m. A demonstration figure is shown in figure 5.1.

The concrete columns are assembled in an open environment and with an ignition temperature of 350C°, are subjected to fire for the studied polymeric coatings. Each column configuration is simulated for 200 sec, and a time step of 1 sec.

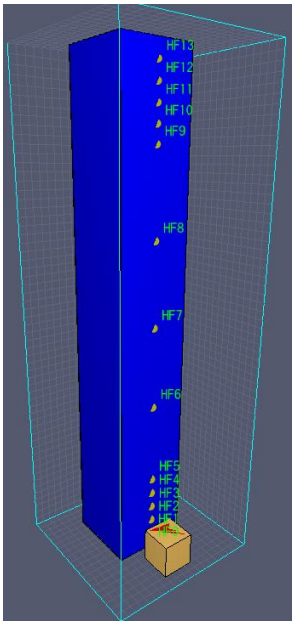

Figure 5.1. Coated Concrete Column FDS Setup

(c) *Masonary Wall*

Typical masonry wall of dimensions (3x3x0.20m) and (3mm) coating thickness are assembled for FDS numerical simulations. Each masonry wall configuration is simulated for 200 sec, and a time step of 1 sec as a part of the single room structural system. Solid phase thermocouple devices are installed on the front

side of the masonry walls (near fire) at intervals (0, 0.1, 0.2, 0.3, 0.4, 0.5, 1.0, 1.5, 2.0, 2.5, 2.6, 2.7, 2.8, 2.9) m to capture the heat flux and coated masonry wall temperature during the simulation.

5.3.2 Structural Integrity

Finite Element Simulations

A finite-element model is constructed to calculate the thermal strains effect introduced by temperature fields in the structural field; the structural strains generally do not affect the temperature distribution. In thermal-stress coupled analysis, nodal temperature from thermal analysis is applied as body force load in a subsequent stress analysis. ANSYS a commercial software is used for finite element analysis represented in this work [123].

The objective of this work is to analyze the effect of fire on different structural elements integrity to predict the failure. Spatial and temporal variation in temperature will result in thermally induced stresses/strains and reduced load bearing capacity that could lead to failure of the structural element. Peak heat flux Q(t), captured by thermocouple devices from FDS simulations, is applied to the concrete columns and the masonry walls. This step is followed by, a thermal transient finite element simulation to calculate the nodal temperature distribution correspondent to the applied peak heat flux Q(t). The nodal temperature distribution, generated from the thermal finite element analysis, is applied to solve for the stresses/strains developed in the structural elements.

5.4 Results and Discussion

5.4.1 Flammability Characterization

1. **Experimental Measurments**

   (a) Cone Calorimeter Setup

   Time dependent HRRs curves obtained from cone calorimeter measurements on polyurea-POSS and epoxy-exfolatiated graphene nanoplatelets plaques ($\sim$1.0 cm thick), are displayed in figure 5.2. The polymer plaques prepared for the candidate materials are exposed to an incident flux of $40kW/m^2$. The HRR plateau occurring during the initial stages of the burn is indicative of quasi-steady burning that is characterized by a thin, well-defined, pyrolysis zone and constant temperature gradient throughout the sample. This is followed by a dramatic increase in HRR as more and more of the sample thickness becomes involved in pyrolysis. The burning behavior of the epoxy plaques is particularly violent as flaming shards were observed to shoot out from the top and sides of the burning plaque. The presence of the graphene additive did, however, appear to mitigate this effect. In addition, the time dependent HRRs plots obtained from cone calorimeter measurements for the polymer-coated cinder blocks are shown in 5.3.

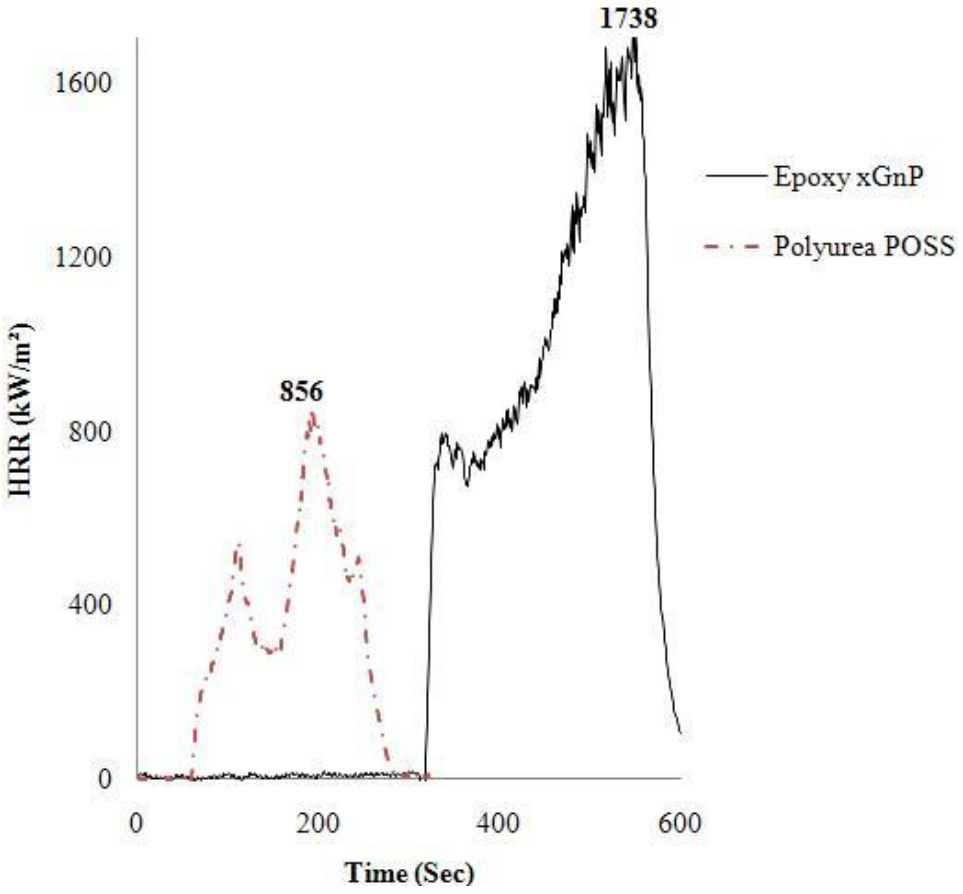

Figure 5.2. Time Dependent HRRs Obtained From Cone Calorimeter Measurements for Polymer Plaques

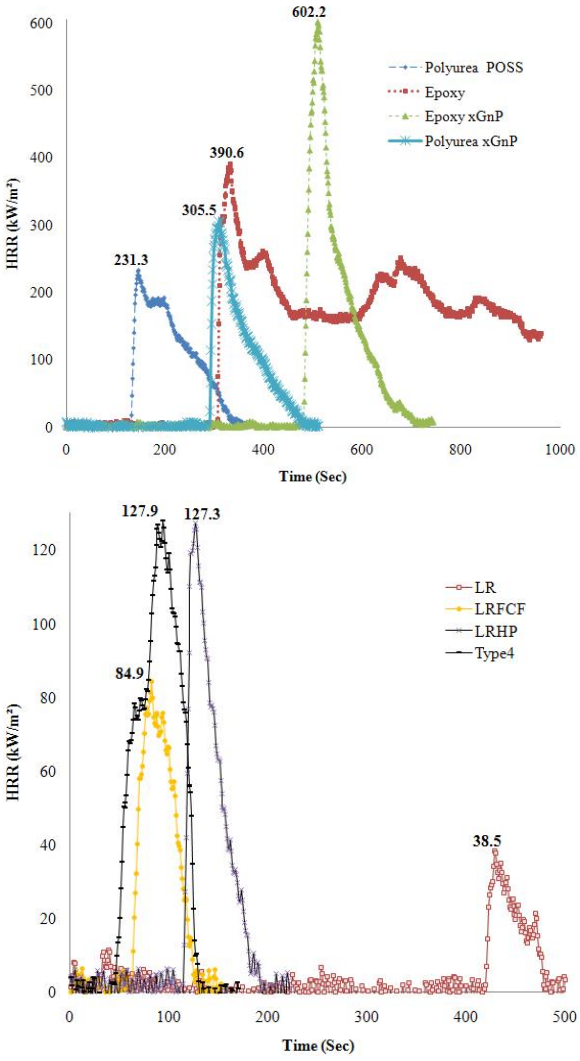

Figure 5.3. Time Dependent HRRs Obtained From Cone Calorimeter Measurements for Coated Cinder Blocks

The peak HRRs (PHRRs) for the polymer plaques are quite high figure5.4, approaching 2000 kW/m^2, which are comparable to values obtained from some of the most flammable thermoplastic polymers that are tested. Furthermore, as revealed by figure 5.5, the presence of the cinder blocks effectively eliminates the strong dependency of HRR on incident heat flux that is observed for the corresponding polymer plaques. This justification will simplify the simulation performance of a single HRR value (rather than a function that describes the dependence of HRR on incident flux) for each simulated candidate material.

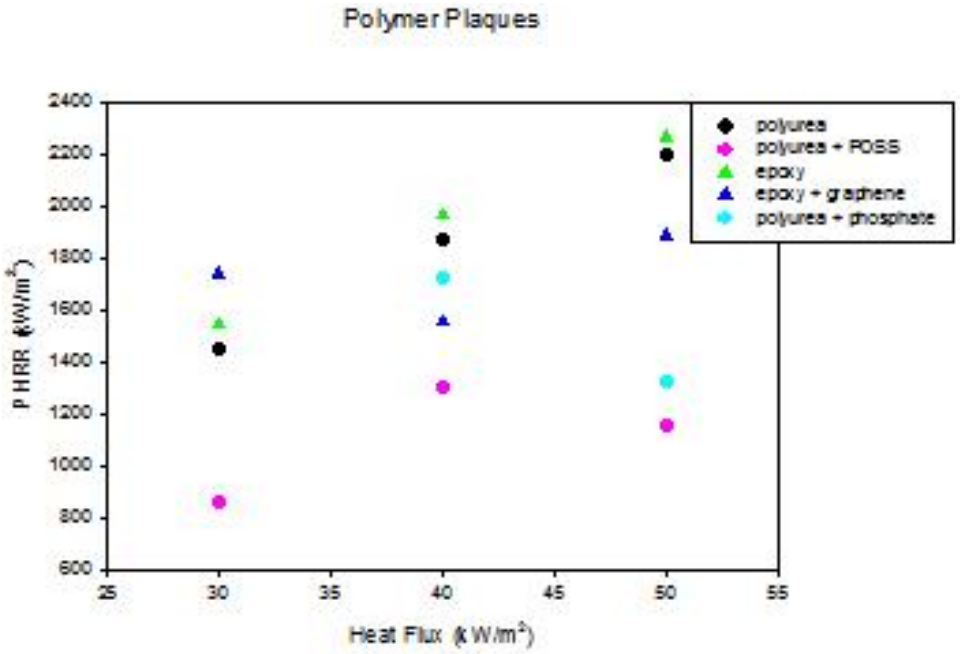

Figure 5.4. Heat Release Rate (HRR) Measurements for Polymer Plaques

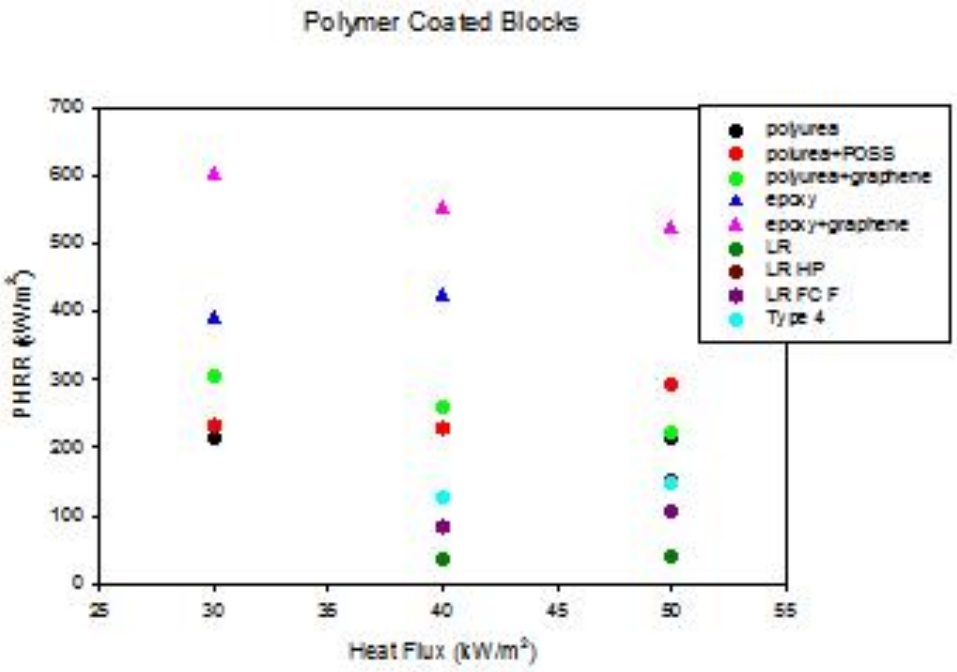

Figure 5.5. Heat Release Rate (HRR) Measurements for Polymer Coated Cinder Blocks

The data listed in table 5.1 indicate that while the presence of the additives (POSS, phosphate, graphene), tend to reduce the HRRs of the polymer plaques, they do not seem to provide much benefit when these materials are used as coatings on cinder blocks. Indeed, the presence of graphene appears to increase the HRR of the epoxy coating significantly.

The results obtained from the cone calorimeter tests indicate that the commercial LR fire retardant coating by far has the best fire performance, as is evidenced while processing the HRR measurements. During the conducted tests, it is noticed that at any time step the flames are confined to a small fraction of the surface area of the coating.

Table 5.1. PHHRs for Candidate Material

Material	Incident Flux ($30\ kW/m^2$)	Incident Flux ($40\ kW/m^2$)	Incident Flux ($50\ kW/m^2$)
Polymeric Plaques			
Polyurea	1450	1875	2201
Polyurea+Phosphate	n.a.	1720	1327
Polyurea+POSS	856	1299	1156
Epoxy	1544	1966	2263
Epoxy+Graphene	1738	1553	1887
Polymeric coated cinder blocks			
Polyurea	213	260	216
Polyurea+POSS	233	229	293
Polyurea+Graphene	305	261	221
Epoxy	391	422	n.a.
Epoxy+Graphene	602	552	552
LR	n.a.	38	39
LR HP	n.a.	127	152
LR FC F	n.a.	84	108
Type 4	n.a.	128	147

The polyurea surprisingly appears to perform better than the epoxy, which has higher PHRRs, drips, and spalls, burning pieces of the epoxy flew off the blocks, during the experiments. The presence of the graphene mitigates the dripping and spalling observed in the pure epoxy coated bricks and generally prolongs ignition times. Unfortunately, the graphene also appears to increase PHRR at low thermal flux. The longer ignition times and higher PHRRs can be due the increase in thermal conductivity. Different heat fluxes did not have a major effect on HRRPA for polymeric materials studied. Polyurea POSS performed the best for fire and thermal degradation.

2. **Numerical Simulations**

(a) *Single Room Fire Model*

Heat release rate per unit volume (HRRPUV) spread snapshots for the simulated coatings generated by FDS are shown in figure 5.6.

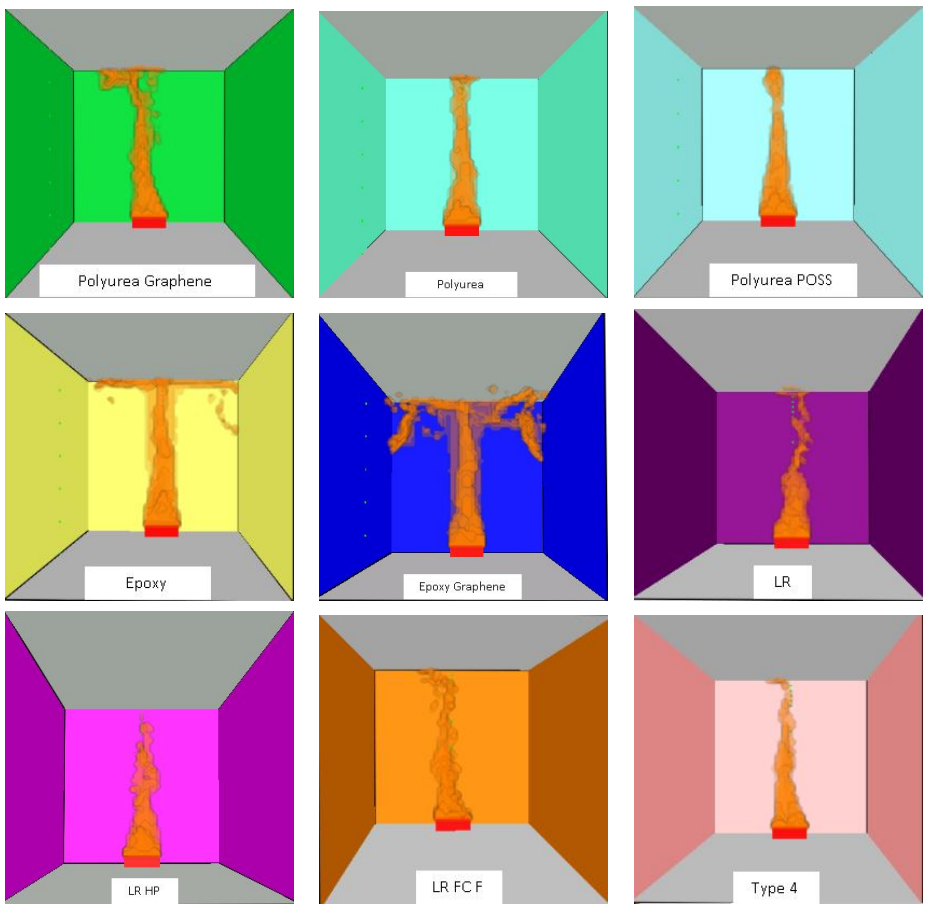

Figure 5.6. HRRPUV for Coated Masonry Walls In a Single Room Model Snap Shots

The blast-resistant and the fire-retardant coatings are distinguished by assigning the average values of the HRRs (per unit area) measured in the cone calorimeter tests. The coatings ignited when the surface temperature exceeded 350 C°. The maximum HRR of the room fire simulated, for the coating material candidates and the control (bare concrete), are listed in table 5.2.

It is shown that addition of POSS and graphene has reduced the HRR for the

polyurea by 2.5%. Graphene platelets addition to epoxy based polymer coatings has a counter effect on the HRR, maximum heat flux, and maximum surface temperatures. The HRR has increased for the epoxy after the graphene addition by 26%. The addition of fire retardant filler such as LRFCF and LR for polyurea has reduced the HRR peak value by 29%.

Table 5.2. Concrete Coated Blocks Maximum HRR of Simulated Fires

Coating Material	Max HRR (kW/m^2)
No Coating	593
Polyurea	850
Epoxy	1120
LR	605
LRHP	621
Polyurea+POSS	827
Type4	608
Epoxy+Graphene	1520
LRFCF	586
Polyurea+Graphene	829

Smoke density is one of the main safety concerns with polymeric composites. The smoke produced by burning a composite is a mixture of small fragments of fiber and ultra fine carbon particles. The short-term exposure of people to smoke released from the burning composites is not a serious health hazard. However, smoke can be extremely dense and thereby reduce the visibility, cause disorientation and make it difficult to fight the fire [122]. Figure 5.7, shows smoke snapshots at 100 sec, for the room FDS model.

(b) *Concrete Column*

Figure 5.8 demonstrates the heat release rate per unit volume (HRRPUV) snapshots for the different simulated coated columns. From 5.8, it is noticed that the polyurea POSS coated column has the less prosperity of flame to spread compared to the rest of the polymeric coatings. Graphene has increased the flame spreading compared to pure epoxy HRRPUV snapshots. Figure 5.9 shows the maximum

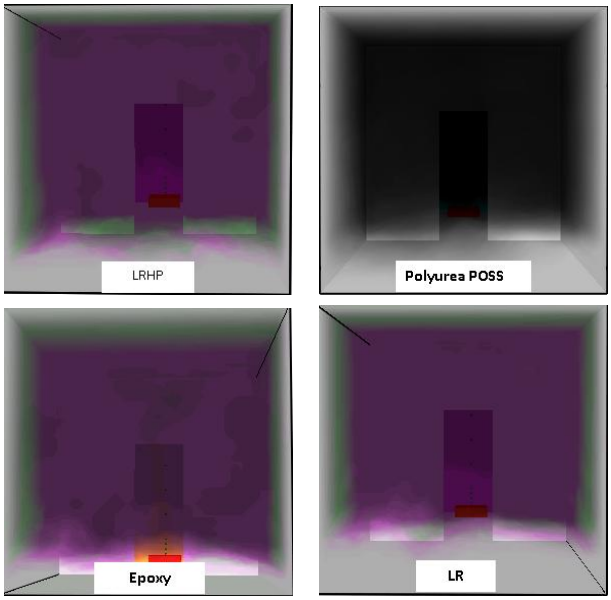

Figure 5.7. Smoke for Coated Walls in a Multiple Room Mode Snap Shots

values of the heat flux plots as a function of time. Tables (5.3, 5.4) summarize the maximum heat flux and maximum temperatures that are captured by the solid phase devices mentioned above. Results in Tables II and III indicate that the polymeric coatings have increased the transferred heat per unit area compared to the uncoated concrete column and compared to the gypsum coated concrete.

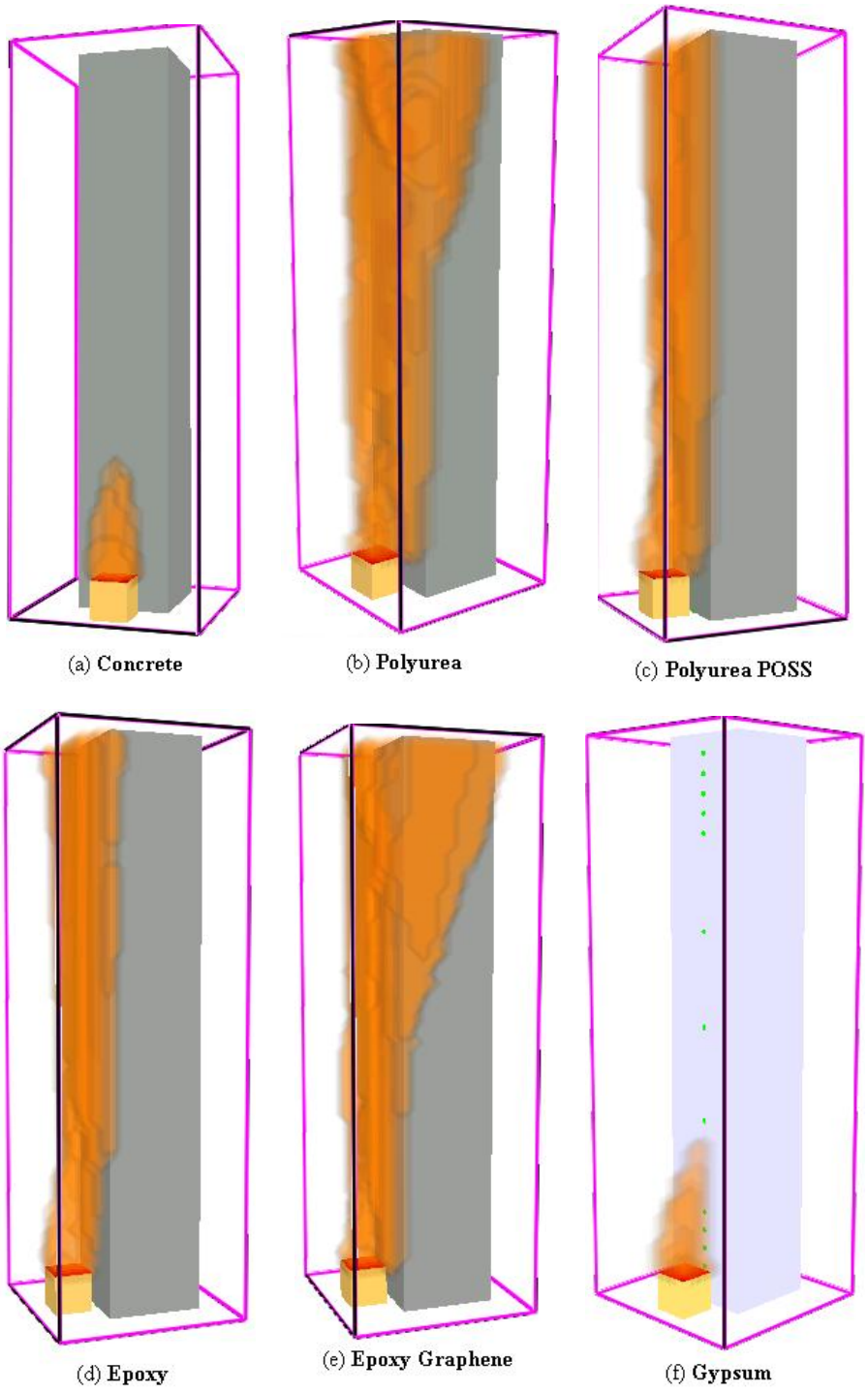

Figure 5.8. HRRPUV for Coated Concrete Columns FDS Snap Shots

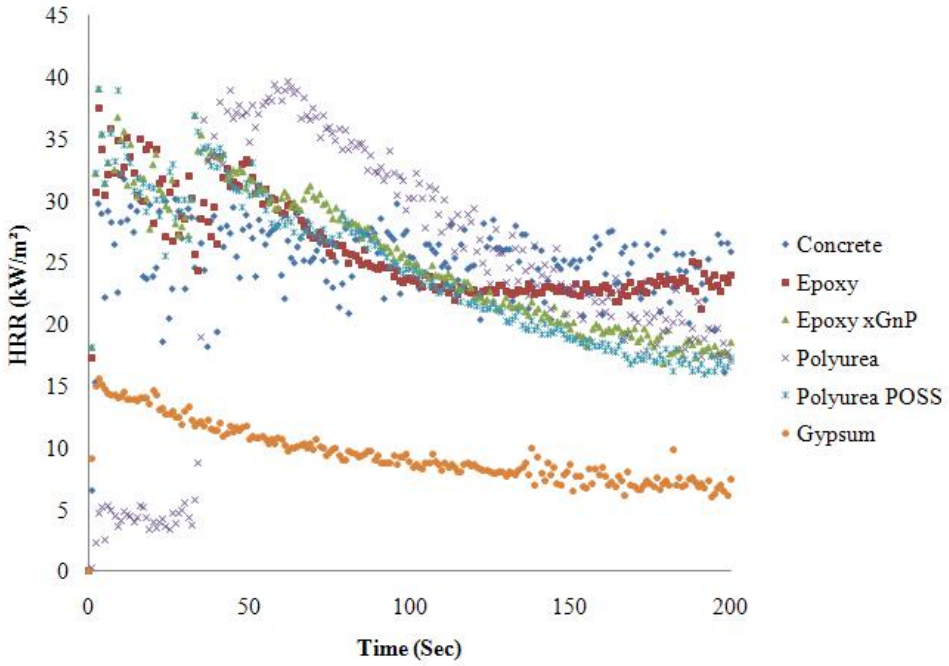

Figure 5.9. Heat Flux Time Evolution Plots for The Concrete Columns

Table 5.3. Maximum Heat Flux From FDS Concrete Column Simulation (kW/m^2)

Height (m)	Concrete	Polyurea	Polyurea +POSS	Epoxy	Epoxy +Graphene	Gypsum
0	0.485	0.436	0.425	0.40	0.386	1.16
0.1	2.173	1.972	1.963	1.86	1.761	3.07
0.2	35.234	28.727	29.017	29.85	25.687	11.93
0.3	38.201	36.123	36.263	33.61	36.912	13.38
0.4	34.775	39.752	39.226	31.43	39.515	12.68
0.5	28.578	39.710	37.062	26.71	37.611	11.37
1	4.501	8.754	6.807	5.85	5.412	2.19
1.5	2.066	3.054	2.737	2.74	0.756	0.71
2	1.304	2.106	1.987	1.66	0.391	0.55
2.5	1.083	1.632	1.536	1.35	0.339	0.64
2.6	0.956	1.496	1.381	1.31	0.325	0.59
2.7	0.841	1.355	1.240	1.25	0.316	0.53
2.8	0.754	1.219	1.122	1.20	0.313	0.47
2.9	0.738	1.108	1.013	1.18	0.309	0.42

Table 5.4. Maximum Temperature From FDS Concrete Column Simulation (C°)

Height (m)	Concrete	Polyurea	Polyurea +POSS	Epoxy	Epoxy +Graphene	Gypsum
0	24.5	53.1	48.9	53.5	26.03	83.69
0.1	42.0	125.8	117.2	126.1	47.45	161.73
0.2	380.3	603.7	593.4	602.0	110.69	382.59
0.3	393.1	649.6	634.1	646.8	532.85	405.16
0.4	365.7	662.8	645.6	660.4	575.29	393.15
0.5	320.6	668.0	649.8	664.2	589.61	364.49
1	76.7	656.7	659.1	657.2	597.34	117.22
1.5	42.9	663.6	668.0	664.8	589.87	57.39
2	35.3	668.6	674.7	667.8	598.81	48.49
2.5	31.7	671.5	672.4	670.3	604.30	45.18
2.6	31.1	669.5	670.3	668.2	605.29	44.56
2.7	30.5	665.0	666.0	663.6	603.42	43.96
2.8	30.0	655.1	657.1	653.7	599.28	43.36
2.9	29.6	630.4	634.5	628.9	590.04	42.83

(c) *Masonary Wall*

Figure (5.10), demonstrates the heat flux Q(t) evolution with time, for the coated masonry walls. Figure 5.11 indicates that the addition of POSS to polyurea tends to lower the monitored surface temperature. Tables (5.5, 5.6) below summarize the maximum heat flux and maximum temperatures that are captured by the solid phase devices at mentioned heights. However, LR has the minimum released heat fluxes and surface temperatures.

Table 5.5. Maximum Heat Flux From FDS Masonary wall simulation (kW/m^2)

Height (m)	Polyurea	Polyurea Graphene	Polyurea POSS	Epoxy	Epoxy Graphene	LR	LR HP	LR FC F	Type 4
0	11.93	11.1	13.0	13.4	13.0	9.8	10.5	9.7	9.8
0.1	14.70	13.4	—	—	—	13.0	12.8	13.0	12.1
0.2	31.97	24.0	—	—	—	26.7	22.7	27.4	22.5
0.3	40.79	24.7	—	—	—	29.7	30.1	30.6	29.8
0.4	46.34	37.5	—	—	—	32.8	36.8	34.0	33.6
0.5	48.59	45.1	46.3	51.7	56.1	33.1	39.4	34.3	34.5
1.0	51.15	47.3	— 51.1	59.9	61.3	27.0	37.6	27.5	30.5
1.5	46.52	49.5	— 51.8	59.9	66.0	17.2	23.8	17.4	15.8
2	28.50	45.0	— 50.7	59.9	65.6	11.1	19.7	10.0	13.5
2.5	18.93	22.9	— 52.3	62.5	63.4	8.4	16.6	8.1	15.2
2.6	18.29	17.7	—	—	—	8.3	17.2	8.0	15.8
2.7	17.33	17.2	—	—	—	8.2	17.6	7.9	17.4
2.8	16.80	16.2	—	—	—	8.1	17.7	7.8	17.7
2.9	15.94	15.8	—	—	—	8.2	18.4	7.4	17.9

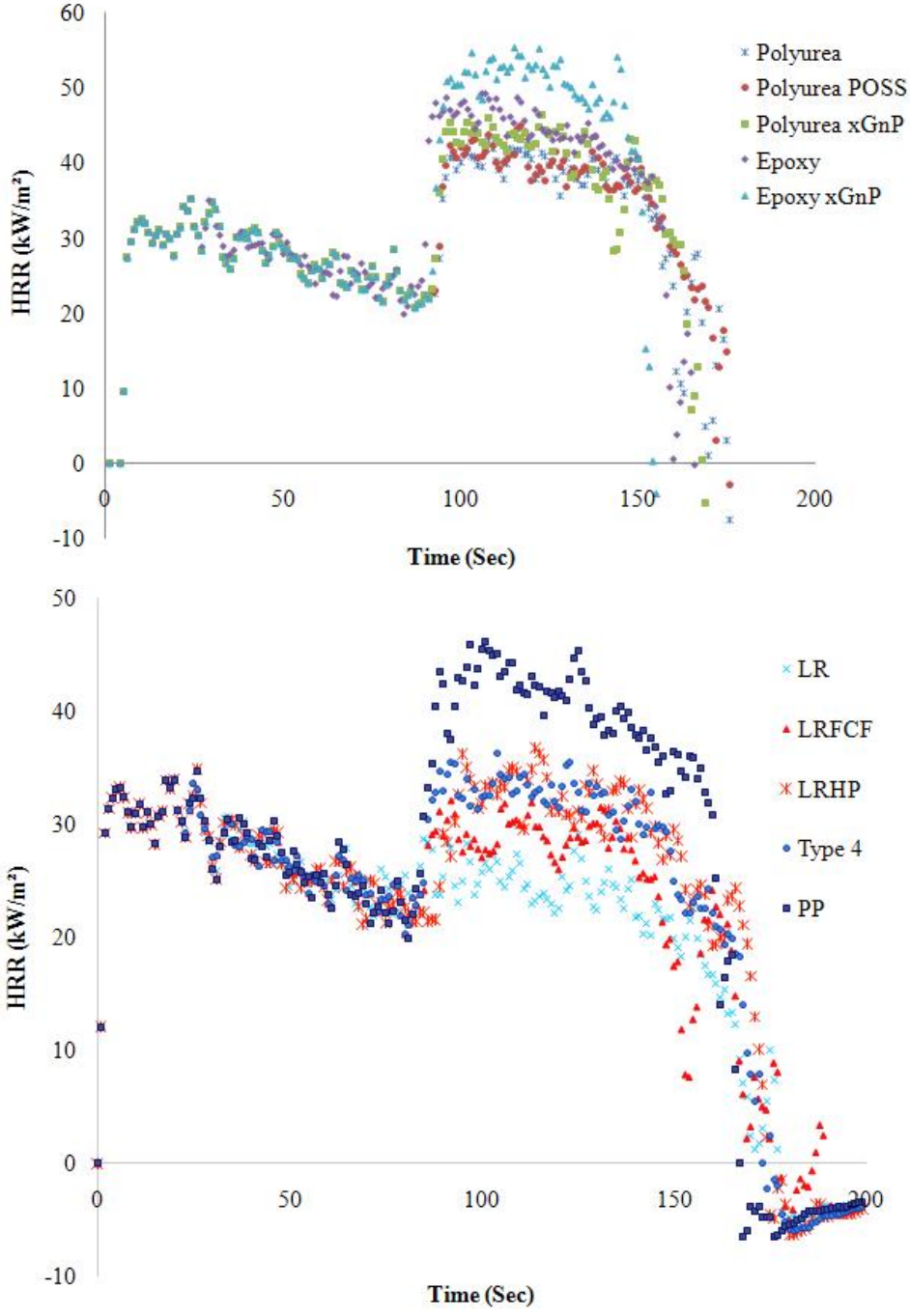

Figure 5.10. Maximum Heat Flux at (0.5m) for Coated Blocks

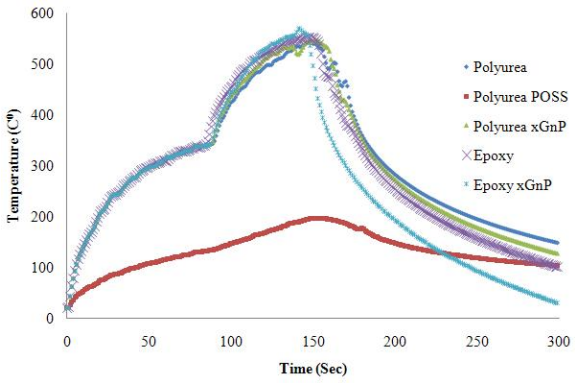

Figure 5.11. Maximum Temperature Profiles From FDS Masonary Wall Simulation (kW/m^2)

Table 5.6. Maximum Temperature From FDS Masonary Wall simulation (C°)

Height (m)	Polyurea	Polyurea Graphene	Polyurea POSS	Epoxy	Epoxy Graphene	LR	LR HP	LR FC F	Type 4
0	197.25	203.7	205.4	218.9	219.2	171.3	180.5	173.5	182.0
0.1	239.21	245.3	246.7	260.8	262.6	209.8	220.6	213.1	222.0
0.2	422.86	429.6	431.3	450.5	443.4	361.7	383.0	371.8	387.0
0.3	485.31	493.5	493.0	497.9	489.8	394.3	432.0	412.8	436.0
0.4	531.97	536.0	540.5	540.8	540.7	426.2	480.1	454.2	485.0
0.5	542.59	541.8	550.0	552.0	561.8	424.6	488.8	457.1	493.0
1	529.51	500.0	515.0	519.3	570.2	350.7	444.8	390.3	441.0
1.5	498.95	426.2	447.5	446.7	506.8	280.8	364.1	298.0	348.0
2	449.85	368.0	393.3	392.7	451.6	248.8	295.3	253.3	286.0
2.5	408.80	336.1	364.6	369.3	431.2	256.8	266.2	242.5	262.0
2.6	408.01	334.5	364.0	369.4	431.8	257.6	265.2	244.7	261.0
2.7	407.34	334.0	365.7	372.5	437.5	260.4	266.8	247.4	262.0
2.8	409.00	335.0	368.5	376.0	443.2	262.3	268.7	248.3	263.0
2.9	416.96	338.0	372.2	383.6	451.2	266.0	271.9	249.6	267.0

5.4.2 Structural Integrity

1. *Concrete Column*

   The effect of the coated concrete columns is studied using ANSYS coupled thermal-structural analysis. The maximum and minimum stresses are obtained for the simulated concrete columns with geometry similar to geometry constructed for FDS simulations. The concrete columns are exposed to the heat fluxes per unit area, collected from the solid phase thermocouple devices embedded on the front side (near fire) of the concrete column from the FDS simulations. A time dependant thermal nodal analysis is adapted to calculate the temperature nodal distribution and to understand the thermal response of the concrete columns. A typical nodal temperature distribution for a concrete is demonstrated in figure 5.12.

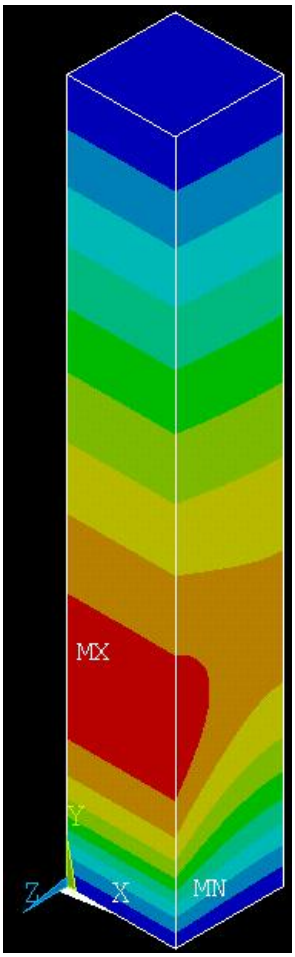

Figure 5.12. Nodal Temperature Distribution in Concrete Coated Columns

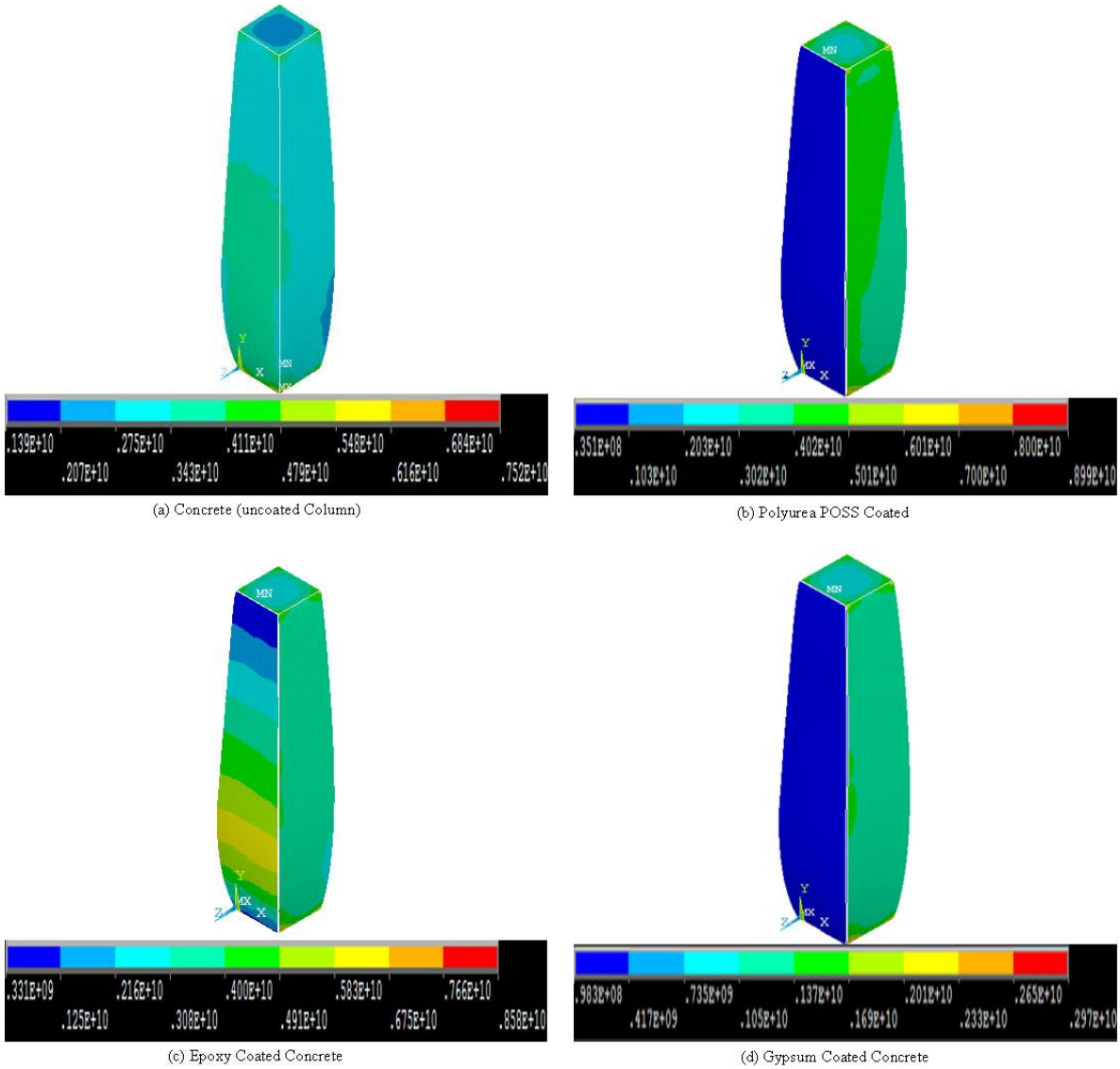

Figure 5.13. Von Mises Stress (Pa) Nodal Distribution in Concrete Coated Columns

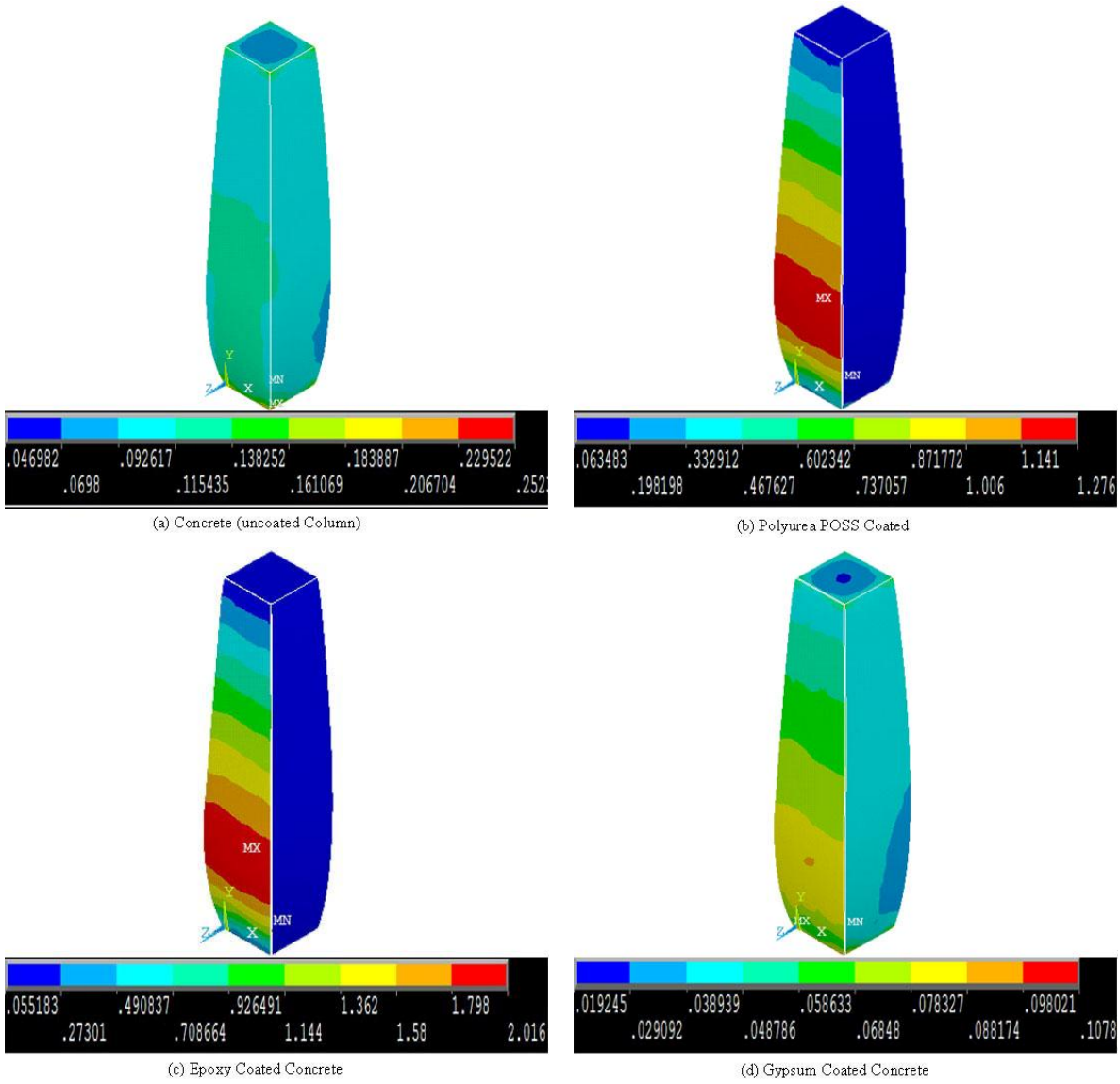

(a) Concrete (uncoated Column)

(b) Polyurea POSS Coated

(c) Epoxy Coated Concrete

(d) Gypsum Coated Concrete

Figure 5.14. Von Mises Strain Nodal Distribution in Concrete Coated Columns

To analyze the effect of the fires on the structural elements and to predict the failure subsequently concrete columns are loaded with the temperature data obtained from the finite element thermal analysis. Spatial and temporal variation, in temperature distribution, results in thermally induced stresses/strains and reduced bearing capacity. Consequently, this could lead to failure of the structure. The Von Mises stresses/strains are shown figures 5.13,5.14. Polyurea based nano-composites performed better than the epoxy based as expected and in agreement with results shown earlier from FDS simulations. Figures 5.13,5.14, demonstrate that the concrete column coated with $10mm$ gypsum performed the best in terms of least HRR, and minimal resulting structural stress/strain.

2. *Masonary Wall*

The effect of polymer reinforced composites coated masonry walls is studied using ANSYS coupled thermalstructural analysis. The maximum/minimum stresses/strains are obtained for the coated masonry walls with the blast-resistant and fire-retardant coatings. The masonry walls are exposed to the heat fluxes per unit area collected from solid phase devices installed on the front side of the masonry wall from the FDS simulations. A time dependant thermal nodal analysis is conducted to calculate the temperature nodal distribution and to apprehend the thermal response of the masonry walls. A typical nodal temperature distribution is shown in figure 5.15.

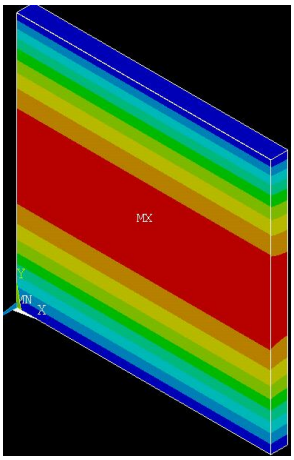

Figure 5.15. Nodal Temperature Distribution in Masonry Coated Walls

The total mechanical Von Mises stress/strains contour plots are shown in figures 5.16, 5.17. The results shown, confirm that the polyurea POSS coated masonry walls performed the best in terms of mechanical stress and strain performance, compared to the other polymeric blast-resistant coatings.

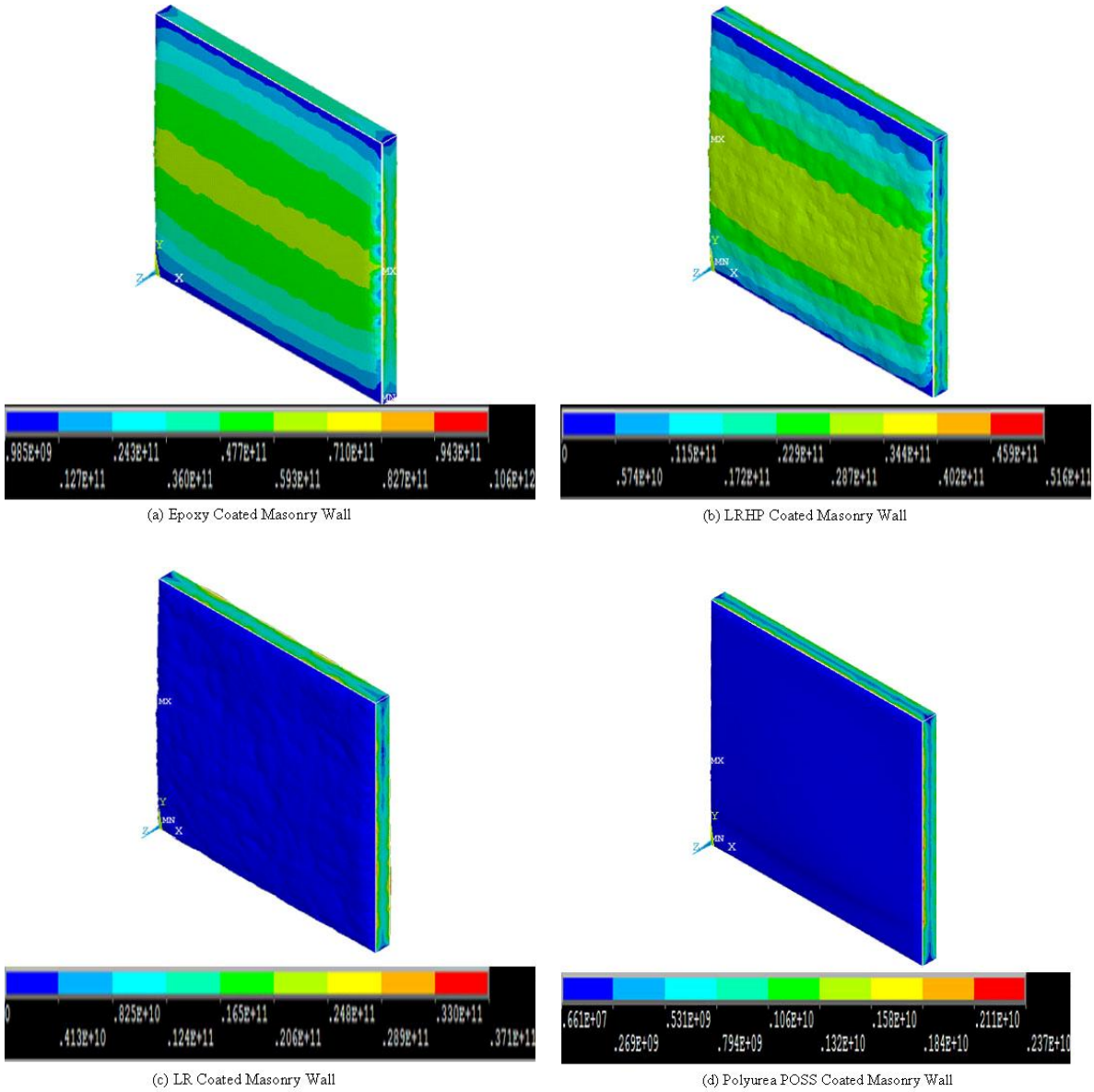

(a) Epoxy Coated Masonry Wall

(b) LRHP Coated Masonry Wall

(c) LR Coated Masonry Wall

(d) Polyurea POSS Coated Masonry Wall

Figure 5.16. Von Mises Stress (Pa) Nodal Distribution in Masonry Coated Walls

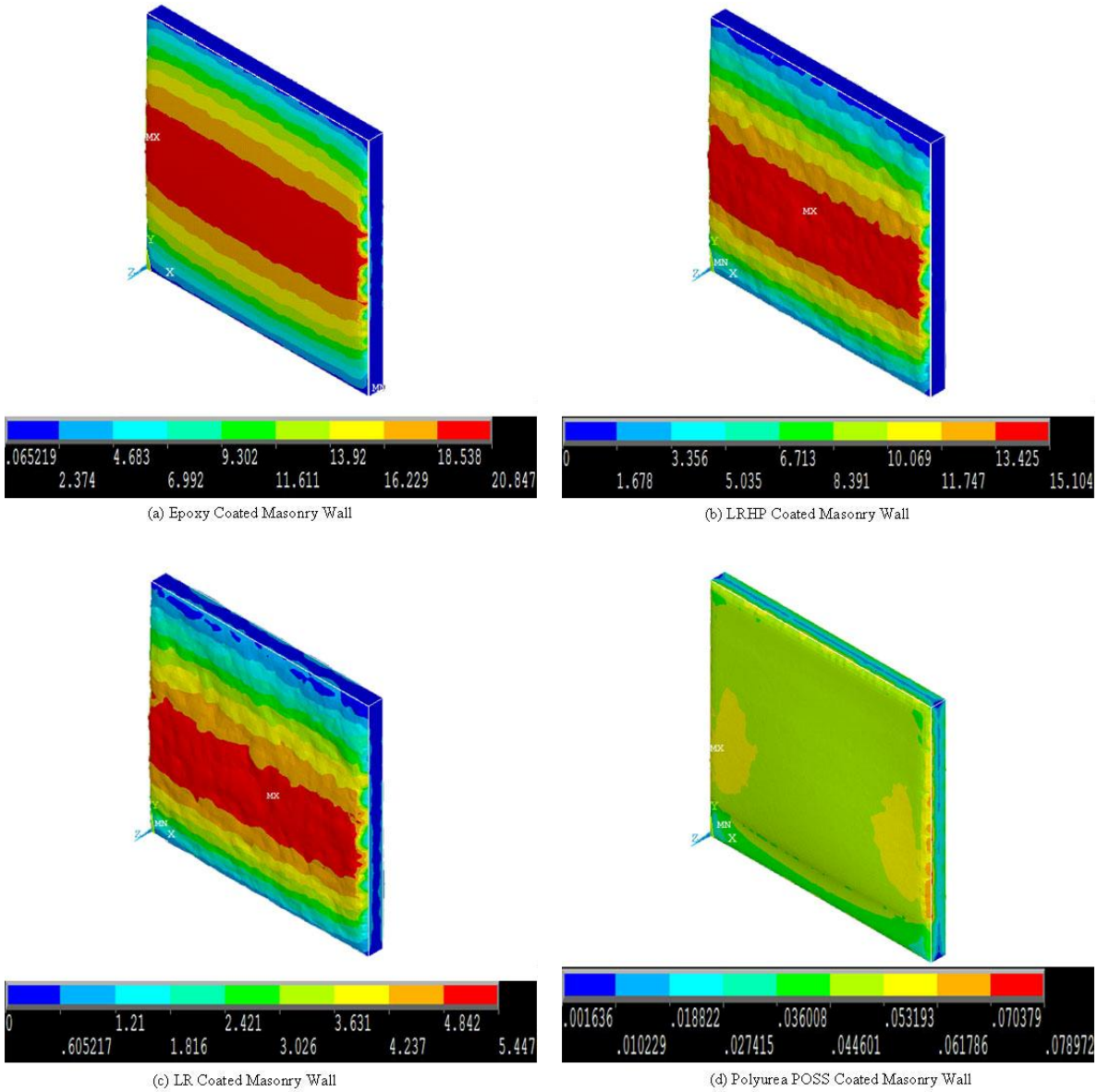

(a) Epoxy Coated Masonry Wall

(b) LRHP Coated Masonry Wall

(c) LR Coated Masonry Wall

(d) Polyurea POSS Coated Masonry Wall

Figure 5.17. Von Mises Strain Nodal Distribution in Masonry Coated Walls

6. CONCLUSIONS AND FUTURE WORK

6.1 Molecular Dynamics Simulations of Nanocomposites and Constituents

In this dissertation the various modeling schemes are investigated using MD simulations for estimating the equivalent continuum mechanical elastic constants of nano-materials composites and their constituents. These elastic constants are found to be sensitive to the nano-material geometry , and the MD simulation conditions. The analysis predicts the following conclusions and remarks:

6.1.1 Molecular Dynamics Simulations of Polymeric Matrices

- Molecular dynamic simulations calculations are studied to obtain elastic properties for several polymers, such as polyethelene,nylon6,6, vinylester, polyurea, and polyurethane
- The molecular dynamic simulations incorporate the effect on elastic properties of unit cell size, thermodynamic ensembles, initial configuration and cutoff point distance
- MD approach is compared to experimental measured values. Results show that molecular dynamic simulation approach is a reliable technique to predict the properties of

polymer material for mechanical properties prediction

6.1.2 Molecular Dynamics Simulations of Nanoreinforcements

Simulations of multi-walled carbon nanotubes

- Simulated mechanical properties of MWCNTs are sensitive to the aspect ratio of the super cell. Even by taking the advantage of periodic boundary condition, a super cell that contains several periodic unit cells is required in order to obtain finite mechanical properties. The number of repeated units of a super cell also needs to increase with the increased number of CNT walls in order to maintain a proper aspect ratio of the super cell

- The number of layers of a MWCNT poses a significant challenge for computer simulation time. Increasing the number of layers, not only increases the number of atoms in each periodic unit cell, but also increases the number of unit cells required in a super cell. For example a periodic unit cell for a three-walled carbon nanotube contains 120 atoms. With a super cell of 8 unit cells, 960 atoms are required. For a four-walled CNT, 30 unit cells are generally required, leading to 6000 atoms

- It is shown that E_{11} tends to reach a constant value when the number of CNT walls becomes three or more. This converging result may allow MWCNT to be simulated with fewer number of walls, leading to significant saving in CPU time

- It is also observed that the effect of temperature path of the simulation appears to be small. The mechanical properties are found to be dependent only on the final temperature state

- MWCNT build setup, either by individual or sequential method, does not affect the elastic constants
- The equilibrated periodic unit cells of MWCNT are not affected by the thermodynamic ensemble used to control dynamic loading
- Thermostat and barostat algorithms are some of the critical coupling effects on obtained mechanical properties of MWCNT. It is very important to choose the right combined algorithms. NVT thermodynamic is recommended to be simulated with an Anderson thermostat algorithm. For NPT thermodynamic ensemble, it is recommended to use the Berendsen barostat, coupled with Parrinello thermostat
- Results obtained from various types of loadings applied to MWCNT show that MWCNTs behaves as an equivalent linear elastic material, and are transversely isotropic

Simulations of Graphene/Graphite

- Mechanical properties obtained from MD simulations for graphene, are E_{11} of 1.3 TPa and a υ of 0.30 , in plane graphene sheet direction
- Number of layers has minimal effect on simulated mechanical engineering properties for multi layered graphite periodic cells
- Results obtained from various types of loadings applied to graphite show that graphite behaves as an equivalent linear elastic material, and is transversely isotropic

6.1.3 Molecular Dynamics Simulations of Interfacial Strength

- Interfacial strength for the graphene is found to be double the interfacial strength of the double layered of graphite
- Graphite and CNT have comparable interfacial strengths

- Vinylester bromination highly enhances the interfacial strength of vinylester nanocomposistes

The interface is an important constituent of carbon-polymer nano composites, which has been modeled in the present research with reasonable success

6.1.4 Molecular Dynamics Simulations of Nanocomposites

- Exfoliated graphene nano platelet composite simulations show improved mechanical properties in comparison with the vinylester reinforced with graphite nanocomposites

As a concluding remark, molecular dynamics is a very useful atomic simulation tool in the computation of elastic properties for nanocomposite materials as shown in this work. However, the computational time of MD simulation is tremendous for systems with large number of atoms. Fortunately faster computer hardware is more affordable, and better MD code and algorithms are currently available. Therefore, the careful selection of the forcefield, simulation and geometrical parameters, in MD simulation can vastly impact the obtained properties of interest.

It is believed that the specific findings reported in this dissertation, as well as the general conclusions drawn from the findings, may assist in the future investigation of equivalent continuum mechanics properties for nano-materials, and perhaps other carbon based nano materials.

6.2 Cementitious Nano-Material Simulations and Experimental Evaluation

This section employs the multiscale bottom-up multiscale approach to characterize the cementitious nanocomposites morphology. Our main objective of this preliminary work is to understand the basic properties and interpretation of the cementitious nanocomposites from atomic to macro scales in terms of chemical, mechanical, physical, electrical, structural, and strength aspects. Further research will drive this work for an accurate physical-chemical multiscale depicted micro, nano, and atomic models.

6.2.1 Cementitious Nanocomposite Sample Preparation

Nano C_3S is synthesized via the sol gel method. However, the C_3S is milled to a submicro particle size, under environmental exposure. Due to particle size and high-surface area, a hydration process took place pre packaging. This is concluded also through the x-ray diffraction analysis for the anhydrous and hydrated nano C_3S particles. For future investigation, it is recommend to enhance the controlled milling environment.

A TGA analysis for (G) and (FG) illustrates a certain instability for the exfoliated graphene platelets, which could be the existence of organic/inorganic impurities in the analyzed samples. However, due to high-surface area of the graphene platelets, it is hard to disperse the platelets for more than a 0.5% by weight of a w/c ratio =0.45. Several batches are prepared to achieve a suitable homogenous distribution of the exfoliated graphene platelets. For future research, chemical dispersions will be explored in details.

6.2.2 Numerical Simulation

Cementitious composites are receiving an intensive interest as a new generation of structural materials, this is due the combination of physical, chemical, strength, and high-durability properties. In order, to deliver improvement in the cement properties due nano

reinforcement, a good fiber-matrix interaction is required. An exceptional fiber attributes are only employed when a strong bond allows load transfer from the matrix to the fiber. Molecular dynamic simulations are utilized to obtain the interfacial strength between pristine graphene (G) /functionalized graphene (FG) edges -C-S-H molecular structures. The MIT C-S-H model is used in this study. Four functionalization groups are investigated: $(OH), (=O), (NH_2), (COOH)$. From MD simulations, it is shown that a good interfacial strength exists between the G-C-S-H. However, the functionalized graphene are more favorable than the pristine platelets. In addition, the interfacial strength for the FG-C-S-H composites, is variable, and dependent on the electrostatic forces of the functional group.

6.2.3 Experimental Evaluation

X-ray Powder Diffraction

The x-ray diffraction internal standard test performed indicates no chemical composition variation in the hydrated cementitious nanocomposites. Despite, the results obtained, the improvement in the mechanical properties of the cementitious nanocomposites, could be correlated to several distinct aspects. Similarly, physical interlocking, homogenization, porosity, and surface area of the nano additives.

Atomic Force Microscopy (AFM)

From the work presented in this dissertation, it has been found that the AFM is a promising technique to image and characterize the different phases of the cementitious nanocomposites. The C-S-H gel crystals are identified by spherical particles of different sizes and different packing densities. The particle sizes are in the range of $> 100nm - 500nm <$. Phase imaging for the different cementitious specimens demonstrates the effect of the nano additive on the phase formation, surface roughness, and the C-S-H structures clusters distribution. From the force deflection plots, the results exhibit an alteration in the surface adhesions, this could be due the difference in Van der Waals forces present at the specimen surface corresponding

to the different nano additives. On the other hand, the deviation in the slopes, can be correlated to the stiffnesses at the indentation position. For further precise characterizations for the relative Young's modulus values obtained, a grid indentation is required to map the different phases accurately.

Scanning Electron Microscopy (SEM)

The understanding of the phase composition of hydraulic cementitious nanocomposites should provide a new vision into early-age hydration characteristics, nano additives-cement interaction, in which will help in promoting the new materials generation. These measurements can be achieved by imposing the SEM imaging.

The SEM imaging for cementitious nanocomposites has led to the following remarks:

- From the SEM imaging for gold sputtered cementitious specimens, it is confirmed that the nano additives favor the formation of small-sized crystals of portlandite ($Ca(OH)_2$).
- For the exfoliated graphene-cement samples, the SEM imaging has distinguished a graphene platelet in the presence of a HD C-S-H, which coexists with our MD interfacial strength simulations, in which it shows a high interfacial strength in the order of 1.00 GPa between the C-S-H and the exfoliated graphene platelet.
- Some of the nano additives, such as the Nano Diamonds and the OctaTMA POSS, seem to exhibit healing properties. This is illustrated by the healed micro-cracks in some of the demonstrated SEM images.
- Nano C_3S SEM imaging, demonstrates a calcium carbonate domination. This could be due the uncontrolled milling for the unhydrated nano C_3S samples. However, a small percentage of calcium hydroxide is traced in the hydrated C_3S samples, relative to the other cementitious nano cement samples

A paramount of quantitative data can be provided for materials characterization and for

microstructural models as input for micostructure computer based models of the cementitious nanocomposite complex materials from SEM imaging.

Resonant Ultrasound Spectroscopy (RUS)

Resonance ultrasound spectroscopy is an experimental method that is conducted to measure the mechanical properties of our cementitious nanocomposites at the meso scale. RUS extracts the elastic constants from the resonance frequency of tested specimen. The results obtained from this technique for the regular cement paste are very interesting and are in the range of typical values of hydrated cement at early ages reported in the literature. For all the cementitious nanocomposites, it has shown a significant improvement in the mechanical properties. The increments in the elastic properties are promising, considering a very low weight percentage of nano additives.

Electrochemical Impedance Spectroscopy (EIS)

Electrochemical impedance spectroscopy is a quite new and effective experimental technique. Many of the electrical chemical and interfacial properties can be extracted from identical conducting electrodes adhered at the samples parallelepiped surfaces. The main objective of this study, is to optimize the electrical conductivity for use in solid state electrochemical devices and sensors. To characterize the microstructures of the cementitious nanocomposite models, in which, grains can be described, the grain boundaries of different phase composition can be identified, nano additives dispersion, and porosity.

The results can be represented in different forms, such as nyquist, phase-fequency, amplitude-frequency plots, physical equivalent circuit, and electrical permittivity. In this study, cementitious nanocomposite samples are tested for both dry and wet conditions. From the dry condition testing, it is revealed that although the nano particles are added in a very low weight percentage, it effected the electrical permittivity of the cement. However, some of the tested materials have a more conductive behavior, and others had a less conductive

behavior compared to regular cement. On the other hand, for the wet condition testing, the results are showing more deviation in the impedance characterization from the regular cement. This is concluded from the phase and amplitude plots. At dry condition, the specimens tend to have a multi-capacitance behavior.Meanwhile, for the wet testing condition,the amplitude-phase plots exhibit a resistance behavior at low frequency ranges <1Hz, contrary to dry testing conditions. However, a phase disturbance is observed, this could be affected by the microstructure, and implies phase hetrogeneity. For a future detailed characterization, equivalent circuit models will be proposed and checked into thoroughly.

Material Testing Systems (MTS)

Results obtained from this destructive testing are very promising. The purpose of conducting this test is to calculate the ultimate compressive strength of cementitious nanocomposites, and compare them to the regular cement paste. It is shown that Nano Diamond-Cement composite, performed the best among the tested cementitious nanocomposites in terms of ultimate compressive strength. A 41% increment with respect to regular cement is obtained for a w/c ratio of 0.45 and a weight percentage of 0.5% by weight nano additive. On the other hand, the OctaTMA POSS-Cement composite,showed a 21% improvement in the compressive strength, for cementitious nanocomposites with a w/c ratio of 0.45 and a weight percentage of 0.5% by weight nano additive. This could be due to many factors which include, (1) the healing properties that both materials exhibit mixed with cement, (3) due to change of packing densities of the cementitious nanocomposites, (3) compatibility with hydrated cement particles, (4) homogeneity of specimens, (5)...etc. To verify these remarks, an ASTM standardized test is required, and further micro and nano characterization are compulsory.

6.3 Experimental Evaluation and Numerical Simulations of Nano-Materials in Infrastructure Fire Applications

The polymeric nano-composite coatings had similar behavior in terms of maximum heat flux and stress/ strains. It is shown that the addition of POSS and graphene had reduced the HRR of polyurea by about 2.5%. On the other hand, addition of graphene platelets to epoxy coatings had a counter effect on the HRR, maximum heat flux, and maximum surface temperatures. The HRR has increased for the epoxy after the addition of graphene by 26%. The addition of fire retardant filler, such as LRFCF and HP for polyurea, has reduced significantly the HRR peak value by 29%. LR performed the best in terms of maximum HRR and smoke density and visibility.

6.4 Future Work

- To build a database for the advanced nanocomposite characterizations, to utilize a specific substance to deliver a desired performance efficiently
- To use the multi scale approach as a guide for fabricating and controling of nanostructures and ultimately design materials to deliver a deserted property, through MD simulations and multiscale experimental evaluation
- To obtain the equation of state parameters, and develop PHSCT computational molecular model to predict performance of new designed designed polymeric materials
- To develop a physical model that can predict with accuracy the effect of nano additives on the C-S-H packing density and on mechanical properties of cementitious nanocomposites

- To explore different w/c ratio's effect
- To examine higher weight percentage of nano additives
- To investigate in depth the nanocement production and environmentally controlled milling
- To analyze the impact on the kinetics behavior of cementitious nanocomposites
- SEM on later stages
- RUS measurements at high temperatures and pressures
- To explore the chemical dispersion technique, due to limitations of mechanical dispersion, regarding the nano additives.
- To design an Ultra High Performance Concrete (UHPC) that can be processed at room temperature, have low shrinkage, have non toxic characteristics, have compatibility with nano materials, to combine the traditional properties with new ones, and to expand on smart concrete
- To carry on more AFM measurements to obtain a reliable statistical analysis, where it is possible to derive a physical and chemical model for the C-S-H

BIBLIOGRAPHY

Bibliography

[1] Dowling A. et al. *Nanoscience and Nanotechnologies: Opportunities and Uncertainties*, The Royal Society and the Royal Academy of Engineering 2004

[2] http://en.wikipedia.org/wiki/Nanotechnology , Visited on Mar-15-2011

[3] Pitkethley, M.J.; *Nanomaterials-The Driving Force*, Materials Today 2004:7(12):20-29.

[4] Li,X.; Chang,W-C.;Chao, Y.J.; Wang, R.; Chang, M.; *Nanoscale Structural and Mechanical Characterization of a Natural Nanocomposite Material: The Shell of Red Abalone*, Nano Letters 2004:4(4):613-617

[5] Wang, R. Z.; Sou, Z.; Evans, A. G.; Yao, N.; Askay, I. A.; *Nanoscale Structural and Mechanical Characterization of a Natural Nanocomposite Material: The Shell of Red Abalone*, Journal of Materials Research 2001:16:2845-2493

[6] Lan, T. T.; Kaviratna, P. D.; Pinnavaia, T. J.; *Mechanism of Clay Tactoid Exfoliation in Epoxy-Clay Nanocomposites*, Journal of Chemistry of Materials 1995:7(11):2144.

[7] Shi, H.; Lan, T.; Pinnavaia, T.J.; *Interfacial Effects on The Reinforcement Properties of Polymer/Organoclay Nanocomposites.*, Chemistry of Materials 1996:8:1584-1590

[8] Vaia, R. A.; Price, G.; Ruth, P. N.; Nguyen, H. T.; Lichtenhan, J.; *Polymer/Layered Silicate Nanocomposites as High Performance Ablative Materials*, Applied Clay Science 1999:15(1):67-92.

[9] LeBaron, P. C.; Wang, Z.; Pinnavaia, T. J.; *Polymer-Layered Silicate Nanocomposites: An Overview* , Applied Clay Science 1999:15(1):11-29.

[10] http://minerals.usgs.gov/ds/2005/140/cement.pdf , Visited on May-10-2011

[11] Bernard O.; Ulm F.-J.; Lemarchand E.; *A Multiscale Micromechanics-Hydration Model for The Early-Age Elastic Properties of Cement-Based Materials*, Cement and Concrete Research 2003:33(9):1293-1309.

[12] Ulm. F.-J.,; Constantinides,G; Heukamp, F.H.; *Is concrete a poromechanics matieral?-A multiscale investigation of poroelastic properties*, Materials and structures Concrete Science and Engineering, 2004:37(265):43-58

[13] Feng, L.; Christian, M.; *Micromechanics Model for The Effective Elastic Properties of Hardened Cement Pastes*, Acta Materiae Compositae Sinica, 2007:24(2):184-189.

[14] Haecker, C.-J.; Garboczi, E. J.; Bullard, J.W.;Bohn, R.B.; Sun, Z.; Shah, S.P.; Voigt, T.; *Modeling the Linear Elastic Properties of Portland Cement paste*, Cement and concrete

research 2005:35(10):1948-1960.

[15] Al-Ostaz, A.; Wu, W.; Cheng, A.H.-D.; Song, C.R.; *A molecular Dynamics and Micropooromechanics Study on the Mechanical Properties of Major Constituents of Hydrated Cement*, Composites B 2009:41(7):543-549.

[16] Wu, W.; Al-Ostaz, A.; Cheng, A.H-D.; Song, C.R.; *Concrete as A Hierarchical Structural Composite Material*, International Journal for Multiscale Computational Engineering 2010:8(6):585-595.

[17] Ginebra, M.P.; Driessens, F.C.M.; Planell. J.A.; *Effect of The Particle Size on the Micro and Nanostructural Features a Calcium Phosphate Cement: a kinetic analysis*, Biomaterials 2004:25:3453-3462.

[18] Meyer, J. C.; Geim, A. K.; Kastnelson, M. I.; Novoselov, K. S.; Booth, T. J.; Roth, S.; *The Structure of Suspended Graphene Sheets*, Nature 2007:446:60.

[19] Frenkel, D.; Smit, B.; *Understanding Molecular Simulation from Algorithms and Applications*, San Diego: Academic Press, 2002.

[20] Anderson, H.C.; *Molecular Dynamics Simulations at Constant Pressure and-or Temperature*, Journal of Chemical Physics 1980:72:2384.

[21] Parrinello, M.; Rahman, H.; Vashishta, P.; *Structural Transitions in Superionic Conductors*, Physical Review Letter 1983:50(14):1073.

[22] Odegard, G.M.; Gates, T.S.; Nicholson, L.M.; Wise, C.; *Equivalent Continuum Modeling With Application to Carbon Nanotubes*, NASA ICASE report NASA/TM 2002-211454.

[23] Odegard, G.M.; Gates, T.S.; Nicholson, L.M.; Wise, C.; *Equivalent Continuum Modeling of Nano-Structured Materials*, NASA ICASE report NASA/TM-2001-210863.

[24] Li, C.; Chou, T.; *A Structural Mechanics Approach for The Analysis of Carbon Nanotubes*, International Journal of Solids and Structures 2003:40:2487-2499.

[25] Zhang, P.; Huang, Y.; Geubelle, P.H.; Klein, P.A.; Hwang, K.; *The Elastic Modulus of Single-Wall Carbon Nanotubes: A Continuum Analysis Incorporating Interatomic Potentials*, International Journal of Solids and Structures 2002:39:3893-3906.

[26] Zhang, P.; Huang, Y.; Gao, H.; Hwang, K.; *Fracture Nucleation in Single-Wall Carbon Nanotubes Under Tension: a Continuum Analysis Incorporating Interatomic Potentials*, Transactions ASME 2002:69:454-458.

[27] Arroyo, M.; Belytschko,T.; *Finite Crystal Elasticity of Carbon Nanotubes Based on The Exponential Cauchy-Born Rule*, Physical Review B 2004:69:115415.1-115415.11.

[28] Jiang, L.Y.; Huang, Y.; Jiang, H.; Ravichandran, G.; Gao, H.; Hwang, K.C.; et al.; *A cohesive Law for Carbon Nanotube/Polymer Interfaces Based on the Van der Waals Force*, Journal of Mechanics and Physics of Solids 2006:54:2436-2452.

[29] Brenner, D.W.; *A Cohesive Law for Carbon Nanotube/Polymer Interfaces Based on The Van der Waals Force*, Physical Review B 1991:42(15):9458-9471.

[30] Tersoff, J; *Empirical Interatomic Potential for Silicon with Improved Elastic Properties*, Physical Review B 1988:38:14.

[31] Yakobson, B.I.; Campbell, M.P.; Brabec, C.J.; Bernholc, J.; *High Strain Rate Fracture and C-chain Unraveling in Carbon Nanotubes*, Computational Materials Science 1997:8:341-348.

[32] Belytschko, T.; Xiao, S.P.; Schatz, G.C.; Ruoff, R.S.; *Atomistic Simulations of Carbon Nanotube Fracture*, Physical Review B 2002:65(23) -235430.1-235430.7.

[33] MS Modeling 4.0 *Online Help Manual*, Accelrys Inc., 2005.

[34] http://en.wikipedia.org/wiki/Force_field_(chemistry) *The Free Web Based Encyclopedia*, Visited on 05-01-2006.

[35] Sun, H.; Ren, P.; Fried, J. R.; *Compass: An Ab Initio Force-Field Optimized for Condensed-Phase Applications - Overview with Details on Alkane and Benzene Compounds*, Journal of Physical Chemistry B 1998:102: 7338.

[36] Gompper, G.; Schick, M.; *Soft Matter:Complex Colloidal Suspensions*, Weinheim, Wiley-VCH, 2006.

[37] Rapaport, D.C; *The Art of Molecular Dynamics Simulation*, Cambridge UK,Cambridge University Press, 1995.

[38] Mansfield, K.F.; Theodorou, D.N.; *Molecular Dynamics Simulation of Glassy Polymer Surface*, Macromolecules 1991:24(23):6283-6294

[39] Al-Ostaz, A.; Pal,G.; Mantena, P.R.; Cheng, A.H.-D.; *Molecular Dynamics Simulation of SWCNT-Polymer Nanocomposite and its Constituents*, Journal of Material Science 2008:43:164.

[40] Theodorou, D.N.; Suter, U. W.; *Detailed Molecular Structure of a Vinyl Polymer Glass*, Macromolecules 1985:18(7):1467-1478

[41] Varley, R. J.; Groth, A. M.; Leong, K. H.; *The Role of Nanodispersion on The Fire Performance of Organoclay Polyamide Nanocomposites*, Composite Science and Technology 2007:68:2882.

[42] Figiel, L.; Dunne, F.P.E.; Buckley, C. P.; *Computational Modelling of Large Deformations in Layered Silicate/PET Nanocomposites Near the Glass Transition*, Modelling and Simulation in Materials Science and Engineering 2010:18:15001.

[43] Valavala, P.K.; Odegard, G.M.; *Thermodynamically Consistent Multiscale Constitutive Modeling of Glassy Polymer Materials*, IUTAM Symposium on Modelling Nanomaterials and Nanosystems Proceedings of the IUTAM Symposium, Aalborg, Denmark 2008:19.

[44] Zeng, Q. H.; Yu, A. B.; Lu, G. Q.; *Molecular Dynamics Simulations of Organoclays and Polymer Nanocomposites*, International Journal of Nanotechnology 2008:5:277.

[45] Harkin Jones, E.; Figiel, L.; Spencer, P.; Abu Zurayk, R.; Al Shabib, W.; Chan, V.; Rajeev, R.; Soon, K.; Buckley, P.; Sweeney, J.; Menary, G.; Armstrong, C.; Assender, H.; Coates, P.; Dunne, F.; McNally, T.; Martin, P.; *Performance Enhancement of Polymer Nanocomposites via Multiscale Modelling of Processing and Properties* , Plastics, Rubber and Composites 2008 37:(2-4):113-123.

[46] Karger-Kocsis, J.; Gryshchuk, O.; Schmitt, S.; *Vinyl Ester/Epoxy-Based Thermosets of Interpenetrating Network Structures: An Atomic Force Microscopic Study*, Journal of Materials Science 2003:38(3):413-420.

[47] Derkane Momentum 640-900 *Epoxy Vinyl Ester Resin*, 2004

[48] Treacy, M. M .J.; Ebbesen, T. W.; Gibson, T. M.; *Exceptionally High Young's Modulus Observed for Individual Carbon Nanotubes*, Nature 1996:381: 680.

[49] Salvetat, J.P.; Bonard, J.M.; Thomson, N. H.; Kulik, A. J.; Farro, L.; Bennit, W.; Zuppiroli, L.J.; *Mechanical Properties of Carbon Nanotubes*, Journal of Applied Physics A 1999: 69: 255-260

[50] Ruoff, R. S.; Qian, D.; Liu, W. K.; *Mechanical Properties of Carbon Nanotubes: Theoretical Predictions and Experimental Measurements*, C. R. Physique 2003:4: 993.

[51] Li, C.; Chou, T-W.; *Elastic Moduli of Multi-Walled Carbon Nanotubes and The Effect of Wan der Waals Forces*, Composites Science and Technolgy 2003:63(11):1517-1524.

[52] Batra, R.C.; Sears, A.; *Continuum Models of Multi-Walled Carbon Nanotubes*, International Journal of Solids and Structures 2007: 44:7577.

[53] Zhang, Y. Y.; Wang, C. M.; Tan, V.B.C.; *Torsional responses of double-walled carbon nanotubes via molecular dynamics simulations*, Journal of Applied Physics 2008:103:053505.

[54] Mouras,S.; Hamm, A.; Djurado, D.; Cousseins J.-C.; *Synthesis of First Stage Graphite Intercalation Compounds With Fluorides*, Revue de Chimie Minerale, 1987, 24:572.

[55] Novoselov, K.S.; Geim, A. K.; Morozov, S. V.; Jaing, D.; Zhang, Y.; Dubonus, S.V.; Grigrieva, I.V.; Firsov, A. A.; *Electric Field Effect in Atomically Thin Carbon Films*, Science 2004:306:666-669.

[56] Novoselov, K.S.; Jaing, D.; Schedin, F.; Booth, T.J.; Khotkevich,V.V.; Morozov, S.M.; GeimA.K.; *Two-Dimensional Atomic Crystals*, Proceedings of the National Academy of Sciences of the United States of America 2005:102(30):10451-10453.

[57] Lee, C.; Wei, X.; Kysar, J.W.; Hone, J.; *Measurement of the Elastic Properties and Intrinsic Strength of Monolayer Graphene*, Science 2008:321:385-388.

[58] http://en.wikipedia.org/wiki/Graphene , visited on Aug-15-2010

[59] Lu, J. P.; *Elastic Properties of Carbon Nanotubes and Nanoropes*, Physical Review Letters 1997:79:1297-1300.

[60] Johnson, S. G.; Joannopoulos, J.D.; *Introduction to Photonic Crystals: Blochs Theorem Band Diagrams, and Gaps (But no Defects)*, Pamphlet 2003.

[61] Lu, T.; Miao, X.; Metcalf, H.; *Nonadiabatic transitions in finite-time adiabatic rapid passage*, Physical Review A 2007:75):063422.

[62] Lambin, Ph.; Meunier, V.; Rubio, A.; *Electronic Structure of Polychiral Carbon Nanotubes*, Physical Review B 2000:62(8):5129-5135

[63] Shen, L.; Li, J.; *Transversely Isotropic Elastic Properties of Single-Walled Carbon Nanotubes*, Journal of Physical Review B 2004:69 (04):045414

[64] Christensen, R.; *Mechanics of Composite Materials*, Fl, Krieger Publishing Company Malbar 1991.

[65] Rakov, E.G.; *The Chemistry and Application of Carbon Nanotubes*, Russian Chemical Reviews 2001:70:827-863.

[66] Liu, Y.; Wang, Q.; *Transport Behavior of Water Confined in Carbon Nanotubes*, Physical Review B 2005:72(8):085420.

[67] Jakubov, T. S.; Mainwaring, D.E.; *Direct Calculations of The Dispersion Interaction Between Fullerenes and Their Equation for The Potential Energy*, Adsorption 2008:14(4-5):727.

[68] Bengtzelius, U.; *Dynamics of a Lennard-Jones system closet o the glass transition*, Physical Review A 1986:34(6):5059-5069.

[69] Leach, R.A.; *Molecular Modelling Principles and Application*, Pearson Education EMA, 2001.

[70] Keidar, M.; *Factors effecting synthesis of a single wall carbon nanotubes in arc discharge*, Journal of Physics D: Applied Physics 2007: 40:2388.

[71] Levchenko, I.; Osrtikov, K.; Keidar, M.; Xu, S.; *Deterministic nanoassembly: CVD or PECVD?*, Applied physics letter 2006:89:033109.

[72] Huang, Z.P.; Xu, J.W.; Ren, Z.F.; Wang, J.H.; *Growth of highly oriented carbon nanotubes by plasma-enhanced hot filament chemical vapor deposition*, Applied Physics Letters 1998:73(26):3845.

[73] Chhowalla, M.; Teo, K.B.K.; Ducati, C.; Rupesinghe, N.L.; Amaratunga, G.A.J.; Ferrari, A.C.; Roy, D.; Robertson, J.; Milne, W.I.; *Growth Process Conditions of Vertically Aligned Carbon Nanotubes Using Plasma Enhanced Chemical Vapor Deposition*, Journal Applied Physics 2001:90(10):5308.

[74] Iijima, S.; *Helical Microtubules of Graphitic Carbon*, Nature 1991:354: 56.

[75] Ostrikov, K.; *Colloquium: Reactive Plasma as a Versatile Nanofabrication Tool*, Reviews of Modern Physics 2005:77:489.

[76] Jacques, D.; Villain, S.; Rao, A.M.; Andrews, R.; Derbyshire, F.; Dickey, E.C.; Qian, D.; *Synthesis of Multiwalled Carbon Nanotubes*, Kentucky/University of Kentucky 2003: unpublished

[77] Gao, H.; Wu, X.B.; Li, J.T.; Wu, G.T.; Lin, J.Y.; Wu, K.; Xu, D.S.; *Hydrogen adsorption of open-tipped insufficiently graphitized multiwalled carbon nanotubes*, Journal Applied Physics 2003:83:3389.

[78] Kong, J.; Franklin, N. R.; Zhou, C.; Chapline, M.G; Peng, S.; Cho, K.; Dai, H.; *Nanotube Molecular Wires as Chemical Sensors*, Science 2000:287:622.

[79] Levchenko, I.; Ostrikov, K.; Keidar, M.; Xu, S.; *Microscopic Ion Fluxes in Plasma-Aided Nanofabrication of Ordered Carbon Nanotip Structures*, Journal Applied Physics 2005:98:064304.

[80] Parrinello, M.; Rahman, H.; Vashishta, P.; *Structural Transitions in Superionic Conductors Physical*, Review Letter 1983:50(14):1073.

[81] Parrinello, M.; Rahman, H.; *Crystal Structure and Pair Potentials: A molecular Dynamics Study*, Physical Review Letter 1980:45:1196-1199.

[82] Parrinello, M.; Rahman, H.; *Polymorphic Transitions in Single Crystals: A New Molecular Dynamics Method*, Journal of Applied Physics 1981:52(12):7182.

[83] Gou, J.; Minaie, B.; Wang, B.; Liang, Z.; Zhang, C.; *Computational and Experimental Study of Interfacial Bonding of Single-Walled Nanotube Reinforced Composites*, Computational Materials Science:2004:31:225-236

[84] Wagner, H. D.;Vaia, R. A.; *Nanocomposites: issues at the interface* , Materials Today 2004:7(11):38-42

[85] Liao K.; Li, S.; *Characteristics of Carbon Nanotube-Polystyrene Interface*, Applied Physics Letters 2001:79(25):4225-4227.

[86] Xiao, M.; Sun, L.; Liu, J.; Li., Y.; Gong, K.; *Synthesis and Properties of Polystyrene/Graphite Nanocomposites*, Polymer 2002:43:2245:2248

[87] Mehta, P.K.;, Monteiro, P.J.M.; *Concrete Structure, Properties, and Materials*, Prentice Hall, New Jeresy 073632, 1987.

[88] Czernin, W.; *Cement Chemistry and Physics for Civil Engineers*, Chemical Publiching Co., New York, 1962.

[89] Aiu, M.; Huang, C.P.; *The Chemistry and Physics of Nano-Cement*, Retrieved from http://www.ce.udel.edu/cibre/reu/REU06/Aiu%20Report.pdf.

[90] Danilenko, V.V.; *On The History of the Discovery of Nanodiamond Synthesis*, Physics of the Solid State 2004: 46(4):581-584.

[91] Boikova, M.V.; Gavrilov, S.D.; Gavrilicheva, N.A.; *On The History of the Discovery of Nanodiamond Synthesis*, J. Forsyte. 2009:1:415.

[92] Osawa, M.; Inaguma, M.; Takahashi, M.; Kataoka, F.; Kruger, A.; Osawa, E.; *Preparation and Behavior of Brownish, Clear Nanodiamond Colloids*, Advanced Materials 2007:19(9):1201-1206

[93] Rosca, I.D.; Watari, F.; Uo, M.; Akasaka, T.; *Oxidation of Multiwalled Carbon Nanotubes By Nitric Acid*, Carbon 2005:43(15):3124-3131.

[94] Pellenq, R.J-M.; Van Damme, H.; *Why Does Concrete Set? The Nature of Cohesion Forces in Hardened cement based materials*, MRS Bulletin

[95] Selvam R.P.; Subramani, V.J.; Murray, S.; and Hall, K.; *Potential Application of Nanotechnology on Cement Based Materials*, Project Report MDOT 2095/3004 2009.

[96] Richardson, I.G.; Groves, G.W.; *The Microstructure and Microanalysis of Hardened Cement Pastes Involving Ground Granulated Blast-Furnace Slag*, Journal of Material Science 1992:27:6204-6212.

[97] Richardson, I.G.; *The Nature of C-S-H in Hardened Cements*, Cement and Concrete Research 1999:29:1131-1147.

[98] Taylor, H. F. W.; *Cement Chemistry*, Thomas Telford Publishing, London 1997.

[99] Jennings H. M. *A Model for the Microstructure of Calcium Silicate Hydrate in Cement Paste*, Cement and Concrete Research 2000:30(1):101-116

[100] Pellenq, R.; Kushima, A.; Shahsavari, R.; Van Vilet, K.J.; Bushler, M.J.; Yip,S.; Ulm, F-J.; *A Realistic Molecular Model of Cement Hydrates*, Proceedings of the National Academy of Sciences of the United States of America 2009.

[101] Sanchez, F.; Zhang, L.; *Molecular Dynamics Modeling of The Interface Between Surface Functionalized Graphatic Structures and Calcium-Silicate-Hydrate: Interaction Energies, Structure, and Dynamics*, Journal of Colloid and Interface Science 2008:323:349-358.

[102] Walenta, G.; Fullmann, T.; *Advances Quantitative XRD Analysis for Clinker Cements and Cementitious Additions*, International Centre for Diffraction Data 2004:47:287-296.

[103] Binning, G.; Quate, C.F.; Gerber, Ch.; *Atomic Force Microscope*, Physical Review Letter 1986:56(9): 930-933.

[104] Constantinides, G.; and Ulm, F.-J.; *The Nanogranular Nature of C-S-H*, Journal of the mechanics and physics of solids 2007:55:64-90.

[105] Tildesley, A.; *Computer Simulation of Liquids*, Oxford Science Publications, 1987.

[106] Leisure,R.G.; Willis, F. A.; *Resonant Ultrasound Spectroscopy*, Journal of Physics:Condensed Matter 1997:9(28):6001.

[107] Maynard, J.; *Resonant Ultrasound Spectroscopy*, Physics Today 1996:49(1):26-31.

[108] Wu, W.; Al-Ostaz, A.; Gladden, J.; Cheng, A.H.-D.; Li, G.; *Measurement of Mechanical Properties of Hydrated Cement Paste Using Resonant Ultrasound Spectroscopy*, Journal of ASTM 2010:5(7):2657

[109] Wang, D.; Wilkie, C.A.; *Fire Properties of Polymer Nanocomposites*, Solid Mechanics and Its Application 2006:143: 287-312.

[110] Dreisbach, J.; *Flammability characteristics of painted concrete blocks*, Master thesis University of Marylandd NIST GCR 2002:02-832: 1-101.

[111] Quintiere, J.G.; *A Simulation Model for Fire Growth on Materials Subject to a Room/Corner Test*, Fire Safety Journal, 1993:20(18):313-339.

[112] Saito, K.; Quintiere, J.G.; Williams, F.A.; *Upward Turbulent Flame Spread, in Fire Safety Science*, Proc. Of the First International Symposium, eds. C.E. Grant and P.J. Pagni, Hemisphere, Washington, DC, 1986.

[113] Quintiere, J.G.; *Fundamentals of Enclosure Fire zone Models*, Journal of Fire Protection Engineering 1989:1:99-119.

[114] Dietenberger, M.A.; *Analytical Modeling of Fire Growth on Fire-Resistive Wood-based Materials with Changing Conditions.*, In: 17th Annual BCC Conference on Flame Retardancy 2006:13-24.

[115] Clearly, T.G.; Quintiere, J.G.; *A Framework for Utilizing Fire Property Tests*, NISIR 1991:4619: 1-40.

[116] Brown, J.E.; Braun, E.; Twilley, W.H.; *Cone calorimeter evaluation of the flammability of composite materials*, Center for Fire Research 1988

[117] McGraw, J.R. Jr.; Mowrer, F.W.; *Flammability of Painted Gypsum Wallboard Subjected to Fire Heat Fluxes*, Proceedings of Interfram 1999:2:1-6.

[118] Gilman, J. W.; Jackson C.L.; Morgan A.B.; Harris, R. Jr.; *Flammability properties of polymer-layered-silicate nanocomposites. Polypropylene and polystyrene nanocomposites*, Journal of chemistry of materials 2002:12:866-1873.

[119] Prasad, K.; Baum,H.R.; *Coupled fire dynamics and thermal response of complex buildings*, Proceedings of the combustion Institute 2005:30(2): 2255-2262.

[120] McGrattan, K.B.; Hostikka, S.; Floyd, J.E.; *Fire Dynamics Simulator (Version 5), Users Guide.*, Gaithersburg, MD: National Institute of Standards and Technology NIST Special Publication 2007:1019-5: 1-230.

[121] Forney, G.P.; *Smokeview (Version 5), A Tool for Visualizing Fire Dynamics Simulation Data*, Volume I: User's Guide. Gaithersburg, MD: National Institute of Standards and

Technology NIST Special Publication 2007:1017-1.

[122] Mouritz, A.P.; Gibson, A.G.; *Fire Properties of Polymer Composite Materials*, Netherlands, Springer, 2006.

[123] ANSYS Manual *ANSYS Coupled-Field Analysis Guide*, ¡http://steflikk6.cs.binghamton.edu/ nano/nanotube/documents/guide.pdf¿

[124] Babrauskas, V.; *Development of the Cone Calorimeter A Bench-Scale Heat Release Rate Apparatus Based on Oxygen Consumption*, Fire and Materials 1984:8(2):81-95.

[125] Huggett, C.; *Estimation of Rate of Heat Release by Means of Oxygen Consumption Measurements*, Fire and Materials 1980:4(2): 61-65.

[126] Mowrer, F.W.; *The Effect of Blistering on the Ignition and Flammability of Painted Gypsum Wallboard*, Proceedings of Fire and Materials 2001.

[127] Walton, W.D., *Computer Fire Models for Enclosures*, The SPE Handbook of Fire Protection Engineering Third Edition, 2002:Chapter 7,Section, 3, pp. 3/189-193.

VITA

Hunain Said Alkhateb was born in Philadelphia-Pennsylvania, USA, in 1980. She grew up in Kansas State. However, Alkhateb moved with her family to Jordan where she received her Bachelor degree in Civil Engineering from Jordan University of Science and Technology, Jordan, 2003. Before she came to the United States in 2006, she had been working as a structural designer for 3 years at a consulting engineering office in Amman-Jordan. From 2006-2011, she was a graduate research assistant in Department of Civil Engineering, The University of Mississippi, where she pursued both her Master and Doctoral degrees in Civil Engineering with an emphasis in Micro/ Nano Mechanics.

Being at the University of Mississippi Nano Infrastructure group, Alkhateb was given exceptional opportunities to broaden her vision through a wide-variety of courses from multiple engineering disciplines; civil, mechanics of materials, mechanical, and chemical backgrounds. Throughout her graduate research studies, she accumulated a unique extensive knowledge in multiscale modeling of polymer concrete composites, with emphasis on Micromechanics and Nanomechanics. From the technical aspect, she has conducted a strong background in molecular modeling of nanocomposites (polymeric nanocomposites, and cementitious nanocomposites) and their constituents. Alkhateb has studied the damage mechanisms in composite materials using numerical-discrete modeling, correlated the detailed microstructure morphology to the local damage initiation and propagation, the effective stress-strain response and

the overall strength of composites with coated randomly arranged inclusions using statistical data collected numerically. She has developed a stochastic model to predict the strength and crack path and the joint effect of random shape, size and distribution on fracture of polymer concrete composites. From the experimental perspective, she has developed operational skills on the following instruments; sol gel cement synthesis, AFM, SEM, EIS, RUS, MTS, DMA, and TGA. She has several publications, in regards of micro mechanics, molecular dynamics simulations of advanced materials, and multiscale evaluation on cementitous nanocomposites in preparation. Alkhateb was able to distinguish herself as a motivated graduate student by receiving the graduate research achievement award 2010, dissertation fellowship award 2011, and she is a member at the national scholars honor society. Alkhateb strengthened her communication skills from working closely with diversity of people with different nationalities and backgrounds, both in academia and industry. She also learned a great deal about communicating with highly educated people national and international wise through workshops and conferences participated.